Numerical analysis of a limestone underground mine based on a room and pillar underground mine in Spain.

SANTIAGO PAYÁN DURÁN

Fakultät für Geowissenschaften, Geotechnik und Bergbau ((Faculty 3)
TU Bergakademie Freiberg
09599 Freiberg Germany
Otto-Meißer-Bau, Gustav-Zeuner-Straße 12

STATUTORY DECLARATION

Hereby, I declare that I elaborated this thesis independently, and that I have not used additional sources/resources from the indicated in the document and in the bibliography, and that all quoted material have been appropriately marked. This predisposition also applies to the images, figures and other pictorial representations.

27.03.2018 Santiago Payan

ACKNOLEDGEMENTS

First I would like to thank Prof. Dr Ing. Heinz Konietzky for his time, his patience, his constructive criticism, his technical expertise on the area, as well as his much appreciated and valuable advices and recommendations, that allowed me to bring this research to fruition.

Another special thanks goes to Dr. Ing. Raul Husillos, without whom this research will have not been possible. Thank for giving me the assistance and support necessary to establish, define and develop the research topic and the subsequent investigation.

I want to be send special regards to Dr. Ing. Martin Herbst and his colleagues at the geotechnical institute for their assistance during the computing and processing of the models, that constitute the bulk of this thesis investigation.

I will also like to thank Prof. Dr. Carsten Drebenstedt, Prof. Dr. Peter Moser and Dr. Günther Lippmann, for their support during my master studies of Advance Mineral Resources Development at the TU Bergakademie Freiberg and the Montan Universität Leoben, it was an unforgettable experience. Special thanks to the other professors that took the time to pass their knowledge to me and my fellow students and give me the tools and foundations to achieve successful career.

Finally, but not least important, I would like to thank my parents, sisters, and extended family for their unwavering support of my dreams, which have proven invaluable being so far away from home. I truly owe them all.

TABLE OF CONTENTS

Pg.

LIST OF FIGURES

Pg.

LIST OF TABLES

Pg.

LIST OF EQUATIONS

Pg.

LIST OF ANNEX

1 INTRODUCTION AND CONCEPTUAL BACKGROUND

1.1 INTRODUCTION AND OBJECTIVES

For the continuous and successful operation of an underground mining operation, the structural stability of the openings, be it adits, shafts, rises, etc., is of upmost importance. The structural stability of an opening and its surrounding rock mass can be influenced by a number of relevant factors, among which are counted the rock mass properties, the geological structure and history, the geomechanical properties of the rock, the depth, and the previous stress history. One factor that is often overlooked, but is as important as the others, is the shape of the opening.

The research topic of how the local distribution of stresses and the stability of the openings of an underground mining operation are influenced by the opening shape, and if it will be possible to extrapolate the results and conclusions to a larger operation area or even the whole rock mass and mining operation was deemed interesting and valuable from a theoretical and practical point of view. Until recently this research area has not been extensively investigated and there is a lot of valuable information and knowledge that can be gained from the study of the influence of the shape on the stability and stress distribution on planned and operating mines.

Although not common, there are varied investigations, researches and papers, backed by laboratory testing, simulations and numerical models, regarding the influence of the shape of a tunnel opening on its structure stability and stress distribution. A study by Koroneos and Theocaris (Koreneos and Theocaris, 1971) studied the influence of gravity on the stress distribution for a circular shaped tunnel. More recently, numerous studies have taken place, like the study the effect of the tunnel shape and support systems on the stability of a deep coal mine in china, with a comparison between a horseshoe shaped tunnel and an inverted arc shaped tunnel (Pinnaduwa and Srisharan, 2016), as well as a study of the wall displacement for circular, d- shaped and modified horseshoe tunnels (Rahmannejad and Ravandi, 2013), and a study about the stresses and strain redistribution for a horse shoe tunnel, a rectangular tunnel and a trapezium tunnel (Ndjaka et al. 2015). These studies have proven the influence that a tunnel or opening shape has on the stress and strain distribution, and subsequently, on the stability of an underground structure.

Nevertheless, the “Cantera de Campanzar” limestone and construction material surface and underground mine granted a very good opportunity to research the effect that the change of the shape of an opening has over the stress distribution, as well as on the stability around the pillar and the under real life conditions, on a currently active room and pillar mine.

Therefore, the objective of this master thesis is to analyze the resultant stress distribution and the stability of the rooftop of the openings and the pillars for different rectangular and horseshoe opening shapes using the distinct element modelling for an underground mine, based on the real-life conditions presented on the Cantera de Campanzar, Gipuzkoa, Spain.

1.2 DISTINCT ELEMENT METHOD

The distinct method is a numerical model designed to, through the interactions between particles like spheres or disc, efficiently solve rock mechanics problems. As illustrated by the first investigators to coin the term and postulate the main concepts behind the method, “The method is based on the use of an explicit numerical scheme in which the interaction of the particles is monitored contact by contact and the motion of the particles modelled particle by particle.” (Cundall and Stark, 1979, pg. 47). Its main difference with the standard discrete element method is that it uses deformable contacts, and an explicit time constraint solution using the non-transformed discrete method equations.

The method is based upon the concept that for a group of stressed particles in direct contact, the equilibrium between the contact forces and the displacements between particles are found through a series of calculations that trace the movements of the individual particles.

The process takes place as a dynamic method in which the speed of propagation depends on the physical properties of the discrete system and its behavior can be represented numerically using a time-stepping algorithm, in which it is assumed that the velocities and accelerations are constant within each time step. The calculation cycle of the time-stepping algorithm requires the repeated application of the law of motion to each particle, a force-displacement law to each contact and a constant update of boundaries positions. These conditions make the problem a transient type problem, were the movements of particles are the result of the propagation of disturbances originating at determined boundaries.

As established by Cundall and Stark, the velocities and acceleration are assumed constant when the time step chosen is so small, or short, that during a single step, disturbances cannot propagate from any particle further that its immediate neighbors. Since the speed at which a disturbance can propagate is a function of the physical properties of the discrete system, a time step can be calculated to satisfy this constraint.

During the progressive calculation steps, at the start of each time step, the set of contacts is updated from the known particle and boundaries positions. The force-displacement law is applied to each contact to keep an update on the contact forces, based on the relative motion between the two particles at the contact and the contact’s constitutive model. Next, the law of motion is applied to each particle to

update its velocity and position based on the resultant force and moment arising from the contact forces and any other forces acting on the particle. In addition, the boundaries positions are updated based on the specified boundaries velocities. Contacts, which may exist between two particles, or between a particle and boundaries, are formed and broken automatically during the course of a simulation. (Itasca, 2016)

“The deformations of the individual particles are small in comparison with the deformation of a granular assembly as a whole. Therefore, precise modelling of a particle deformation is not necessary to obtain a good approximation” (Cundall and Stark, 1979, pg. 49)

Due to its non-linearity and capacity to simulate the interaction between a large amount particles or blocks efficiently, without iterations or excessive usage of memory, the distinct element method is widely used for underground simulations. Among others, the distinct element method have been successfully utilized to analyze the mining induced subsidence on a coal mine (Dowding and O’connor, 1992), to analyze the seepage and stress on the coupling in a jointed rock tunnel (Wang et al, 2009), for the stability analysis of an underground tunnel with and without supports, (Fuxing et all., 2011), and more recently, for the numerical simulation of a hydraulic fracture during the fracking process (Fallahzadeh et al, 2016) and the analysis of stability of a deep coal mine (Pinnaduwa and Srisharan, 2016)

2 CANTERA DE CAMPANZAR

2.1 BACKGROUND

Located in Basque Country, Spain, de Cantera is an operating high quality limestone and construction quarry. The mine started its operation as normal surface operation quarry, but, due to the establishment of a national natural reserve on the border of the mining license area, any further expansion of the mine was severely limited. This circumstance forced the management of the mine to look for alternatives, and the underground expansion of the mine was deemed as the best solution. The mining operation continued as an underground mine using a simple room and pillar method of extraction was readily accepted. The new projected mine design, layout, expected stability and logistic and stability analysis and challenges are addressed on the future Doctoral dissertation “Strain state analysis of a limestone rock mass exposed to change due to underground excavation” by Raul Husillos Rodriguez, doctoral candidate from Universidad de Cantabria.

Figure 1. Cantera Campanzar (Calcinor, 2017)

2.2 UNDERGROUND LAYOUT DESIGN

The current underground design of the Cantera de Campanzar, Gipuzkoa, Spain, includes an extraction layout of four levels, with a typical room and pillar layout, and initial optimal operational openings of 6 m height, 20 m length and 20 m width, to be expanded to a 20 m height, 22 m length and 22 m width for the uppermost level – Level 1, once the development phase is completed and the extraction process starts.

Consequently, the pillar dimension for the 1st level pillars will be 22 m width (See Figure 2). At lower depths, to improve the stability, the designed room area of extraction decreases and the pillars dimensions increase as shown in Figure 3, Figure 4, and Figure 5.

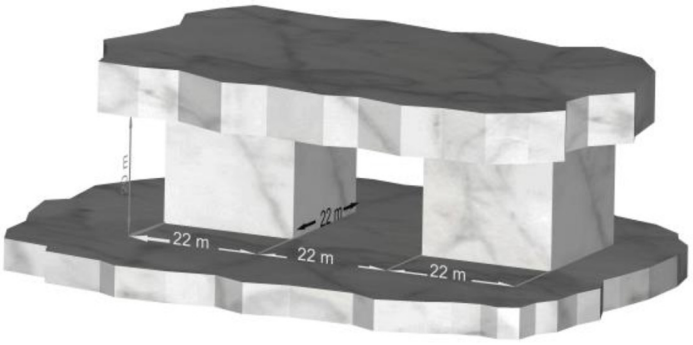

Figure 2. Room and pillar layout uppermost - Level 1 (Castro, 2015)

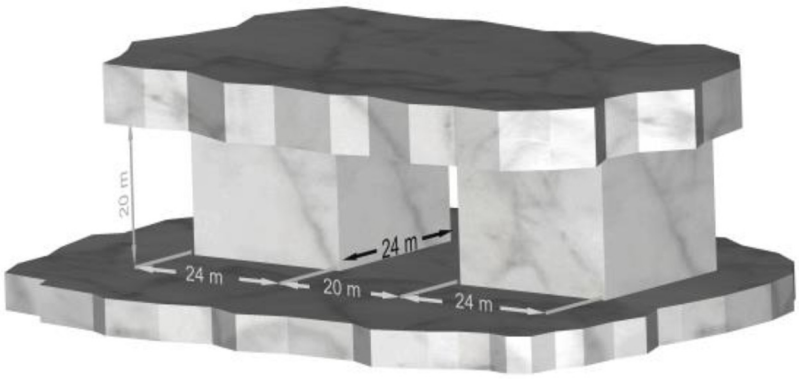

Figure 3. Room and pillar layout - Level 2 (Castro, 2015)

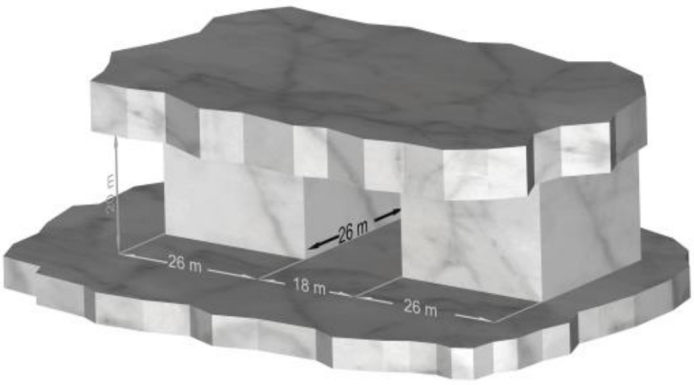

Figure 4. Room and pillar layout - Level 3 (Castro, 2015)

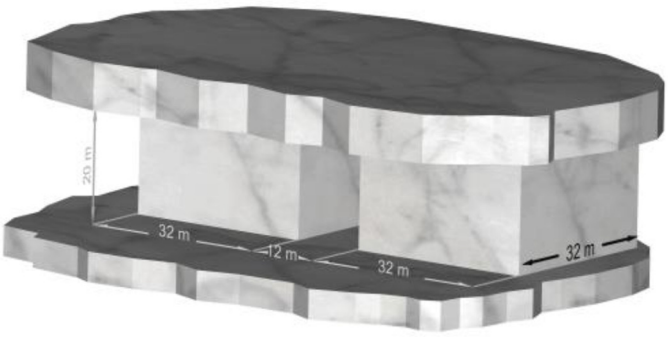

Figure 5. Room and pillar layout - Level 4 (Castro, 2015)

2.3 GEOTECHNICAL SURVEYS

The lithology of the quarry is characterized by massive orogenic limestone from the superior Cretaceous. For a complete summary of the lithology, petrography, geology, geotechnical investigation, laboratory tests, essays, and its corresponding results, please consult the geotechnical and geological report for the Cantera de Campanzar (Castro, 2015)

In total, 15 geotechnical surveys were conducted, 13 without extract test tube and two using the Shelby extract test tube. The mechanical surveys are shown on the Table 1.

Table 1. Geomechanical surveys

Survey	Angle (º)	Length (m)	Further Use

ST-1	90	71	Testing, Video camera monitoring
ST-2	90	71	Testing, Video camera monitoring
S-1	90	64	Video camera and ultrasonic monitoring
S-2	70	50	Video camera monitoring
S-3	70	48	Video camera and ultrasonic monitoring
S-4	90	70	Video camera monitoring
S-5	90	62	Video camera and ultrasonic monitoring
S-6	90	70	Video camera monitoring
S-7	90	70	Video camera monitoring
S-8	90	70	Video camera monitoring
S-9	90	67	Video camera monitoring
S-10	70	50	Video camera monitoring
S-11	70	50	Video camera monitoring
S-12	70	50	Video camera monitoring
S-13	70	50	Video camera monitoring

The geomechanical parameters were obtained from the 2 surveys using Shelby extract test tube, in two different sectors, phase I and II. The parameters obtained were used to evaluate and identify the rock mass and joint and fractures

geomechanical parameters. From the others surveys, the information about the direction of fractures and their dip was obtained. Using the video monitoring, it was possible to recognize the general state of the borehole and the rock mass, as well as the numbers of joints present inside. This is important because it provides, not only the number of joints, but also it shows the real condition of the joints, as well as it thickness and filling.

2.3.1 Geological structure and conditions

The rock mass is heavily fractured, with a complex geological structure and history, characterized by 6 main faults and several joints, that form identifiable joint families. The main faults show a local area influence and the identified joints families are not presents in the all of rock mass. The mine operation area was divided on two areas, which are cataloged as North and South, separated by the fault Nº 6. The areas show dissimilar geological conditions, and were evaluated independently.

6 main faults were observed on site, and were further identified by the geomechanical surveys introduce before. The faults and its direction and dip are shown on the following table (Table 2) and are illustrated on the Figure 6.

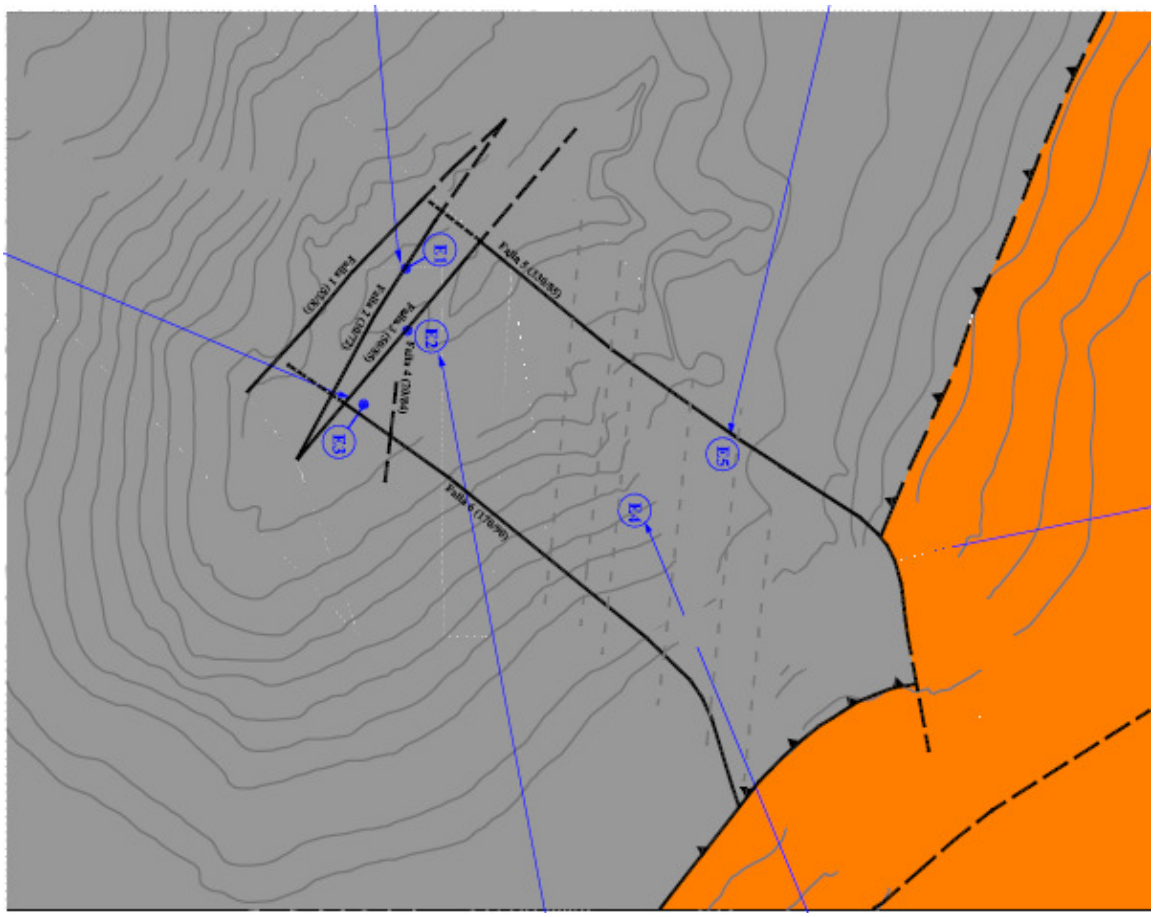

Figure 6. Main faults and its dip and direction (Castro, 2015)

Table 2. Main Faults on the mine site

Faults	Direction/Dip (º)
Fault 1	55/83
Fault 2	30/72
Fault 3	50/85
Fault 4	20/84
Fault 5	330/85
Fault 6	170/90

Additionally, seven joint families and 2 sub-families were identified and are shown on the Table 3 for the north zone, and on Table 4 for the south zone.

Table 3. Joint families and sub-families North zone

Joint Family	Direction/Dip (º)
Joint 1º	33/56
Joint 2	183/43
Joint 2 (bis)	120/60
Joint 3	219/32

Table 4. Joint families and sub-families South zone

Joint Family	Direction/Dip (º)
Joint 1º	27/59
Joint 2	182/44
Joint 4	134/89
Joint 4 (bis)	295/82
Joint 5	21/86
Joint 6	282/43
Joint 7	57/30

2.3.2 Geomechanical properties

The obtained samples of the 2 Shelby tube perforations were subjected to several tests to determine the geomechanical properties of the rock and the joints. The samples were selected from different depths with the purpose to obtain representative results for the whole rock mass.

After testing the obtained Shelby tube samples under a simple compressive strength essay, the following compressive strength, young modulus, shear modulus, and Poisson ratio results were obtained. (Table 5)

Table 5. Simple compressive strength test results

Sample	Depth (m)	Lithology	σc (MPa)	E (GPa)	G (GPa)	v
ST1-M	31,15	Limestone North zone	72,12	65,33	40,18	0,23
ST1-M	52,00	Limestone North zone	76,11	50,56	27,55	0,09
ST1-M	58,00	Limestone North zone	86,63	163,04	-	
ST2-M	20,90	Limestone South zone	95,96	162,02	91,54	0,13
ST2-M	60,70	Limestone South zone	138,47	74,205	46,38	0,25

Then, other samples were subjected to simple tensile strength essays, the results of which are shown on the Table 6.

Table 6. Simple tensile strength test results

Sample	Depth (m)	Lithology	σt (MPa)
ST1-M	11,00	Limestone North zone	7,37
ST1-M	21,00	Limestone North zone	3,83
ST1-M	41,00	Limestone North zone	7,31
ST1-M	51,30	Mineralized zone	2,46
ST1-M	58,30	Limestone North zone	4,46
ST2-M	12,25	Limestone South zone	5,92

ST2-M	21,35	Limestone South zone	5,69
ST2-M	34,50	Limestone South zone	5,69
ST2-M	52,85	Limestone South zone	4,50
ST2-M	64,70	Limestone South zone	5,18

The cohesion and internal friction angle were obtained from triaxial tests, and are shown on the Table 7.

Table 7. Cohesion and internal friction angle

Sample	Depth (m)	Lithology	C (MPa)	ϕ(º)
ST1-M	11,00	Limestone North zone	3,6	72
ST1-M	21,00	Limestone North zone	4,9	65
ST1-M	41,00	Limestone North zone	3,5	61
ST1-M	51,30	Limestone North zone	6.1	65
ST1-M	58,30	Limestone North zone	18,5	46
ST2-M	12,25	Limestone South zone	8,2	62
ST2-M	21,35	Limestone South zone	7,9	62
ST2-M	34,50	Limestone South zone	7,6	60
ST2-M	52,85	Limestone South zone	8,9	63

The parameters for the joints (joint cohesion and joint internal friction angle) were obtained through a direct cut test and in the average results are illustrated at Table 8.

Table 8. Joint geomechanical parameters

Joint family	C (MPa)	ϕ(º)
J1, J2(bis)	0,20	31
J6	1,31	17
J3, J7	0,69	39
J2	0,41	11
J4, J4(bis),J5	0,49	27

The average measure of the density tests for the intact rock was 2,68 gr/cm^3

2.3.3 Rock Mass Rating (RMR)

Using the Bieniawski rock mass classification method, the following summary values for the two zones were obtained. The average results are shown on the Table 9 for the north zone and Table 10 for the south zone.

Table 9. Bieniawski rock mass rating north zone

RMR	Rock classification	Erm (GPa)	C (MPa)	Φ (º)
76	Good rock mass Class II	44,53	3	35

Table 10. Bieniawski rock mass rating south zone

RMR	Rock classification	Erm (GPa)	C (MPa)	Φ (º)
67	Good rock mass Class II	28,05	2.94	35

3 METHODOLOGY AND MODEL DESIGN

3.1 METHODOLOGY CONSIDERATIONS

As stated on Chapter 1., the objective of this study was to analyze the stress distribution and the stability of the pillar and rooftop for different sized rectangular and horseshoe opening shapes on an underground limestone quarry using distinct element modelling, based on the real life conditions presented on the Cantera de Campanzar.

After discussion, it was determined that modelling one or more horizontal mine openings at a significant depth was the best alternative to recreate the real life conditions and behavior, as well as to achieve the objectives for a small regulated area, that can be later extended to a more global scale. As explained before in Chapter 1.2, the distinct element modelling method was chosen due to its ability and capacity to closely recreate the behavior and conditions of a highly fractured sedimentary rock mass, as it considers the behavior and interaction of each formed block individually. The method allows finite displacements and rotations of discrete blocks, and recognizes new contacts automatically as the calculation progresses, allowing a greater accuracy and precision at the moment of modelling the behavior and reactions of the rock mass, not as whole, but as individual blocks interacting with each other. The selected Software for the modelling was the distinctive element modelling software 3dec 5.02.213 from Itasca, which code allows to efficiently create, recreate, analyze and evaluate the various models using the distinct elements numerical method.

Once the adequate modelling method was elected, the next step was limit the scope of the model, as there were some hardware and time consideration to be taken in account. Given that the aim of the study was to compare the stress distribution and the stability of the openings for different size shapes, multiples models and its corresponding analysis were expected. This severely restricted the time of computation, the spacing of the tetrahedral zone grid, the size of the modeled region and, overall, the amount of blocks of the subsequent studied models.

Therefore, the models were designed with these restrictions on mind. The spacing of the tetrahedral grid was constrained between detail and computation velocity, the amount of original identified joints had to be grouped and reduced to decrease the number of blocks on the model, the depth of the analyzed model, and the amount of analyzed shapes. The size of the block model was determined by the size and amount of the openings, the analyzed depth, and the shape of the opening.

The size and shape of the evaluated openings were selected taking under consideration the previous conditions on the mine, and the mine layout and development. Additionally, to the original planned opening, 3 more representative horseshoe shaped openings of variable radius were deemed enough for the study.

Additionally, as illustrated on the Section 2.2, the Cantera de campanzar is operated as a standard pillar room mining operation, which means that the extraction openings are oriented in different semi-perpendicular directions. To represent the faults and joints on the selected different shaped and sized openings, the chosen design joints were rotated 60º and 120º degrees to more accurately replicate their influence on the openings. To further limit the time and amount of variables, the south area was chosen, given that is the largest area and were most of the extraction operations take place, and were its possible to find the longest and most representative joint families, allowing the models a discrete, but also precise characterization of the real life conditions.

Also, due to the high variance of between the geotechnical properties of the rock and joints (see Table 5, Table 6, Table 7, Table 8) on the different zones of the mine, and that the objective is to generate a general calibrated model for the mine, it was deemed necessary modifying the geomechanical properties of the joint families, to more accurately replicate the mine real life conditions.

Therefore, a total of 36 models with variable shapes, joints dip and geomechanical properties were evaluated during the investigation. (See Equation 19)

3.2 BASIC MODEL DESIGN

3.2.1 Basic model block dimensions

The standard block dimensions considered adequate for the modelling needs were defined as 120 m length, 20 m width and 50 m height, large enough to adequately represent the selected modelling region without being overly large. For computational velocity, the creation of an inner region was deemed necessary, where the tetrahedral grid will be closer together and therefore, allow a more detailed computation, which allows an adequate analysis of the model behavior on the area around the openings. This area had a length of 96 m, width of 20 m and height 32 m. The tetrahedral grid spacing was established in 2 m for the outer region and of 1 m for the inner region.

The Figure 7. and Figure 8. show the basic block model layout.

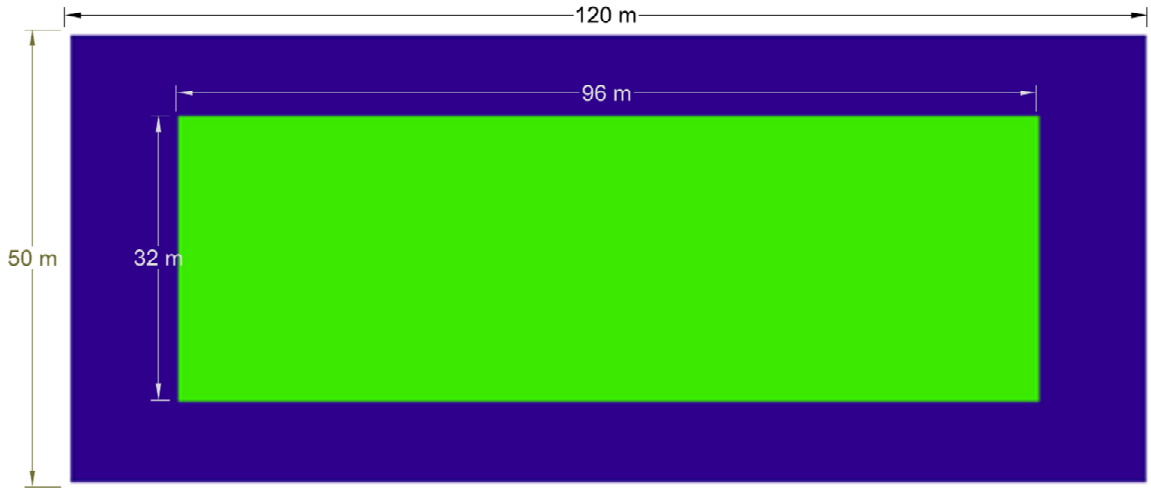

Figure 7. Basic block model Front view

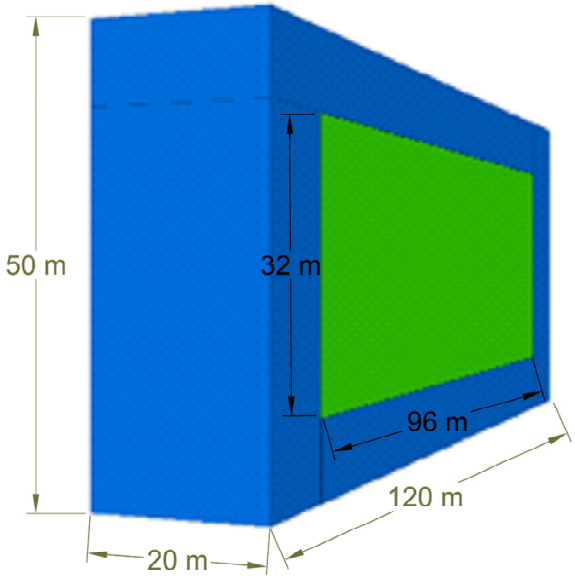

Figure 8. Basic block model Side view

3.2.2 Basic model opening layout

As pointed in the last section (3.1), the scope was restricted to 4 different shapes. The original rectangular opening currently used in extraction and three horseshoe shaped openings with different radius. The rectangular opening selected dimensions were 20 m length and 6 m height, with pillars of 8 m width. Due to time and resources constraints, the decision was made to model 3 parallel openings, as it was considered representative enough for a room and pillar operation, as well as allow the analysis of the critical condition on the middle opening and its pillars. The model layout with the 3 rectangular openings is shown in the Figure 9.

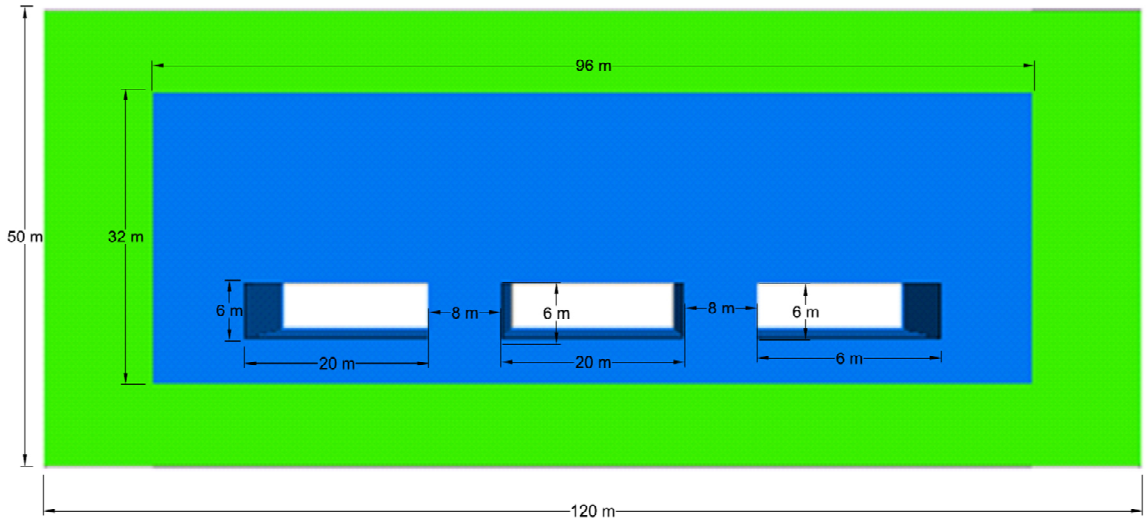

Figure 9. Layout of the rectangular openings model

3.2.3 Basic model intact rock geomechanical properties

The following step was defining the geomechanical properties for the rock mass. The model input parameters regarding the intact rock geomechanical properties were the density, the young modulus, the Poisson ratio, the cohesion, the compression strength, the tensile strength, internal friction angle, and dilation angle of the rock. The previous geotechnical explorations and essays performed on samples collected from perforations with Shelby tube on the mine, see Table 5, Table 6, Table 7, Table 8, Table 9, and Table 10, provided the intact rock geomechanical and rock mass properties. For the modelling, only the parameters from the south area where chosen, for the reasons explained on the previous section (3.1).

Using a weighted average of the values of the Compression strength, Tensile strength, Cohesion, internal friction angle, Young modulus, Shear modulus and dilation angle the respective values where calculated.

$$Compression\ strenght\ weighted\ average\ (MPa) = \frac{95{,}96+138{,}47}{2} = 112.79 \quad \textbf{Equation 1}$$

$$Tensil\ strenght\ weighted\ average\ (MPa) = \frac{5{,}92+5{,}69+5{,}69+4{,}50+5{,}18}{5} = 5{,}4 \quad \textbf{Equation 2}$$

$$Internal\ friction\ angle\ weighted\ average\ (º) = \frac{62+62+60+63}{4} = 63 \quad \textbf{Equation 3}$$

$$Cohesion\ weighted\ average\ (MPa) = \frac{8{,}2+7{,}9+7{,}6+8{,}9}{4} = 8{,}15 \quad \textbf{Equation 4}$$

$$Young\ modulus\ weighted\ average\ (GPa) = \frac{162{,}02+74{,}20}{2} = 118{,}11 \quad \textbf{Equation 5}$$

$$Shear\ modulus\ weighted\ average\ (GPa) = \frac{91{,}54+46{,}38}{2} = 68{,}95$$ **Equation 6**

$$Dilation\ angle\ weighted\ average\ (°) = \frac{19+14+13+15}{4} = 15$$ **Equation 7**

Moreover, the bulk modulus was calculated from the average Young modulus through the following equation. (Equation 8) (Fossum. A.F,1985)

$$K\ (GPa) = \frac{E}{3\times(1-2v)} = \frac{118{,}11\ GPa}{3\times(1-2\times0{,}2)} = 65{,}50\ GPa$$ **Equation 8**

Where:

E= Weighted average young modulus

V= Measured Poisson coefficient

The summary of the intact rock geomechanical properties can be observed in the Table 11.

Table 11. Intact rock geomechanical properties

Property	Value	Units
Density	2680	kg/m3
Depth	100	m
Compression strength (σc)	112,79	MPa
Tensile strength (σt)	5,4	MPa
Cohesion	8,15	MPa
Internal friction angle	62	º
Dilation angle	15	º
Young modulus (E)	118,11	GPa
Shear modulus (G)	68,95	GPa
Poisson ratio (v)	0,20	-
Bulk modulus (k)	65,60	GPa

Additionally, to truly comprehend the behavior of a heavily fractured rock and its joints is necessary to evaluate the rock mass properties. The data values were obtained of previous essays and calculations, as shown on the Table 10. See a summary of the values con in the following table. (Table 12)

Table 12. Rock mass properties

Property	Value	Units
RMR	76	Good Rock
Rock mass Young's modulus	28,05	GPa
Cohesion	0,3	MPa
Internal friction angle	35	º
Rock mass shear modulus (G)	17,50	GPa

3.2.4 Basic model joints geomechanical properties

The next step was defining the joints and faults to be implemented in the model. As shown on the Table 4, there were 7 principal joint families identified on the field. Of these, the families J2, J6 and J7 were identified as the principal joints founded on the rock mass, and act predominantly on the south area. Due to time and computational constraints, as explained at Chapter 1.1, these were the selected joints implemented for the model. The measured spacing between joints on the field was 1 to 2 m, being 2 m the chosen spacing for the models. These considerations allowed to keep the evaluated number of blocks within a manageable amount.

The modelling's input parameters regarding joint geomechanical properties where the joint dip, the joint dip direction, joint normal stiffness, joint internal friction angle, joint shear stiffness joint cohesion and the joint tensile strength. The previous geotechnical explorations and essays performed on samples collected from the perforations with Shelby tubes on the mine site (see Table 4 and Table 8), provided the dip and dip direction of the pertinent joint, the joint internal friction angle and the preliminary cohesion.

Additionally, the joint normal stiffness was calculated using the Equation 9. (Gerrard, 1982)

$$Kn = \frac{EM \times Er}{S\,(Er - Em)} = \frac{28{,}05\ GPa \times 118{,}11\ GPa}{2\ m\ (118{,}11\ GPa - 28{,}05\ GPa)} = 18{,}4\,\frac{GPa}{m} \qquad \textbf{Equation 9}$$

Where:

Em = rock mass Young's modulus;

Er = intact rock Young's modulus;

kn = joint normal stiffness; and

s = joint spacing

Likewise, the joint shear stiffness was calculated using the Equation 10. (Gerrard, 1982))

$$Ks = \frac{17{,}50\ GPa \times 68{,}95\ GPa}{2\ m\ (68{,}95\ GPa - 17{,}50\ GPa)} = 11{,}80\ \frac{GPa}{m}$$ **Equation 10**

Where:

Gm = rock mass Shear modulus;

gr = intact rock Shear modulus;

ks = joint shear stiffness; and

s = joint spacing

The basic model layout with the implemented joints and geomechanical properties is shown on the Figure 10. To improve the computation speeds and reduce the number of blocks, the joints were not applied to the outer block, given the reduced influence displacement and stresses on this zone will have on the openings.

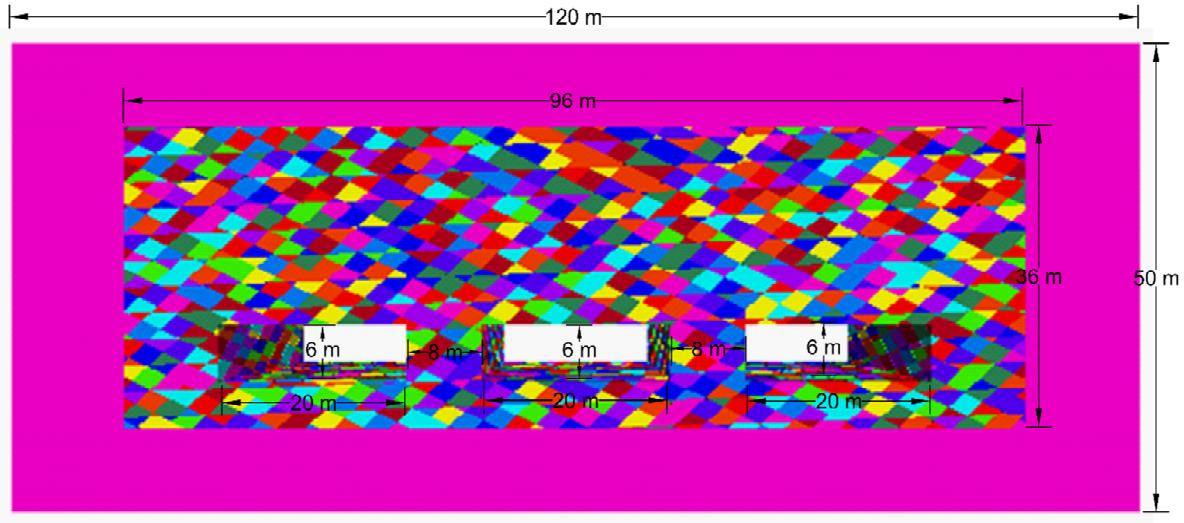

Figure 10. Implemented joints on the basic model layout

Although the cohesion was measured on the field, the huge variability between the obtained data, added to the objective of generating a general calibrated model for the mine that applies for most of the conditions of the mine, led to the decision of varying the cohesion and the tensile strength as the main geomechanical parameters. The tensile strength was obtained from the literature of rocks masses with similar joint properties. (Goodman, 1980)

The summary of the intact rock geomechanical parameters can be observed in Table 13.

Table 13. Joint families and properties

Joint Family	Dip	Dip Direction	Joint cohesion	Internal friction angle	Joint normal stiffness	Joint shear stiffness	Joint tensile strength
Units	(º)	(º)	MPa	(º)	GPa/m	GPa/m	MPa
J2	44	182	3.0	31	18,40	11,80	0,8
J6	43	282	3.0	17	18,40	11,80	0,8
J7	30	57	3.0	39	18,40	11,80	1,0

3.2.5 Basic model depth selection

For the analysis, a depth of 67 m under the top of the mountain was selected, located on the superior surface of the 50 m deep block. This depth represents the lower levels of the mine, allowing the modelling of some of the highest expected loads and stresses experienced by the openings structure during the operation of the mine.

3.2.6 Basic model in-situ initial stresses and boundary conditions and constraints

Once the depth for analysis was selected, it was possible to calculate initial stresses working on the basic model. The vertical stress was calculated at the depth that represented by the superior surface of the model, namely 67 m. An unsaturated condition was assumed as the rock is classified as good and the continuous water management operations performed for the mining operations. The working vertical stress was calculated using the measured density (see Table 11), as shown in the Equation 11.

$$\sigma v = depth \times density \times gravity = 67\,m \times 2680\,\frac{kg}{m^3} \times 9{,}81\,\frac{m}{s^2} = 1761483{,}6\,Pa \quad \textbf{Equation 11}$$

The horizontal stresses were assumed as isotropic and were calculated as shown in the Equation 12.

$$\sigma h = \sigma v \times 0{,}5 = 1761483{,}6\,Pa \times 0{,}5 = 880741{,}8\,Pa \quad \textbf{Equation 12}$$

To model the increase stresses with depth, a gradient in the three dimensions that is applied by depth (z direction) was implemented. This gradient was calculated according to the following equations. (Equation 13, Equation 14, and Equation 15)

$$z\ gradient\ in\ z\ direction = density \times gravity \times m = 2680\ \frac{kg}{m^3} \times 9{,}81\ \frac{m}{s^2} \times m = 26290{,}8\frac{N}{m}$$ **Equation 13**

$$x\ gradient\ in\ z\ direction = zgradient \times 0{,}5 = 26290{,}8\frac{N}{m} \times 0{,}5 = 13145{,}4\frac{N}{m}$$ **Equation 14**

$$y\ gradient\ in\ z\ direction = zgradient \times 0{,}5 = 26290{,}8\frac{N}{m} \times 0{,}5 = 13145{,}4\frac{N}{m}$$ **Equation 15**

Since the mine is located under a mountain and one of the aims of the investigation is to calibrate the model for the field conditions, the influence of the topography on the vertical stress was also taken into account. Since the overall slope gradient of the mountain was measured as 0,46, a gradient in the horizontal (x direction) can be calculated for the three dimensions, as shown in the Equation 16, Equation 17 and Equation 18.

$$z\ gradient\ in\ x\ direction = density \times gravity \times m \times Overall\ slope\ gradient = 2680\ \frac{kg}{m^3} \times 9{,}81\ \frac{m}{s^2} \times m \times 0{,}46 = 12122{,}98\frac{N}{m}$$ **Equation 16**

$$x\ gradient\ in\ x\ direction == zgradient \times 0{,}5 = 12122{,}98\frac{N}{m} \times 0{,}5 = 6061{,}49\frac{N}{m}$$ **Equation 17**

$$y\ gradient\ in\ x\ direction = zgradient \times 0{,}5 = 12122{,}98\frac{N}{m} \times 0{,}5 = 6061{,}49\frac{N}{m}$$ **Equation 18**

A summary of the basic model in-situ stresses and boundaries conditions and constraints are shown in the Table 14.

Table 14. In-situ stresses and boundaries conditions and constraints

Property	Value	Units
Depth	67	m
σv	1761483,6	Pa
σh	880741,8	Pa
z gradient in z direction	26290,8	N/m

x gradient in z direction	13145,4	N/m
y gradient in z direction	13145,4	N/m
Slope gradient	0,46	-
z gradient in x direction	12122,98	N/m
x gradient in x direction	6061,49	N/m
y gradient in x direction	6061,49	N/m

The gravity was implemented separately from the in-situ stresses; therefore, the stresses were introduced in as derived stresses (Kg/m^2) in the model code.

Additionally, to implement the boundary constraints, a velocity of 0 m/s was applied on the faces of the block, with the exception of the top boundary of the model, where the force will be applied, and deformations are expected.

The boundary conditions and constraints are illustrated on the following picture. (Figure 11)

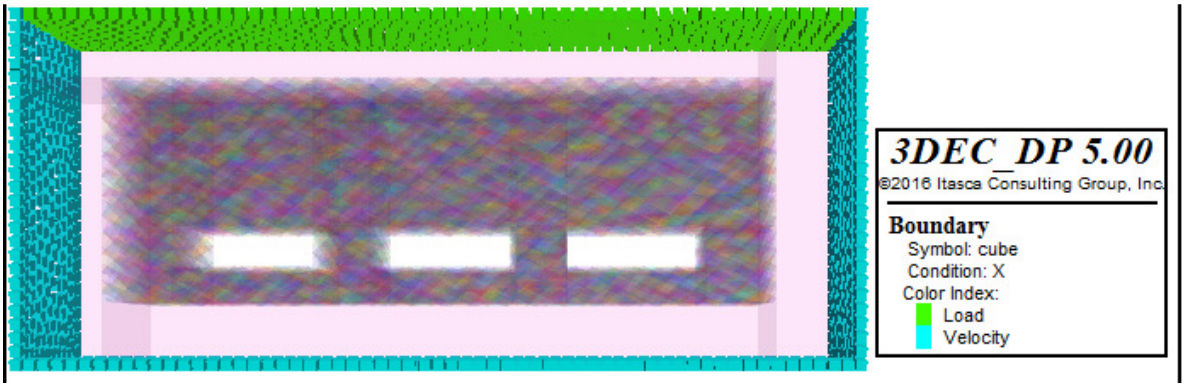

Figure 11. Basic block and boundary conditions

3.2.7 Balancing forces and stability measurements

Finally, the basic model is complete and ready to be executed. The first part of the process consists on balancing the forces of the model through calculation steps. The second part of the process consist on excavating the tunnels, and evaluate the subsequent steps until the forces are balanced, and the model is in equilibrium. During the computation process, several representative points were chosen on the rooftop of each opening, the middle pillars, and the extreme edges of the openings, as observed in the Figure 12. On these points, the velocity, displacement and force

balance was evaluated, to verify the stability of the model as well as to check that the model had achieved convergence.

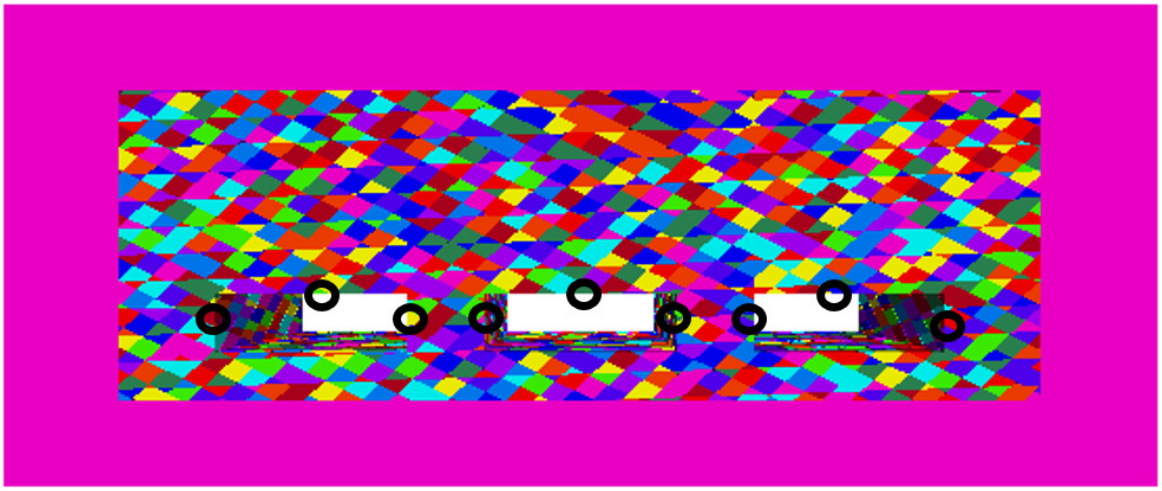

Figure 12. Location of the reference points

4 MODELATION OF THE DIFFERENT OPENINGS MODIFYING THE SHAPE, THE JOINTS FAMILIES DIP, AND THE COHESION AND TENSILE STRENGTH OF THE JOINTS

4.1 MODIFYING OPENINGS SHAPE AND DIMENSION

The first modification on the basic model was changing openings shape and dimension. Taking into account the considerations on Chapter 3.1., the chosen modified shape to modify the current rectangular shape opening to was that of a horseshoe, with a progressively bigger radius. The first radius was defined by the concentration of the maximum principal stress over the middle opening roof. The height of the area of concentration on the min stresses was measured at 2,5 m, as shown on the Figure 13. It is very important to highlight that due to 3dec nomenclature standard, the Maximum and Minimum principal stresses showed by the plotting tools represent the opposite to the chosen force direction.

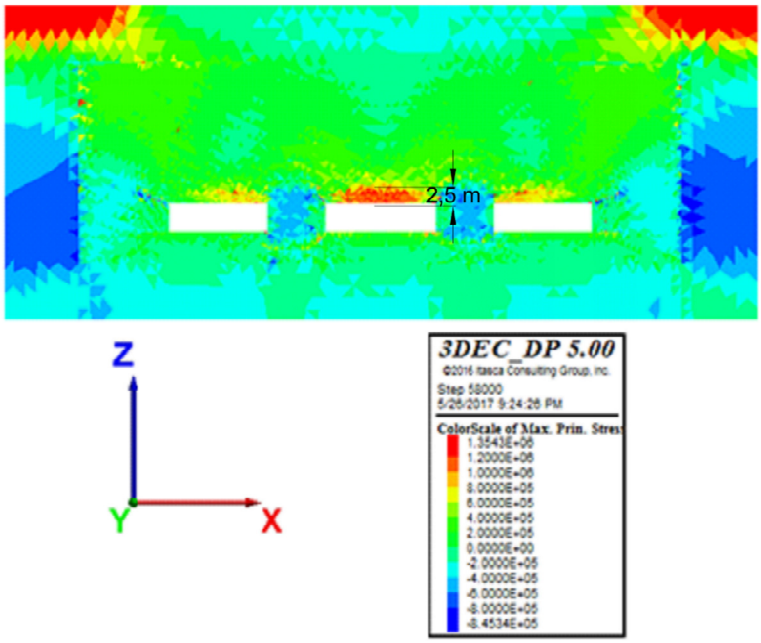

Figure 13. Basic layout model. Max. principal stresses (Pa)

Therefore, the first implemented modified radius was 2,5 m. Subsequently, the two other radius were selected, 3x the original radius (7,5 m). and 5x (12,5 m) times the original radius. A summary of the implemented shapes is shown on the following table (Table 15). The layout of the model with the 2,5 m radius horseshoe shape, 7,5 m radius horseshoe shape, and 12,5 m radius horseshoe shape are shown on the Figure 14, Figure 15, Figure 16.

Table 15. Modified implemented shapes

Shape	Radius (m)
Rectangular	NA
Horseshoe	2,5
Horseshoe	7,5
Horseshoe	12,5

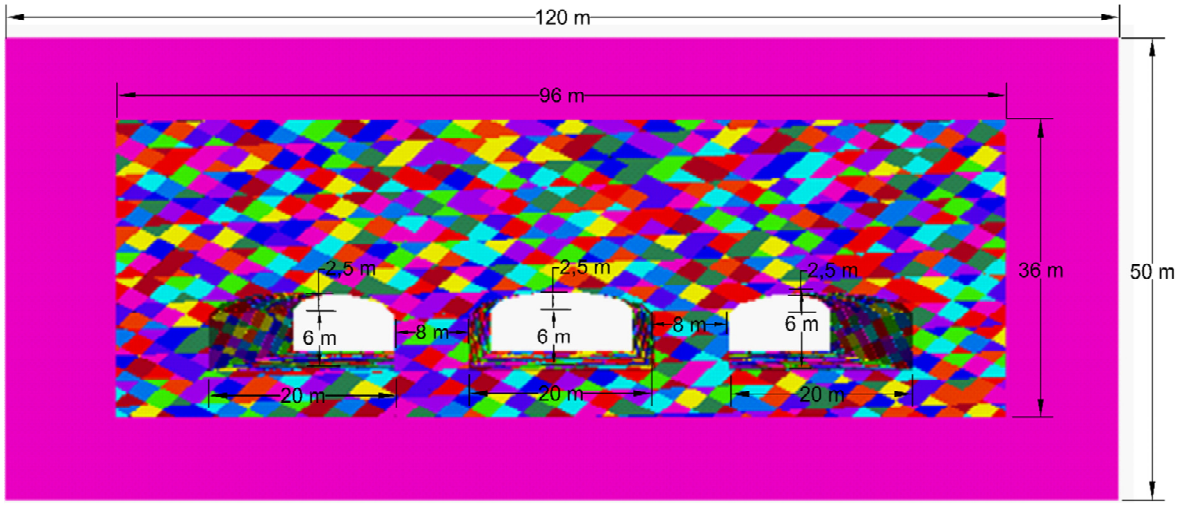

Figure 14. Layout model with a 2,5 m radius horseshoe

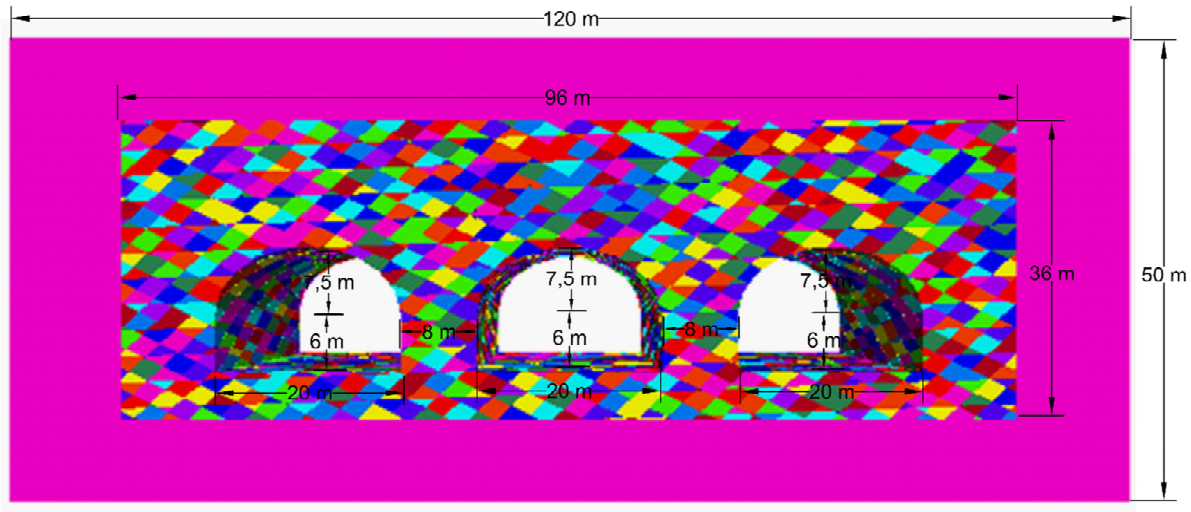

Figure 15. Layout model with a 7,5 m radius horseshoe

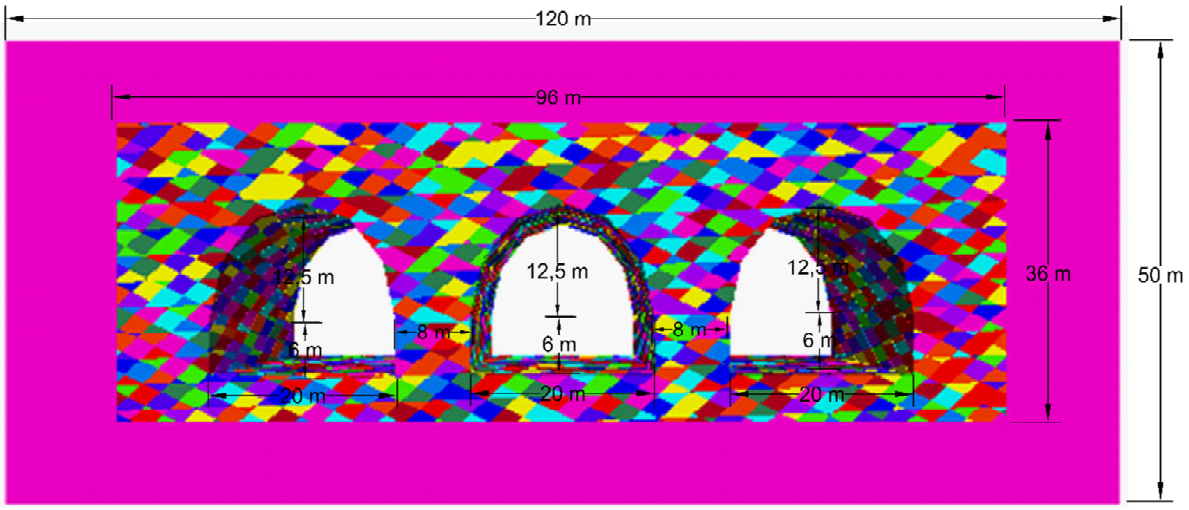

Figure 16. Layout model with a 12,5 m radius horseshoe

4.2 MODYFING THE JOINT DIP ORIENTATION

The second modification implemented on the basic model was the variation of the joint dip direction. Taking into account the considerations on Chapter 3.1., to accurately portray the field conditions for the different opening's orientations typical of a room and pillar underground mining method and the quarry layout, it was necessary to modify the joint dip of the selected joints families. To apply a significant range that represent the geological conditions observed on the field, the selected modification of + 60º and -60º was applied to the joint dip orientation parameter. The Table 16 shows the implemented parameters for the different joint families.

Table 16. Modified dip implemented for the respective joint families

	Joint Family	Dip	Dip Direction
Units	-	(º)	(º)
Initial orientation	J2	44	182
	J6	43	282
	J7	30	57
60º	J2	104	182
	J6	103	282
	J7	90	57
-60º	J2	-16	182

	J6	-17	282
	J7	-30	57

The layout of the models of the basic rectangular model with the initial, and the joint dip modified + 60º and -60º are shown on the Figure 17, Figure 18, and Figure 19, respectively. The same parameter modifications where applied to the models with different openings shapes explained on the previous section (4.1), and the models can be observed on the Annex A.

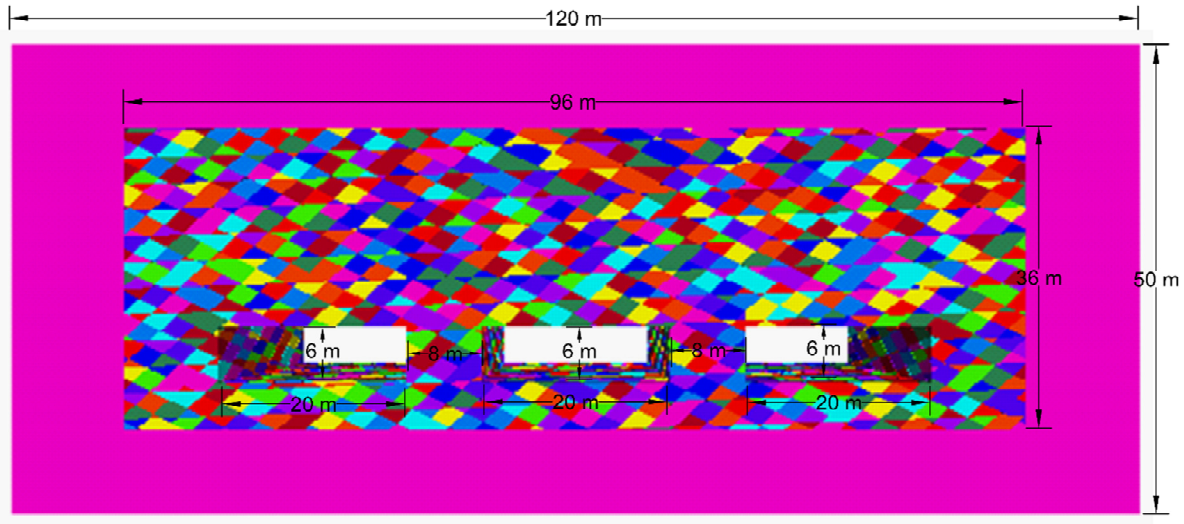

Figure 17. Basic model layout with initial joint dip orientation

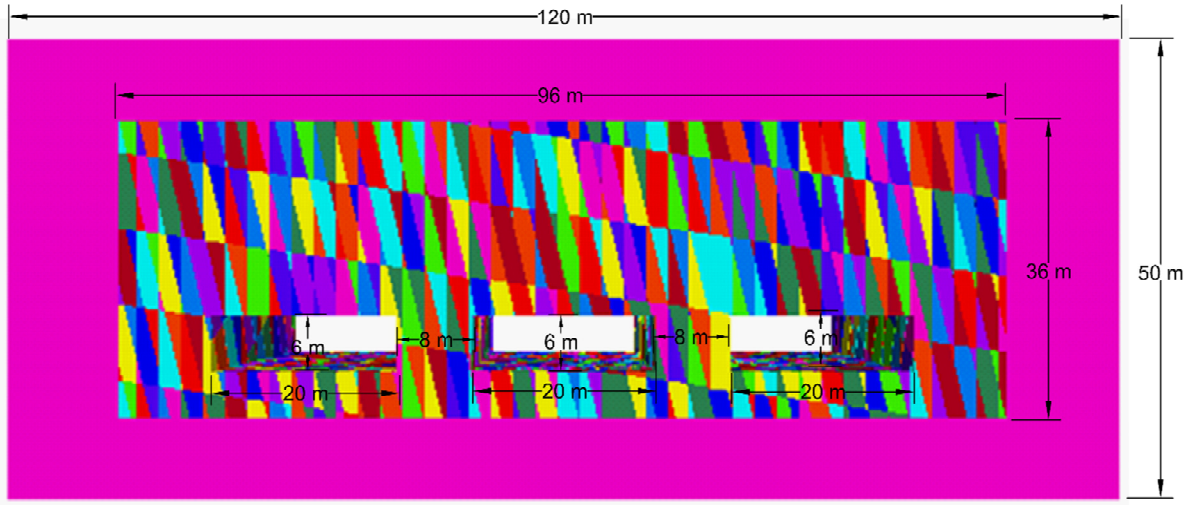

Figure 18. Basic model layout with a 60º joint dip orientation

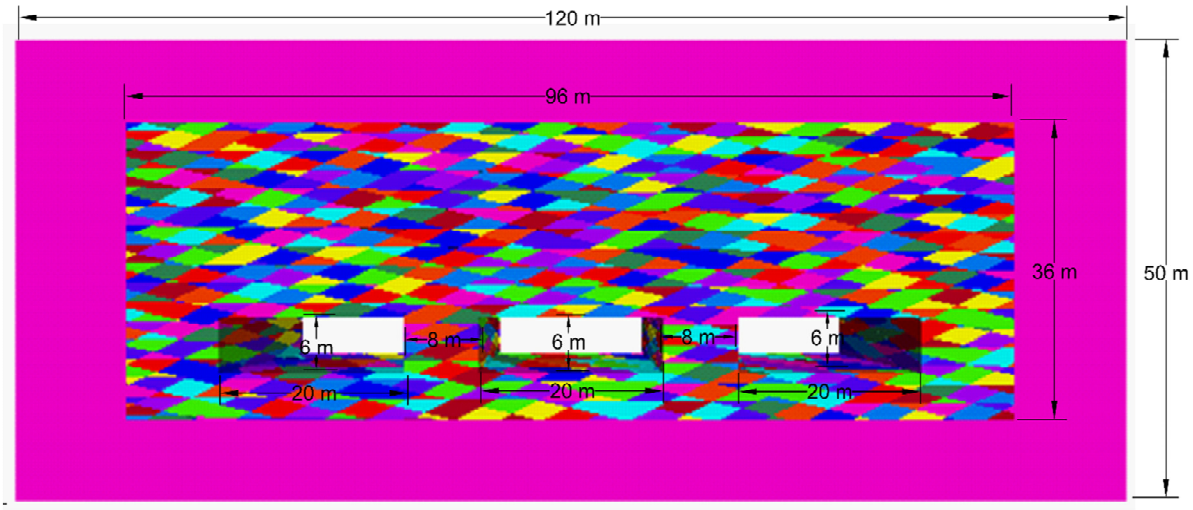

Figure 19. Basic model layout with a -60º joint dip orientation

4.3 MODIFYING THE COHESION AND TENSILE STRENGTH OF THE JOINTS

The third modified parameter were the geomechanical parameters, specifically the selected joint families parameters implemented on the basic model. Taking into account the considerations on Chapter 3.1., initially a tensile strength that varied between 0,5 and 1,0 MPa was implemented. While on the field, the openings show stability and negligible rock fall, the models with a joint cohesion lower than 2,0 MPa and joint tensile strength lower than 0,5 MPa proved unstable and presented rock fall, as shown in the Figure 20. Therefore, the model parameters were calibrated within the chosen ranges to simulate the real life conditions.

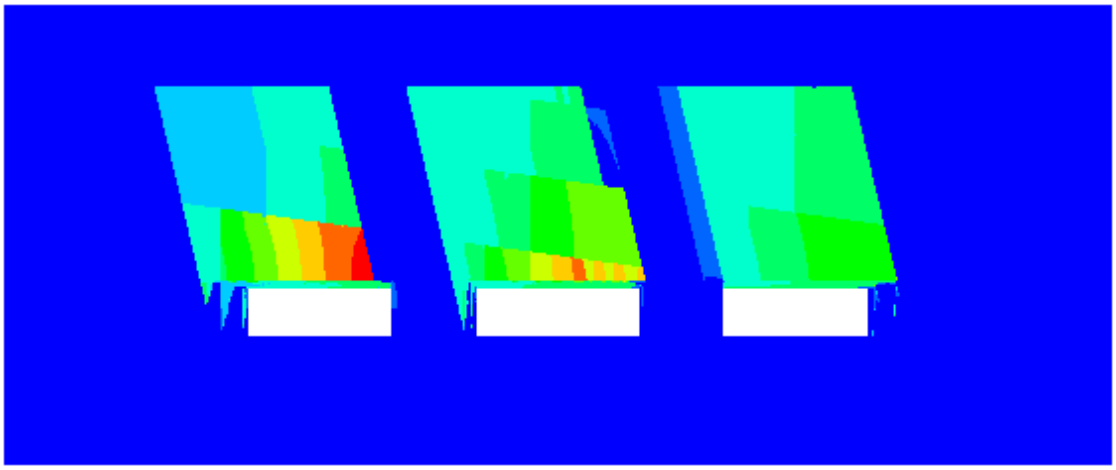

Figure 20. Rooftop fall due to low joint cohesion and tensile strength

The chosen range of variation of the joint cohesion was between 2,0 to 3,0 MPa for all joints families and between 0,5 and 1,0 MPa for the joint tensile strength.

The different selected joint families have different influences on the overall stability of the model. Therefore, the calibrated joint tensile strength of the joint family 2 was determined at 0,5 MPa, joint tensile strength of the joint family 6 varied between 0,8 MPa and 1,0 MPa, and 1,0 MPa joint tensile strength for the joint family 7. These parameters were implemented to represent an initial condition with the best parameters, and subsequent less stable conditions were implemented following the results of the previous models.

In total three geomechanical conditions were selected and are shown in the Table 17.

Table 17. Implemented geomechanical conditions

	Joint Family	Joint cohesion	Internal friction angle	Joint normal stiffness	Joint shear stiffness	Joint tensile strength
Units	**-**	MPa	(º)	GPa	GPa	MPa
Condition 1	J2	3,0	31	18,40	11,80	0,5
	J6	3,0	17	18,40	11,80	1,0
	J7	3,0	39	18,40	11,80	1,0
Condition 2	J2	2,8	31	18,40	11,80	0,5
	J6	2,8	17	18,40	11,80	0,8
	J7	2,8	39	18,40	11,80	1,0
Condition 3	J2	2,1	31	18,40	11,80	0,5
	J6	2,1	17	18,40	11,80	0,8
	J7	2,1	39	18,40	11,80	1,0

4.4 TOTAL LIST OF MODELS

Therefore, a total of 36 different numerical models were evaluated during this study, each one representing a different condition. (See Equation 19)

$$4\ different\ shapes\ \times\ 3\ faults\ and\ joints\ directions\ \times\ 3\ different\ geomechanical\ properties\ conditions = 36\ models$$ **Equation 19**

A summary of the 36 models with the individual conditions and key properties of each one of them can be found adequately listed and numerated on the Table 18.

It is important to highlight that the basic block layout, mass rock properties and the intact rock properties had been shown and discussed previously on the Chapter 3.2, and represent the listed model 1.

Table 18. Summary of the 36 models evaluated during the investigation

Model Number	Shape	Joint dip orientation	Geomechanical condition
1	Rectangular	Initial	Condition 1
2	Rectangular	Initial	Condition 2
3	Rectangular	Initial	Condition 3
4	Rectangular	60º	Condition 1
5	Rectangular	60º	Condition 2
6	Rectangular	60º	Condition 3
7	Rectangular	-60º	Condition 1
8	Rectangular	-60º	Condition 2
9	Rectangular	-60º	Condition 3
10	2,5 m radius horseshoe	Initial	Condition 1
11	2,5 m radius horseshoe	Initial	Condition 2
12	2,5 m radius horseshoe	Initial	Condition 3
13	2,5 m radius horseshoe	60º	Condition 1
14	2,5 m radius horseshoe	60º	Condition 2
15	2,5 m radius horseshoe	60º	Condition 3
16	2,5 m radius horseshoe	-60º	Condition 1
17	2,5 m radius horseshoe	-60º	Condition 2
18	2,5 m radius horseshoe	-60º	Condition 3
19	7,5 m radius horseshoe	Initial	Condition 1
20	7,5 m radius horseshoe	Initial	Condition 2
21	7,5 m radius horseshoe	Initial	Condition 3
22	7,5 m radius horseshoe	60º	Condition 1
23	7,5 m radius horseshoe	60º	Condition 2
24	7,5 m radius horseshoe	60º	Condition 3
25	7,5 m radius horseshoe	-60º	Condition 1
26	7,5 m radius horseshoe	-60º	Condition 2

27	7,5 m radius horseshoe	-60º	Condition 3
28	12,5 m radius horseshoe	Initial	Condition 1
29	12,5 m radius horseshoe	Initial	Condition 2
30	12,5 m radius horseshoe	Initial	Condition 3
31	12,5 m radius horseshoe	60º	Condition 1
32	12,5 m radius horseshoe	60º	Condition 2
33	12,5 m radius horseshoe	60º	Condition 3
34	12,5 m radius horseshoe	-60º	Condition 1
35	12,5 m radius horseshoe	-60º	Condition 2
36	12,5 m radius horseshoe	-60º	Condition 3

5 RESULTS AND ANALYSIS

As explained on Chapter 3.2.7, the 36 models were executed and run through several steps until the unbalanced forces working on the models were balanced after the excavation of the mine openings. Once stable conditions were attained, the stress distribution and the model stability, specially the openings rooftop and the pillars were evaluated and analyzed. The main parameters selected for the evaluation of the model's stability were the displacement magnitude, the joint slip. Plasticity limit indicator and the factor of safety to the stability of the model. The max. principal stresses, min. principal stresses, and the max. shear stresses were the main parameters evaluated regarding the stresses distribution and overall stresses analysis. Additionally, to verify the convergence of the model, the velocity was evaluated step-by-step for the various selected points shown in the Figure 12.

Due to the amount of information derived of the 36 evaluated models, only the most representative models were selected for a more detailed evaluation and analysis, as shown on this chapter, giving a more organized und concise results analysis. For the complete results of all the 36 models, please refer to Annex A.

5.1 BASIC MODEL WITH RECTANGULAR OPENINGS, INITIAL JOINT DIP AND CONDITION 1 GEOMECHANICAL PARAMETERS - MODEL (1)

The initial basic model with rectangular openings was the base model for comparison on which the changes on the stresses distribution and stability was evaluated. As such, the stability behavior and resulting geomechanical parameters will be extensively evaluated. The parameters of the model with basic layout with an initial joint dip and geomechanical condition 1, or for now identified as model 1, see Table 18, has been extensively described and analyzed in the previous chapter and can be seen on the Figure 17.

5.1.1 Model 1 stability evaluation and results

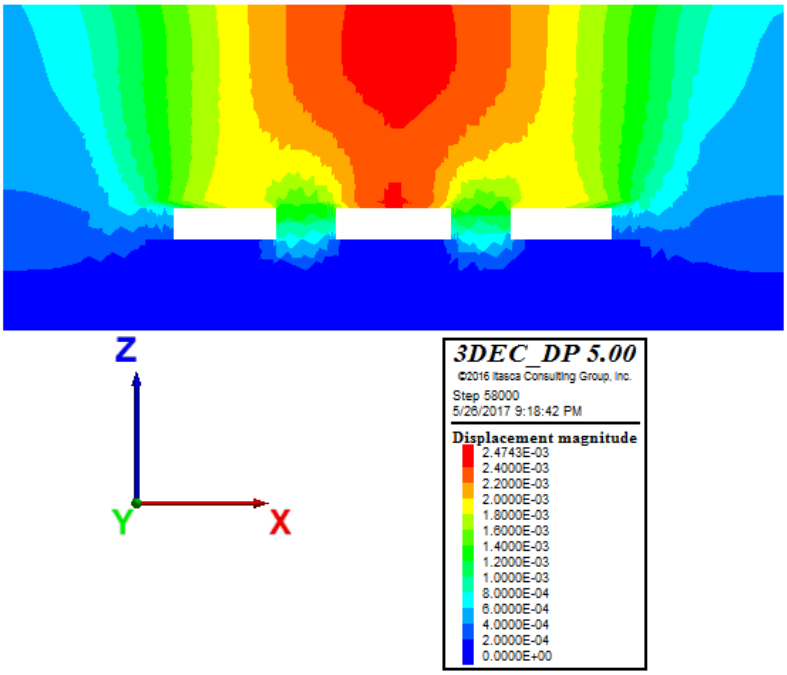

Figure 21. Model 1. Displacement magnitude (m)

As observed on the Figure 21, the magnitude of the displacement of the model is relatively low, with a maximum of 2,47 mm at the rooftop of the middle opening and 1,2 mm on the pillars.

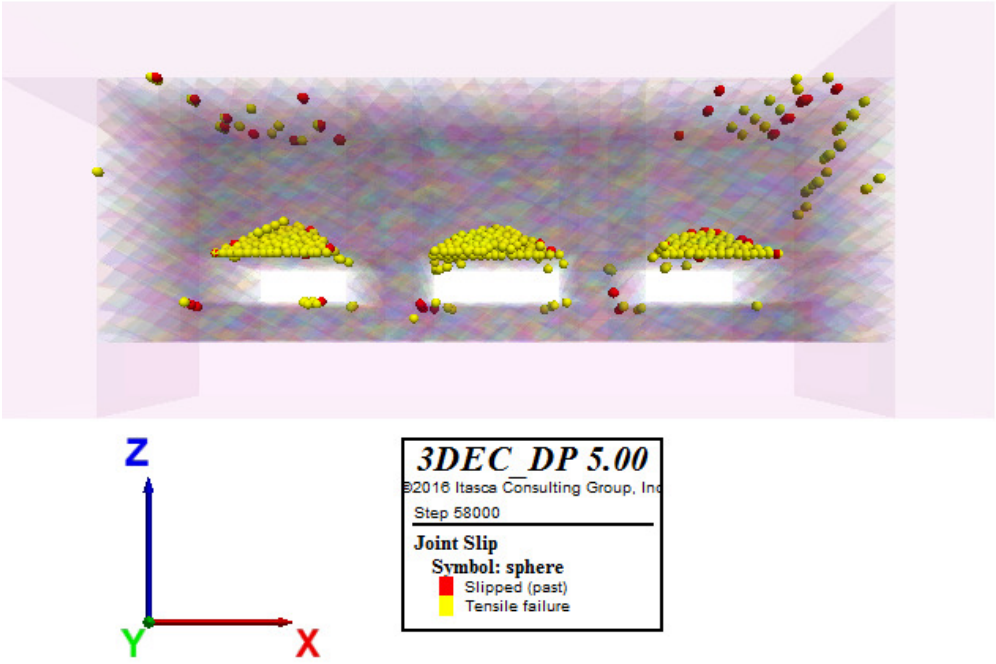

Figure 22. Model 1. Joint slip- Plasticity limit

A further analysis of the joint slip results observed in the Figure 22, shows that the joint failure and plastic deformation by tensile stress is concentrated on the roof of the openings, being this area subject to the highest tensile stresses and susceptible to rock falling and breakage. With a general calculated factor of safety of the model was 2,02, the model shows high general stability with a few unstable localized problems. The factor of safety for all the 36 models is summarized on the Table 22.

In general, the model shows stable behavior, with low subsidence and displacement, with the exception of a few localized problems on the rooftop of the rectangular openings.

5.1.2 Model 1 stresses distribution evaluation and results

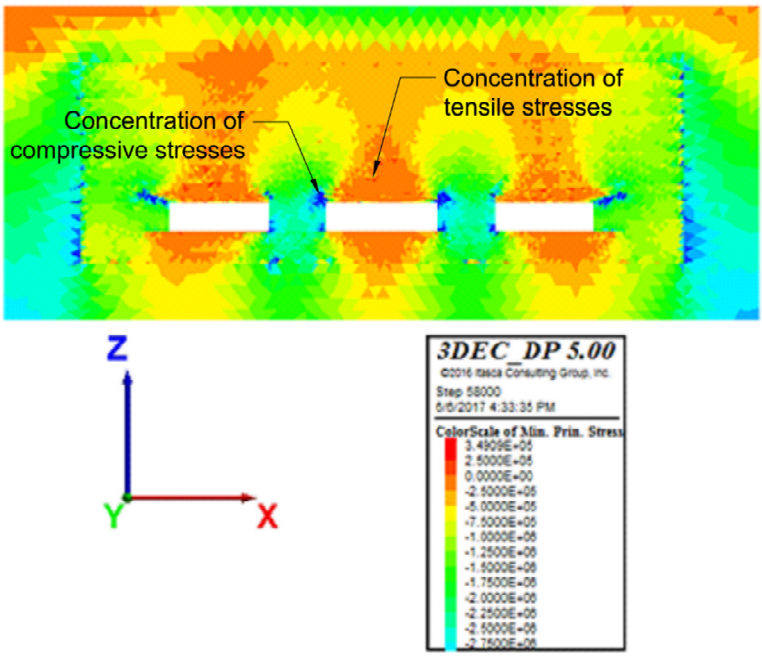

Figure 23. Model 1. Min. principal stresses (Pa)

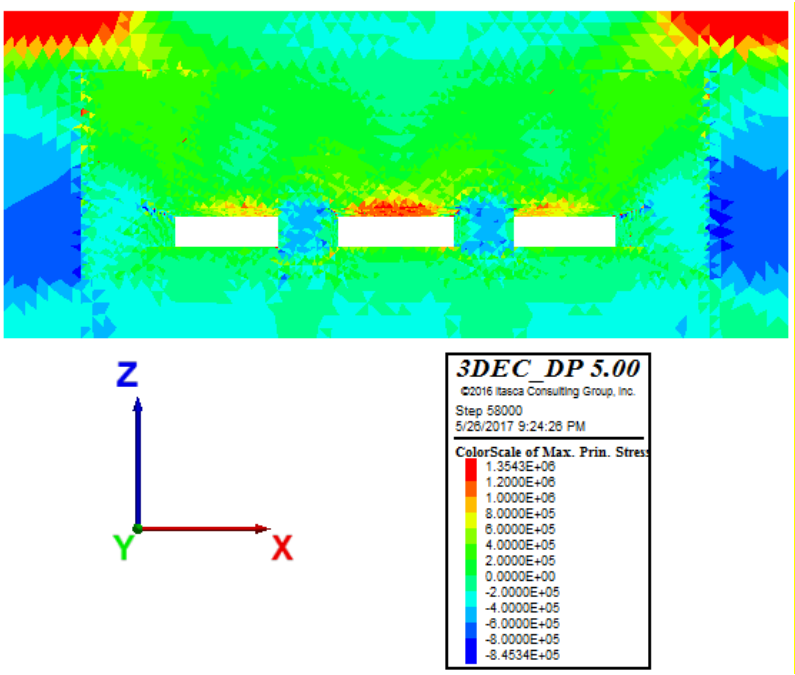

Figure 24. Model 1. Max. principal stresses (Pa)

In Figure 23 and Figure 24 it can be observed how the tensile maximum stresses (positive values) concentrate on the roof of the openings while the pillars are subject to high compression stresses (negative values) on its centroid plane. The edges of the rectangular openings also show a great concentration of compressive stresses. As shown in the next figure (Figure 25), the high concentration of stresses on the rooftop increases the risk of rock fall and other stability and safety risks. On the pillars, the high compressive stresses that act upon the middle plane of the pillar generate high tensile stresses reactions on the edges of the pillars, which tend to fracture, generating a stability and safety risk during the operation of the mine.

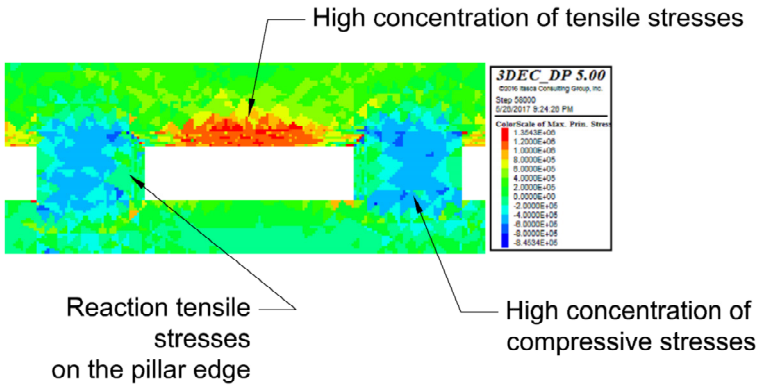

Figure 25. Model 1. Stresses concentration on the rooftop and the pillars of the rectangular opening (Pa)

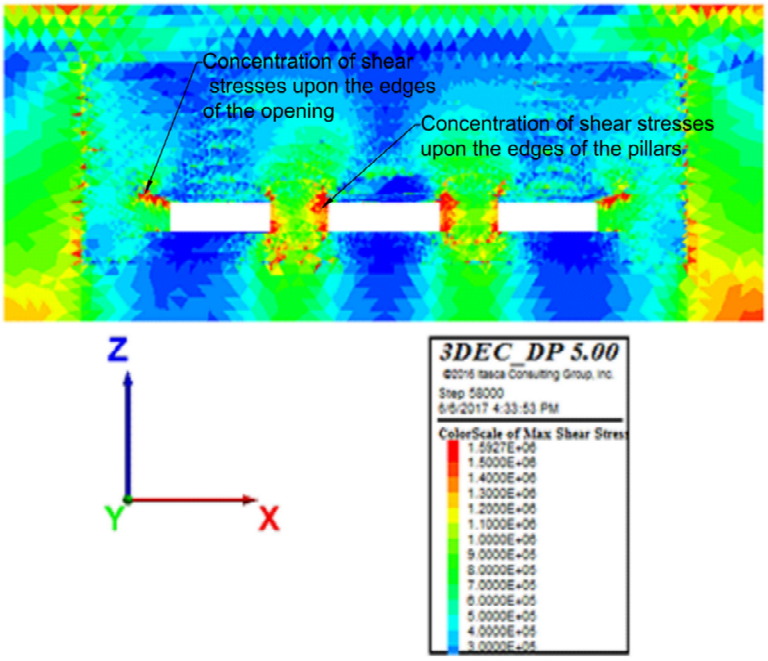

Figure 26. Model 1. Max shear stresses (Pa)

As shown by the Figure 26, the shear stresses concentrate on the edges of the rectangular openings, as well as in the walls of the pillars, due to the lack of a proper stress diffusion and the accumulation of the shear stresses on the edges of the pillars, generating shear stresses that can break the rock and the binding between the joints, lowering the stability of the openings.

Additionally, for monitoring purposes, the Figure 27 shows the history of the velocity of the selected points, showing an end velocity of 0 velocity magnitude/time-step for all the analyzed points convergence of the model was attained, the forces are balanced and no further displacements are expected under the current conditions.

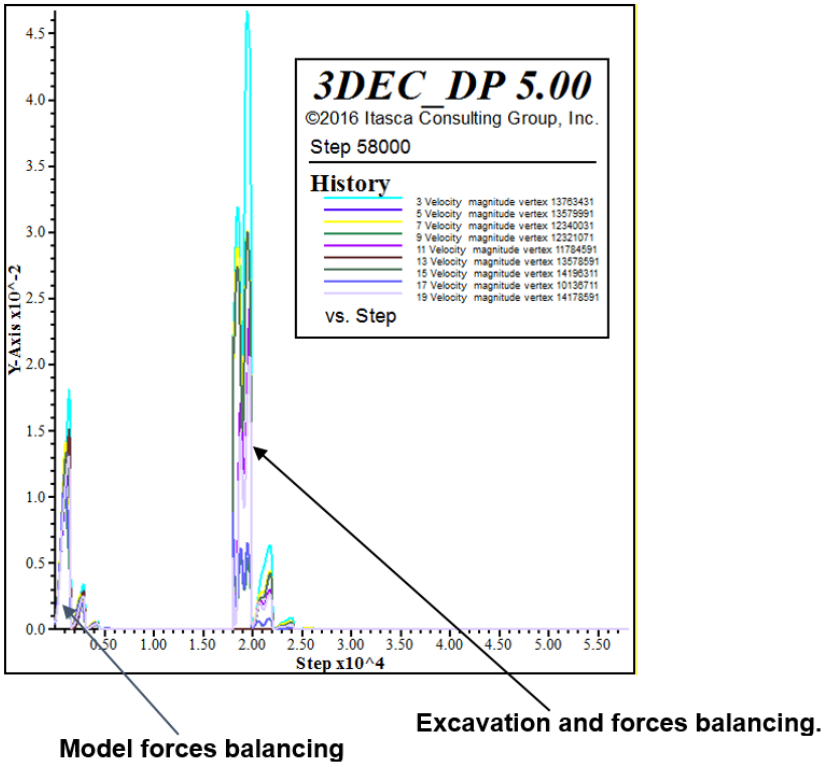

Figure 27. History chart velocities (Velocity magnitude vector vs time-step)

5.2 INFLUENCE OF THE MODIFICATION OF THE GEOMECHANICAL PROPERTIES CONDITIONS ON THE STRESS DISTRIBUTION, AND ROOFTOP AND PILLAR STABILITY

The first step of the analysis consisted on evaluating how the change of the geomechanical properties of the openings within the mine influenced the stress distribution and the rooftop and pillar stability. It was necessary to modify the geomechanical properties of the joints on the basic rectangular opening model to determine the changes on the output parameters and calibrate the model more accurately the field conditions. The basic model with rectangular opening, normal joint dip and under condition 1 geomechanical parameters (model 1) was compared with similar models under condition 2 (Model 2) and condition 3 (Model 3) geomechanical parameters. The different conditions are explained on the Table 17 and on the Chapter 4.3.

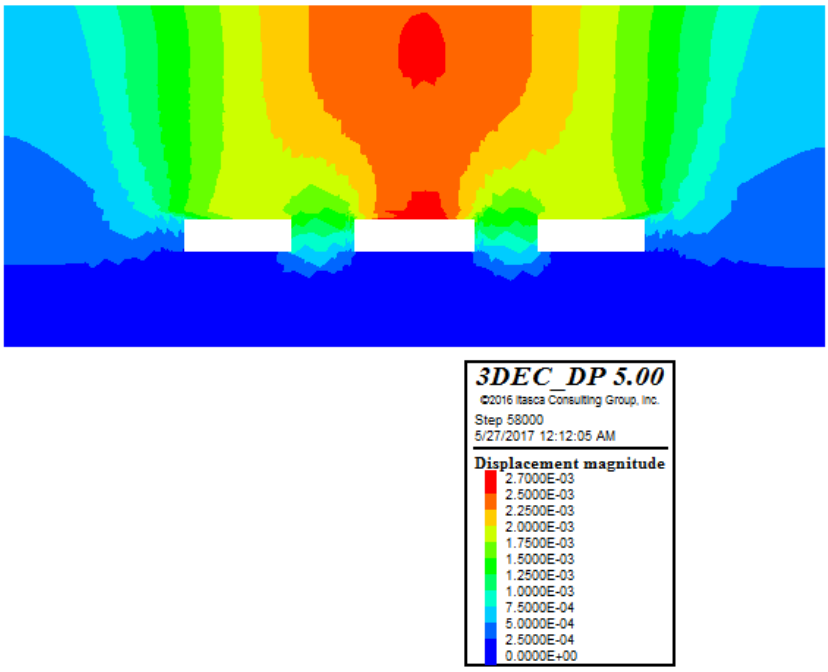

Figure 28. Model 2. General displacement magnitude (m)

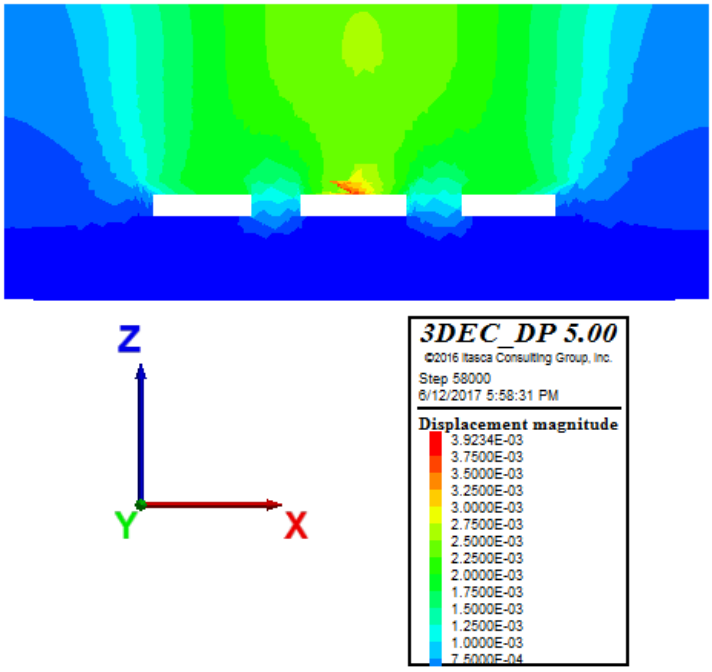

Figure 29. Model 2. Localized displacement magnitude (m)

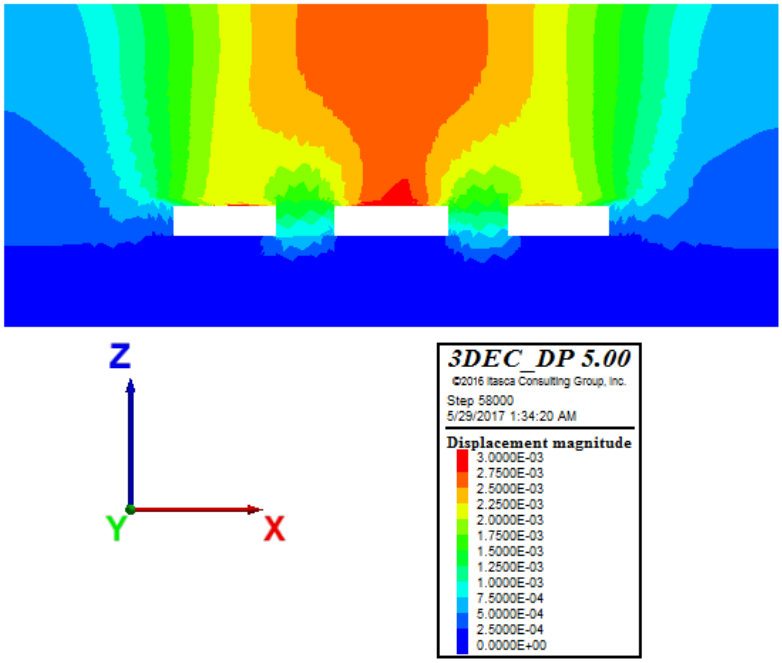

Figure 30. Model 3. General displacement magnitude (m)

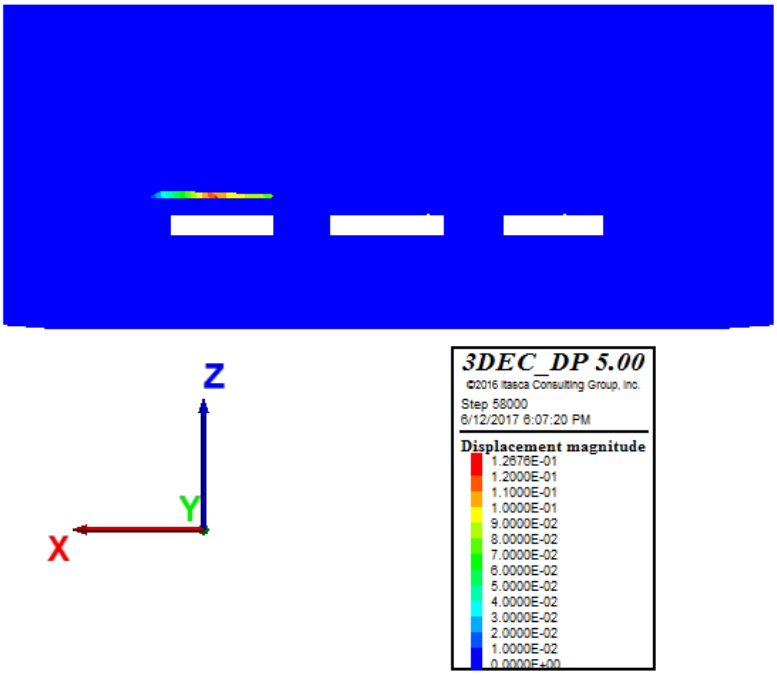

Figure 31. Model 3. Localized displacement magnitude (m)

As expected due to the reduction of the geomechanical parameters of the joints, there is a noticeable increase on the displacement (Figure 28, Figure 30) that is reflected on the openings stability. There is an increase of 2,4 mm to 3,0 mm on the rooftop as well as form 1,2 mm to 1,5 mm on the pillars.

There is also a notorious displacement increase on a few individual blocks on the rooftop as shown on the Figure 29 and Figure 31, reaching the 10 cm on some blocks on top of the left opening.

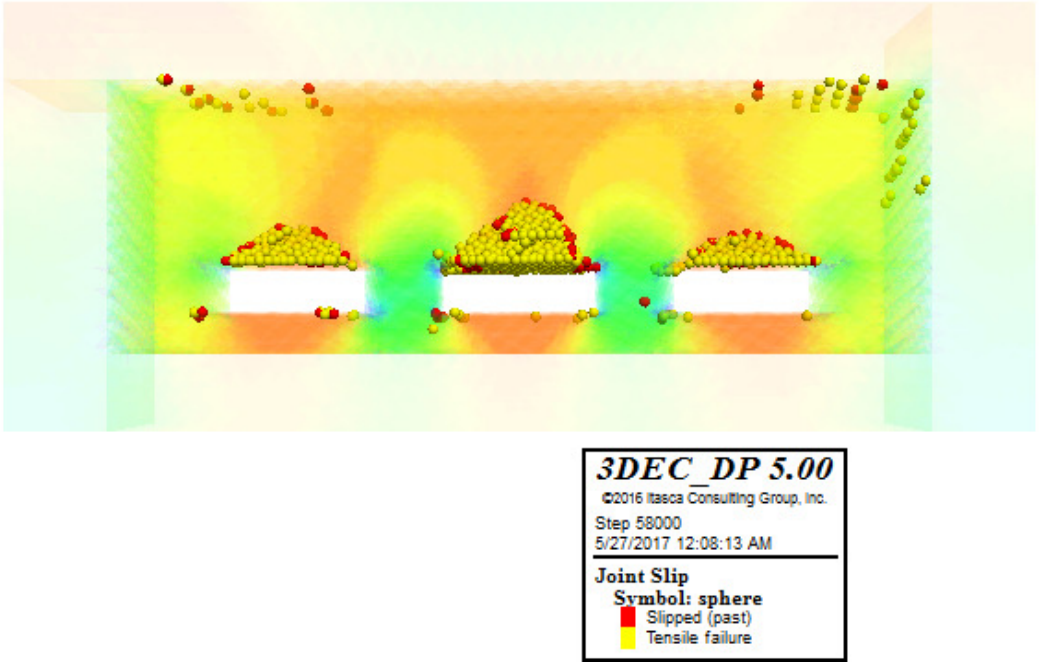

Figure 32. Model 2. Joint slip - Plasticity Limit indicator

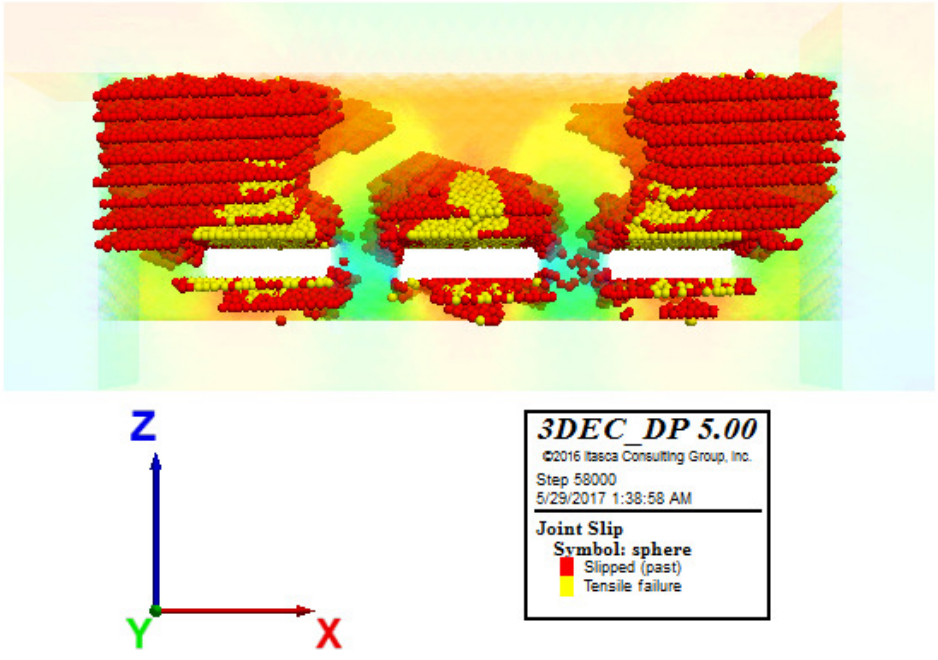

Figure 33. Model 3. Joint slip - Plasticity Limit indicator

There is also a significant increase of the failure of blocks due to tensile failure and plastic deformation, concentrated on the rooftop of the openings, as shown in the Figure 32 and Figure 33.

With the reduction of the value of the geomechanical parameters for the joints, the models show and increased instability, blocks slippage and fracture. This is observed on the behavior of the factor of safety, from a 2,02 for model 1, to 1,68 for model 2 and 1,39 for model 3. The Table 22, at the end of this chapter, shows the factor of safety for the 36 models. The following table (Table 19), shows a comparison of the different displacement and factor of safety results for each modified geomechanical parameter model.

Table 19. Comparison table of the displacement magnitude and Factor of safety results for model 1, model 2, and model 3

Properties	Model 1	Model 2	Model 3
Displacement Magnitude on rooftop (mm)	2,40	2,70	3.0
Factor of safety	2,02	1,68	1.39

The overall stresses and the stress distribution are, as expected, not significantly altered with the modification of the joint geomechanical parameters and therefore, a more extensive analysis of the stress conditions is not necessary. This behavior repeats on the models with varying joints dip and with modified shapes, were the decrease of the joints geomechanical parameters increased the instability, joint slip failure and reduced the factor of safety, but the changes observed regarding the stress distribution were negligible. The full results for all the models are shown on the Annex A.

5.3 INFLUENCE OF THE MODIFICATION OF THE JOINT DIP ORIENTATION ON THE STRESS DISTRIBUTION AND ROOFTOP AND PILLAR STABILITY

The next step of the analysis consisted on evaluating how the change of the joint dip of the joint families within the mine will influence the overall stresses, the stress distribution and the rooftop and pillar stability. The modification of the joint dip of the basic rectangular opening model was chosen to evaluate the different orientations of the openings typical for a room and pillar mining operation as explained in Chapter 4.2. The basic model with rectangular openings and a normal joint dip orientation and under condition 1 geomechanical parameters, was compared with models under the same condition and opening shape but with a modified joint dip of 60º (Model 4)

as shown on the Figure 18, and with a modified joint dip of -60º (Model 7), as shown on the Figure 19. The modified joint dip orientation for the implemented families is shown on the Table 16.

5.3.1 Changes on the model stability after the modification of the joint dip

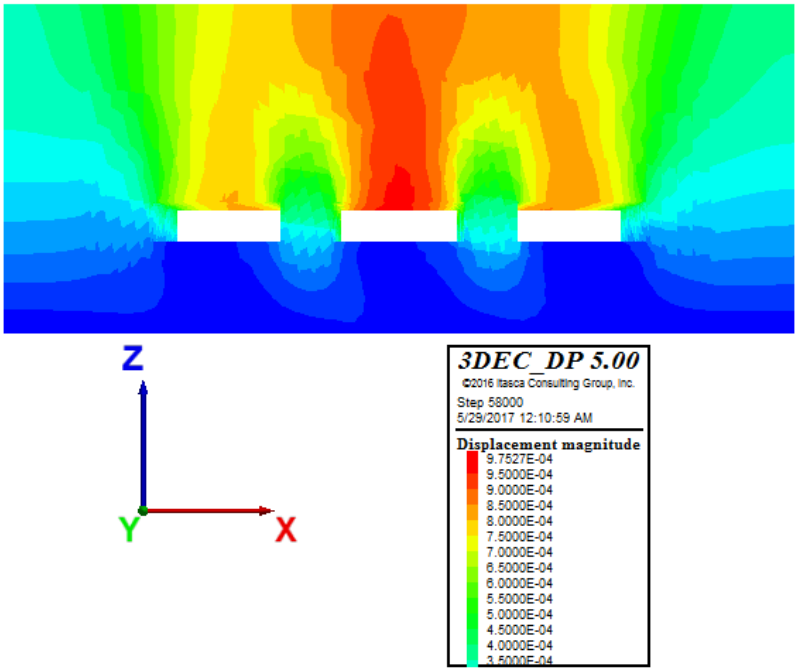

Figure 34. Model 4. Displacement magnitude (m)

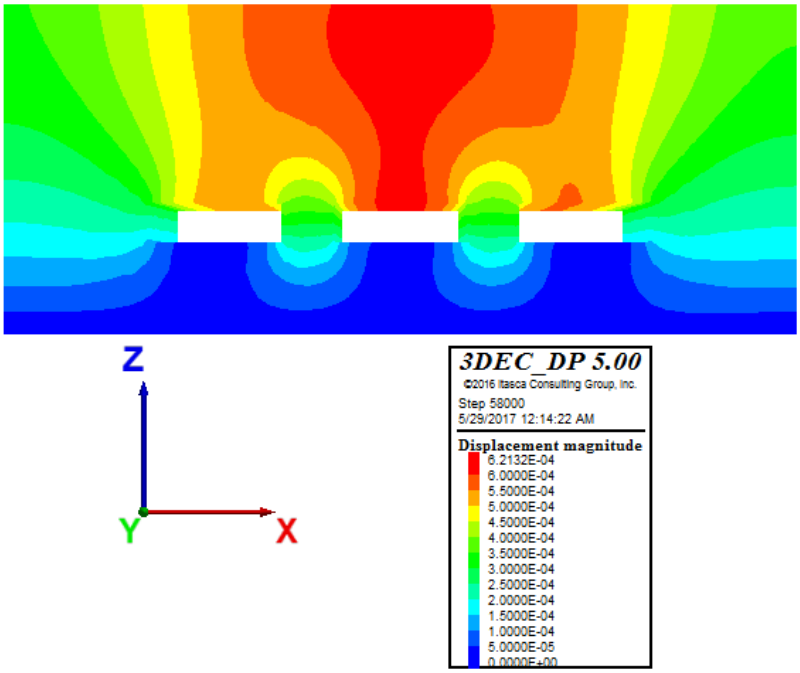

Figure 35. Model 7. Displacement magnitude (m)

The models modified for openings at 60º (model 4) and -60º (model 7) from the original basic model proved to be more stable, especially on the later, with a significant lower displacement on the rooftops and pillars. There are one order of magnitude lower (from mm to 2,4 mm on the rooftop to 0,9 and 0,6 mm), see Figure 34 and Figure 35, than the obtained from the model 1, see Figure 21.

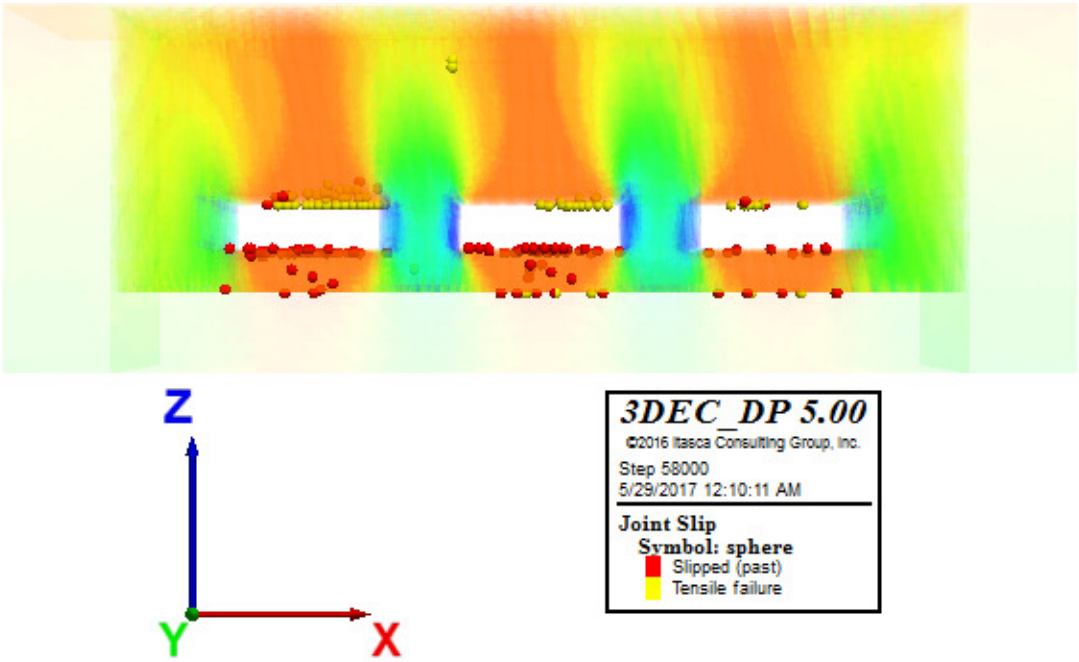

Figure 36. Model 4. Joint slip - Plasticity Limit indicator

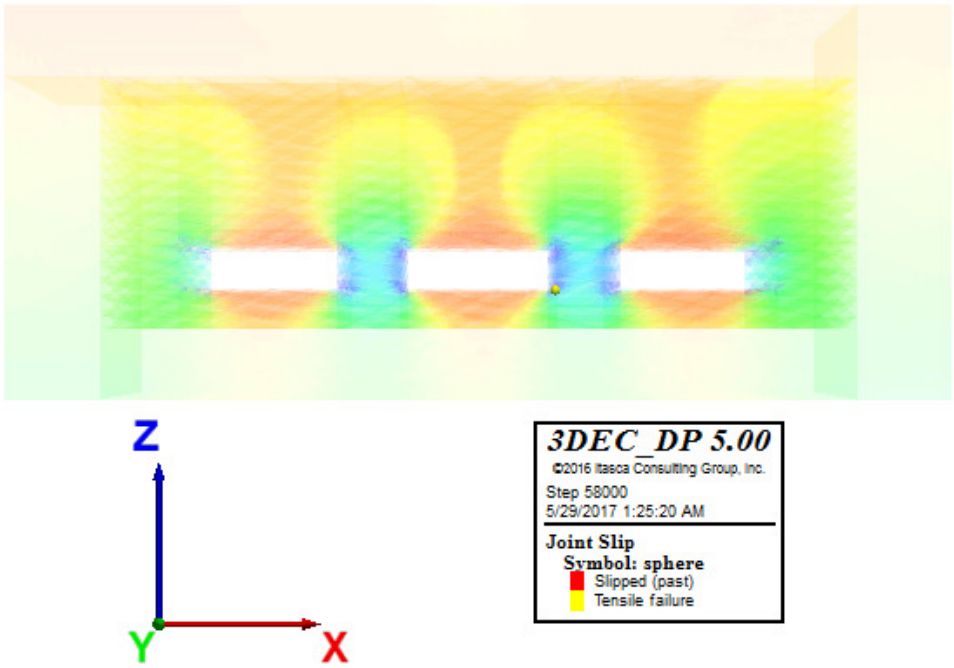

Figure 37. Model 7. Joint slip - Plasticity Limit indicator

As observed on the Figure 36 for model 4, and on Figure 37 for model 7, there is a significant reduction the joint tensile failure and plastic deformation after the dip modification.

In a general context, for all geotechnical parameter conditions and opening shape the models with an orientation at 60º and -60º, presented good stability conditions, with less risks of rock falling, rock burst or joint slippage. The models with a –60º joint dip orientation modification show a significantly higher factor of safety, all models with joint families with this dip modification a calculated factor of safety of more than 3,0. The models with joint families with a dip orientation modification of 60º were significantly more stable, represented by the factor of safety value of 2,58 from model 4, compared with the 2,02 of the standard basic model (model1), that can be seen on Table 22. The Table 20 shows a comparison of the displacement magnitude and factor of safety for the models with modified joint dip.

Table 20. Comparison table of the displacement magnitude and Factor of safety results for model 1, model 4, and model 7

Properties	Model 1	Model 4	Model 7
Displacement Magnitude on rooftop (mm)	2,4	0,9	0,6
Factor of safety	2,02	2,58	>3,0

5.3.2 Changes on the model stresses distribution after the modification of the joint dip

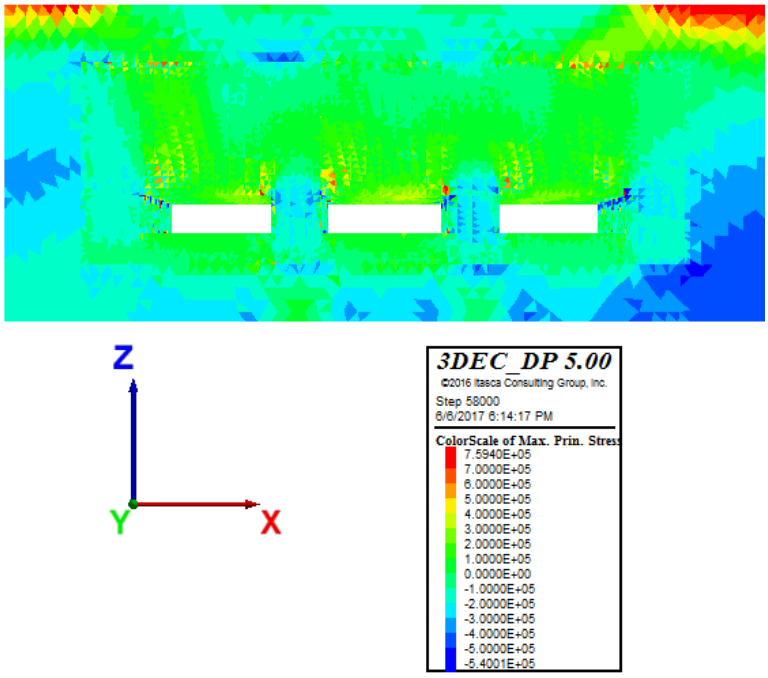

Figure 38. Model 4. Max. principal stresses (Pa)

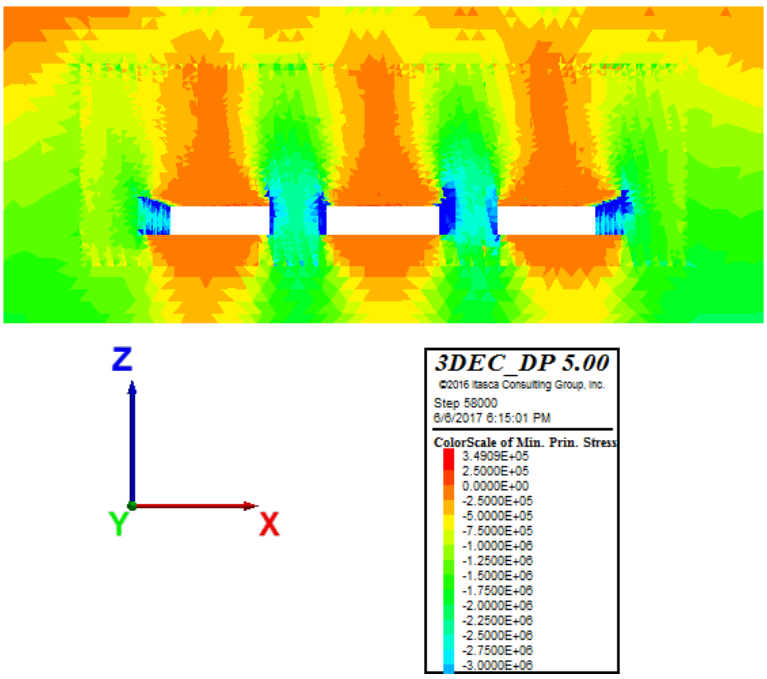

Figure 39. Model 4. Min. principal stresses (Pa)

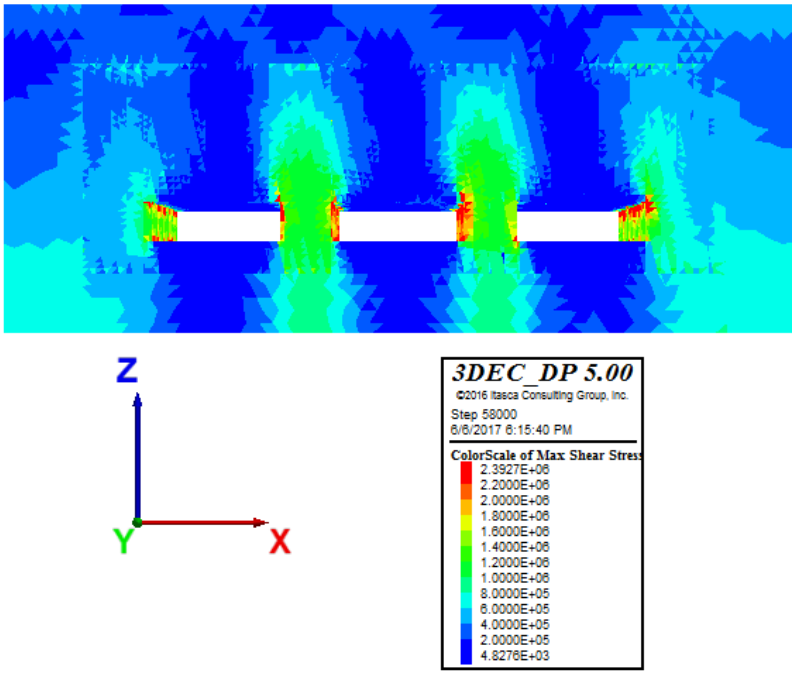

Figure 40. Model 4. Max shear stresses (Pa)

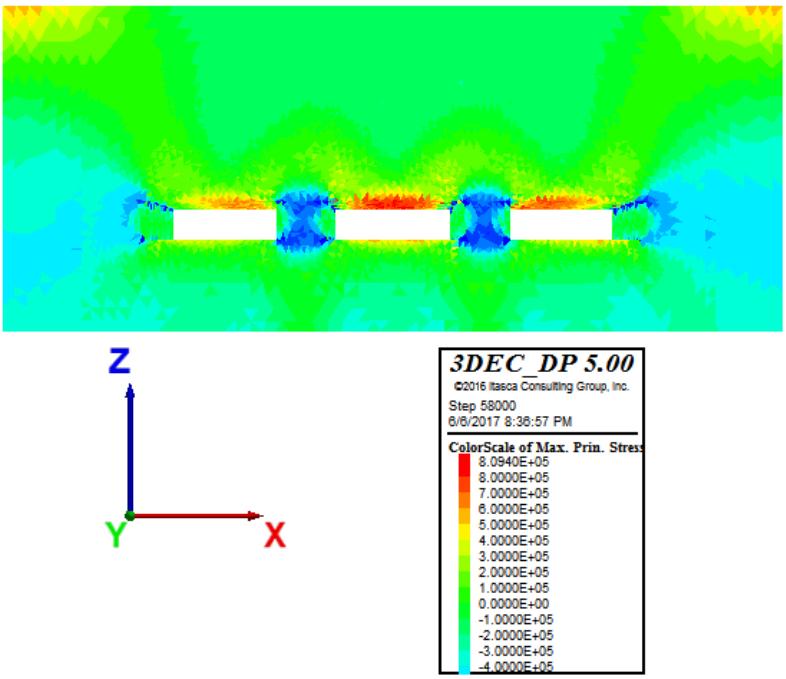

Figure 41. Model 7. Max. principal stresses (Pa)

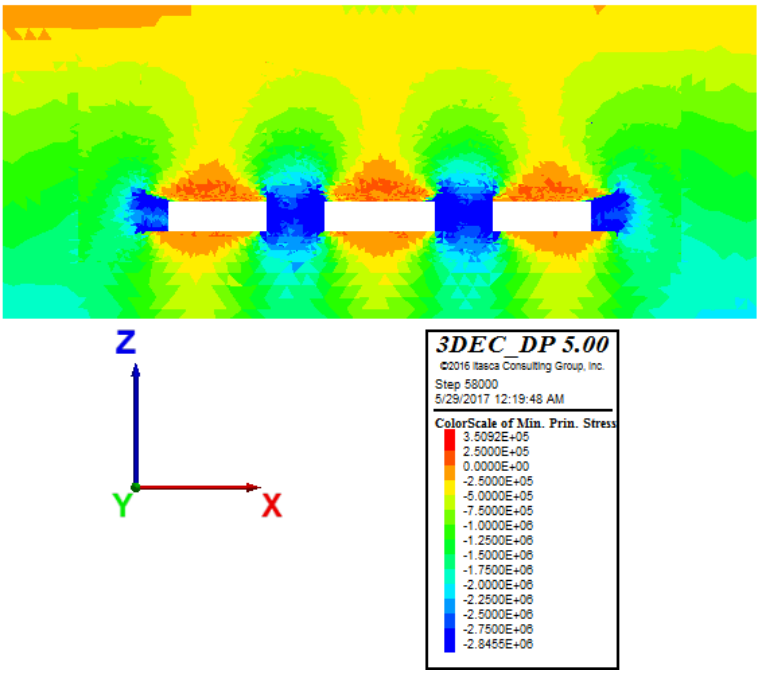

Figure 42. Model 7. Min. principal stresses (Pa)

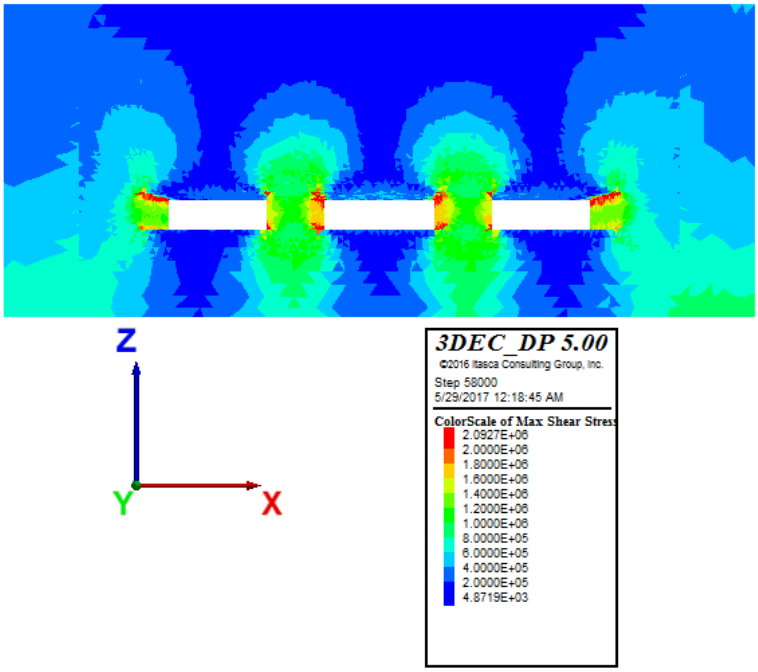

Figure 43. Model 7. Max shear stresses (Pa)

The overall stresses and stress distribution for the modified joint dip models is fairly similar to the one observed on a model with normal joint dip, see Figure 23, Figure 24 and Figure 26. The tensile stresses are concentrated on the rooftop, being the critical region the tensile stress acting on the middle opening roof, and compressive stress act the middle plane of the pillar and with tensile reaction on the edges of the pillar, with the maximum shear stress concentrating on the edges of the rectangular openings and on the pillars edge, as shown in Figure 38, Figure 39, Figure 40, Figure 41, Figure 42, Figure 43. It is very noticeable that the orientation of the stresses follows the joint dip for the models modified 60º degrees, with a more homogenous concentration of stresses on the rooftops following the dip. The normal dip and the modified -60º dip models have a very similar distribution of stresses, with the compressive stresses concentrating on the top and bottom of the pillars and the tensile stresses on the rooftop of the openings, the stresses transferred to the joints.

This behavior repeats for the models with varying joints geomechanical parameters dip and with modified shapes, were the modification of the dip of the different joint families show models with increased stability and factor of safety, but the changes observed regarding the stress distribution were not significant. These evaluations, results, and analysis proved to be follow a similar behavior for other models under the same joint families dip orientations, but with a different geomechanical parameters and a with different openings shape. The full results for all the models are shown on the Annex A.

5.4 INFLUENCE OF THE MODIFICATION OF THE OPENING SHAPE ON THE STRESS DISTRIBUTION AND ROOFTOP AND PILLAR STABILITY

The final step of the analysis consisted on evaluating how the modification of the openings' shape within the mine will influence the stress distribution and the rooftop and pillar stability, which was the main objective of this study. As explained on the previous Chapter 4.1, three horseshoe shaped openings with a different radius additional to the basic rectangular opening layout were deemed optimal for the current study. As explained on the previous sections 5.2 and 5.3, the modified joint dip orientation and geomechanical parameters influenced the regional and local stability of the blocks on the model, but did not have a heavy influence on the overall stresses and stress distribution on the model. As the condition 3 of the geomechanical parameters, as well as the normal slip orientation condition, showed to be the most critical condition regarding the rooftop and pillar stability, showing a diminishing factor of safety and an increased joint slippage, the basic model with rectangular openings and a normal joint dip orientation and under condition 3 geomechanical parameters (Model 3), shown in Figure 9, was compared with models under the same condition and joint orientation but with a modified horseshoe shape with 2,5 m of radius (Model 12), shown on the Figure 14, with 7,5 m of radius (Model 21), shown on the Figure 15 and with a 12,5 m of radius horseshoe shape openings model (model 30), shown on the Figure 16.

5.4.1 Evaluation and analysis of the resultant stability changes after modifying the shape of the openings

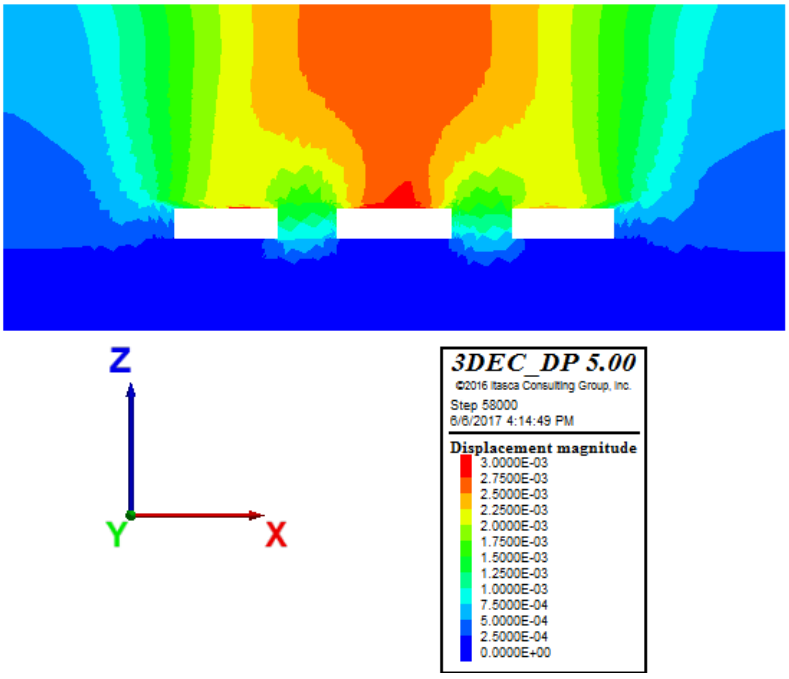

Figure 44. Model 3. General displacement magnitude (m)

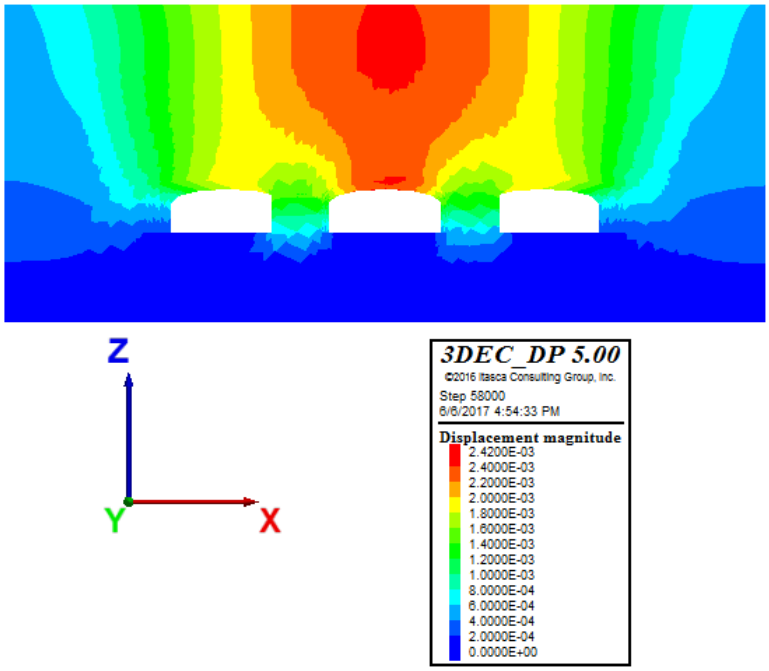

Figure 45. Model 12. General displacement magnitude (m)

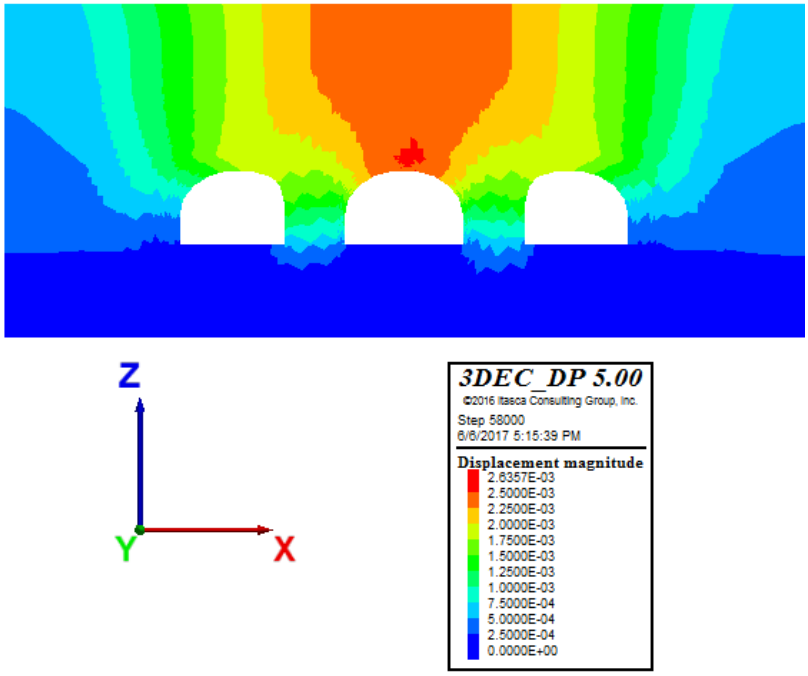

Figure 46. Model 21. General displacement magnitude (m)

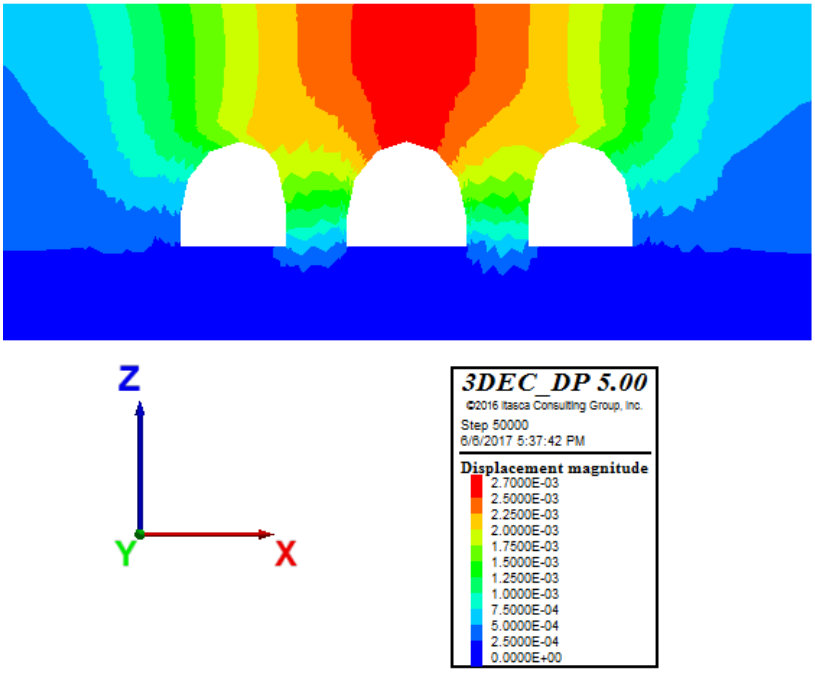

Figure 47. Model 30. General displacement magnitude (m)

As shown on the Figure 44, Figure 45, Figure 46, and Figure 47, the modification of the shape lightly influences the general displacement, with a reduction of the general displacement magnitude from 3,0 mm from a rectangular opening to 2,7 mm for a horseshoe shape with 12,5 m of radius, a 10% decrease over the rectangular shape opening. (See Table 19.)

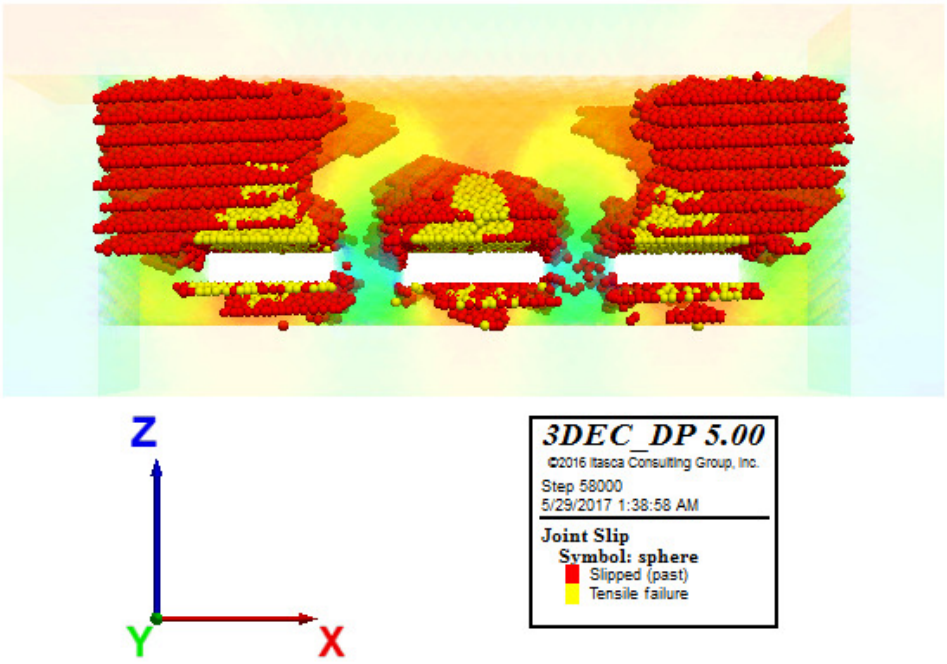

Figure 48. Model 3. Joint slip - - Plasticity Limit indicator

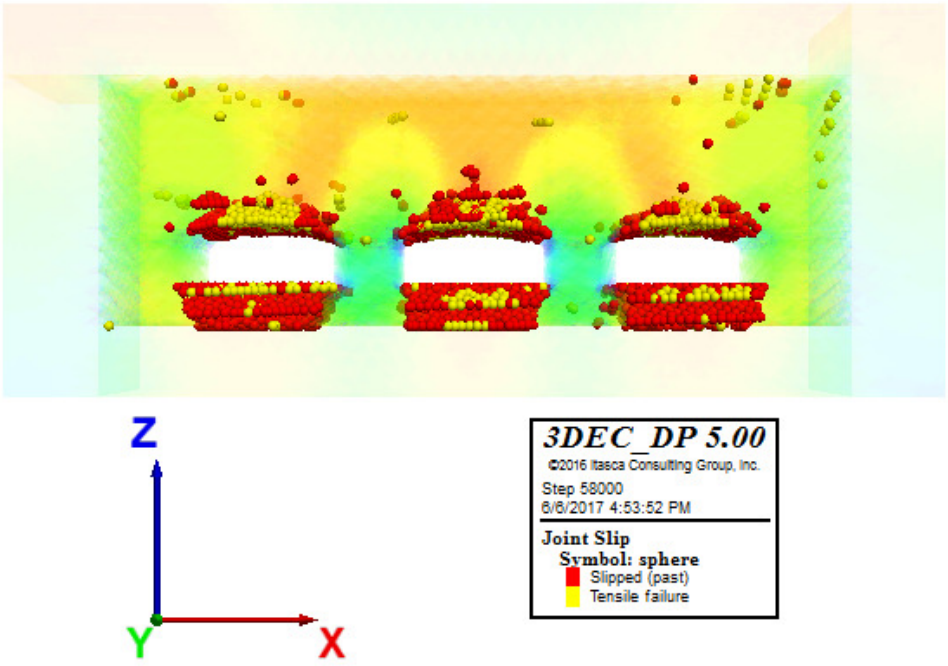

Figure 49. Model 12. Joint slip - - Plasticity Limit indicator

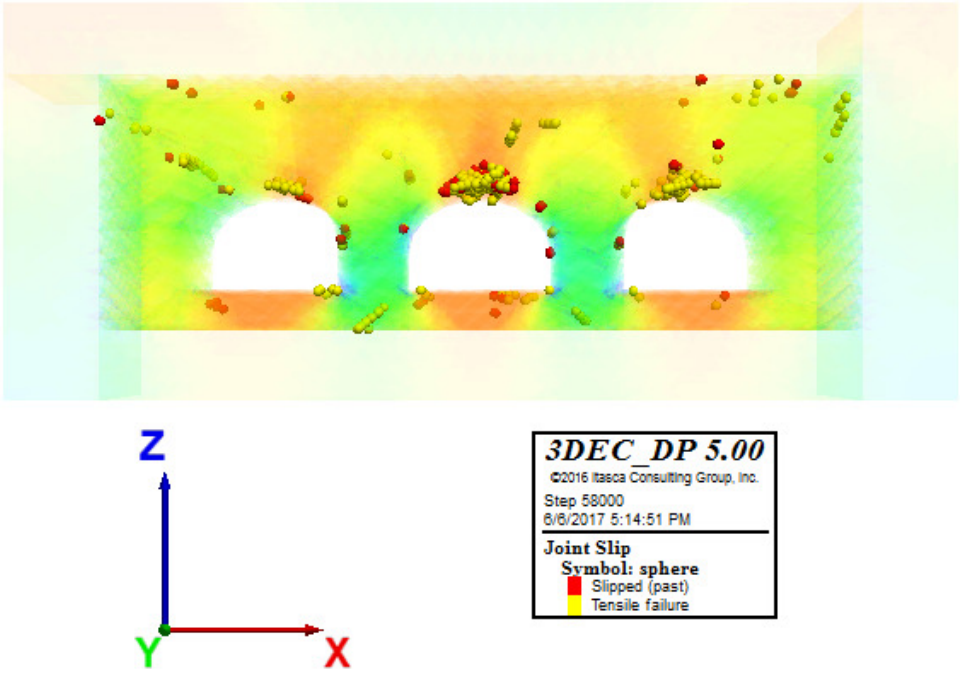

Figure 50. Model 21. Joint slip - - Plasticity Limit indicator

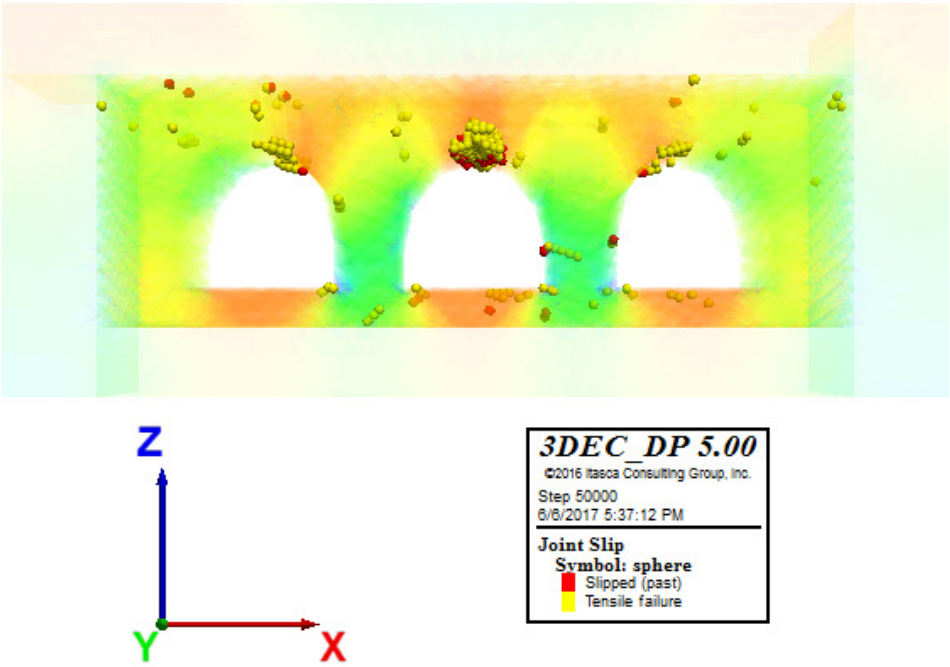

Figure 51. Model 28. Joint slip - - Plasticity Limit indicator

The increased stability after changing a rectangular extracting opening for a circular extracting opening is notorious after evaluating the joint slippage and plastic deformation. After comparing the results for each model, shown on Figure 48, Figure 49, Figure 50, Figure 51, there is a decrease on the joint slippage and tensile failure of the blocks, that helps avoid rock breakage and rock burst, both on the rooftop of the openings, as well as in general, is clearly observed.

This is supported by the improvement of the safety factor along with the increase of the radius the horseshoe shaped opening. The factor of safety increases from 1,39 for a rectangular shaped opening to more than 3,0 for a horseshoe shaped opening, going from an almost limit stability condition to a very stable condition.

Table 21. Comparison table of the displacement magnitude and Factor of safety results for model 3, model 12, model 21 and model 30

Properties	Model 3	Model 12	Model 21	Model 30
Displacement Magnitude on rooftop (mm)	3,0	2,4	2,8	2,7
Relative Decrease of the displacement	-	20	6	10

magnitude on rooftop (%)				
Factor of safety(-)	1,39	1,53	2,56	>3,0
Relative increase of the Factor of safety (%)	-	10	84	>115

5.4.2 Evaluation and analysis of the resultant stress distribution changes after modifying the shape of the openings

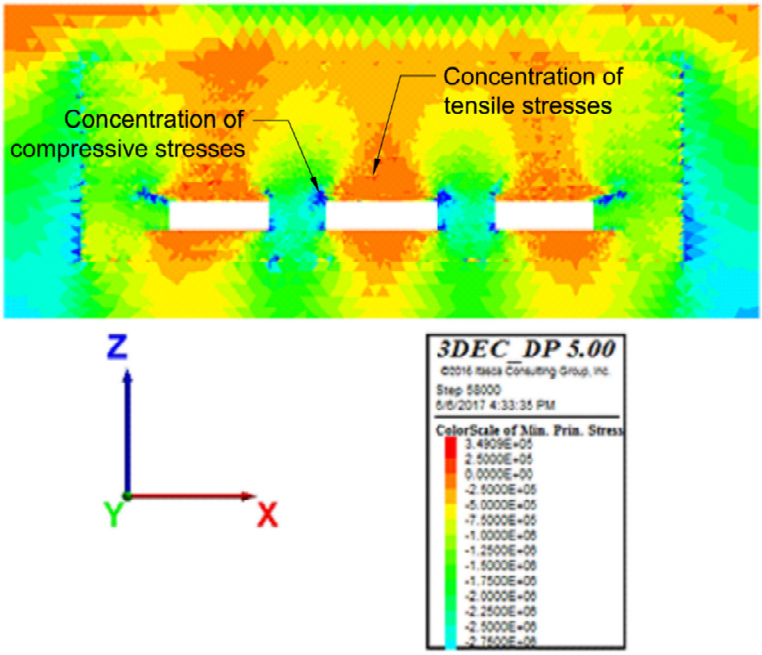

Figure 52. Model 3. Max. principal stresses (Pa)

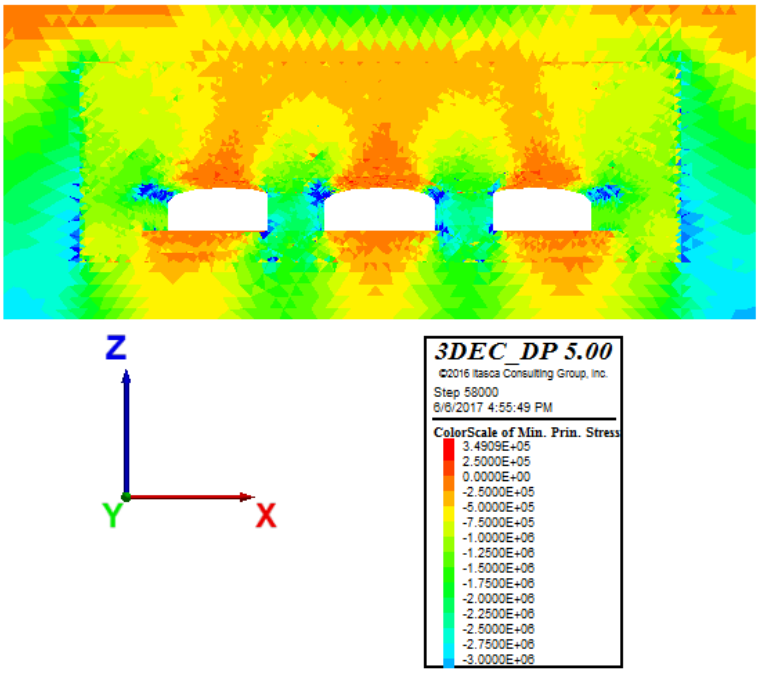

Figure 53. Model 12. Max. principal stresses (Pa)

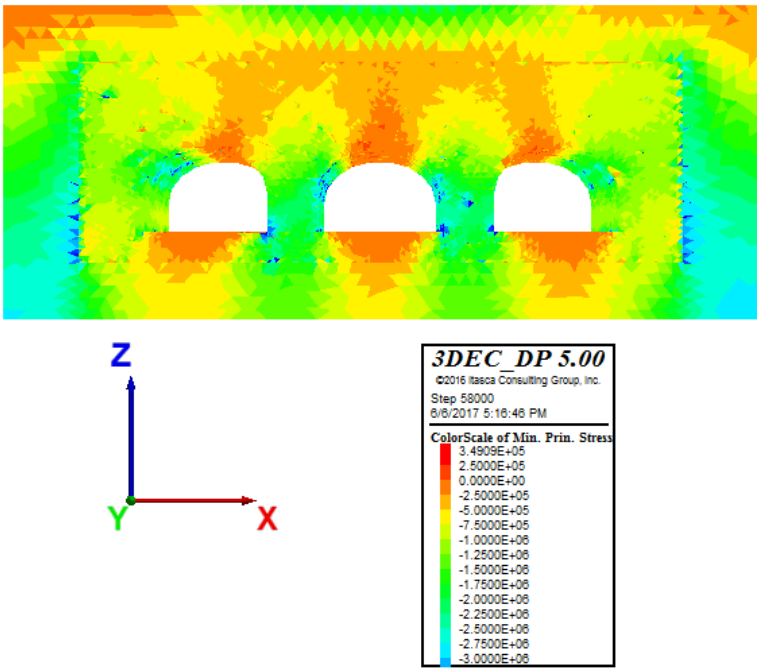

Figure 54. Model 21. Max. principal stresses (Pa)

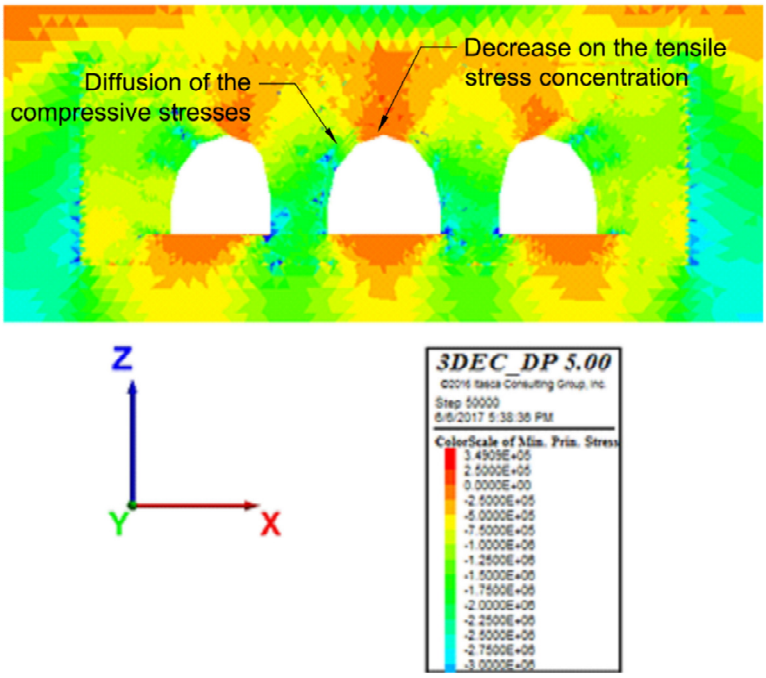

Figure 55. Model 30. Max. principal stresses (Pa)

The stresses distribution is deeply influenced by the shape of the opening. As shown in the Figure 52 and analyzed in Chapter 5.1.2, the tensile stresses concentrate on the rooftop of the rectangular openings, negatively influencing the stability of the rooftop of rectangular openings. A modification of the shape to a horseshoe shape diffuses the stresses much better, avoiding the concentration of stresses on small area an transferring it more efficiently to the pillars, as shown on Figure 53, Figure 54 and Figure 55. It is also imperative to highlight the diffusion of the concentration of the compressive stresses on the edges of the rectangle, avoiding the fracturing and weakening of the opening edges.

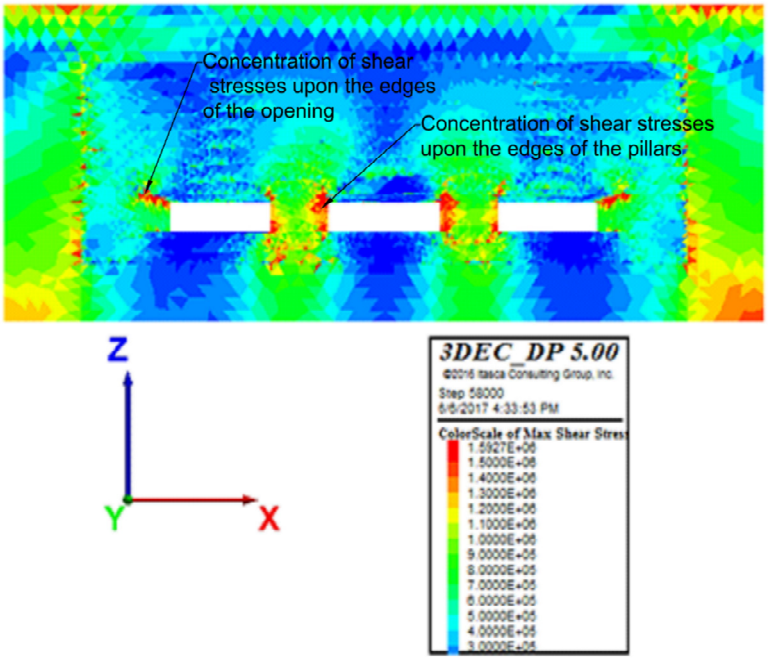

Figure 56. Model 3. Max shear stresses (Pa)

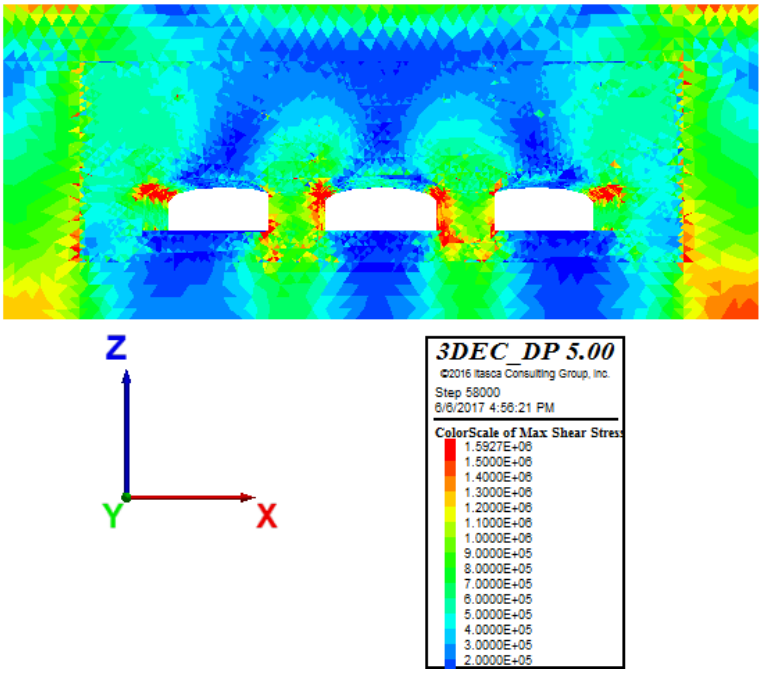

Figure 57. Model 12. Max shear stresses (Pa)

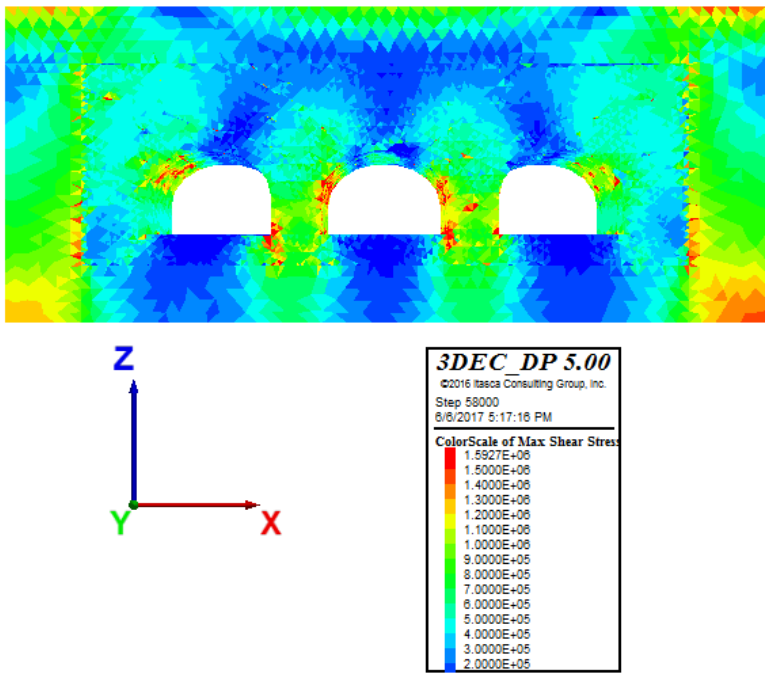

Figure 58. Model 21. Max shear stresses (Pa)

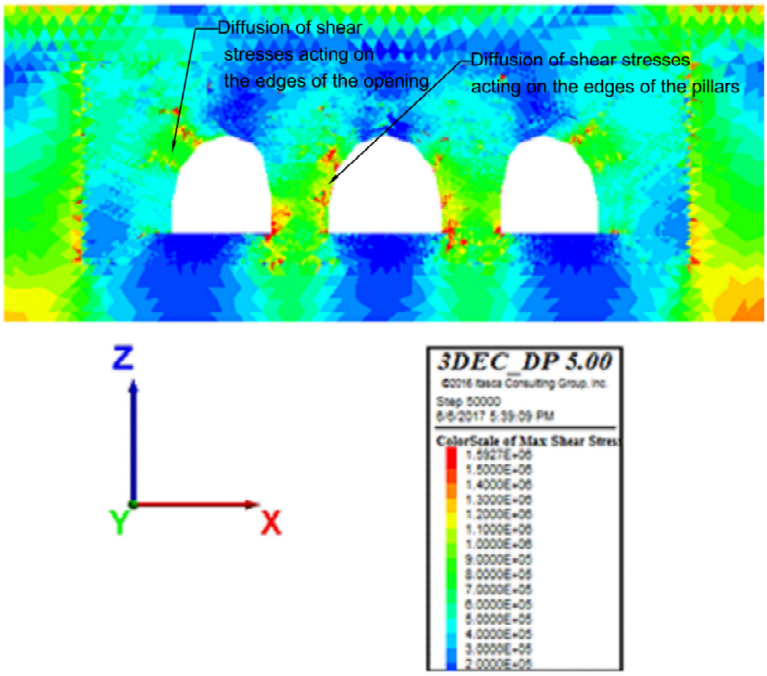

Figure 59. Model 30. Max shear stresses (Pa)

The shear stresses are profoundly influenced by the opening shape, as large changes on the distribution of stresses are observed when comparing a rectangular opening shape with a horseshoe shape. As shown on Figure 56, Figure 57, Figure 58, and Figure 59, a horseshoe shape with a circular long shape diffuses the stress

concentration upon the edges of the opening and on the edge of the pillars, improving the stability of the opening, mitigating the block slippage and plastic deformation among joints and rock break.

5.5 SUMMARY TABLE OF THE FACTOR OF SAFETY FOR THE 36 MODELS

Table 22. Summary table of the different models Factor of safety

Model Number	Shape	Joint dip condition	Geomechanical condition	Factor of safety
1	Rectangular	Initial	Condition 1	2,02
2	Rectangular	Initial	Condition 2	1,68
3	Rectangular	Initial	Condition 3	1,39
4	Rectangular	60º	Condition 1	2,58
5	Rectangular	60º	Condition 2	2,30
6	Rectangular	60º	Condition 3	2,73
7	Rectangular	-60º	Condition 1	>3,0
8	Rectangular	-60º	Condition 2	>3,0
9	Rectangular	-60º	Condition 3	>3,0
10	2.5 m radius horseshoe	Initial	Condition 1	1,99
11	2.5 m radius horseshoe	Initial	Condition 2	1,76
12	2.5 m radius horseshoe	Initial	Condition 3	1,53
13	2.5 m radius horseshoe	60º	Condition 1	2,62
14	2.5 m radius horseshoe	60º	Condition 2	2,43
15	2.5 m radius horseshoe	60º	Condition 3	2,23
16	2.5 m radius horseshoe	-60º	Condition 1	>3,0
17	2.5 m radius horseshoe	-60º	Condition 2	>3,0
18	2.5 m radius horseshoe	-60º	Condition 3	>3,0

19	7.5 m radius horseshoe	Initial	Condition 1	3,0
20	7.5 m radius horseshoe	Initial	Condition 2	2,75
21	7.5 m radius horseshoe	Initial	Condition 3	2,56
22	7.5 m radius horseshoe	60º	Condition 1	2.84
23	7.5 m radius horseshoe	60º	Condition 2	2.58
24	7.5 m radius horseshoe	60º	Condition 3	2.27
25	7.5 m radius horseshoe	-60º	Condition 1	>3,0
26	7.5 m radius horseshoe	-60º	Condition 2	>3,0
27	7.5 m radius horseshoe	-60º	Condition 3	>3,0
28	12.5 m radius horseshoe	Initial	Condition 1	>3
29	12.5 m radius horseshoe	Initial	Condition 2	>3
30	12.5 m radius horseshoe	Initial	Condition 3	3
31	12.5 m radius horseshoe	60º	Condition 1	>3,0
32	12.5 m radius horseshoe	60º	Condition 2	>3,0
33	12.5 m radius horseshoe	60º	Condition 3	>3,0
34	12.5 m radius horseshoe	-60º	Condition 1	>3,0
35	12.5 m radius horseshoe	-60º	Condition 2	>3,0
36	12.5 m radius horseshoe	-60º	Condition 3	>3,0

6 CONCLUSIONS

After evaluating and analyzing the different models with the different opening shapes, some visible and notorious changes regarding the stress distribution and pillar and rooftop stability were identifiable.

Table 23. Summary table of the different models analysis and recommendations

Model Number	Observations	Analysis
1	Initial dip, Rectangular, Condition 1, 2,02 FS	The model shows good stability, average displacement, and tensile and compression stresses concentration.
2	Initial dip, Rectangular, Condition 2, 1,68 FS	The model shows decreased stability, increased displacement, and tensile and compression stresses concentration.
3	Initial dip, Rectangular, Condition 3, 1,39 FS	The model shows low stability, increased displacement, and tensile and compression stresses concentration.
4	Dip at 60°, Rectangular, Condition 1, 2,58 FS	The model shows good stability, low displacement, and tensile and compression stresses concentration.
5	Dip at 60°, Rectangular, Condition 2, 2,3 FS	The model shows good stability, low displacement, and tensile and compression stresses concentration.
6	Dip at 60°, Rectangular, Condition 3, 2,73 FS	The model shows good stability, low displacement, and tensile and compression stresses concentration.
7	Dip at - 60°, Rectangular, Condition 1, >3,0 FS	The model shows very good stability, low displacement, and tensile and compression stresses concentration.
8	Dip at - 60°, Rectangular, Condition 2, >3,0 FS	The model shows very good stability, low displacement, and tensile and compression stresses concentration.
9	Dip at - 60°, Rectangular, Condition 3, >3,0 FS	The model shows very good stability, low displacement, and tensile and compression stresses concentration.
10	Initial dip, horseshoe with 2,5 m radius, Condition 1, 1,99 FS	The model shows good stability, average displacement, and relative diffusion of the tensile and compression stresses concentration.

11	Initial dip, horseshoe with 2,5 m radius, Condition 2, 1,76 FS	The model shows decreased stability, increased displacement, and relative diffusion of the tensile and compression stresses concentration.
12	Initial dip, horseshoe with 2,5 m radius, Condition 3, 1,53 FS	The model shows decreased stability, increased displacement, and relative diffusion of the tensile and compression stresses concentration.
13	Dip at 60°, horseshoe with 2,5 m radius, Condition 1, 2,62 FS	The model shows good stability, low displacement, and tensile and relative diffusion of the compression stresses concentration.
14	Dip at 60°, horseshoe with 2,5 m radius, Condition 2, 2,43 FS	The model shows good stability, low displacement, relative diffusion of the tensile and compression stresses concentration.
15	Dip at 60°, horseshoe with 2,5 m radius, Condition 3, 2,23 FS	The model shows good stability, low displacement, relative diffusion of the tensile and compression stresses concentration.
16	Dip at - 60°, horseshoe with 2,5 m radius, Condition 1, >3,0 FS	The model shows very good stability, low displacement, relative diffusion of the tensile and compression stresses concentration.
17	Dip at - 60°, horseshoe with 2,5 m radius, Condition 2, >3,0 FS	The model shows very good stability, low displacement, relative diffusion of the tensile and compression stresses concentration.
18	Dip at - 60°, horseshoe with 2,5 m radius, Condition 3, >3,0 FS	The model shows very good stability, low displacement, relative diffusion of the tensile and compression stresses concentration.
19	Initial dip, horseshoe with 7,5 m radius, Condition 1, 3,0 FS	The model shows very good stability, low displacement, and a large diffusion of the tensile and compression stresses concentration.
20	Initial dip, horseshoe with 7,5 m radius, Condition 2, 2,75 FS	The model shows very good stability, low displacement, and a large diffusion of the tensile and compression stresses concentration.
21	Initial dip, horseshoe with 7,5 m radius, Condition 3, 2,75 FS	The model shows very good stability, low displacement, and a large diffusion of the tensile and compression stresses concentration.

22	Dip at 60°, horseshoe with 7,5 m radius, Condition 1, 2,84 FS	The model shows very good stability, low displacement, and a large diffusion of the tensile and compression stresses concentration.
23	Dip at 60°, horseshoe with 7,5 m radius, Condition 2, 2,58 FS	The model shows very good stability, low displacement, and a large diffusion of the tensile and compression stresses concentration.
24	Dip at 60°, horseshoe with 7,5 m radius, Condition 3, 2,27 FS	The model shows good stability, low displacement, and a large diffusion of the tensile and compression stresses concentration.
25	Dip at - 60°, horseshoe with 7,5 m radius, Condition 1, >3,0 FS	The model shows very good stability, low displacement, and a large diffusion of the tensile and compression stresses concentration.
26	Dip at - 60°, horseshoe with 7,5 m radius, Condition 2, >3,0 FS	The model shows very good stability, low displacement, and a large diffusion of the tensile and compression stresses concentration.
27	Dip at - 60°, horseshoe with 7,5 m radius, Condition 3, >3,0 FS	The model shows very good stability, low displacement, and a large diffusion of the tensile and compression stresses concentration.
28	Initial dip, horseshoe with 12,5 m radius, Condition 1, >3,0 FS	The model shows very good stability, low displacement, and the concentration of tensile and compression stresses is mostly diffused.
29	Initial dip, horseshoe with 12,5 m radius, Condition 2, >3,0 FS	The model shows very good stability, low displacement, and the concentration of tensile and compression stresses is mostly diffused.
30	Initial dip, horseshoe with 12,5 m radius, Condition 3, 3,0 FS	The model shows very good stability, low displacement, and the concentration of tensile and compression stresses is mostly diffused.
31	Dip at 60°, horseshoe with 12,5 m radius, Condition 1, >3,0 FS	The model shows very good stability, low displacement, and the concentration of tensile and compression stresses is mostly diffused.

32	Dip at 60°, horseshoe with 12,5 m radius, Condition 2, >3,0 FS	The model shows very good stability, low displacement, and the concentration of tensile and compression stresses is mostly diffused.
33	Dip at 60°, horseshoe with 12,5 m radius, Condition 3, >3,0 FS	The model shows very good stability, low displacement, and the concentration of tensile and compression stresses is mostly diffused.
34	Dip at - 60°, horseshoe with 12,5 m radius, Condition 1, >3,0 FS	The model shows very good stability, low displacement, and the concentration of tensile and compression stresses is mostly diffused.
35	Dip at - 60°, horseshoe with 12,5 m radius, Condition 2, >3,0 FS	The model shows very good stability, low displacement, and the concentration of tensile and compression stresses is mostly diffused.
36	Dip at - 60°, horseshoe with 12,5 m radius, Condition 3, >3,0 FS	The model shows very good stability, low displacement, and the concentration of tensile and compression stresses is mostly diffused.

While the basic model with rectangular openings shows a stable behavior, with low subsidence and displacement, as represented by a total displacement of less than 3,0 mm at the rooftop of the middle opening and of only 1,2 mm on the pillars, and a relatively high factor of safety of 2,02, it was observed that the tensile maximum stresses concentrate on the roof of the openings while the pillars are subject to high compressive stresses. This was further confirmed by the observed tensile slippage and plastic deformation due to joint failure on the rooftop of the openings.

The shear and compressive stresses also concentrated on the edges of the rectangle openings, as observed on the Figure 25, a troublesome behavior that could led to rock breakage and stability problems. Furthermore, shear stresses and reaction tensile stresses to the compressive stresses on the center of the pillar also concentrated on the pillar edges, which could lead to rock burst and joint slips.

With the reduction of the value of the geomechanical parameters for the joints, the models show an increased instability, blocks slippage and plastic deformation as reflected by the reduction of the factor is observed from a 2,02 for the basic - model 1, to and 1.39 for the model with the lowest geomechanical parameters - model 3, as well as by the increase of the displacement magnitude form 2,4 mm to 3,0 mm

on the rooftop as well as form 1,2 mm to 1,5 mm on the pillars. Some localized stability problems on the opening's rooftop, were few individual blocks show a larger strain and possible block and rock falls were also identified.

The models with the modified joint families dip at 60º and -60º from the original basic model proved to be more stable, especially the later, with a significant lower displacement on the rooftops and pillars. These models with an orientation at 60º and -60º, presented good stability conditions with higher factors of safety. The models with a –60º joint dip orientation modification show a significantly higher factor of safety, all models with joint families with this dip modification had a calculated factor of safety of more than 3,0. The stress distribution showed a similar behavior similar to the models with joint families with normal dip, but there was a very significant decrease on the risk of joint slippage and block tensile failure.

After analyzing and identifying the critical behaviors supplied by the models modified with different geomechanical joint parameters and joint families dip orientation, the changes due to the modification of the shape were analyzed. The results showed that modifying the shape form from a rectangle to a horseshoe lightly influences the general displacement, with a reduction of the general displacement magnitude on the rooftop of the middle opening, with a progressive decrease with a larger radius, until reaching a 10% decrease over the rectangular shape opening.

The increased stability after changing a rectangular extracting opening for a horseshoe shape opening is notorious after evaluating the joint slippage and plastic deformation. A decrease on the amount of blocks subject to joint slippage and tensile failure is easily identifiable. This is supported by the improvement of the safety factor along with the increase of the radius the horseshoe shaped opening, that in some cases reaches over 100%, or over >3,0 on most cases

A modification of the shape to a horseshoe shape showed how the stresses are diffused, avoiding the concentration of stresses on small area a transferring it more efficiently to the pillars. There is a lesser concentration of tensile stresses on the rooftop, as well as a lower concentration of compressive stresses on the edges of the opening. The shear stresses on the edges of the openings and the edges of the pillars are also greatly diffused, with a direct relationship with the radius of the horseshoe opening shape.

After evaluating all results, it can be concluded that there is a direct relationship between the change of the opening shape and the attainment of a more stable structure behavior, with less strain and higher factor of safety. This could be an effect of a more efficient stress distribution due to the removal of troublesome angles that concentrate shear and compressive stresses.

It can also be concluded that the stability of the openings improves proportionately with the increase diameter of the horseshoe shaped opening, so it is advisable for the further development of the openings during the extraction process of Cantera de

Campanzar, the rectangular openings of approx. 20 m X 20 m X 20m should be replaced for a corresponding horseshoe opening, if the logistic, equipment, and mining methodology are appropriate or can be adapted for this opening shapes. Other circular shape, like inverse arc, d-shape or egg shape will be also possible, although further studies are recommended for these shapes.

7 RECOMMENDATIONS

This research had a restricted scope, with limited time and computational resources. Therefore, there is a lot that can be further investigated or expanded upon:

1) Lowering the spacing of the tetrahedral grid will give a more precise model of the mine.
2) Only a few (3) of the 7 joint families were utilized for the models, the use of all or at least more of them could yield more precise and interesting results.
3) Only the south zone of the mine was modelled, the modelling of the north zone will be interesting, specially to compare the different behaviors.
4) The study can be expanded to more openings to better recreate the room and pillar mine layout, or even the whole mine operation could be modeled.
5) It is advisable to expand the research to further mine openings (Circular, d-shape, inverted arc, etc.), with variable radius and dimensions.
6) This research was based upon the specific conditions of “Cantera Campanzar” surface and underground quarry. Although the results are likely to be applicable to other projects or operations, a specific study for each condition is recommended.
7) After studying and analyzing the positive influence that the modification of the rectangular openings to large diameter horseshoe ones has on the overall stability, stress distribution and safety, the usage of horse shoe or similar shapes is recommended, as long as the methodology, equipment, logistics and other construction and operation conditions allow the excavation of a circular shaped opening.

8 BIBLIOGRAFICAL REFERENCES

1) Calinor, www.calcinor.com/es/calcinor/empresas-calcinor/, 2018
2) Castro. J. Estudio geotécnico del proyecto de explotación transferencia de minería de exterior a minería subterránea en la Cantera de Campanzar no 4.743. 2015.
3) Cundall P.A., Strack O.D.L., A discrete numerical model for granular assemblies, in Géotechnique, Volume 29, issue 1, 1979, p. 47 - 65.
4) Dai Y., Wang Y., Wang. Y., Coupling Analysis on Seepage and Stress in Jointed Rock Tunnel with the Distinct Element Method, Y. Yuan, J.Z. Cui and H. Mang (eds.), Computational engineering section, 2009, p. 1059 - 1054.
5) Dowding Ch. H., O'connor K.M., Distinct Element Modeling and Analysis of Mining-induced Subsidence, in Rock Mechanics and Rock engineering, Volume 25, 1992, p. 1 - 24.
6) Fallahzadeh S.H., Fatahi H., Mofassal H., Masood M., Numerical simulation for the determination of hydraulic fracture initiation and breakdown pressure using distinct element method, in Journal of natural Gas Science and Engineering, Volume 3, 2016, p. 1219 – 1232
7) Fossum, A. F., Technical Note: Effective Elastic Properties for a Randomly Jointed Rock Mass, in International journal of rock mechanics and mining sciences, chapter 22, issue 6,1985, pg. 467-470.
8) Fuxing J., Kulatilake P., Zhengxing Y., Effect of Tunnel Shape and Support System on Stability of a Tunnel in a Deep Coal Mine in China, in Geotechnical and Geological Engineering, Volume 30, Issue 2, 2012, p. 383 - 394.
9) Gerrard, C. M.,Elastic Models of Rock Masses Having One, Two and Three Sets of Joints, in International journal of rock mechanics and mining sciences, issue 19,1982, pg. 15-23.
10) Gerrard, C. M., Equivalent Elastic Moduli of a Rock Mass Consisting of Orthorhombic Layers, in International journal of rock mechanics and mining sciences, issue 19,1982, pg. 9-14.
11) Goodman, R. E., Introduction to Rock Mechanics. New York: John Wiley and Sons,1980).
12) Husillos R., Strain state analysis of a limestone rock mass exposed to change due to underground excavation by Raul Husillos Rodriguez, Universidad de Cantabria, 2017
13) Itasca, Distinct Element Method, www.itascacg.com/software/pfc/distinct-element-method, 2016

14) Koroneos P. S., Theocaris P. S., Stress Distribution Around a Tunnel Situated in a Layer Under the Action of Gravity, in Rock Mechanics, Volume 4, 1972, p. 139 - 154.

15) Ndjaka J.M.P, Ngueyep L.L., Ndop J., Numerical Investigations of Stresses and Strains Redistribution around the Tunnel: Influence of Transverse Isotropic Behavior of Granitic Rock, In Situ Stress and Shape of Tunnel, in Journal of mining science, Volume 51, issue 3, 2015, p. 497 - 505.

16) Rahmannejad R., Ravandi E., Wall displacement prediction of circular, D shaped and modified horseshoe tunnels in non-hydrostatic stress fields, in Tunneling and underground Space Technology, Volume 34, 2013, p. 54 - 60.

17) Srisharan S., Pinnaduwa H.S.W., Discontinuum–Equivalent Continuum Analysis of the Stability of Tunnels in a Deep Coal Mine Using the Distinct Element Method, in Rock Mechanics and Rock Engineering, Volume 49, 2016, p. 1903 – 1922

ANNEX A. COMPLETE RESULTS FOR THE 36 MODELS

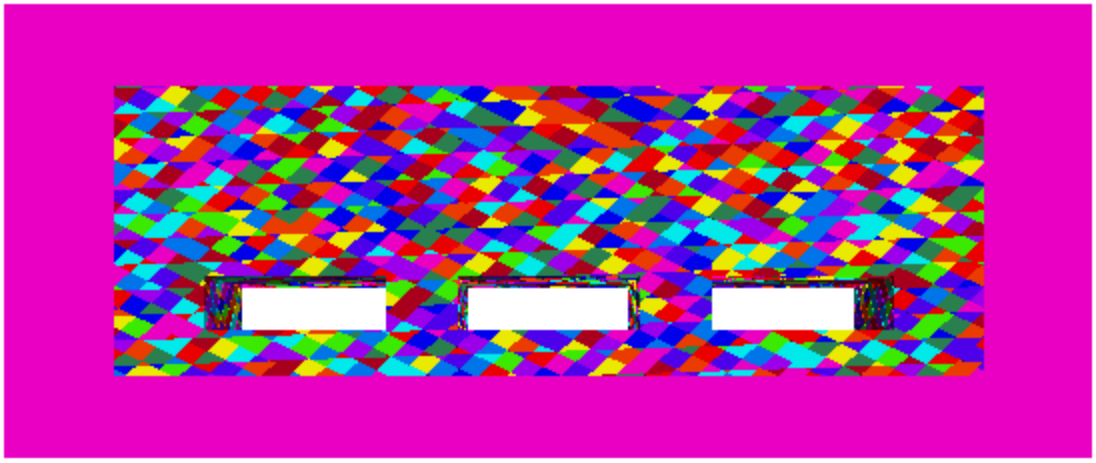

Figure 60. Model 1. Layout

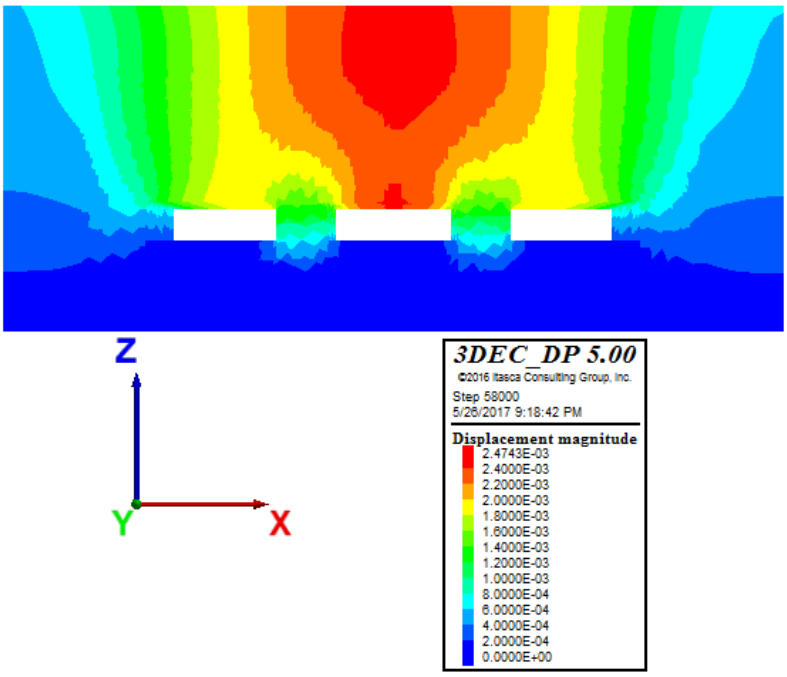

Figure 61. Model 1. Displacement magnitude (m)

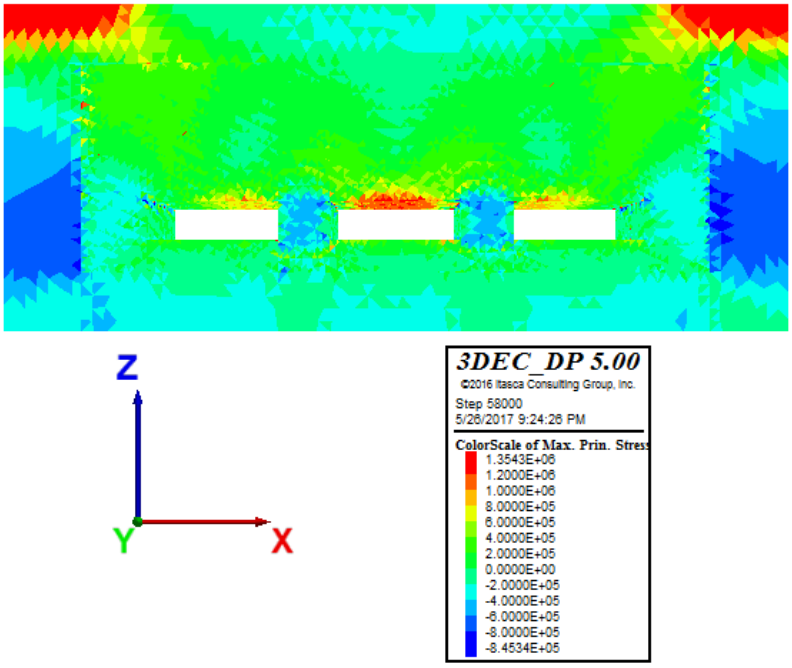

Figure 62. Model 1. Max. principal stresses (Pa)

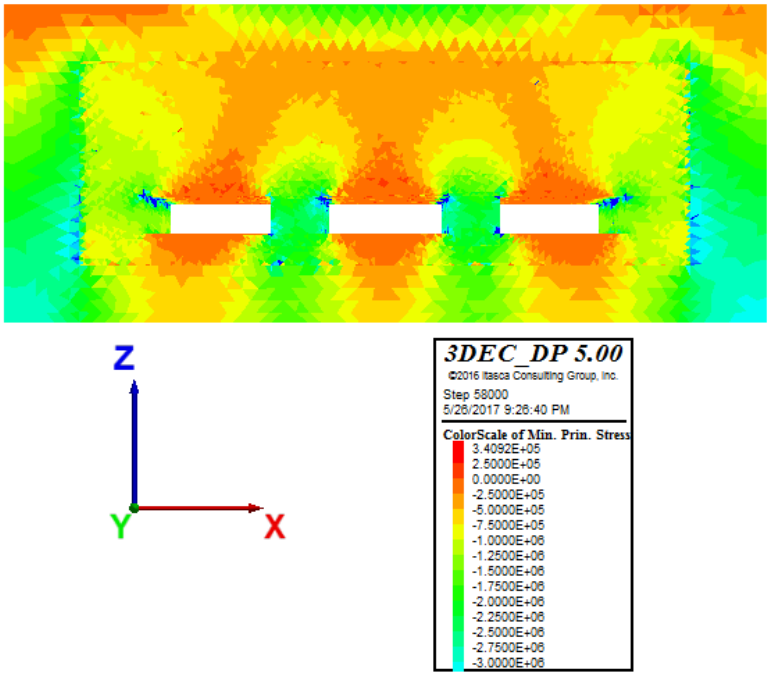

Figure 63. Model 1. Min. principal stresses (Pa)

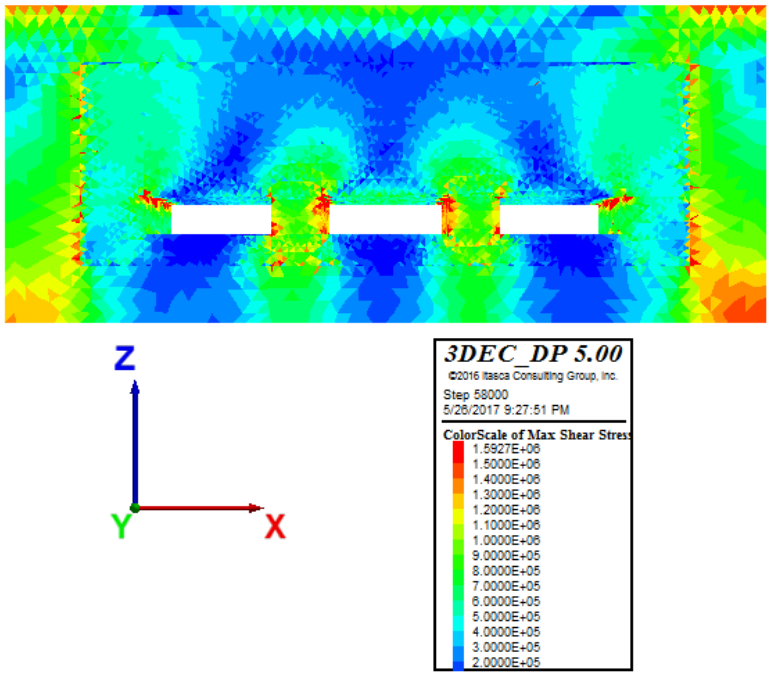

Figure 64. Model 1. Max shear stresses (Pa)

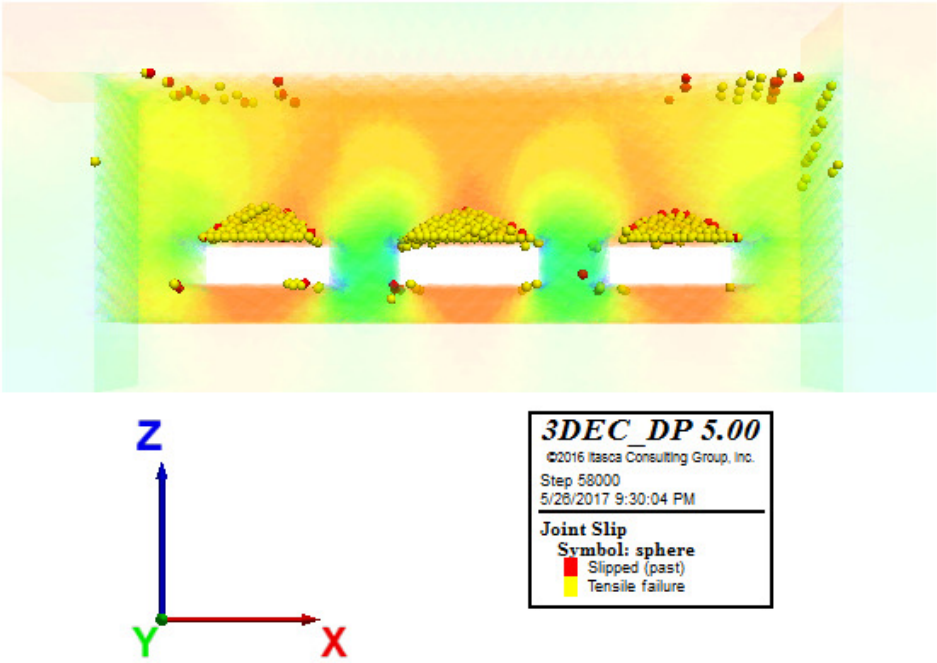

Figure 65. Model 1. Joint slip - Plasticity Limit indicator

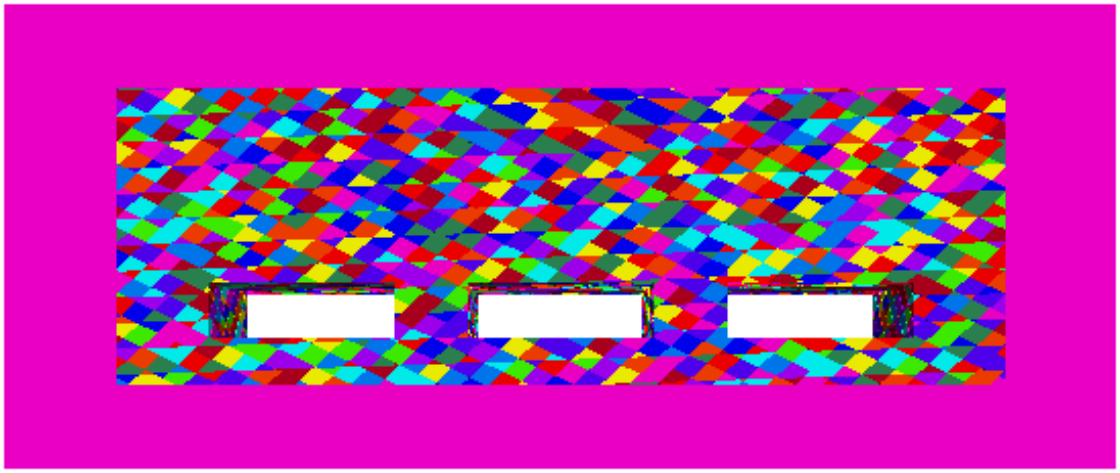

Figure 66. Model 2. Layout

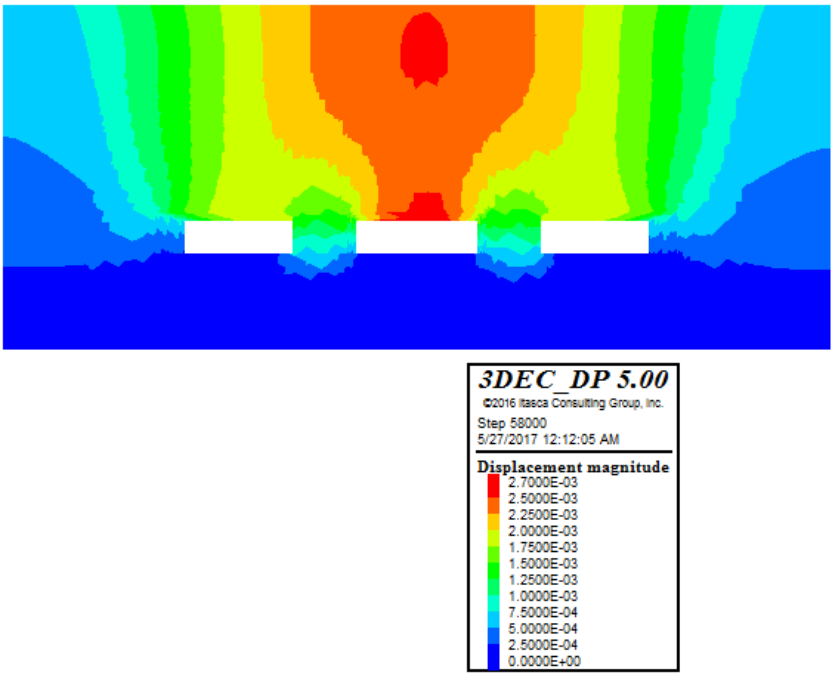

Figure 67. Model 2. Displacement magnitude (m)

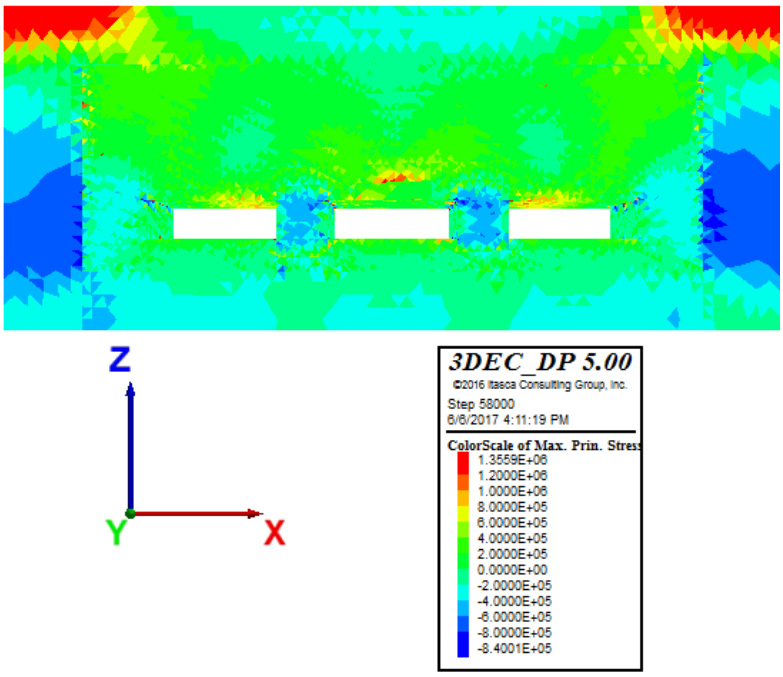

Figure 68. Model 2. Max. principal stresses (Pa)

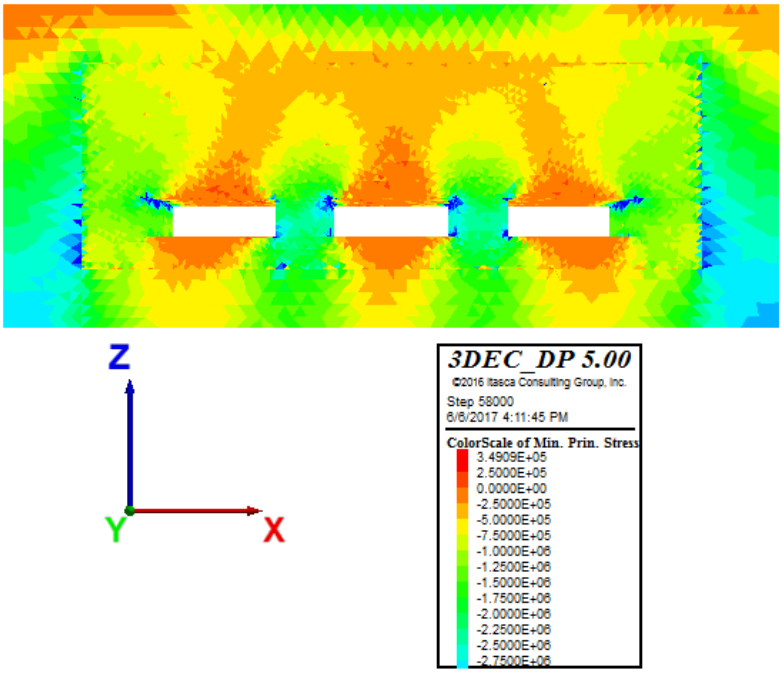

Figure 69. Model 2. Min. principal stresses (Pa)

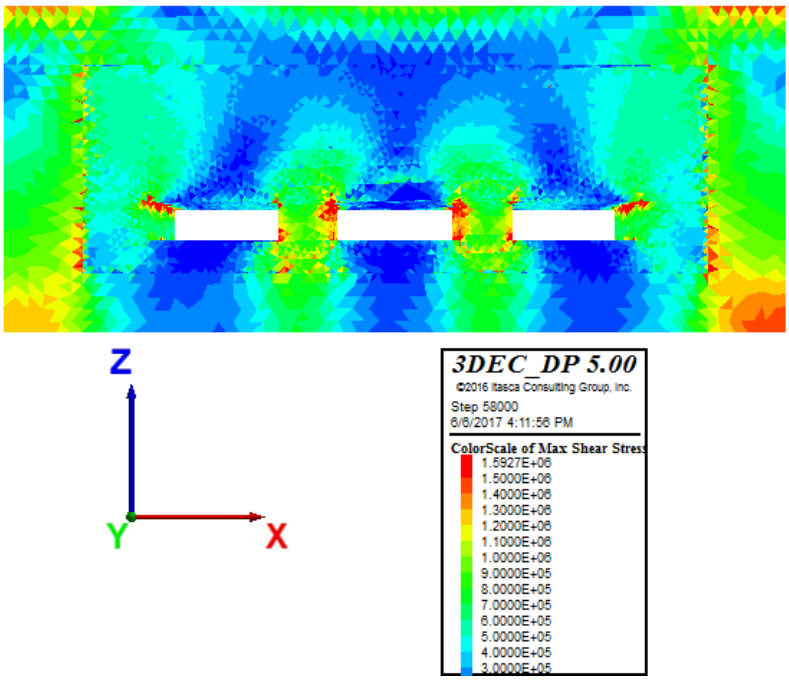

Figure 70. Model 2. Max shear stresses (Pa)

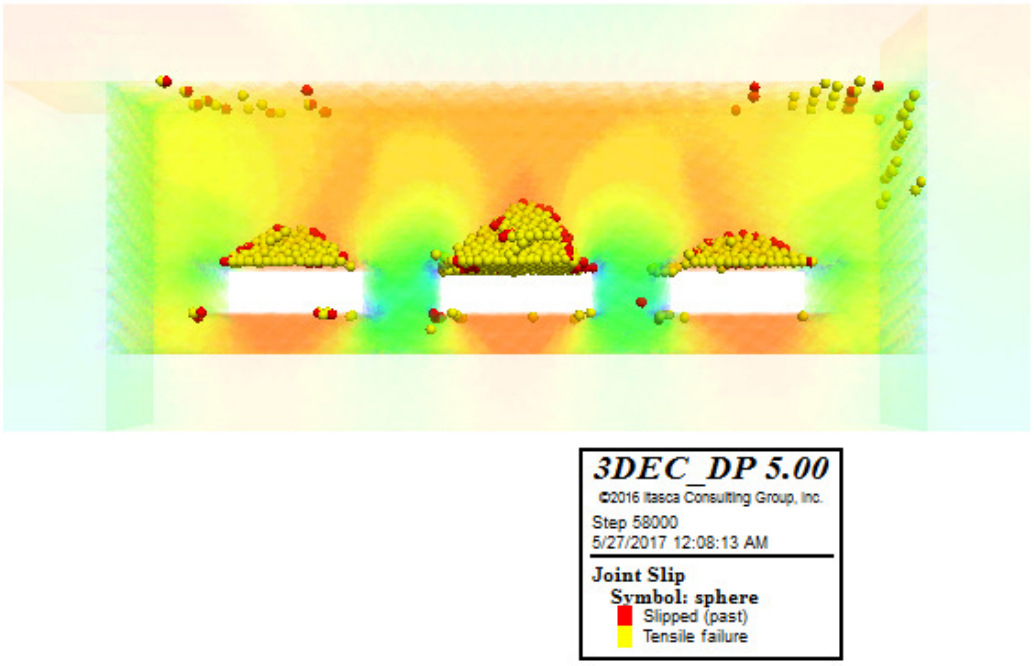

Figure 71. Model 2. Joint slip - Plasticity Limit indicator

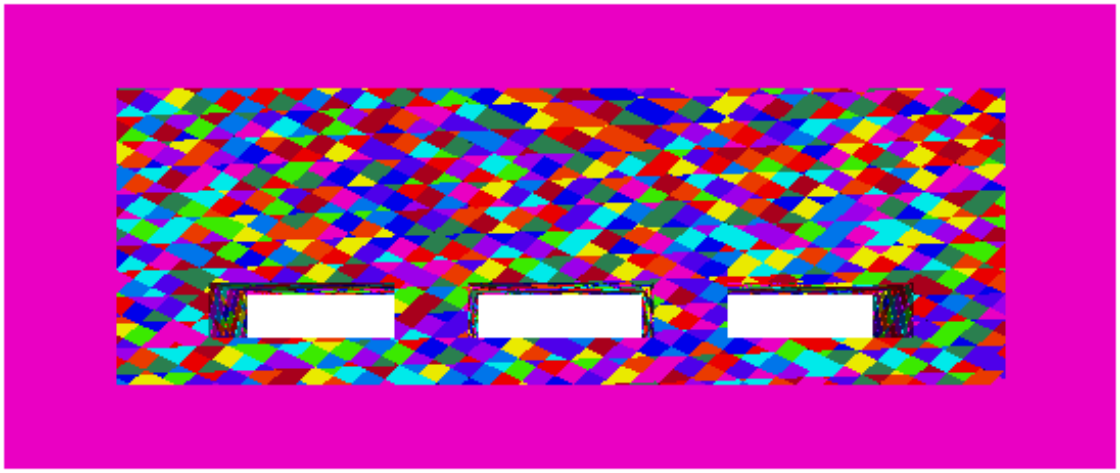

Figure 72. Model 3. Layout

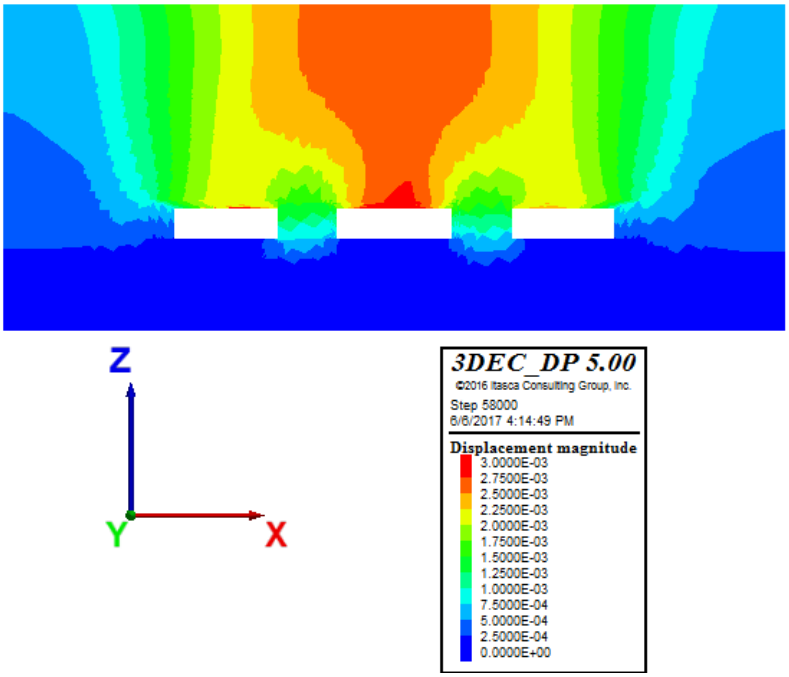

Figure 73. Model 3. Displacement magnitude (m)

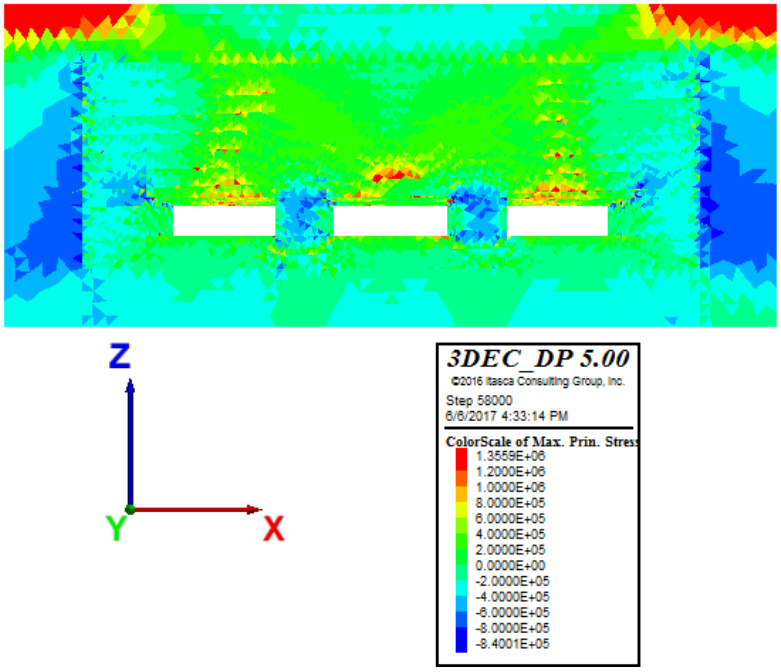

Figure 74. Model 3. Max. principal stresses (Pa)

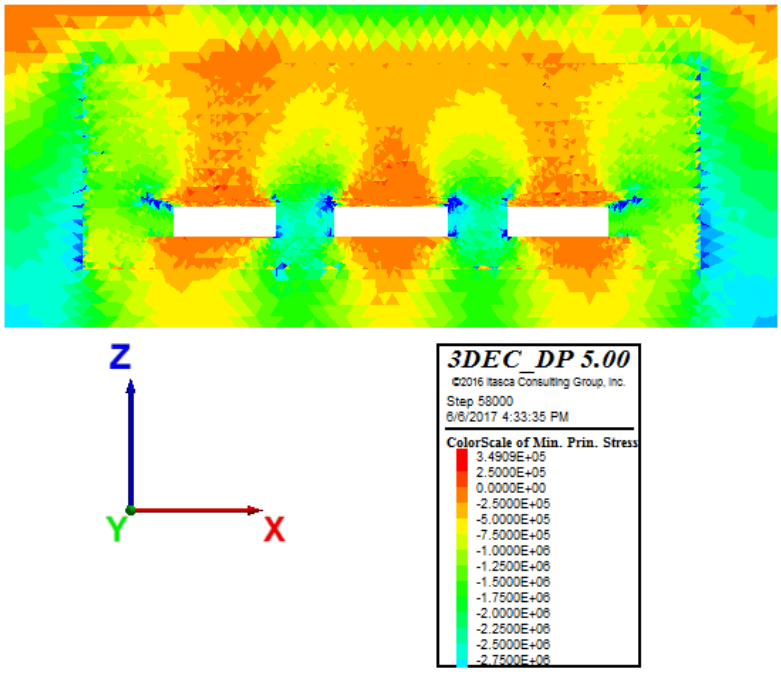

Figure 75. Model 3. Min. principal stresses (Pa)

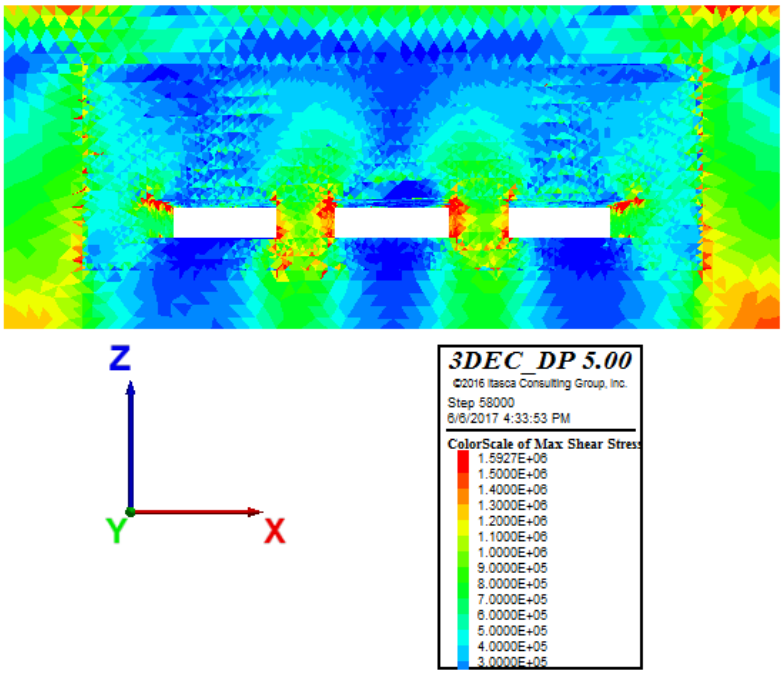

Figure 76. Model 3. Max shear stresses (Pa)

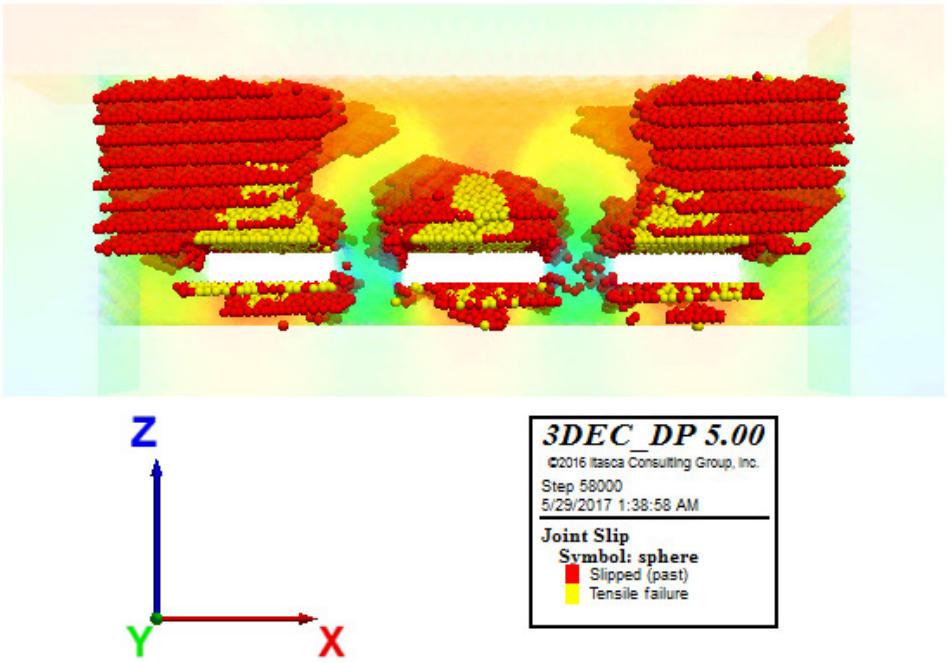

Figure 77. Model 3. Joint slip - Plasticity Limit indicator

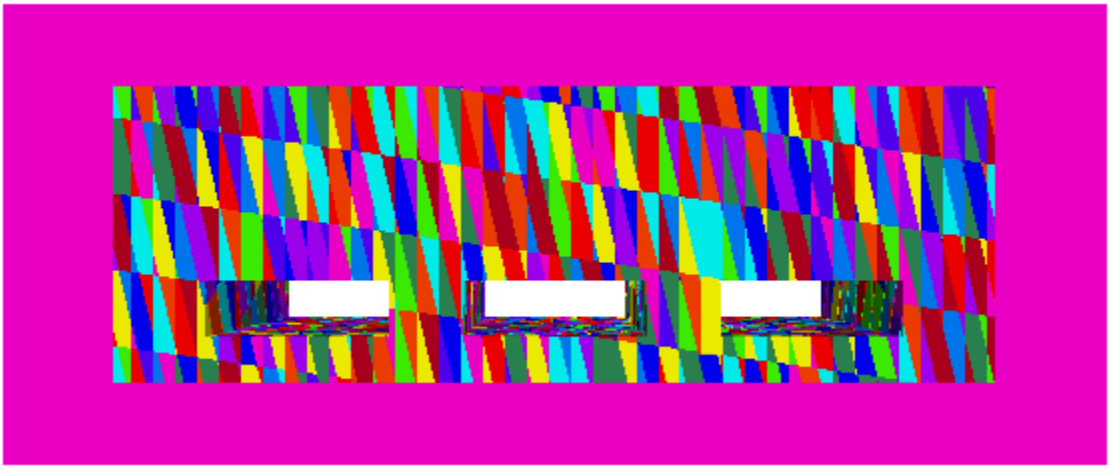

Figure 78. Model 4. Layout

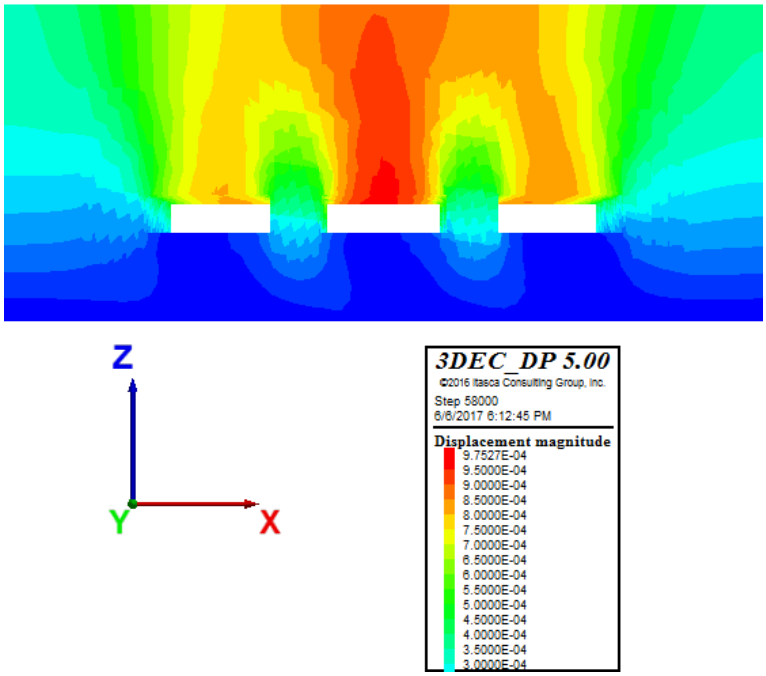

Figure 79. Model 4. Displacement magnitude (m)

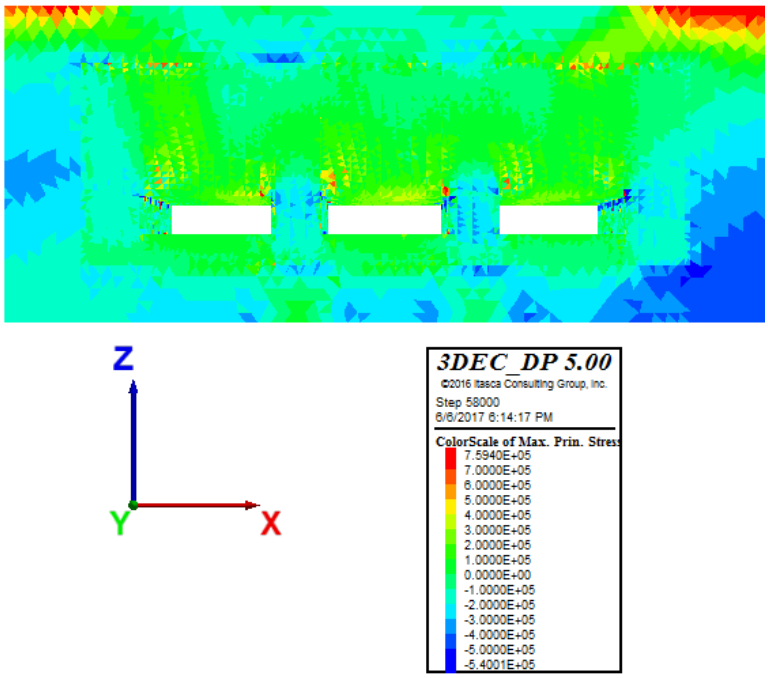

Figure 80. Model 4. Max. principal stresses (Pa)

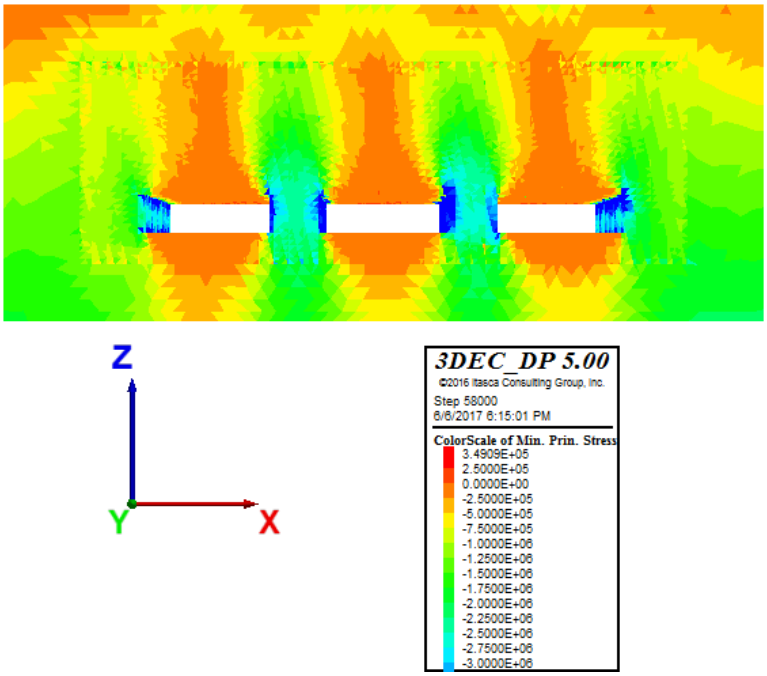

Figure 81. Model 4. Min. principal stresses (Pa)

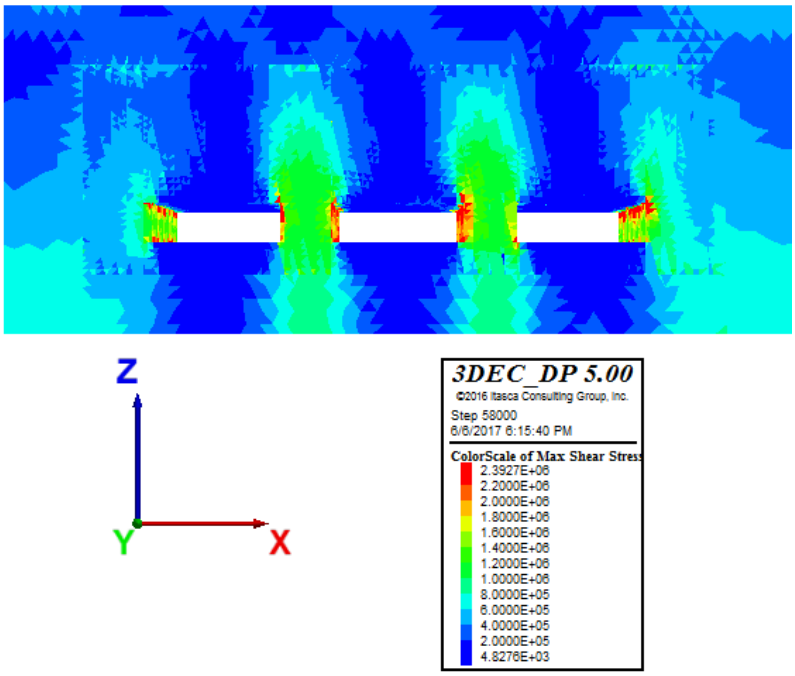

Figure 82. Model 4. Max shear stresses (Pa)

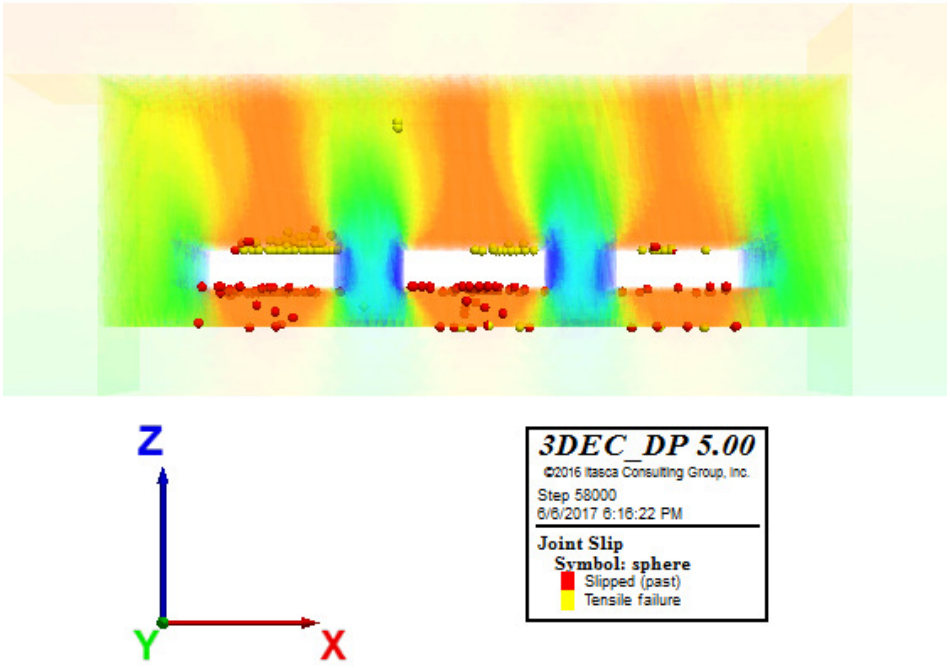

Figure 83. Model 4. Joint slip - Plasticity Limit indicator

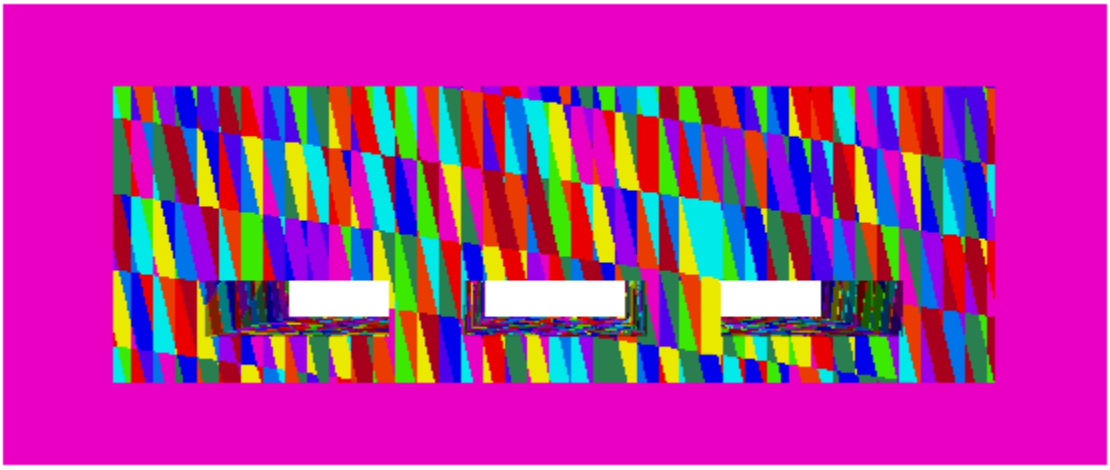

Figure 84. Model 5. Layout

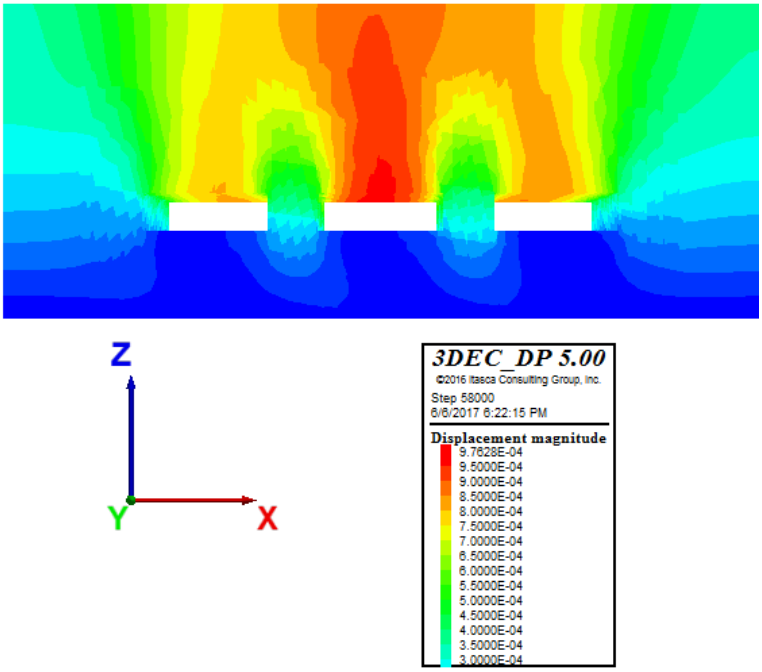

Figure 85. Model 5. Displacement magnitude (m)

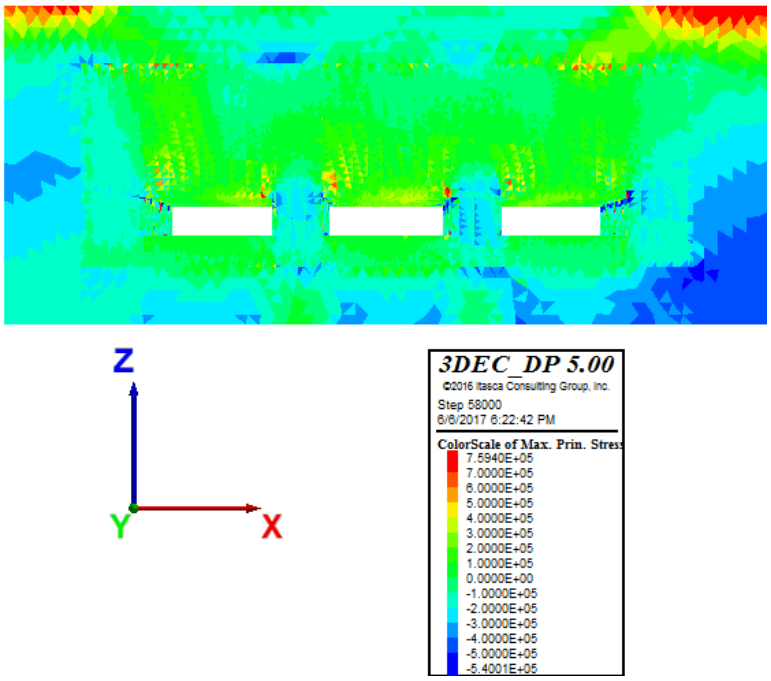

Figure 86. Model 5. Max. principal stresses (Pa)

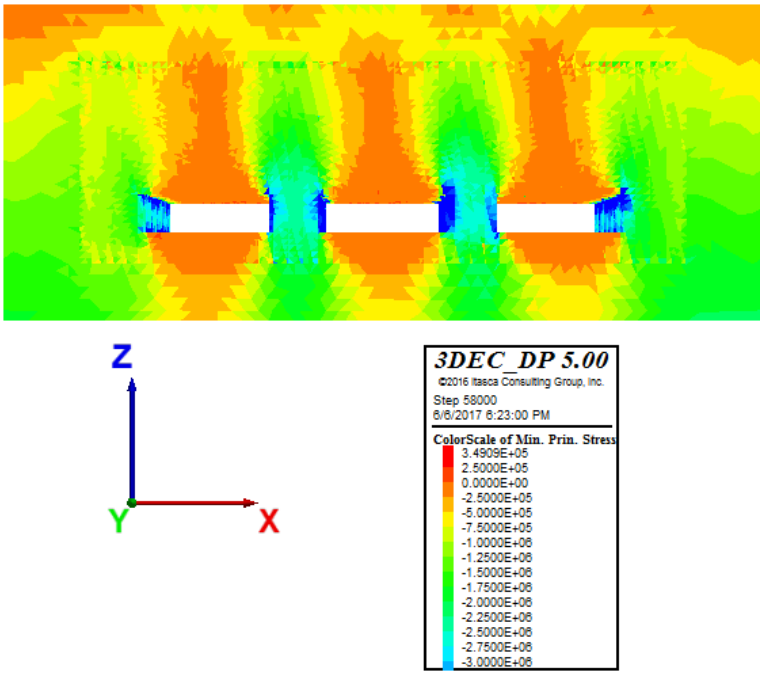

Figure 87. Model 5. Min. principal stresses (Pa)

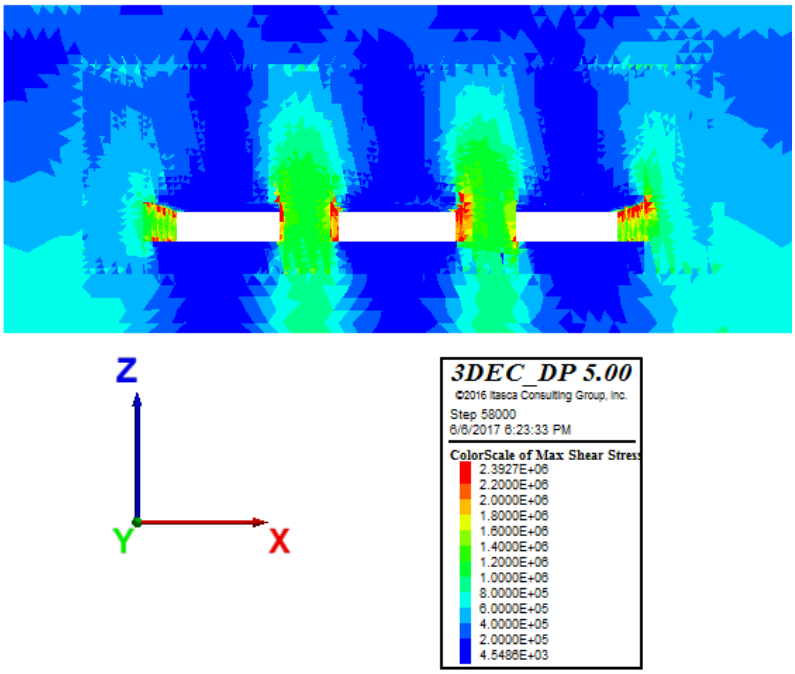

Figure 88. Model 5. Max shear stresses (Pa)

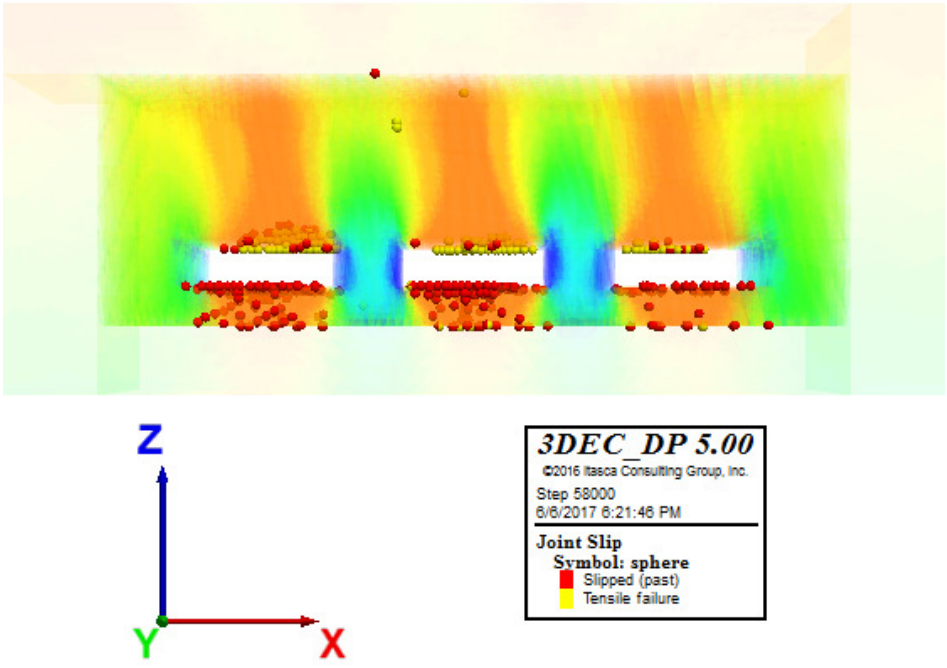

Figure 89. Model 5. Joint slip - Plasticity Limit indicator

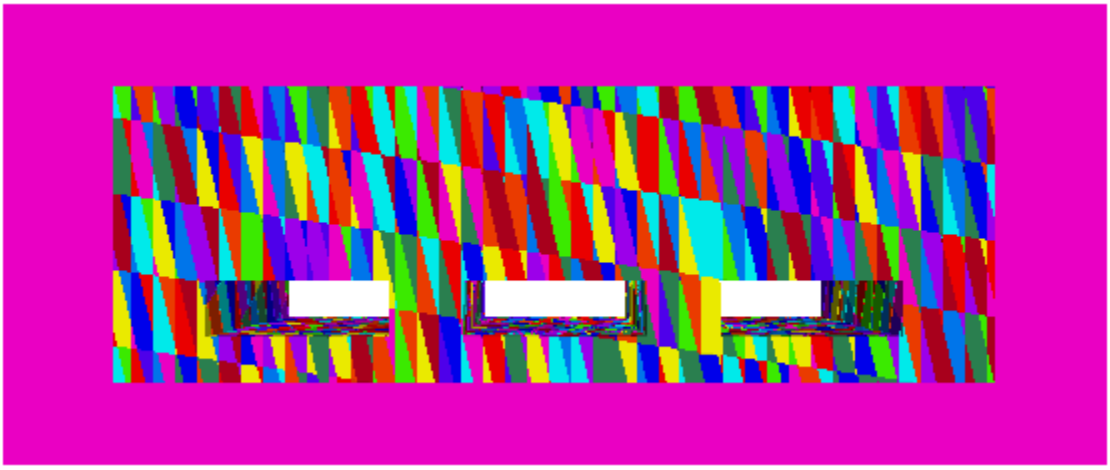

Figure 90. Model 6. Layout

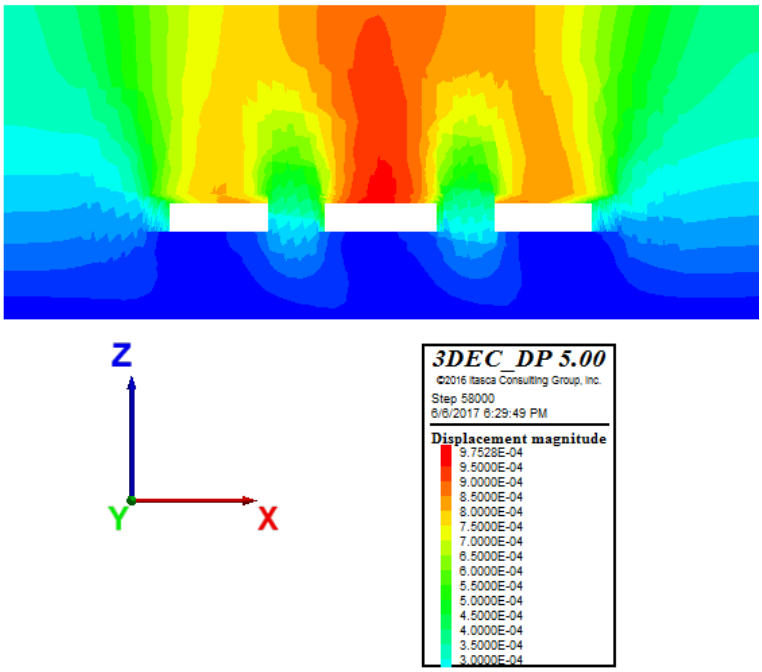

Figure 91. Model 6. Displacement magnitude (m)

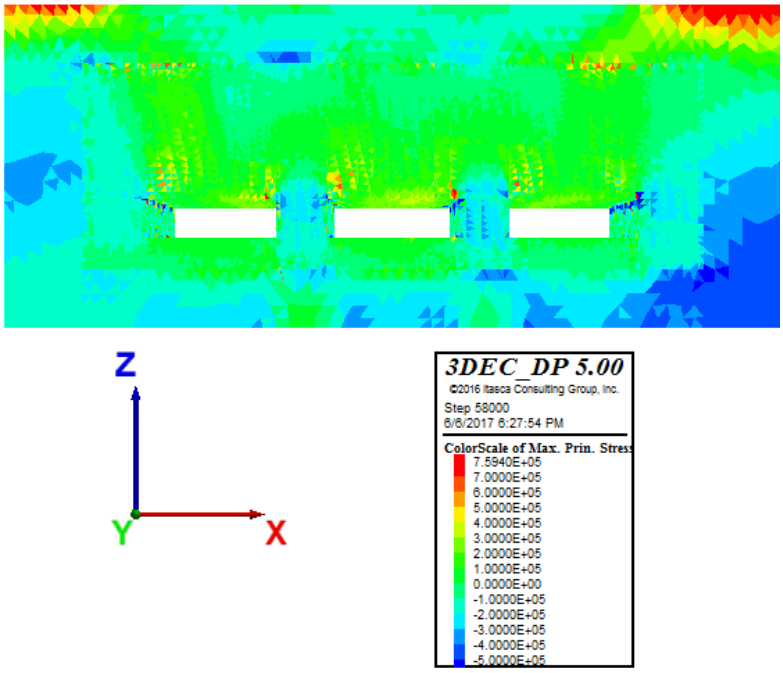

Figure 92. Model 6. Max. principal stresses (Pa)

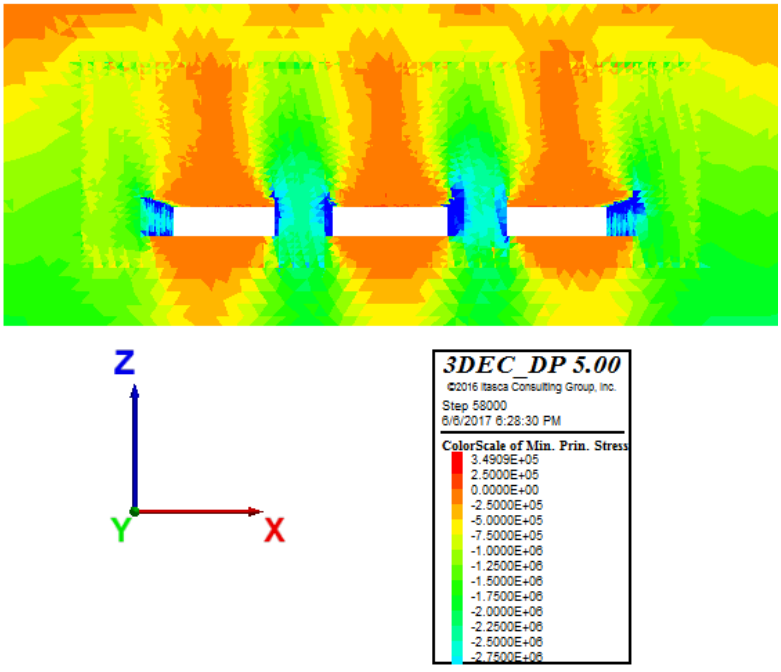

Figure 93. Model 6. Min. principal stresses (Pa)

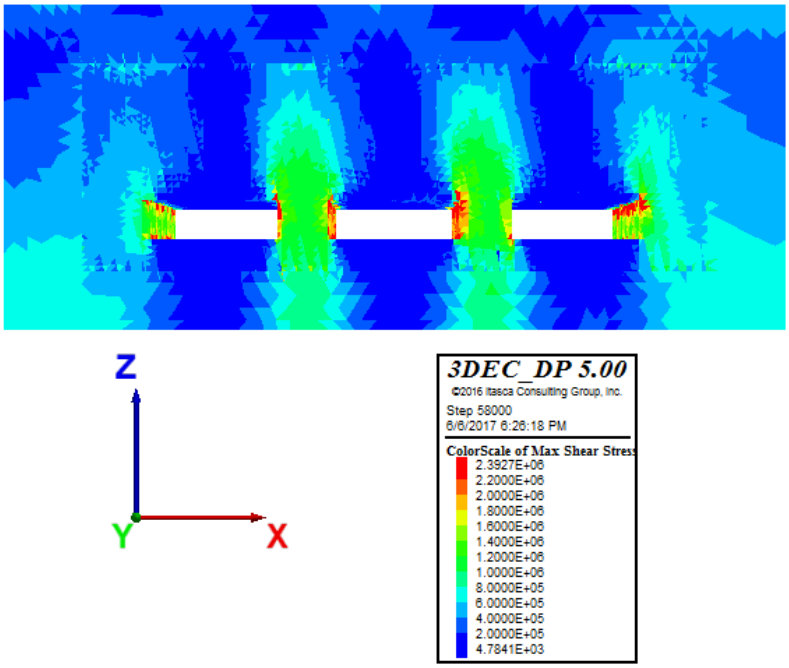

Figure 94. Model 6. Max shear stresses (Pa)

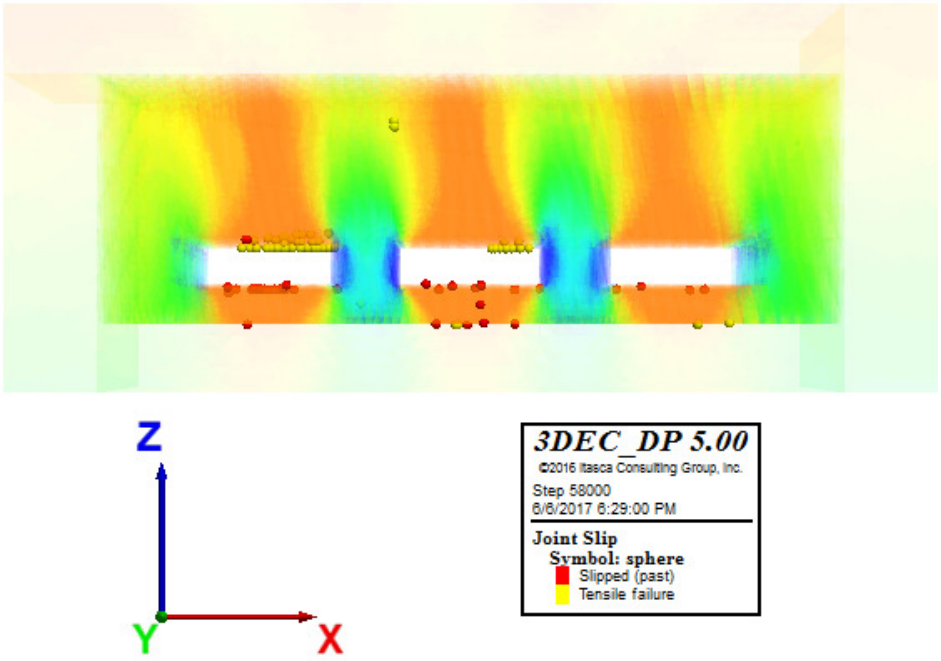

Figure 95. Model 6. Joint slip - Plasticity Limit indicator

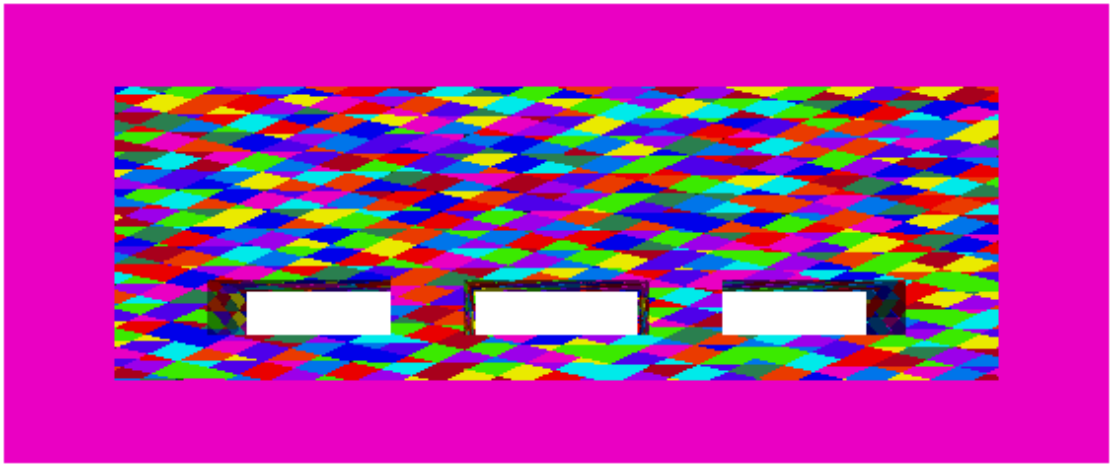

Figure 96. Model 7. Layout

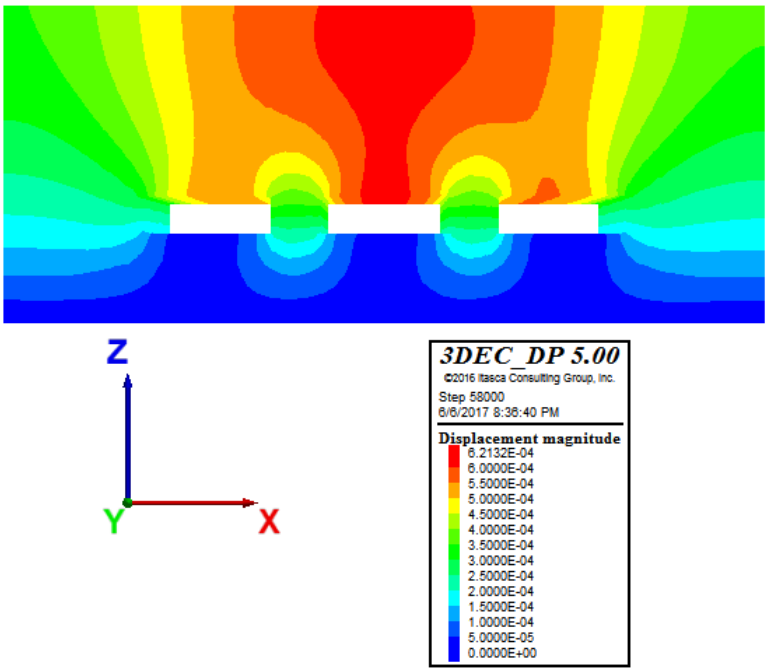

Figure 97. Model 7. Displacement magnitude (m)

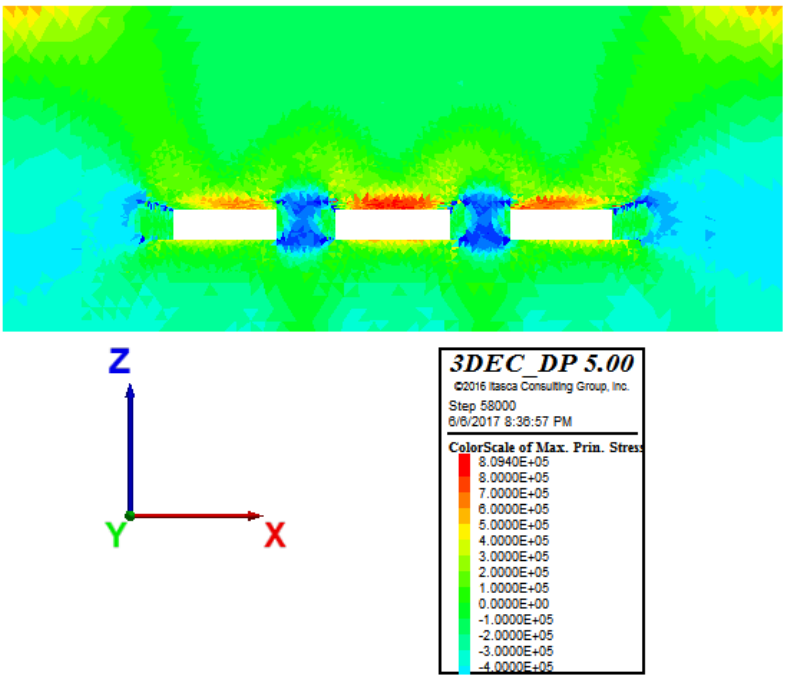

Figure 98. Model 7. Max. principal stresses (Pa)

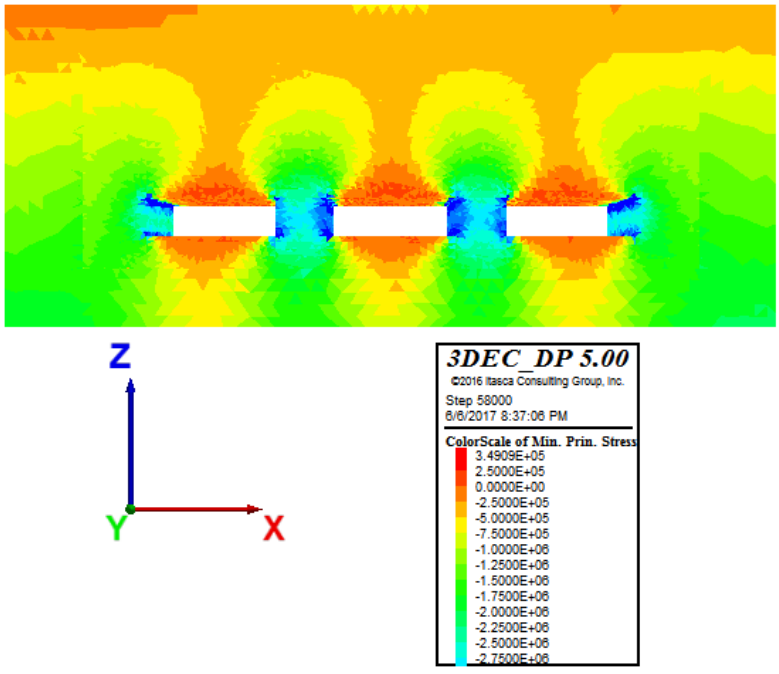

Figure 99. Model 7. Min. principal stresses (Pa)

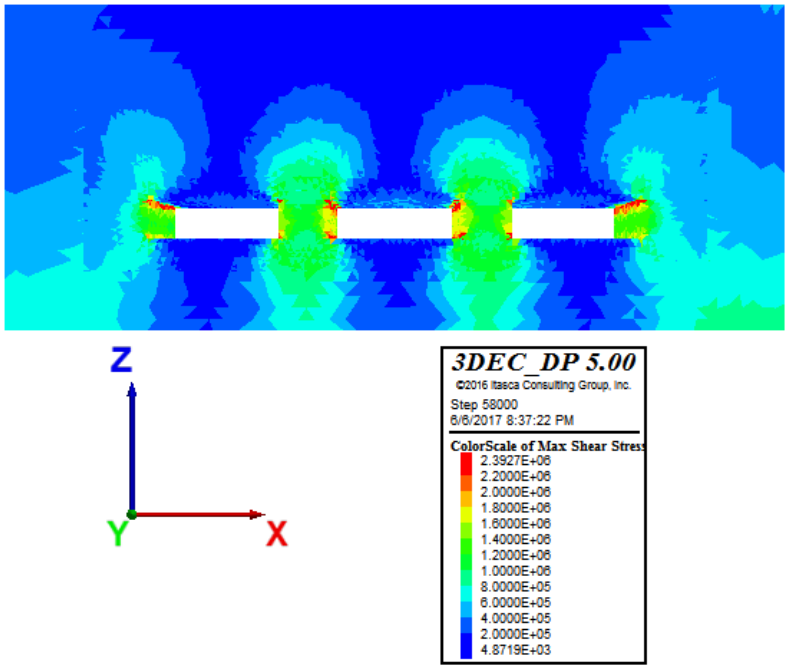

Figure 100. Model 7. Max shear stresses (Pa)

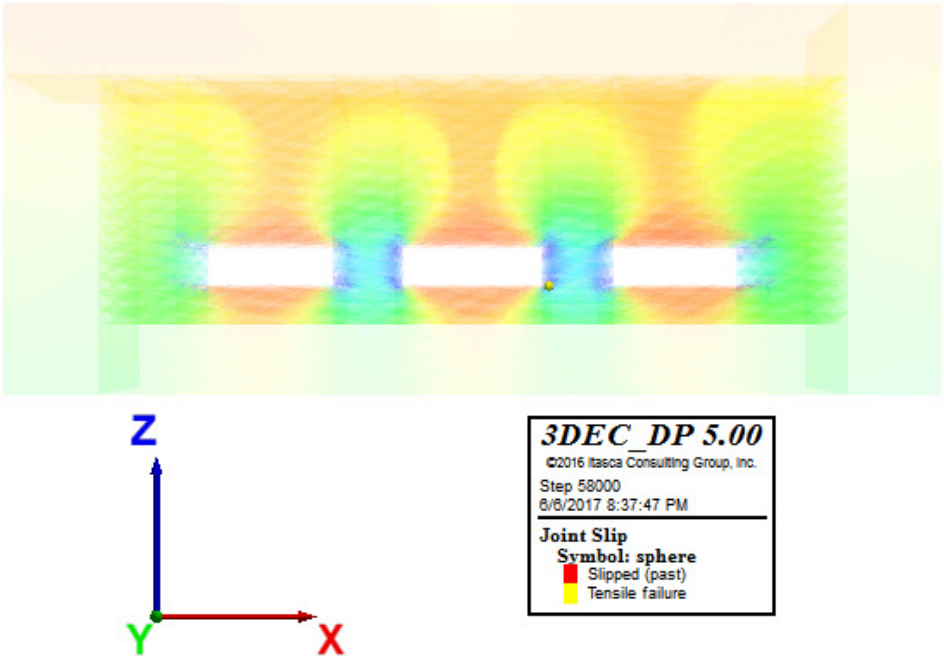

Figure 101. Model 7. Joint slip - Plasticity Limit indicator

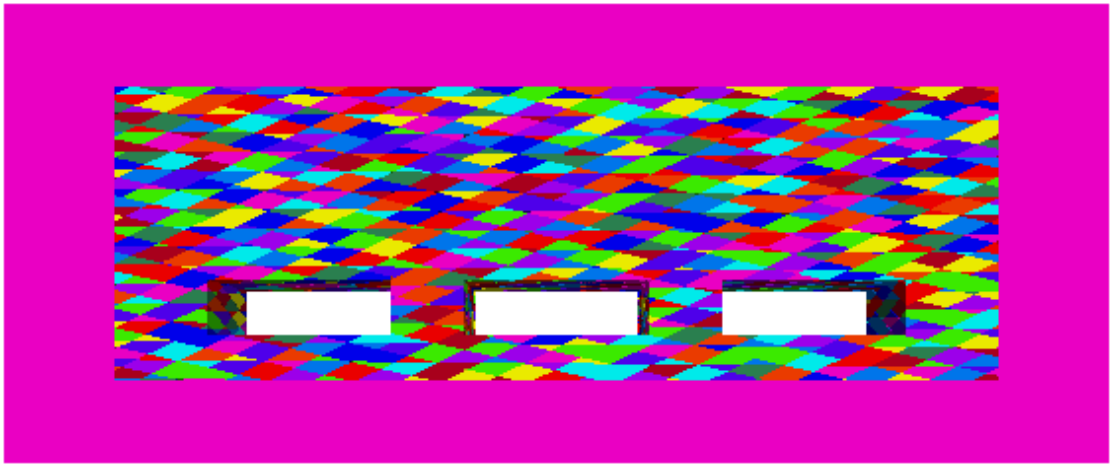

Figure 102. Model 8. Layout

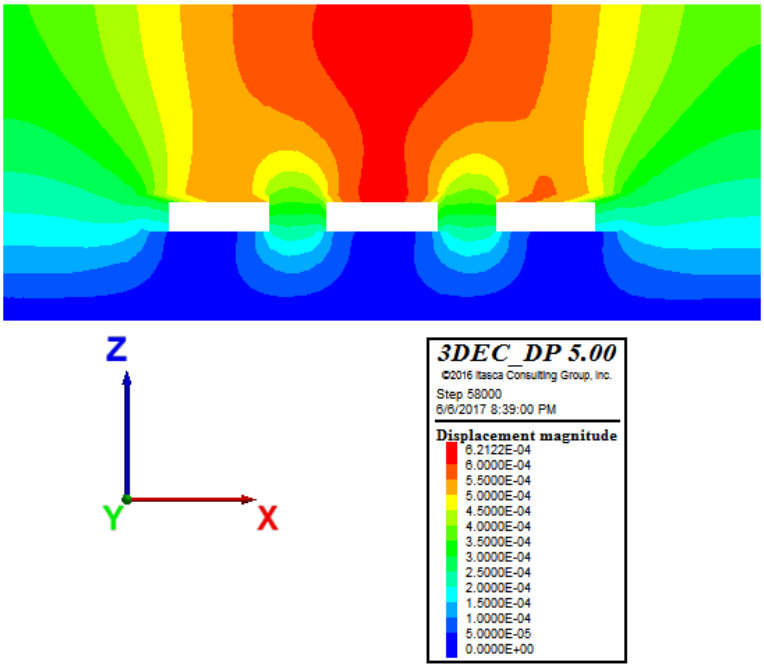

Figure 103. Model 8. Displacement magnitude (m)

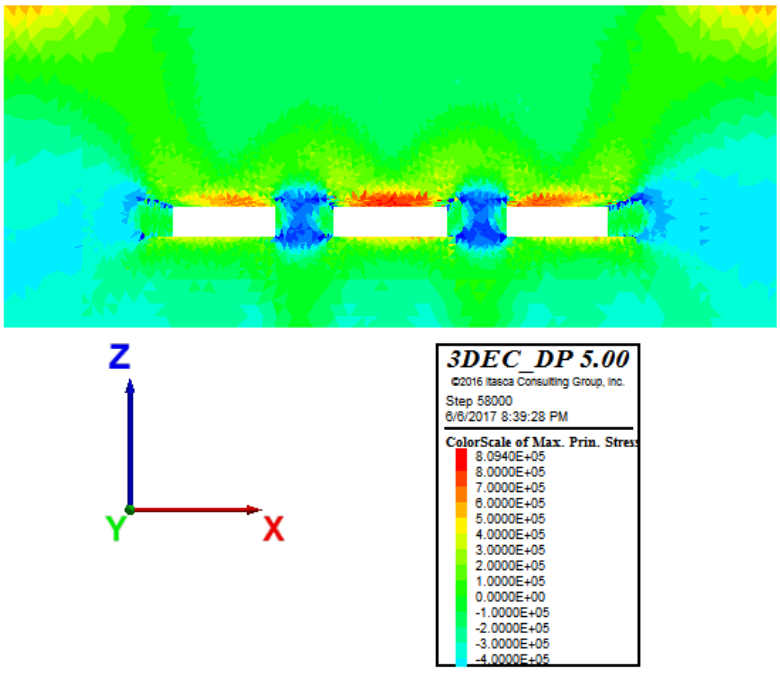

Figure 104. Model 8. Max. principal stresses (Pa)

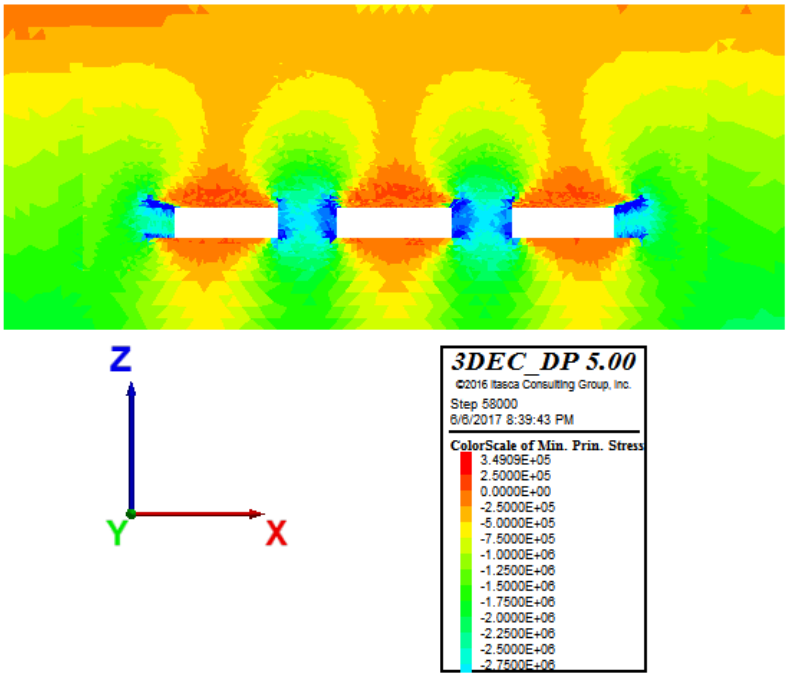

Figure 105. Model 8. Min. principal stresses (Pa)

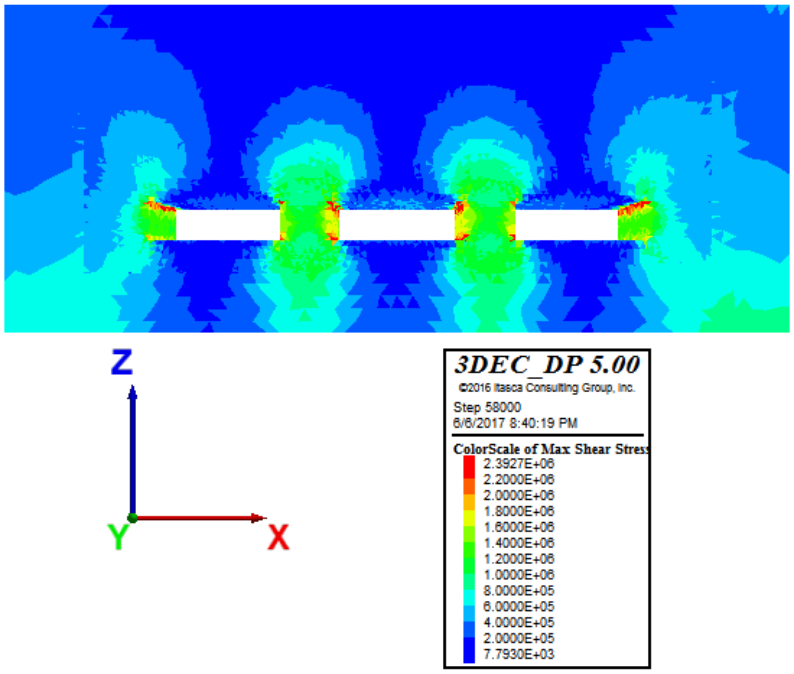

Figure 106. Model 8. Max shear stresses (Pa)

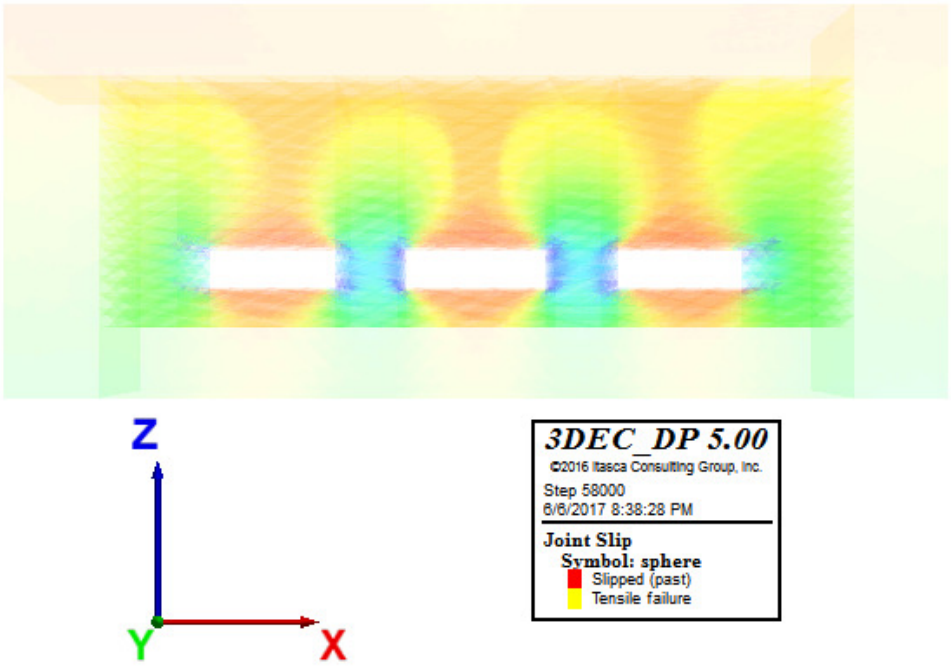

Figure 107. Model 8. Joint slip - Plasticity Limit indicator

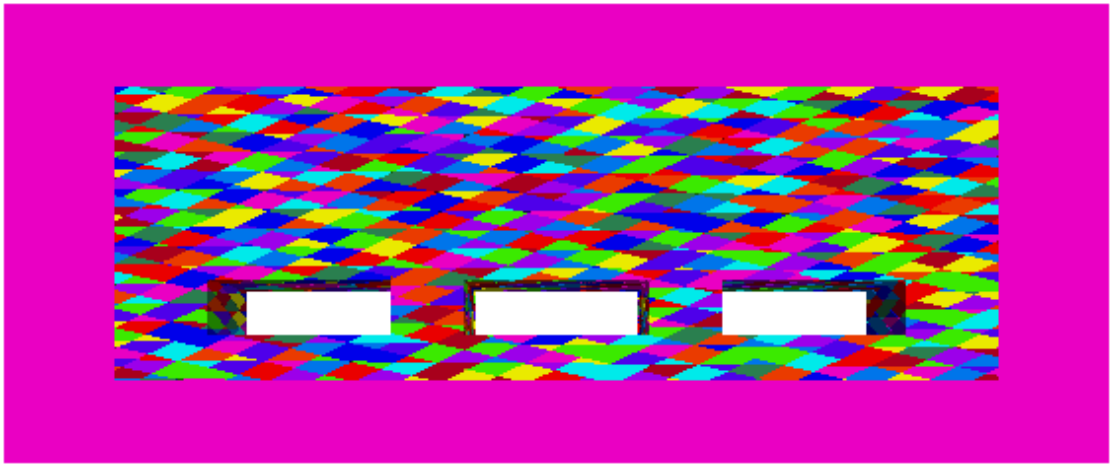

Figure 108. Model 9. Layout

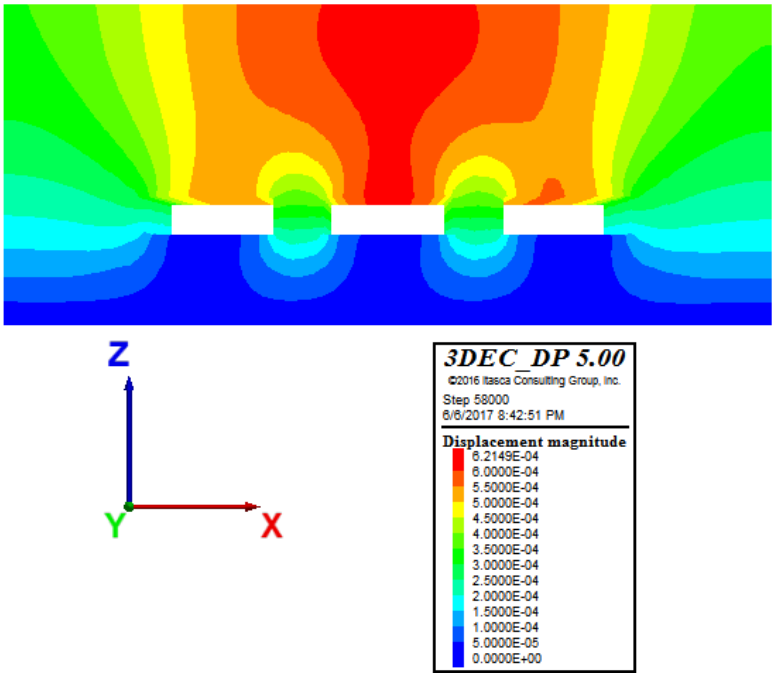

Figure 109. Model 9. Displacement magnitude (m)

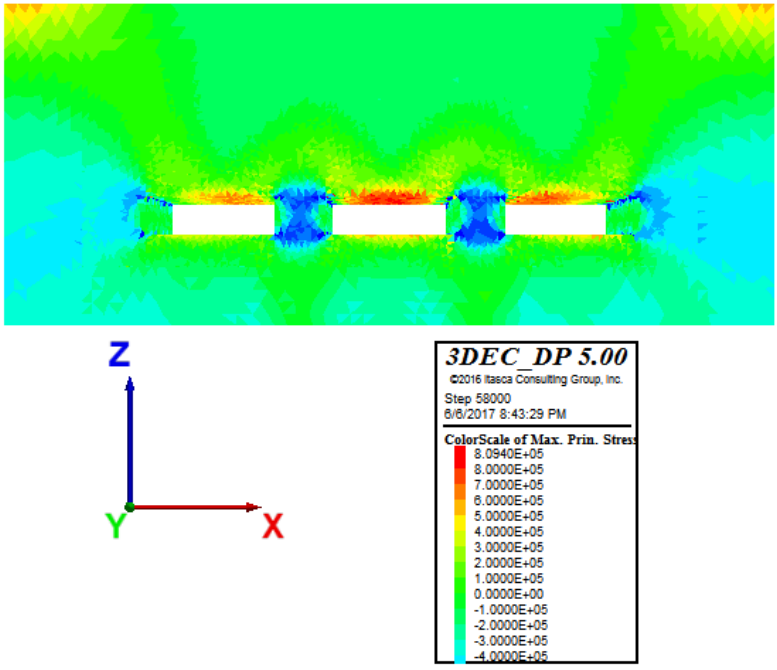

Figure 110. Model 9. Max. principal stresses (Pa)

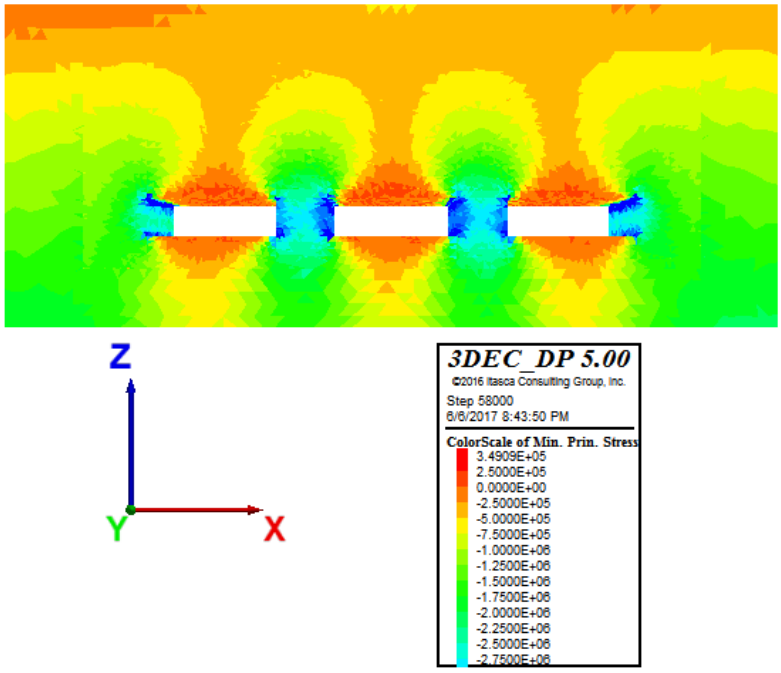

Figure 111. Model 9. Min. principal stresses (Pa)

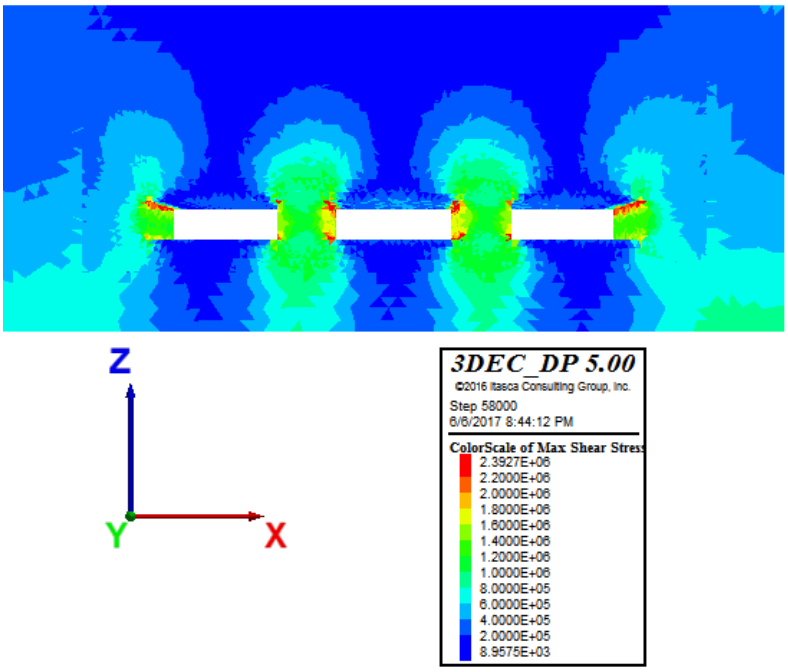

Figure 112. Model 9. Max shear stresses (Pa)

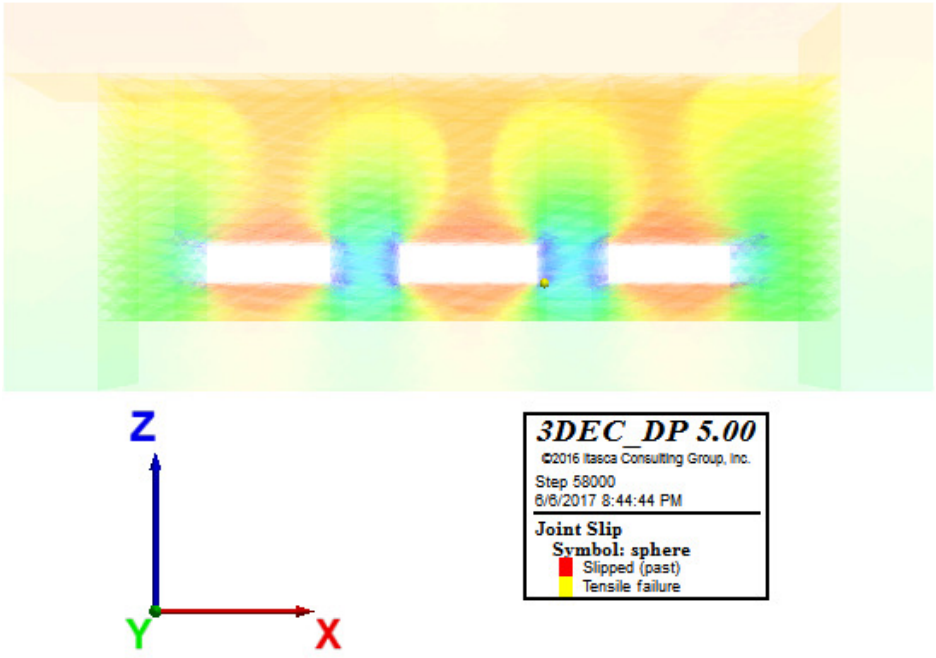

Figure 113. Model 9. Joint slip - Plasticity Limit indicator

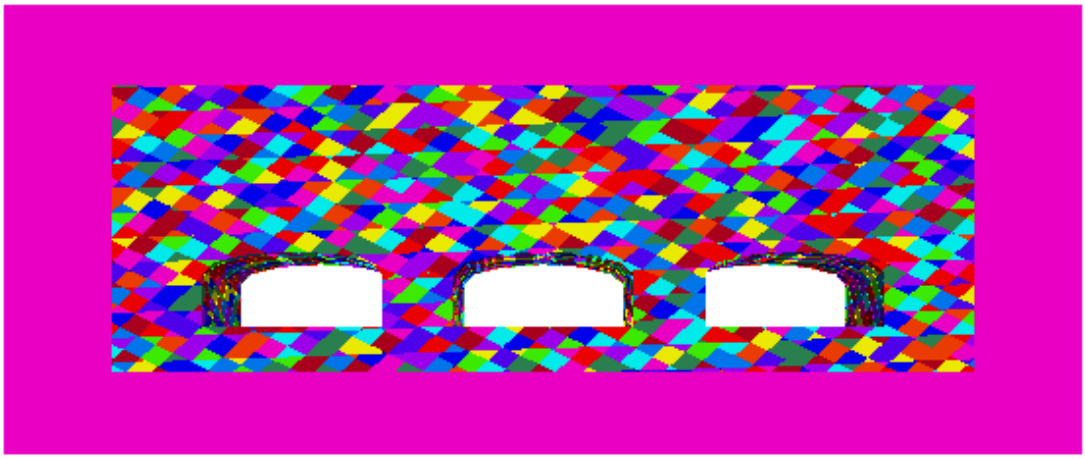

Figure 114. Model 10. Layout

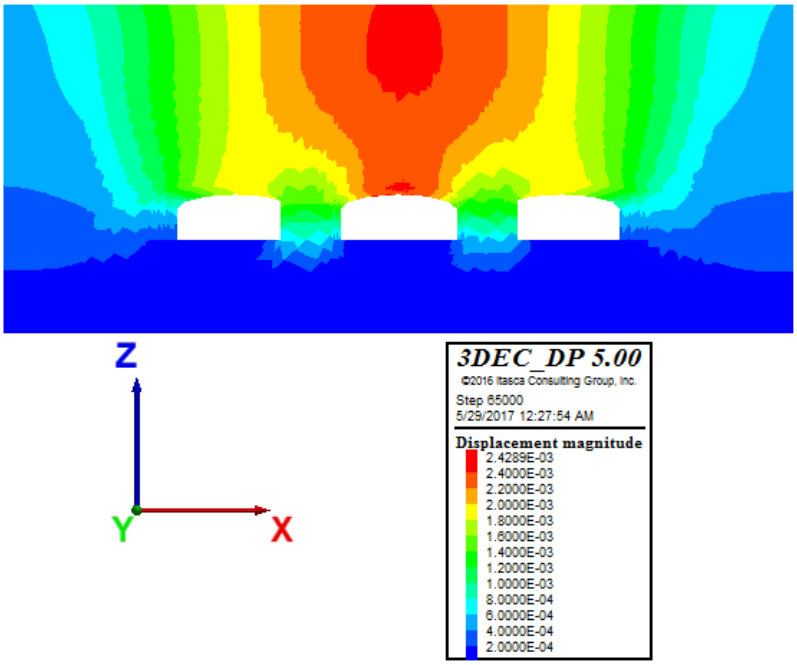

Figure 115. Model 10. Displacement magnitude (m)

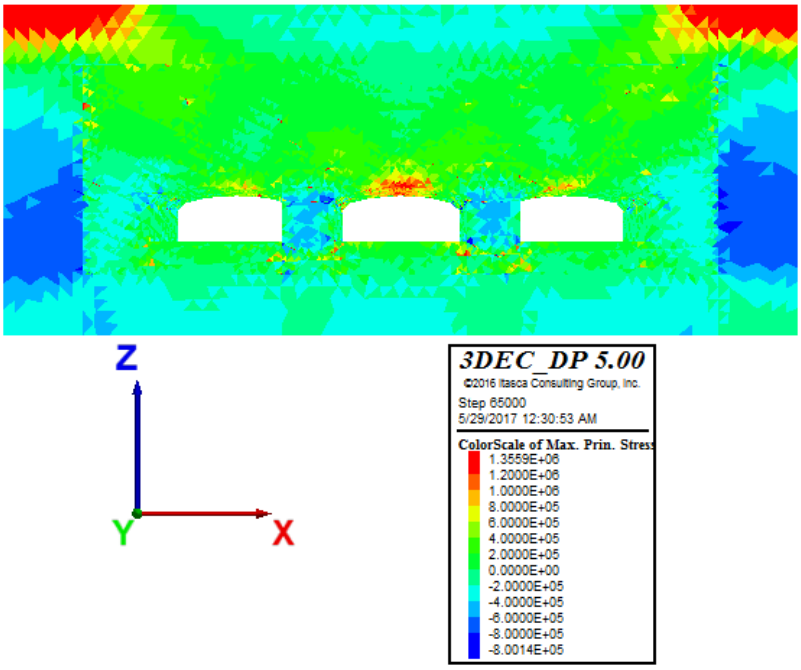

Figure 116. Model 10. Max. principal stresses (Pa)

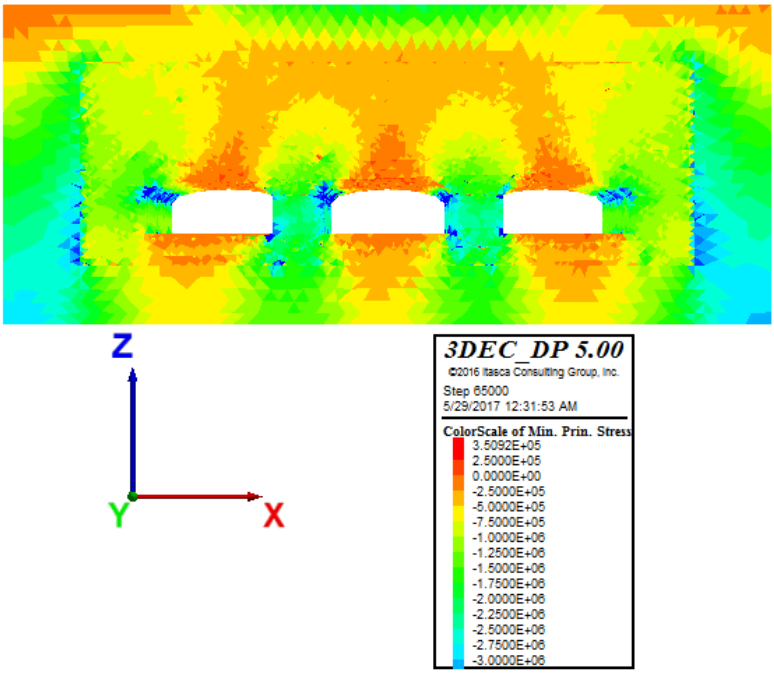

Figure 117. Model 10. Min. principal stresses (Pa)

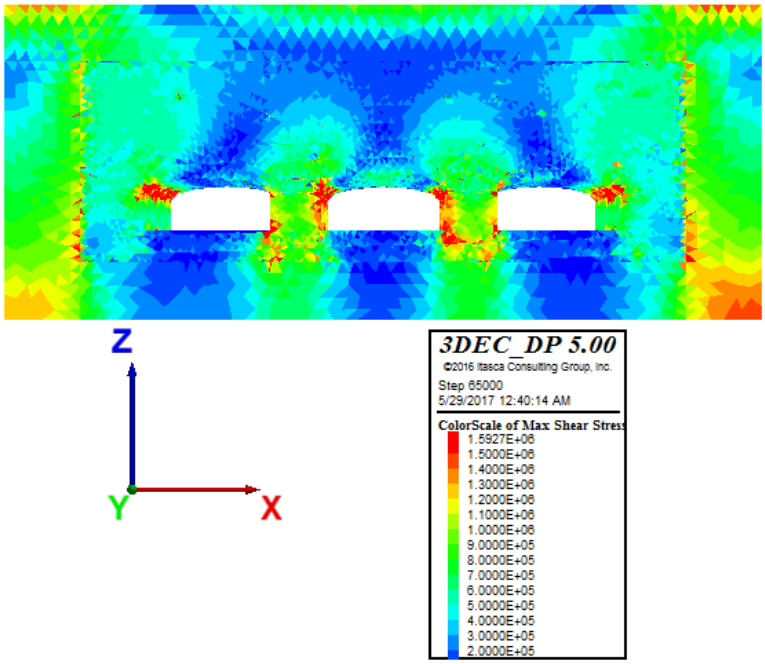

Figure 118. Model 10. Max shear stresses (Pa)

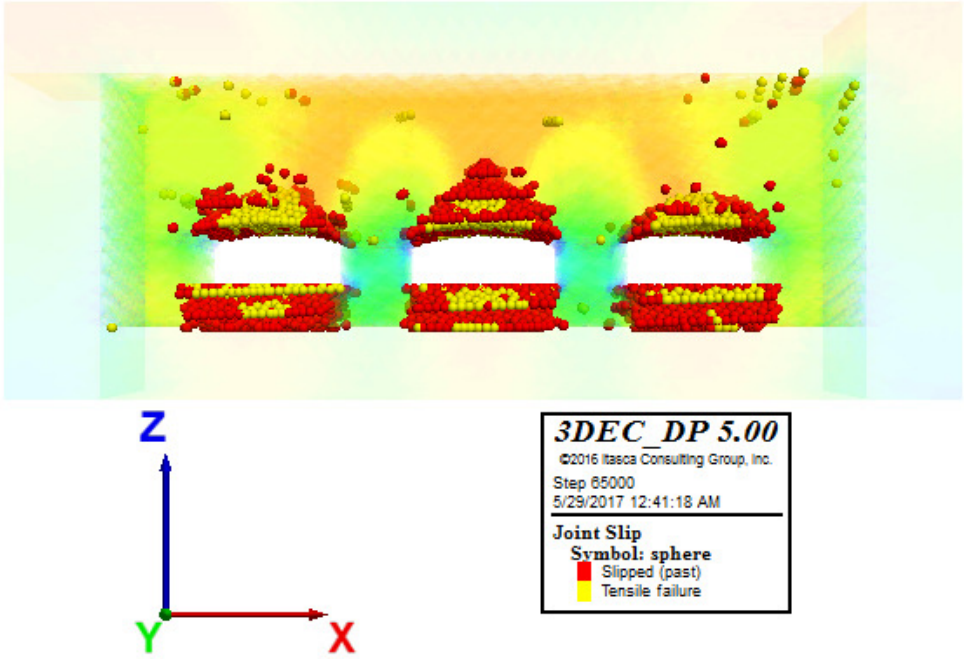

Figure 119. Model 10. Joint slip - Plasticity Limit indicator

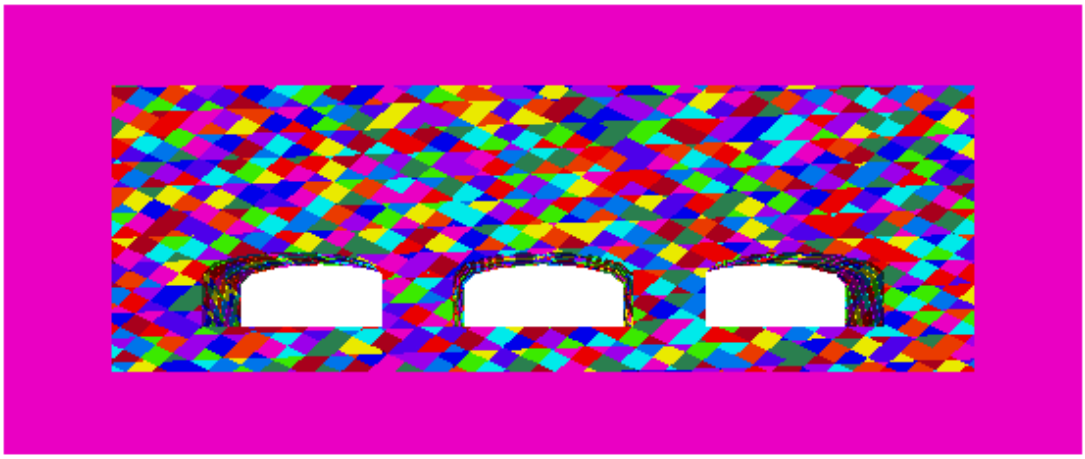

Figure 120. Model 11. Layout

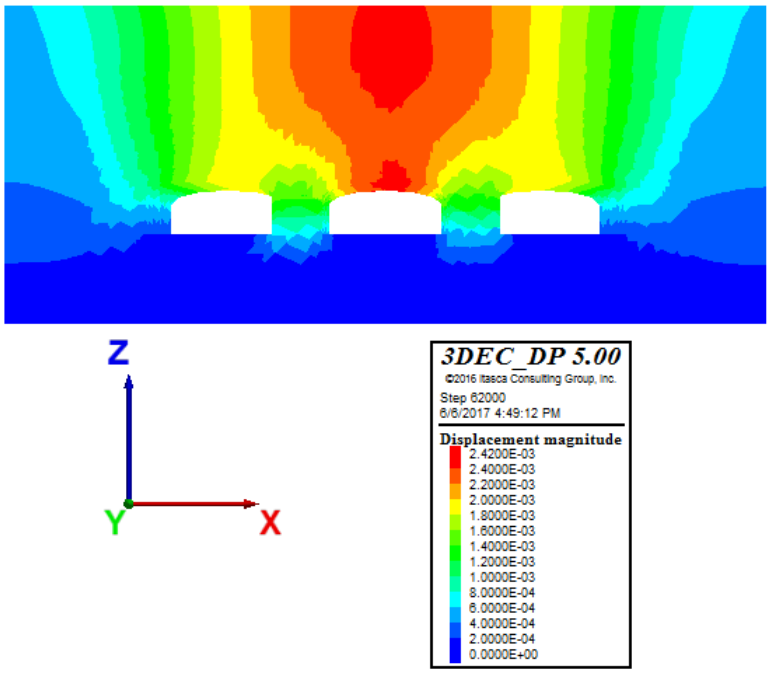

Figure 121. Model 11. Displacement magnitude (m)

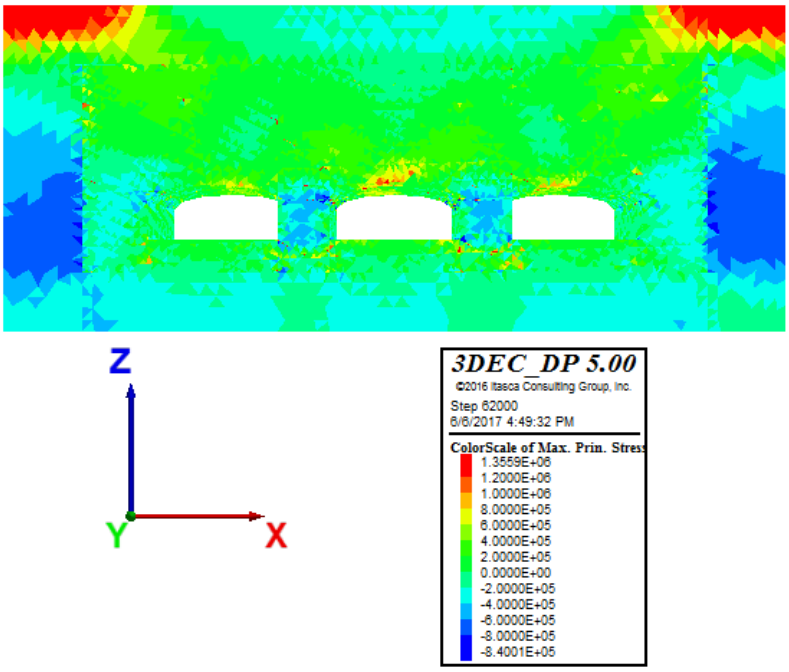

Figure 122. Model 11. Max. principal stresses (Pa)

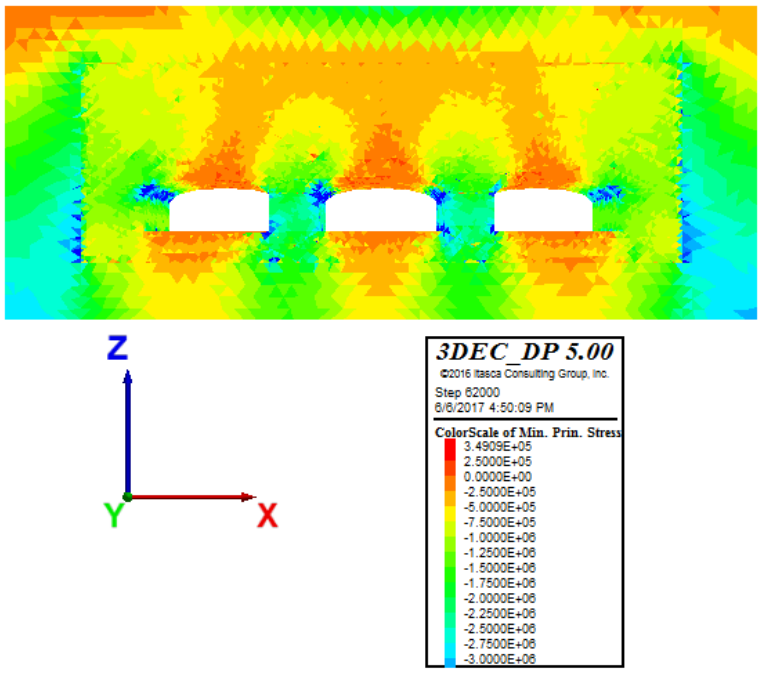

Figure 123. Model 11. Min. principal stresses (Pa)

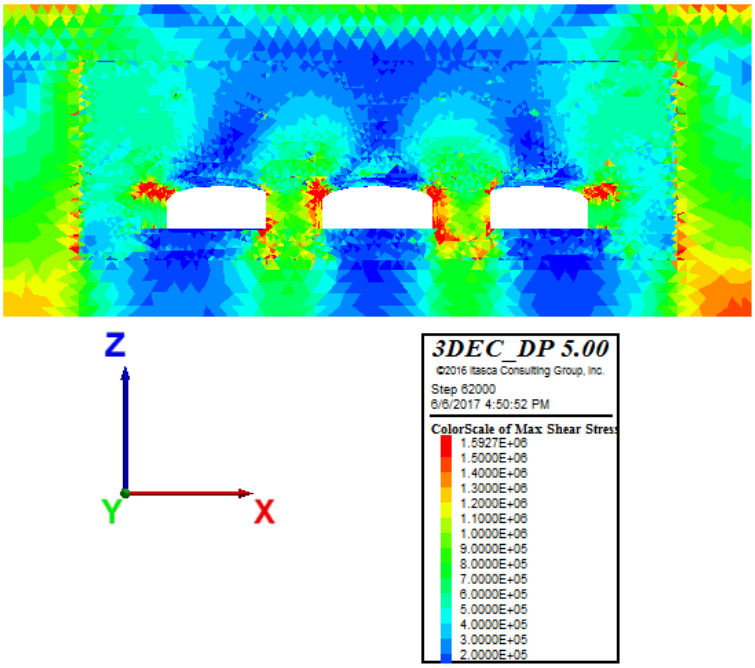

Figure 124. Model 11. Max shear stresses (Pa)

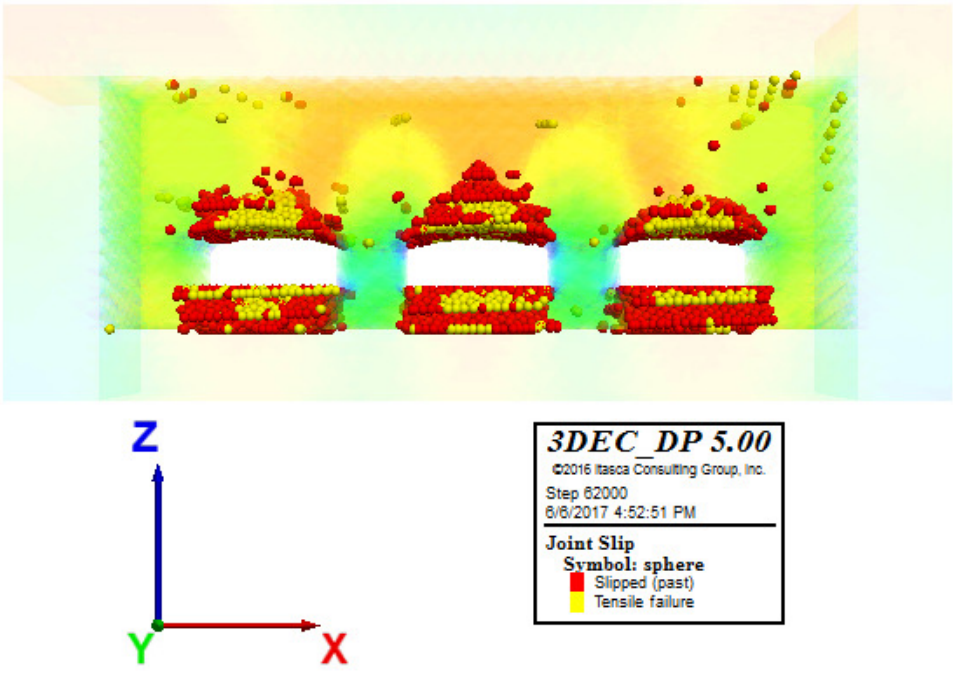

Figure 125. Model 11. Joint slip - Plasticity Limit indicator

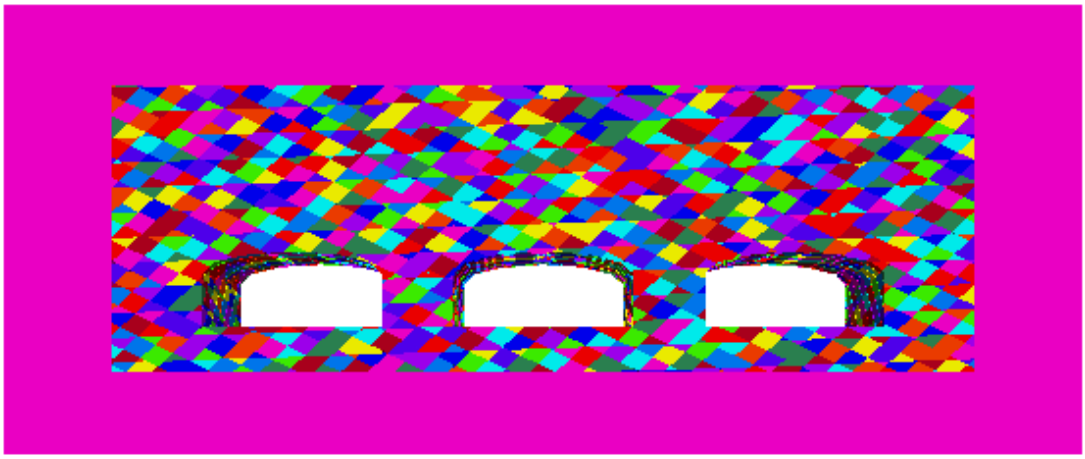

Figure 126. Model 12. Layout

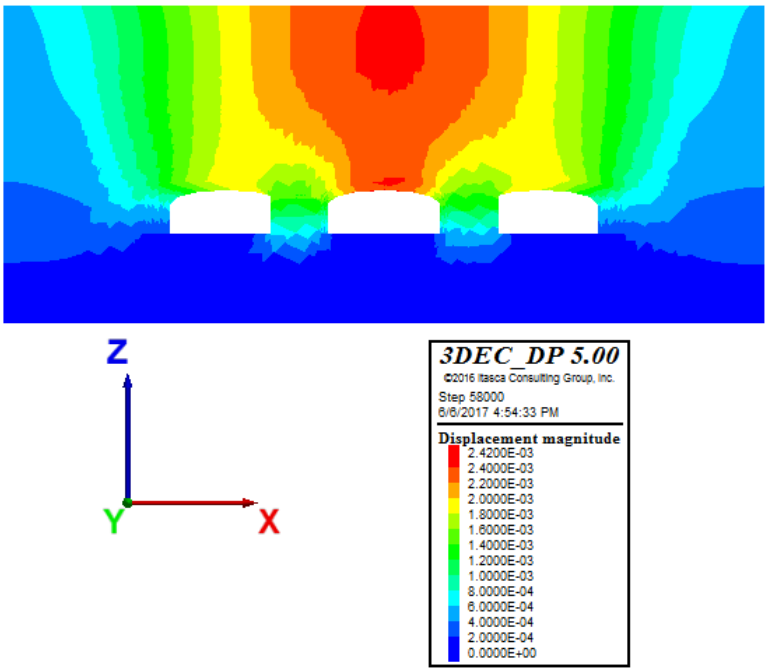

Figure 127. Model 12. Displacement magnitude (m)

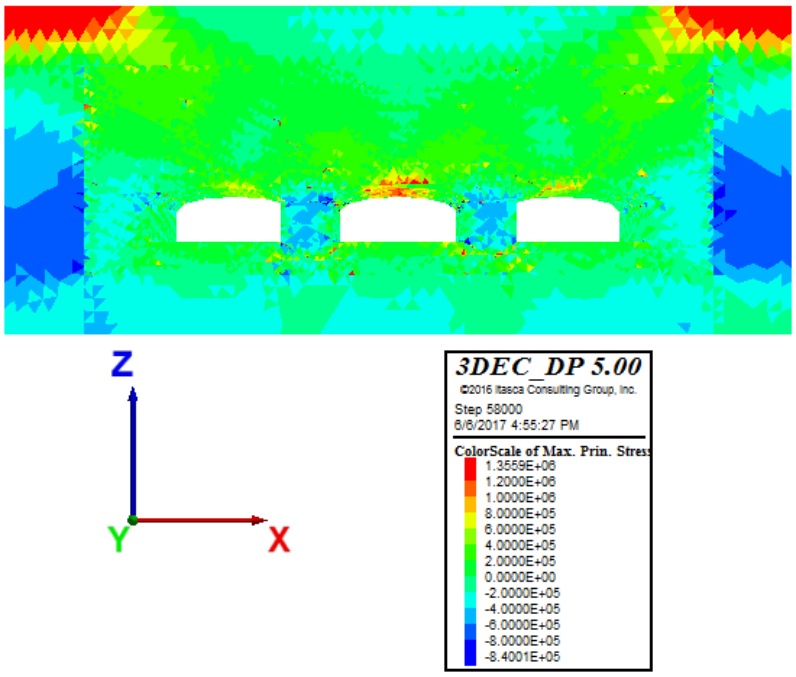

Figure 128. Model 12. Max. principal stresses (Pa)

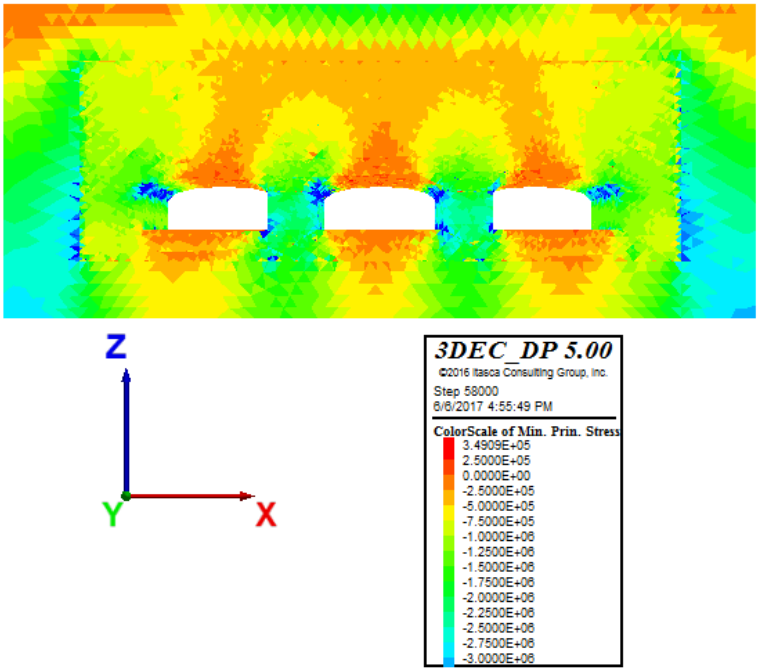

Figure 129. Model 12. Min. principal stresses (Pa)

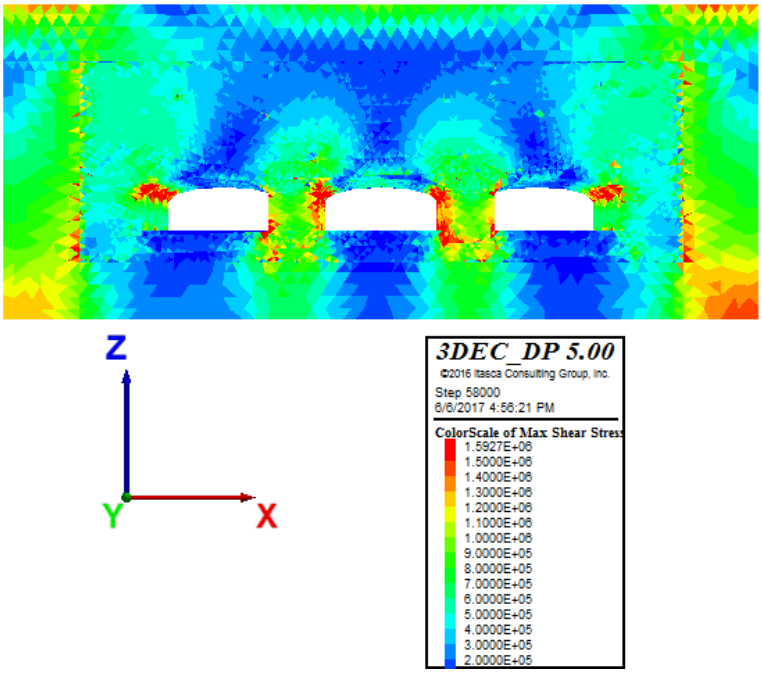

Figure 130. Model 12. Max shear stresses (Pa)

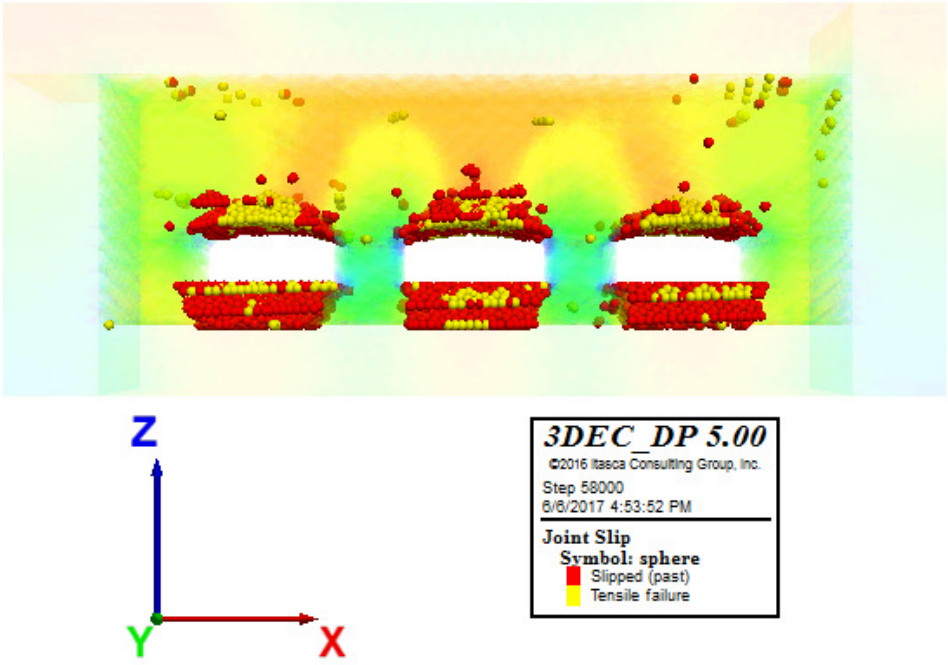

Figure 131. Model 12. Joint slip - Plasticity Limit indicator

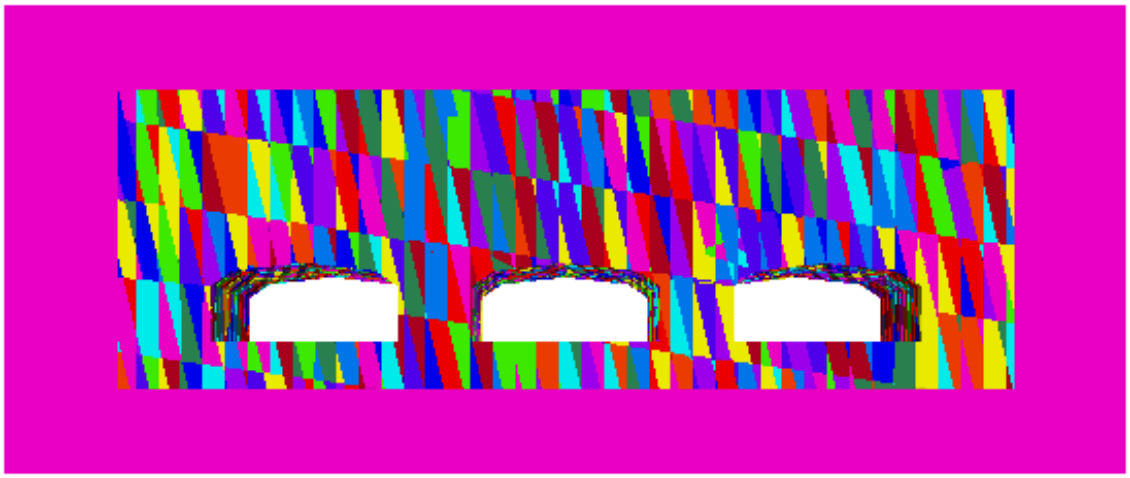

Figure 132. Model 13. Layout

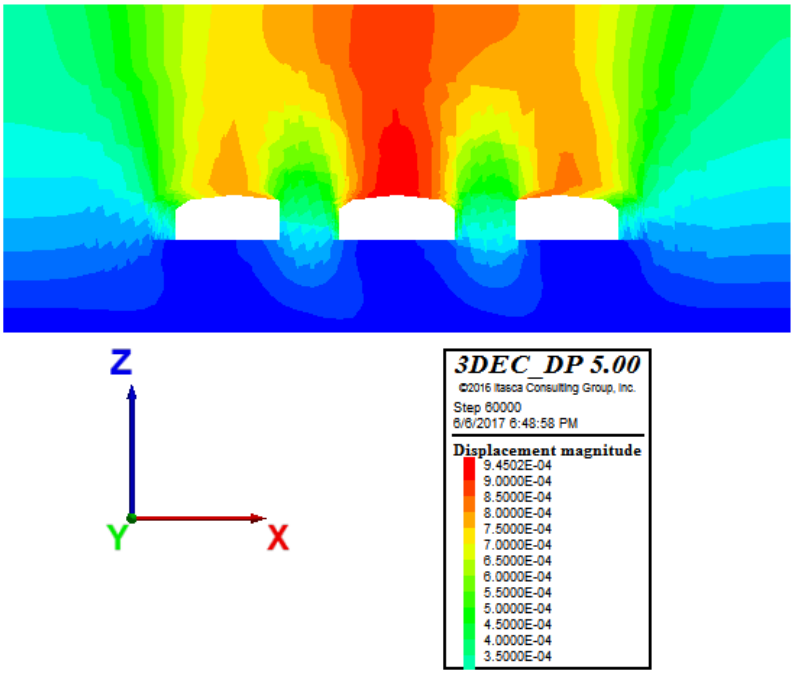

Figure 133. Model 13. Displacement magnitude (m)

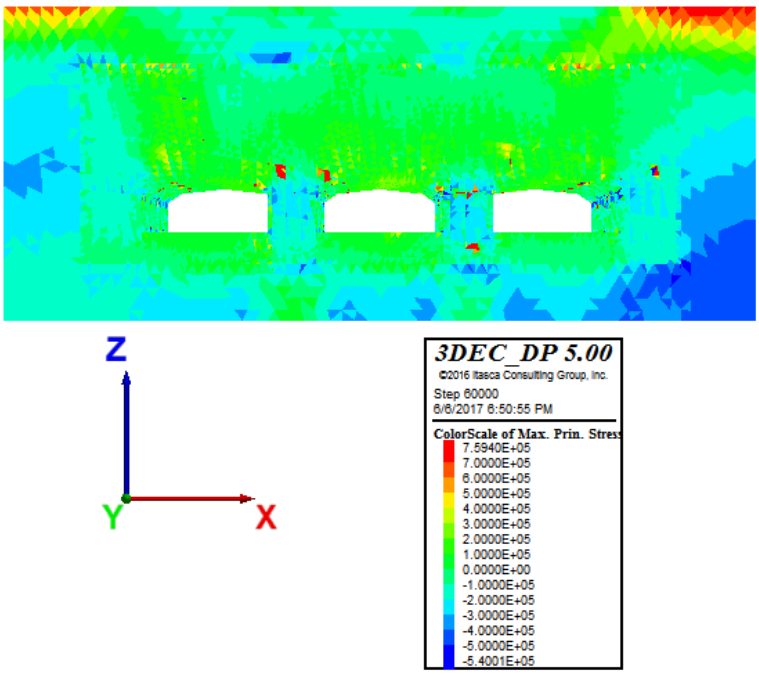

Figure 134. Model 13. Max. principal stresses (Pa)

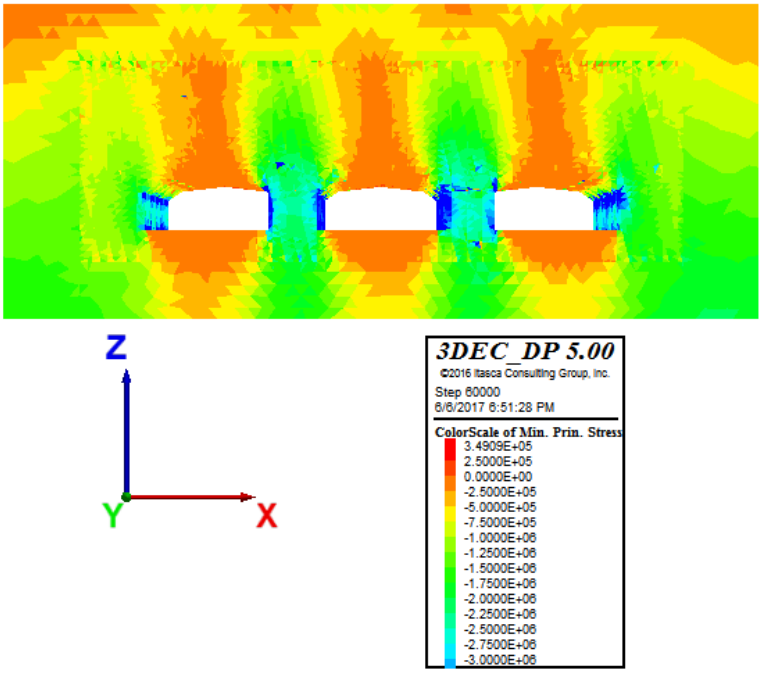

Figure 135. Model 13. Min. principal stresses (Pa)

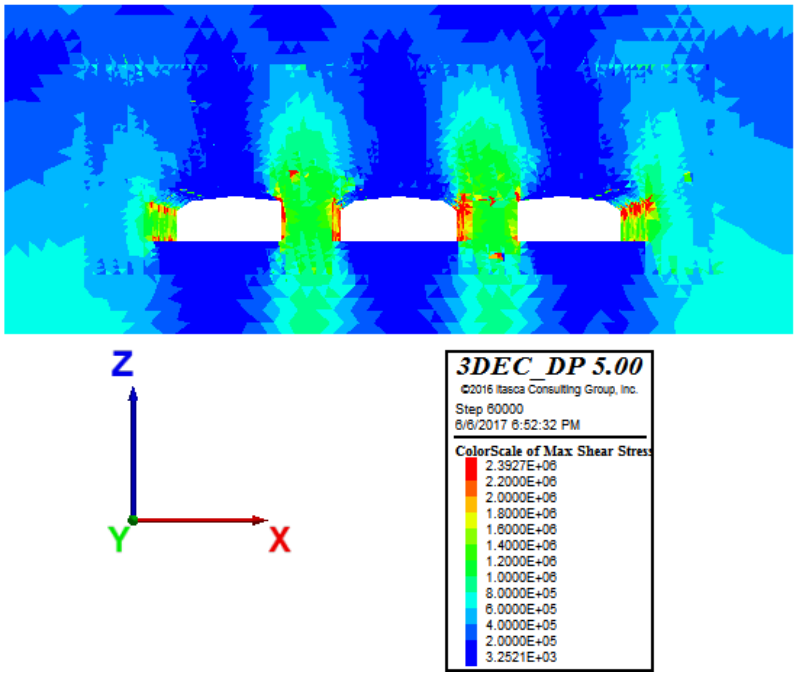

Figure 136. Model 13. Max shear stresses (Pa)

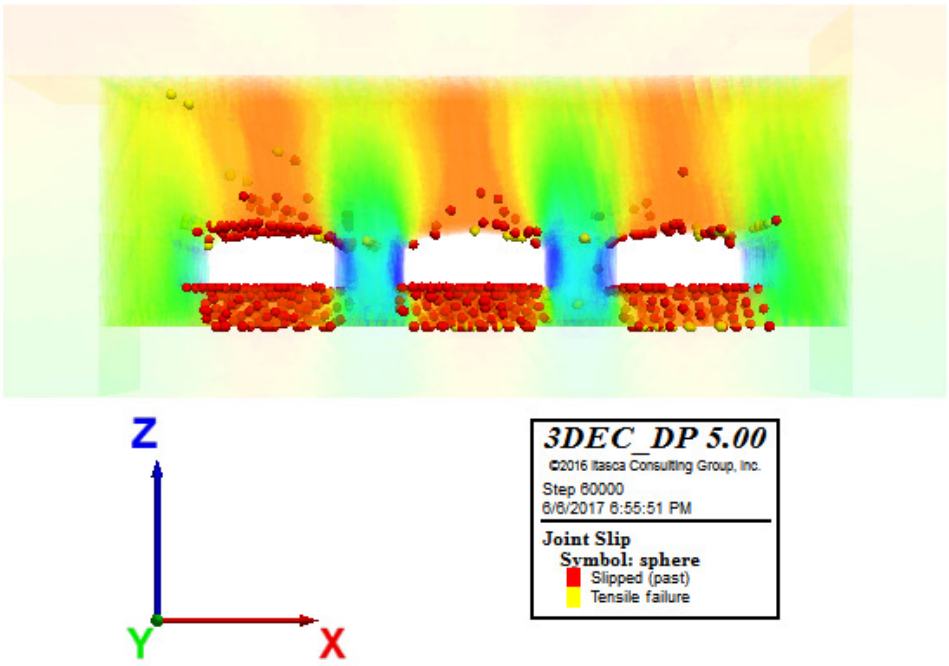

Figure 137. Model 13. Joint slip - Plasticity Limit indicator

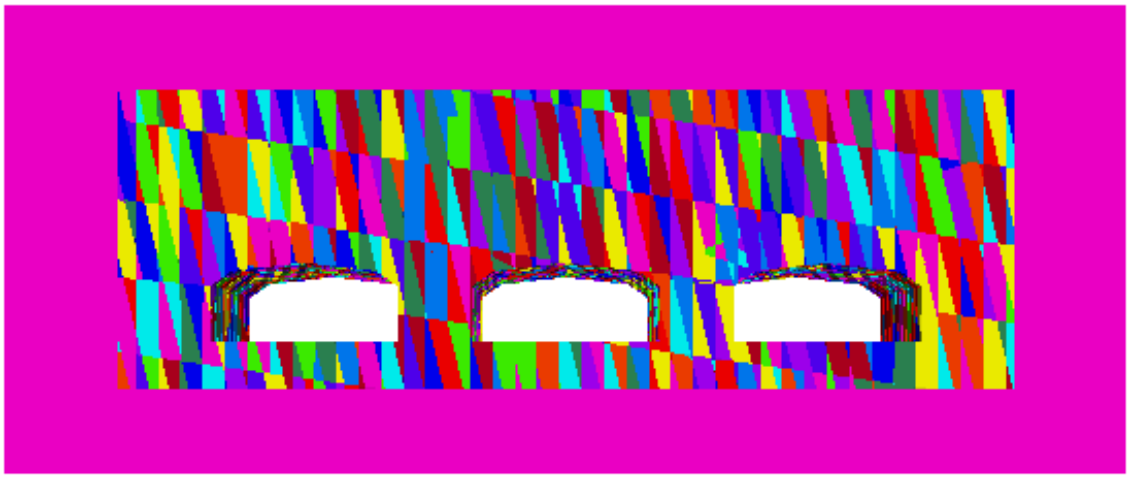

Figure 138. Model 14. Layout

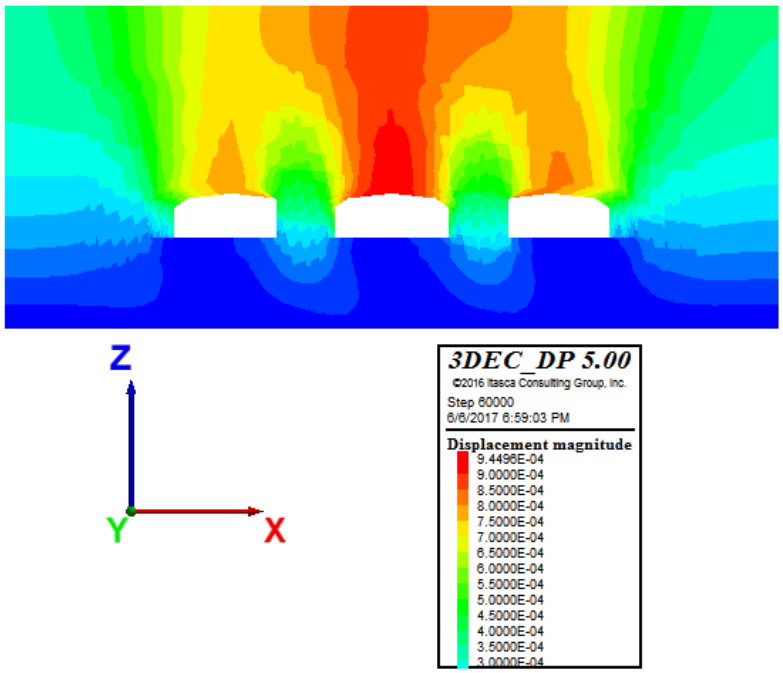

Figure 139. Model 14. Displacement magnitude (m)

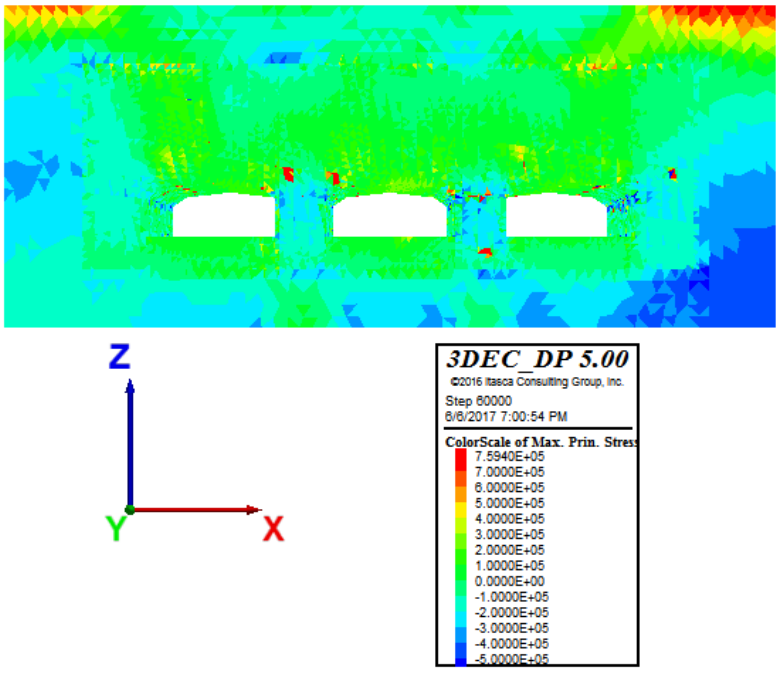

Figure 140. Model 14. Max. principal stresses (Pa)

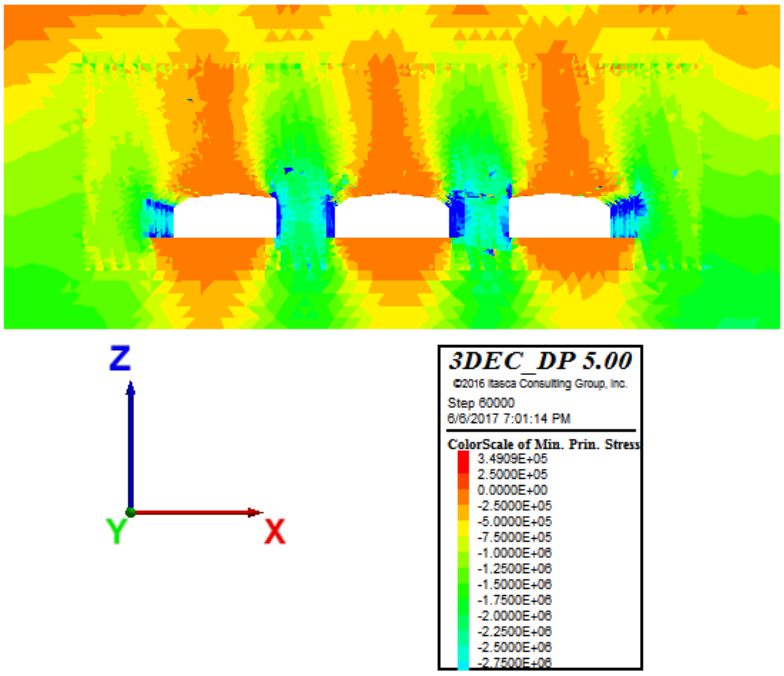

Figure 141. Model 14. Min. principal stresses (Pa)

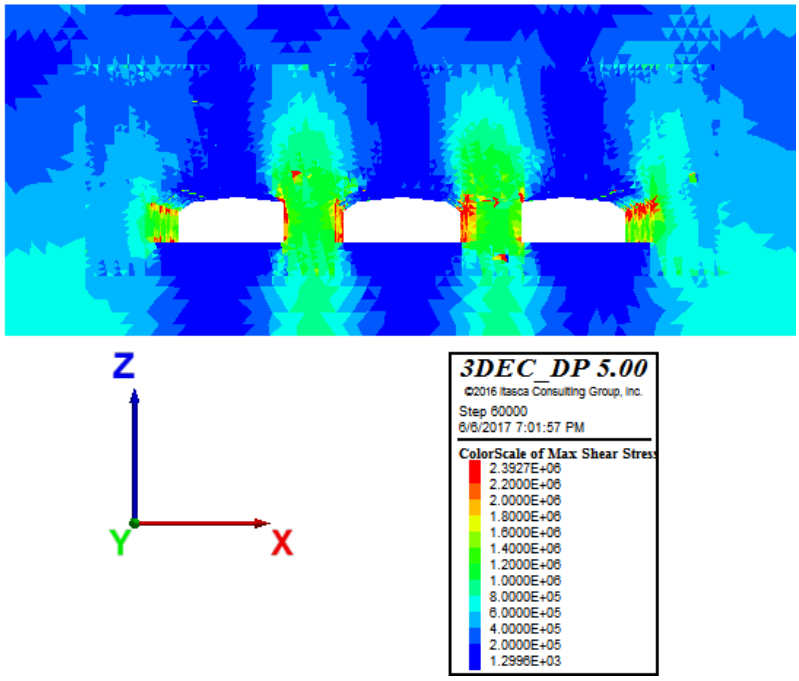

Figure 142. Model 14. Max shear stresses (Pa)

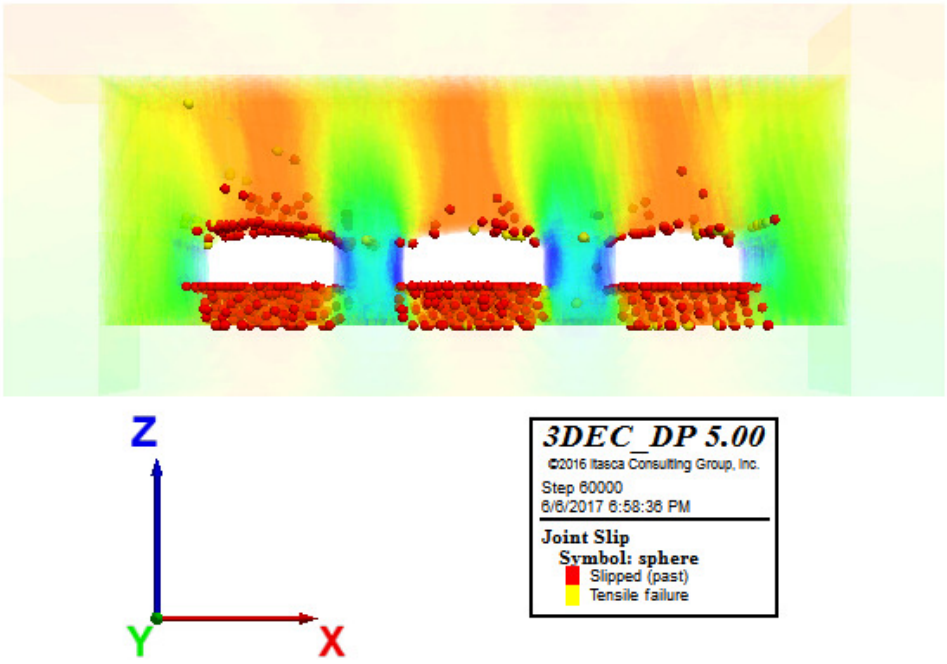

Figure 143. Model 14. Joint slip - Plasticity Limit indicator

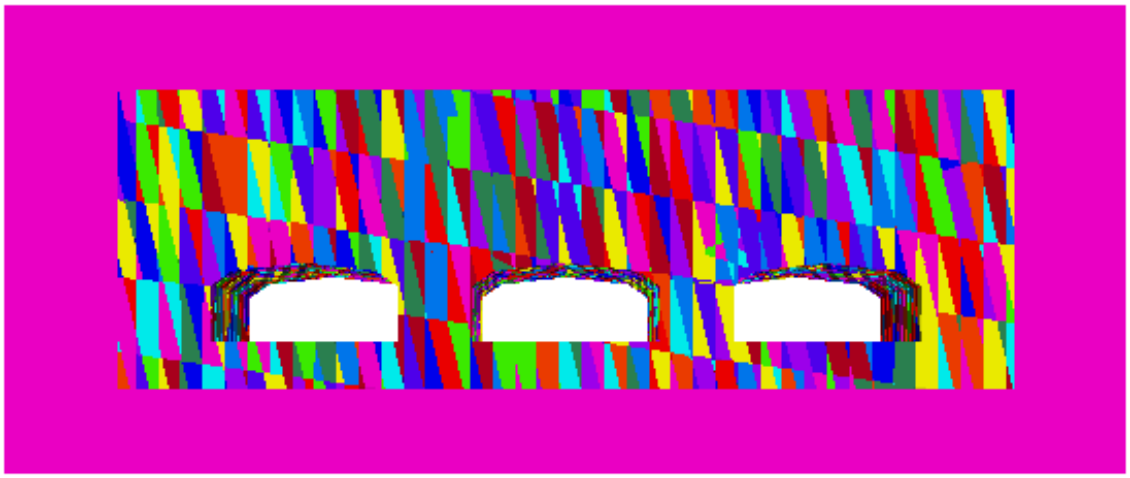

Figure 144. Model 15. Layout

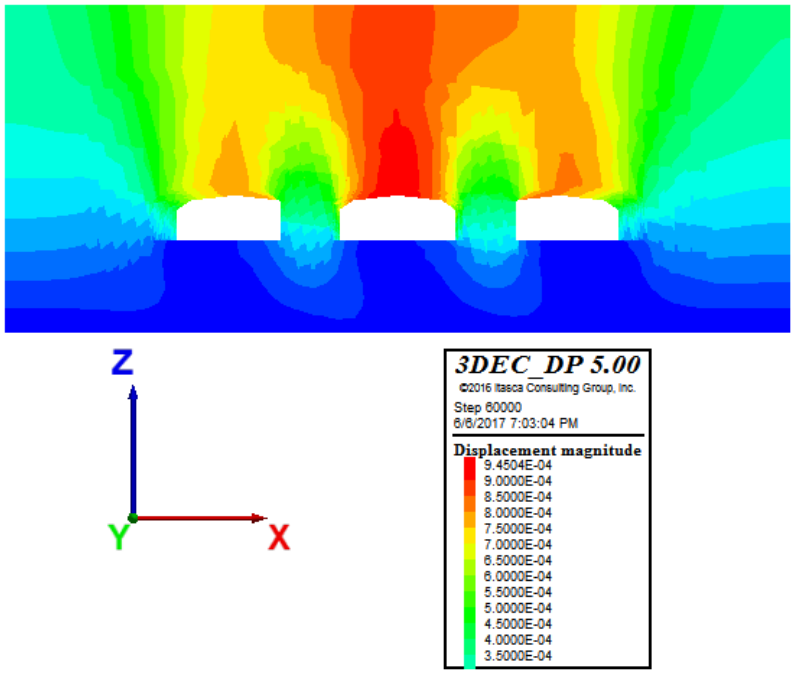

Figure 145. Model 15. Displacement magnitude (m)

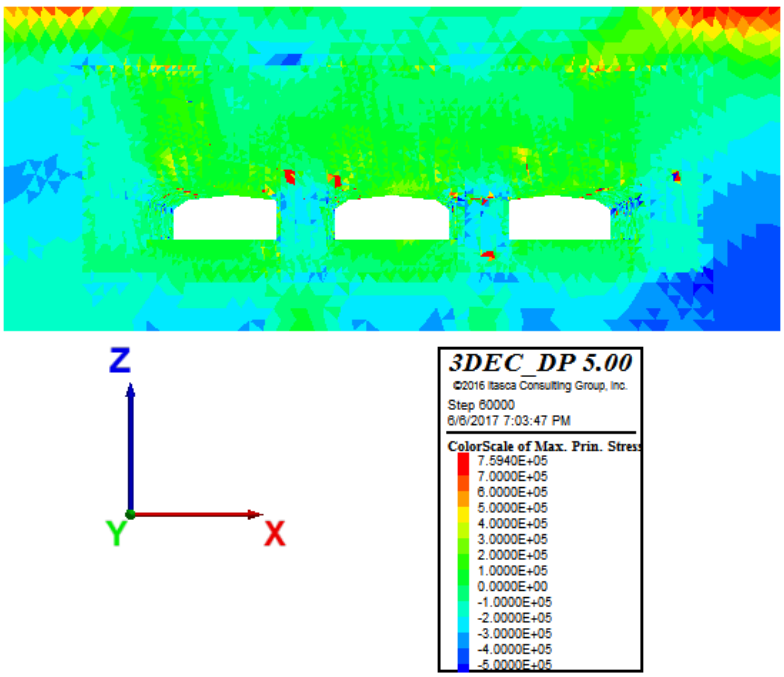

Figure 146. Model 15. Max. principal stresses (Pa)

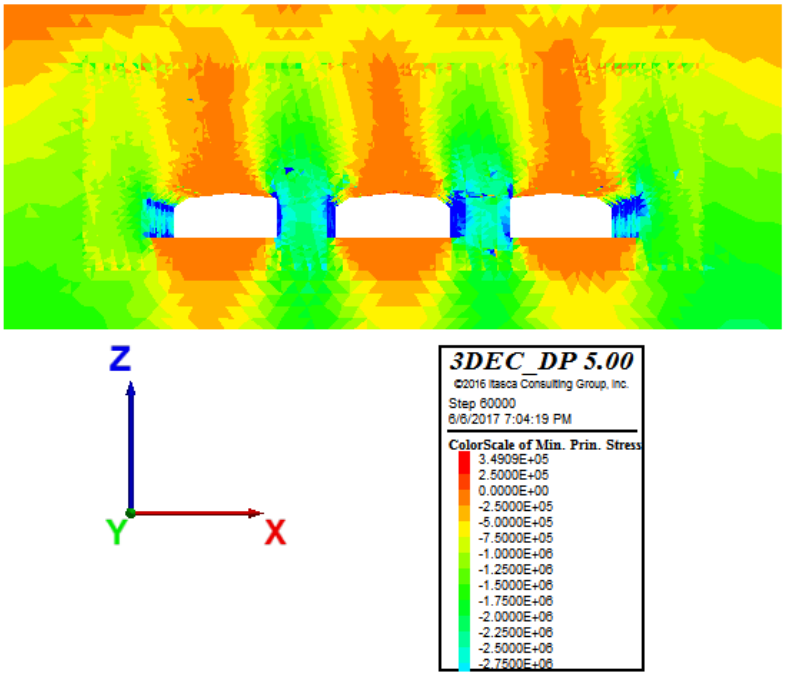

Figure 147. Model 15. Min. principal stresses (Pa)

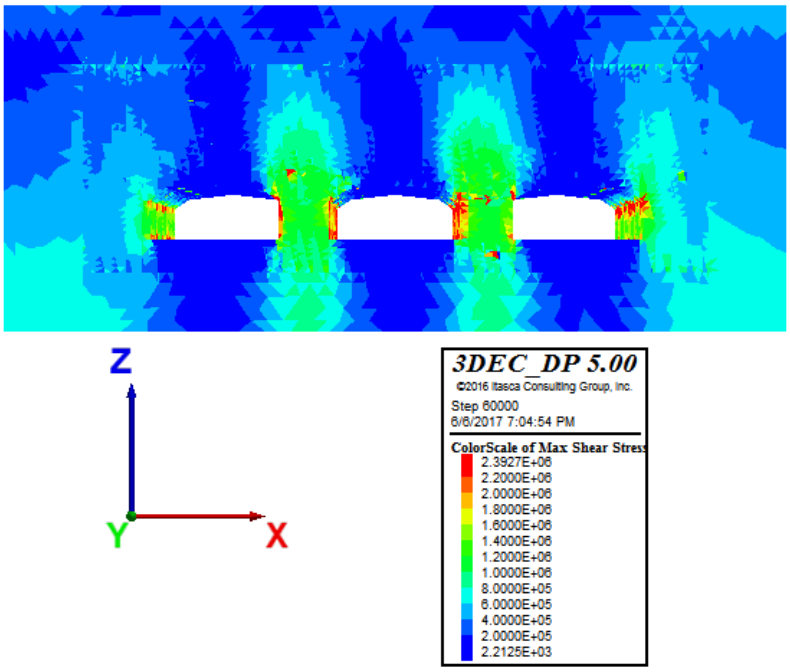

Figure 148. Model 15. Max shear stresses (Pa)

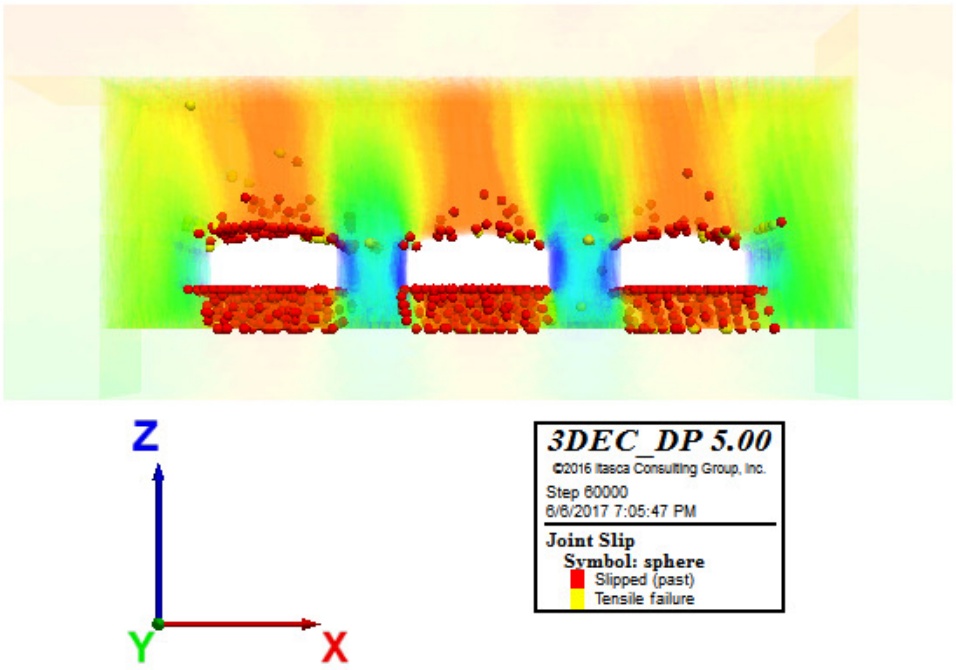

Figure 149. Model 15. Joint slip - Plasticity Limit indicator

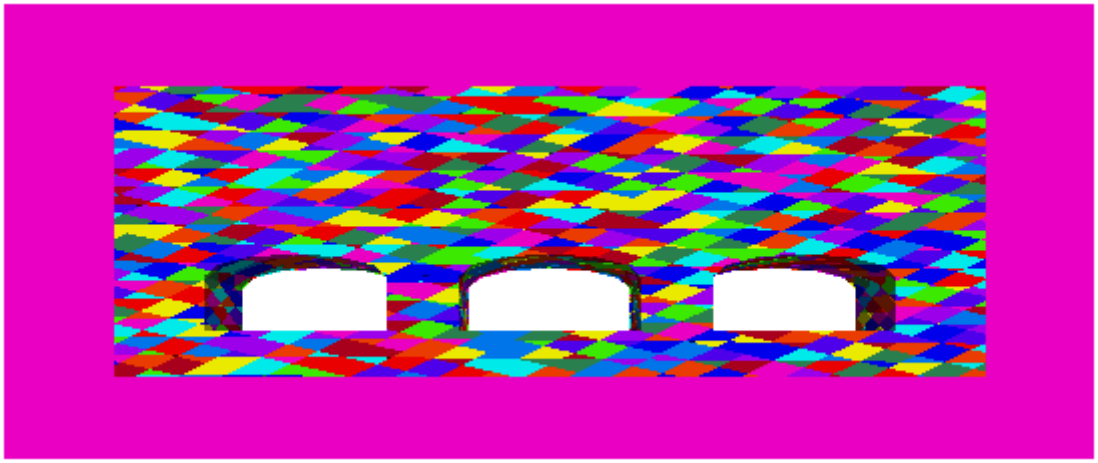

Figure 150. Model 16. Layout

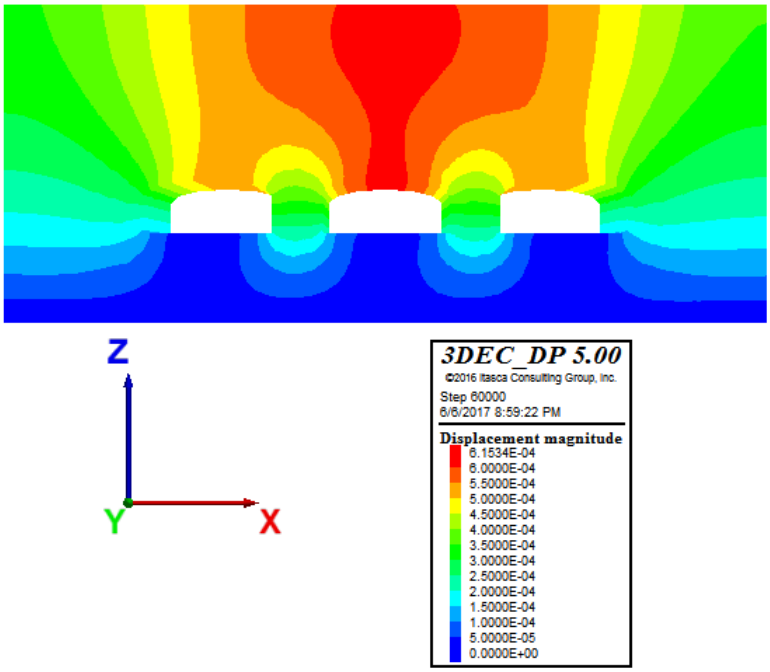

Figure 151. Model 16. Displacement magnitude (m)

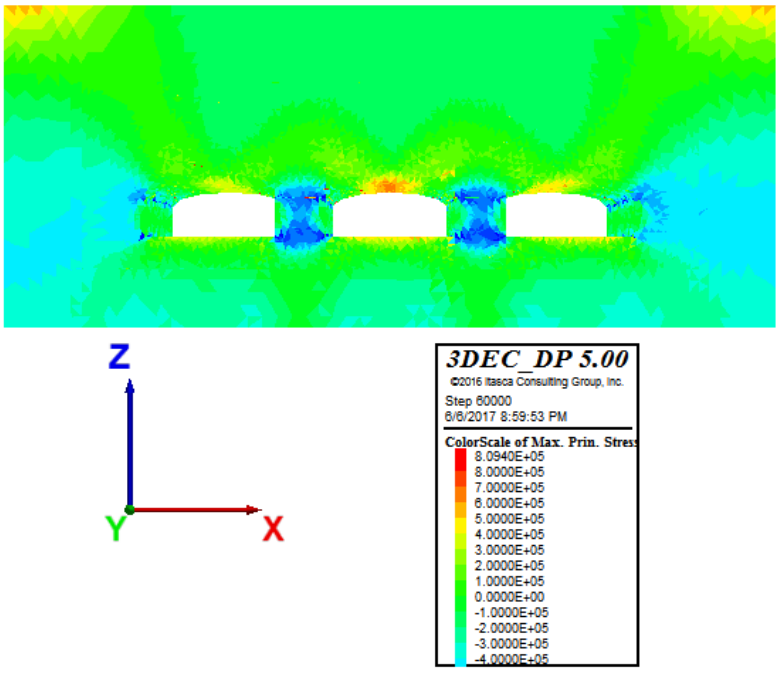

Figure 152. Model 16. Max. principal stresses (Pa)

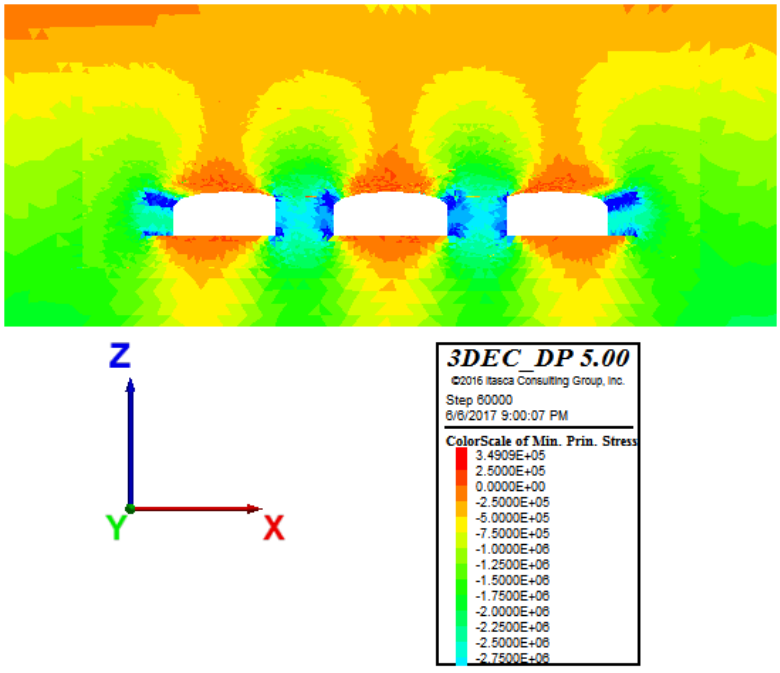

Figure 153. Model 16. Min. principal stresses (Pa)

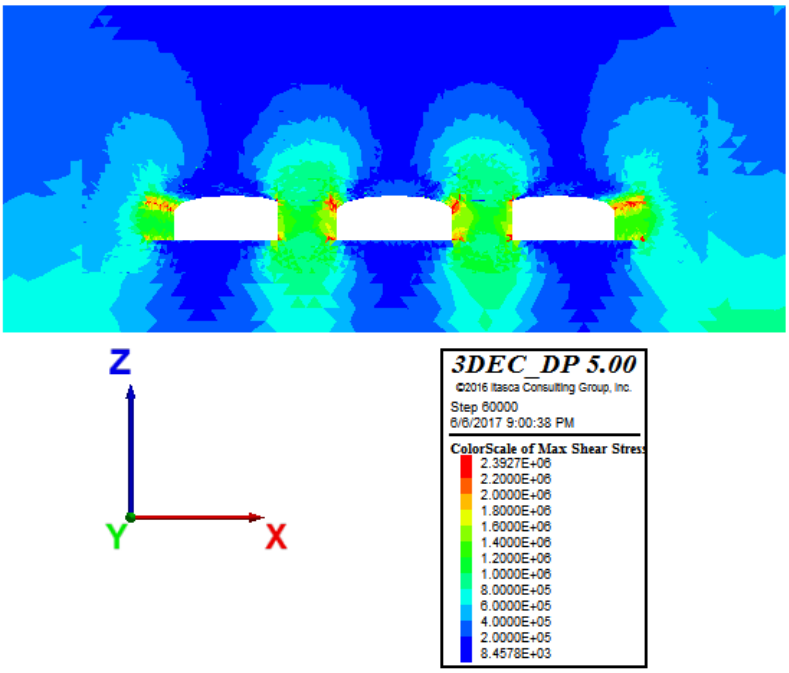

Figure 154. Model 16. Max shear stresses (Pa)

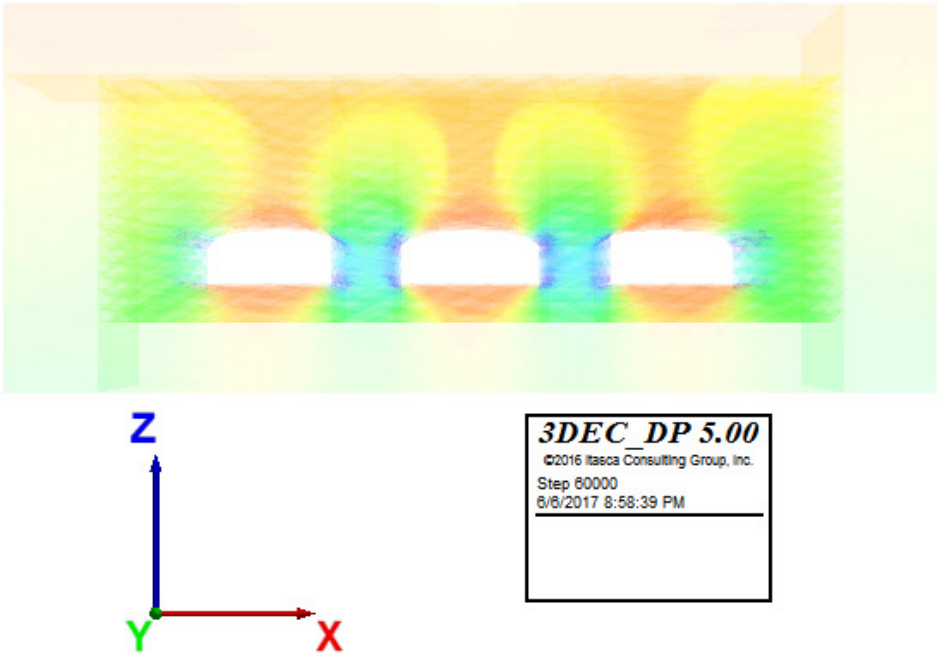

Figure 155. Model 16. Joint slip - Plasticity Limit indicator

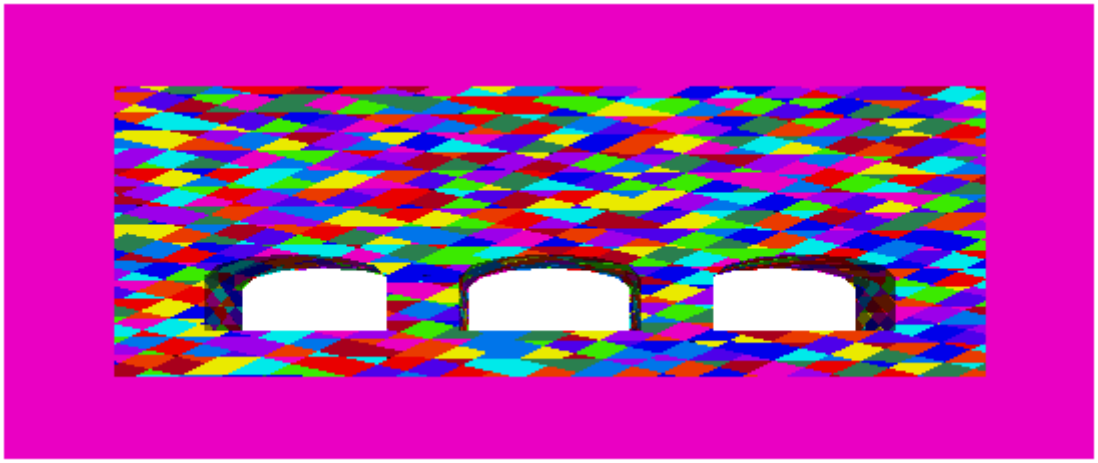

Figure 156. Model 17. Layout

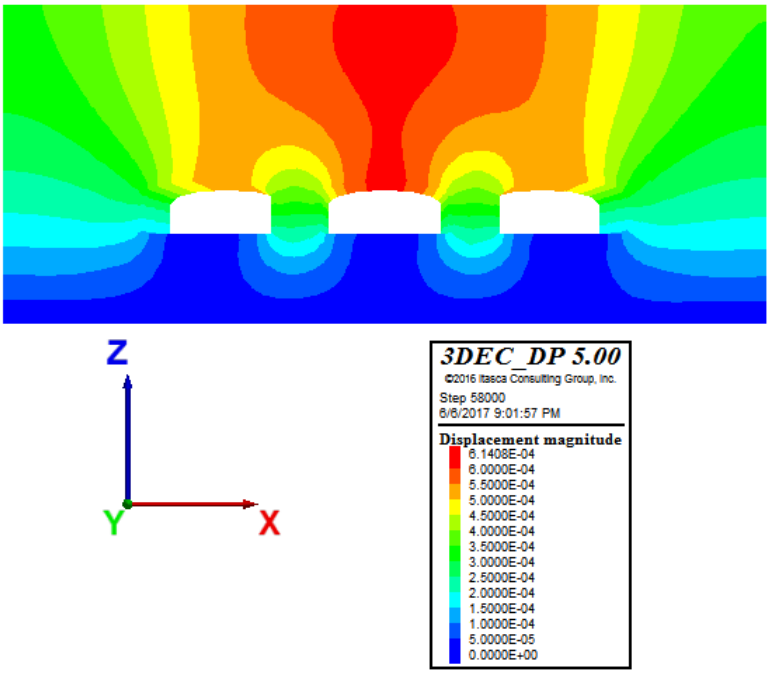

Figure 157. Model 17. Displacement magnitude (m)

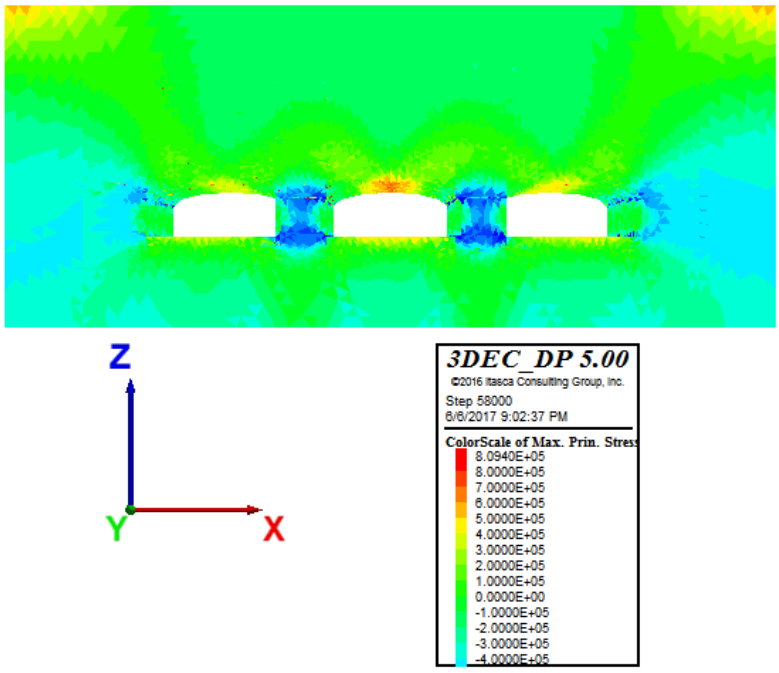

Figure 158. Model 17. Max. principal stresses (Pa)

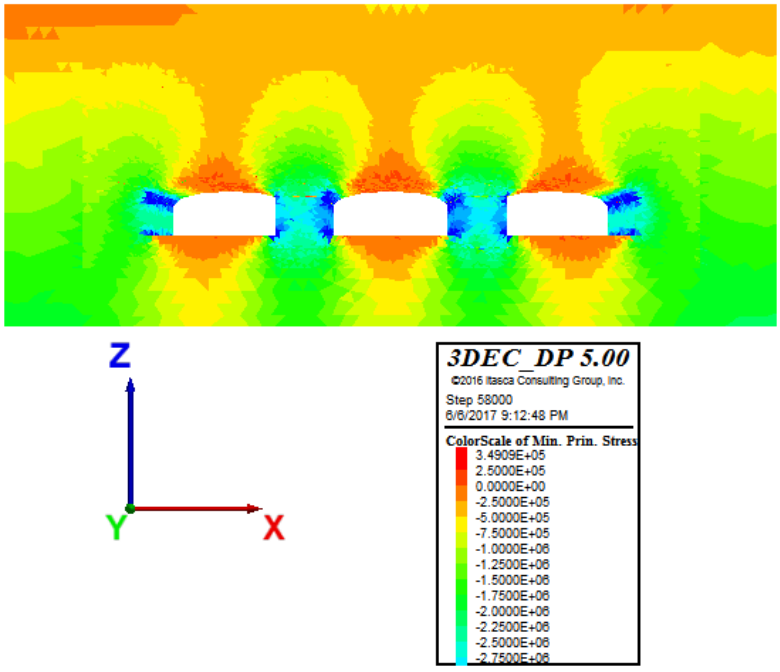

Figure 159. Model 17. Min. principal stresses (Pa)

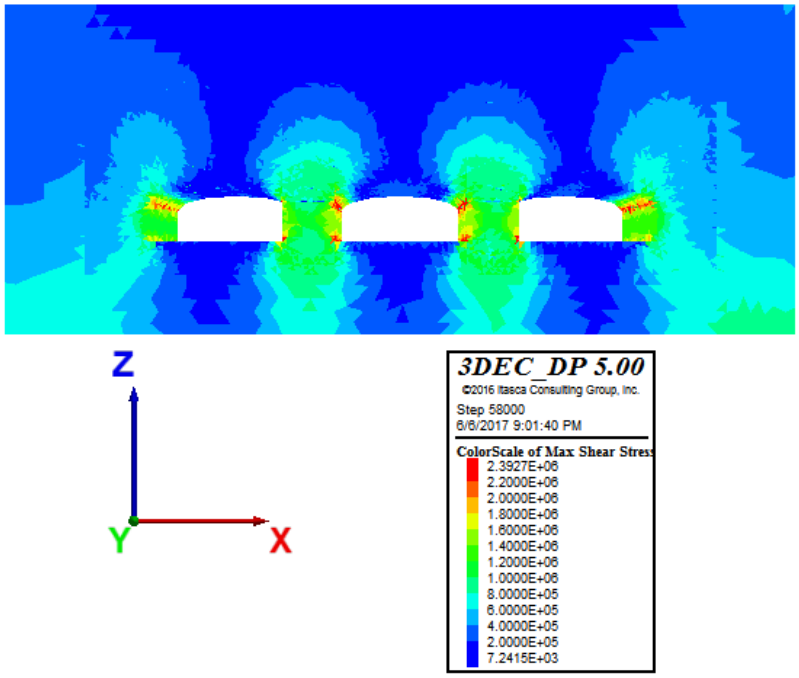

Figure 160. Model 17. Max shear stresses (Pa)

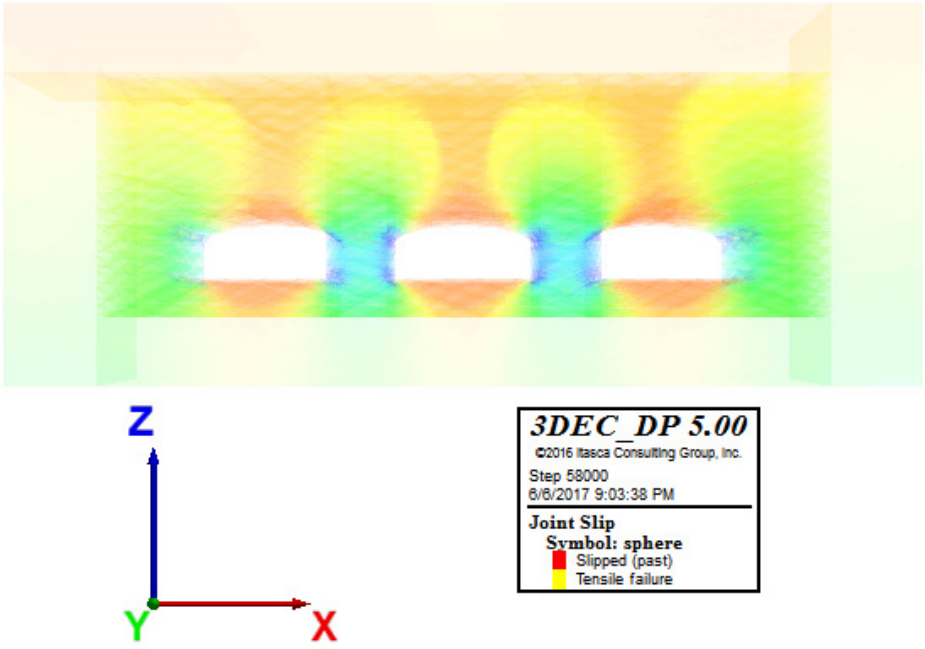

Figure 161. Model 17. Joint slip - Plasticity Limit indicator

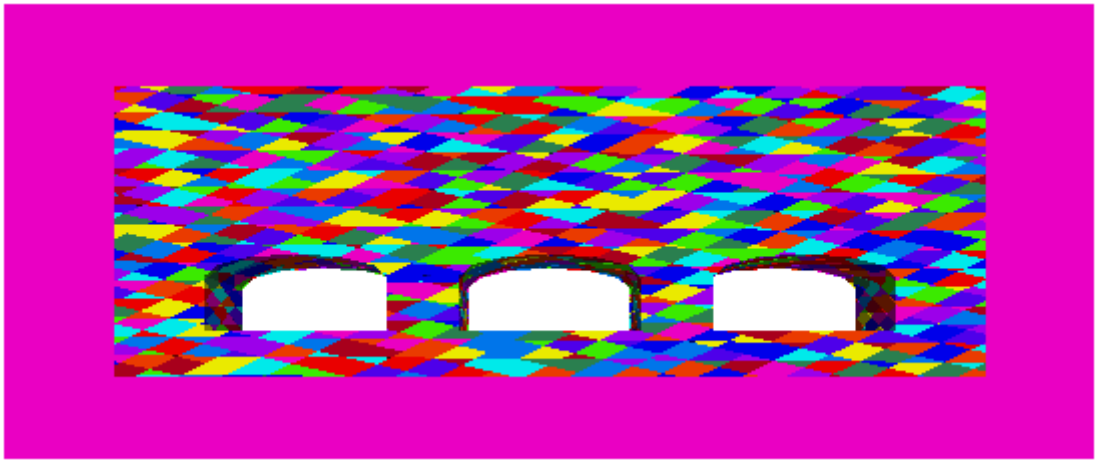

Figure 162. Model 18. Layout

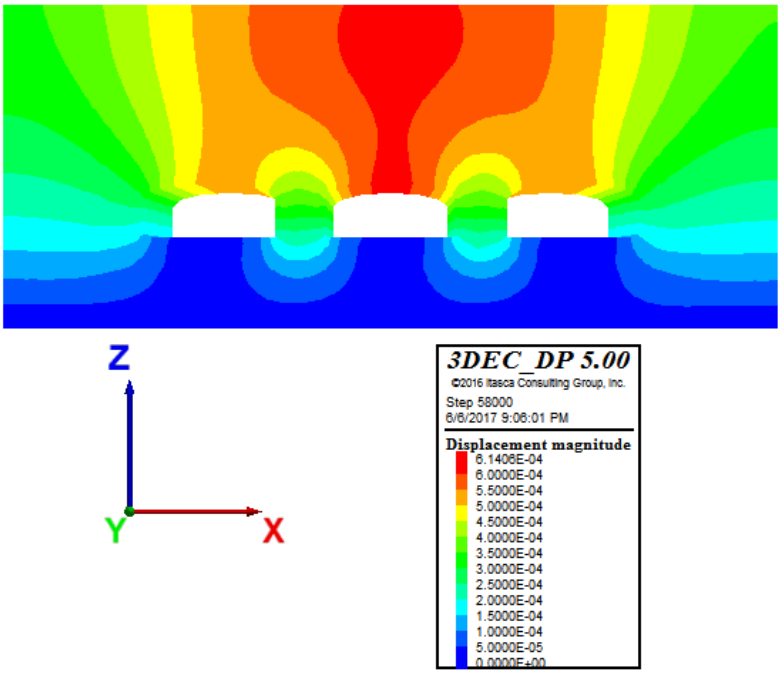

Figure 163. Model 18. Displacement magnitude (m)

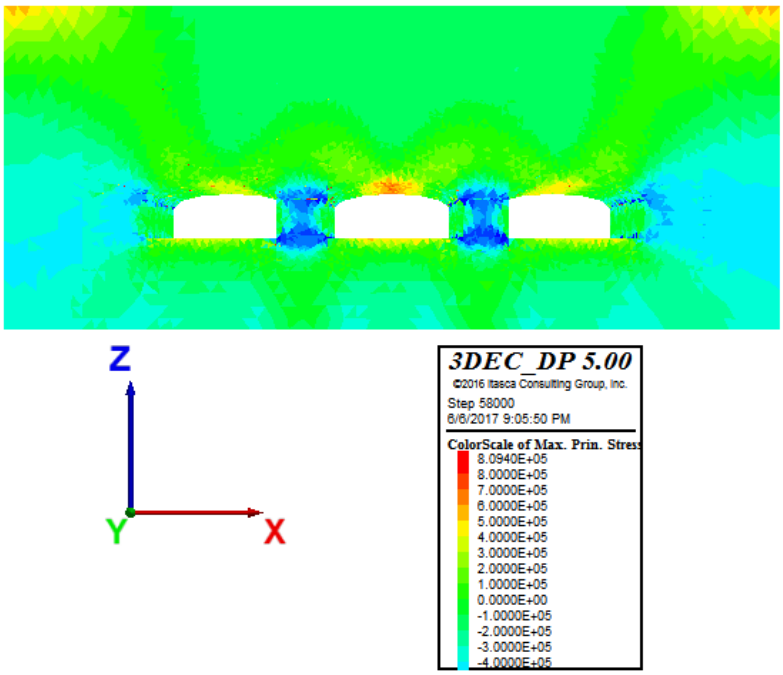

Figure 164. Model 18. Max. principal stresses (Pa)

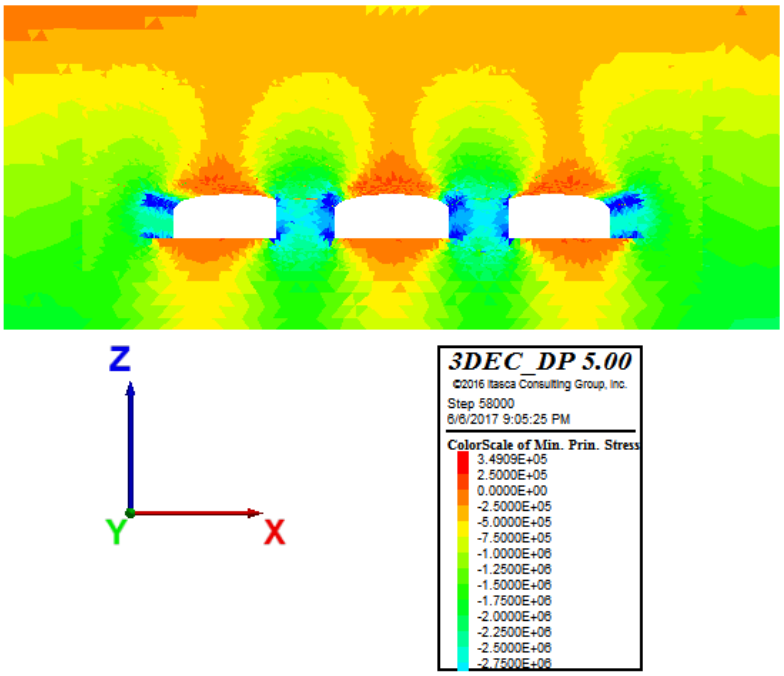

Figure 165. Model 18. Min. principal stresses (Pa)

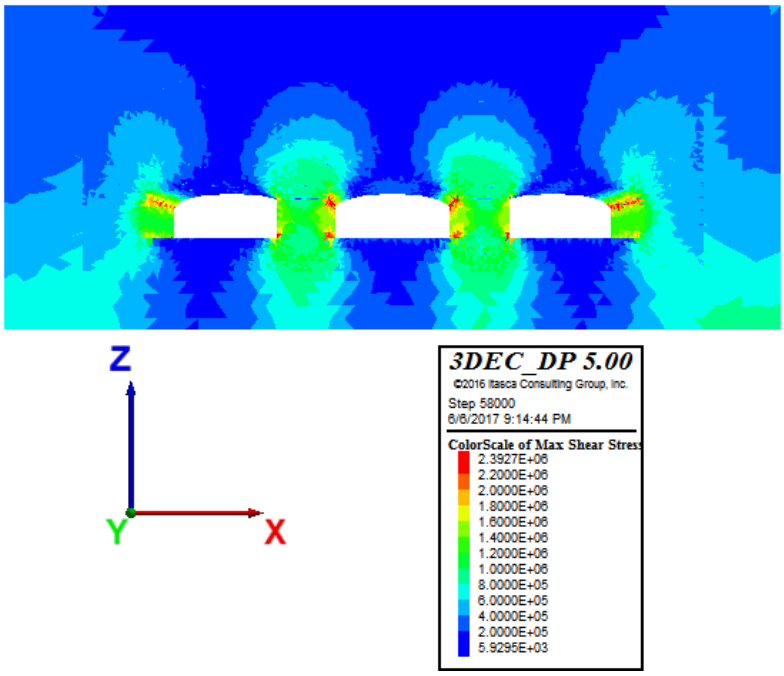

Figure 166. Model 18. Max shear stresses (Pa)

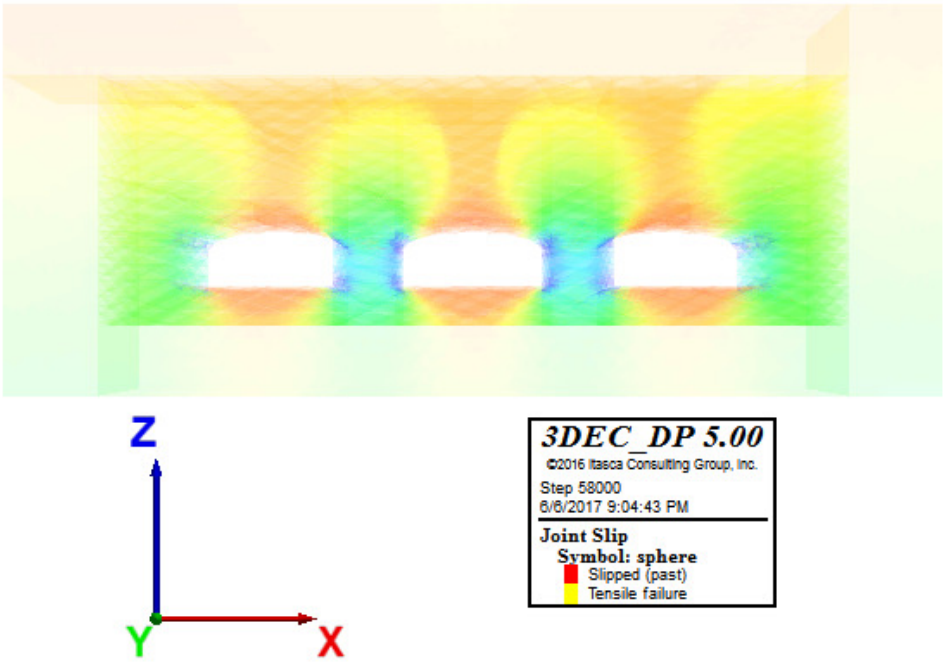

Figure 167. Model 18. Joint slip - Plasticity Limit indicator

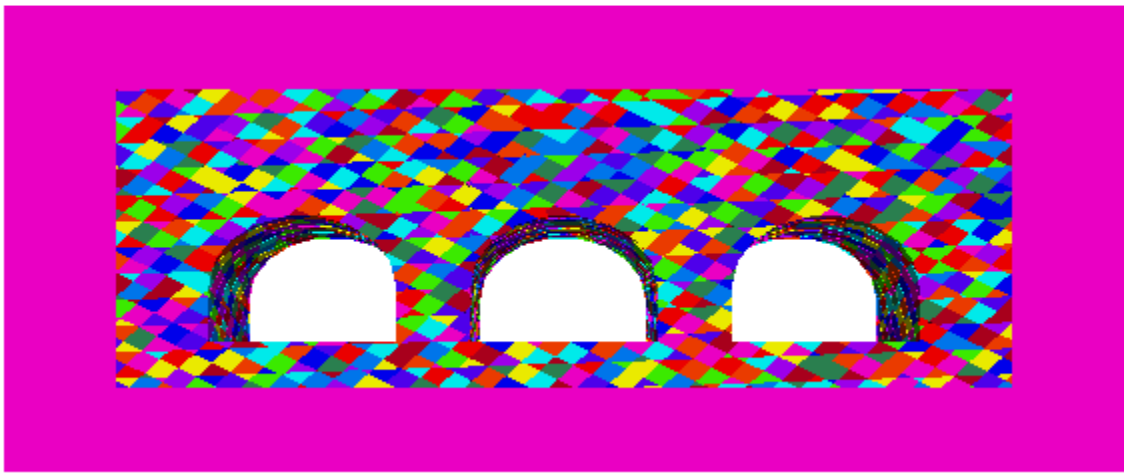

Figure 168. Model 19. Layout

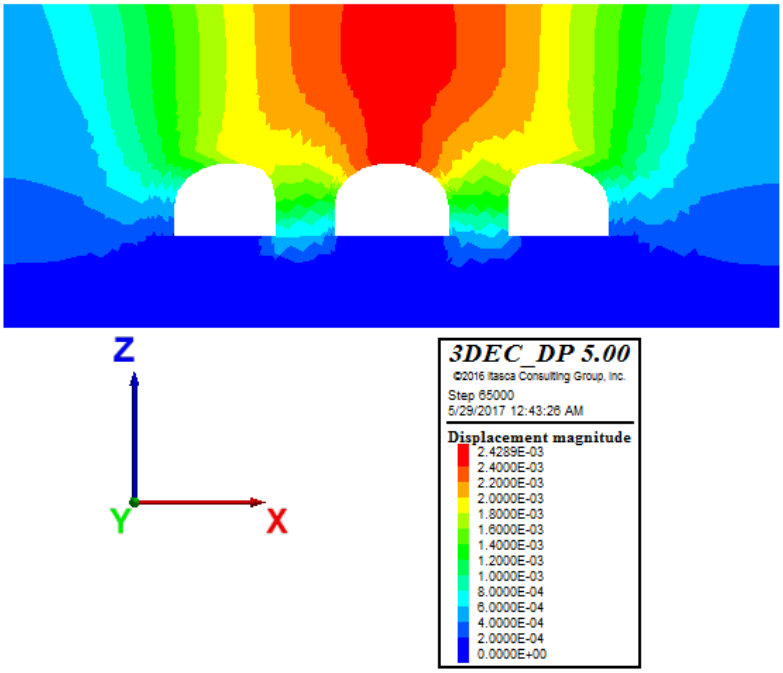

Figure 169. Model 19. Displacement magnitude (m)

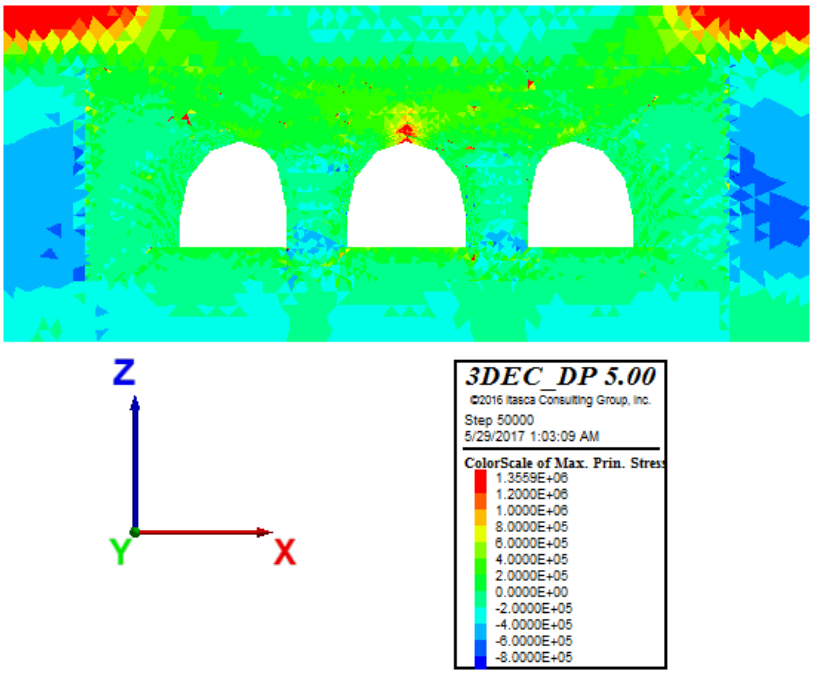

Figure 170. Model 19. Max. principal stresses (Pa)

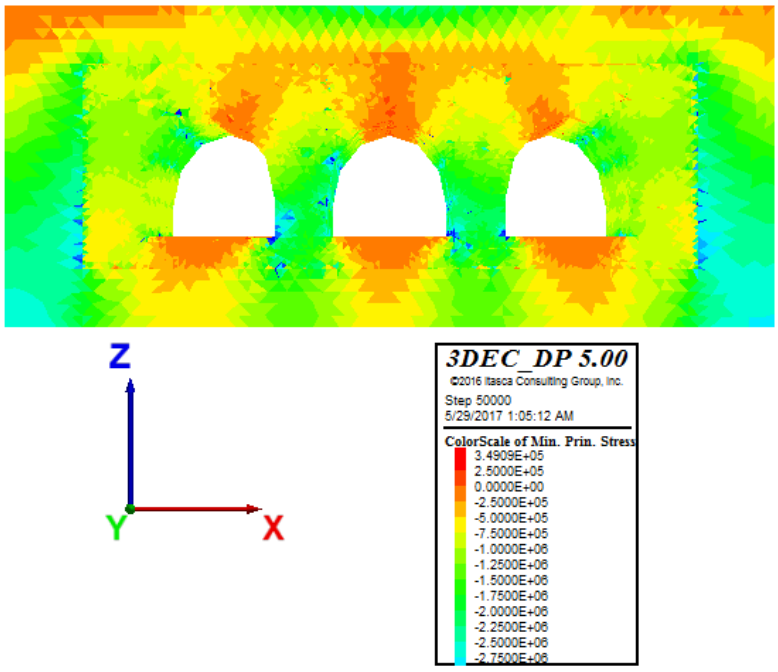

Figure 171. Model 19. Min. principal stresses (Pa)

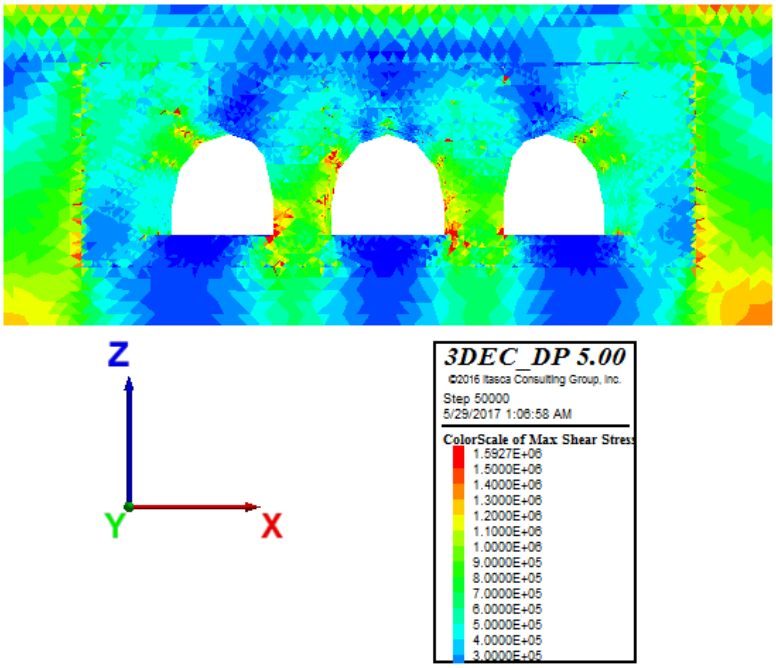

Figure 172. Model 19. Max shear stresses (Pa)

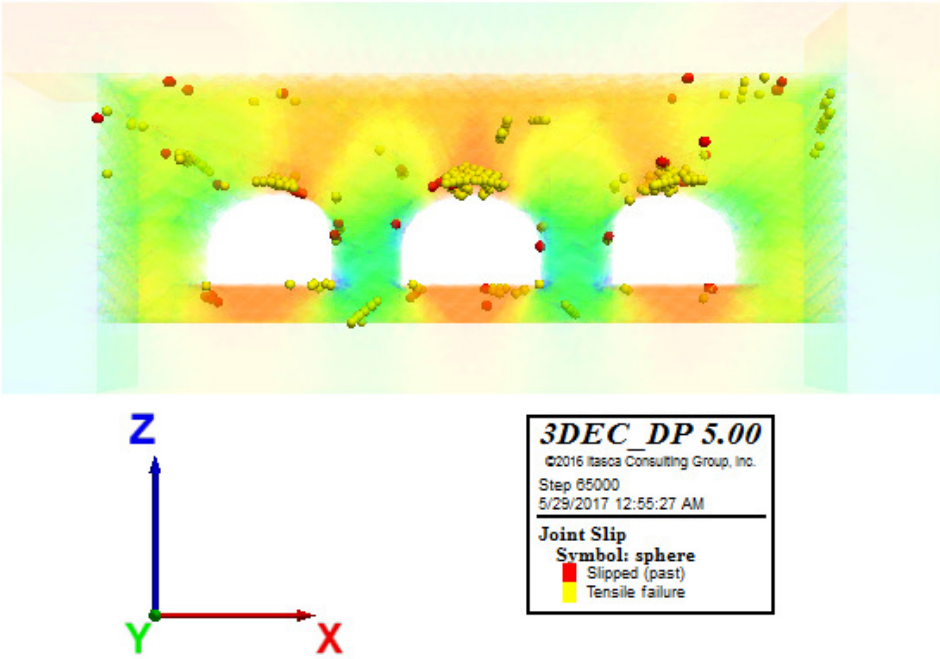

Figure 173. Model 19. Joint slip - Plasticity Limit indicator

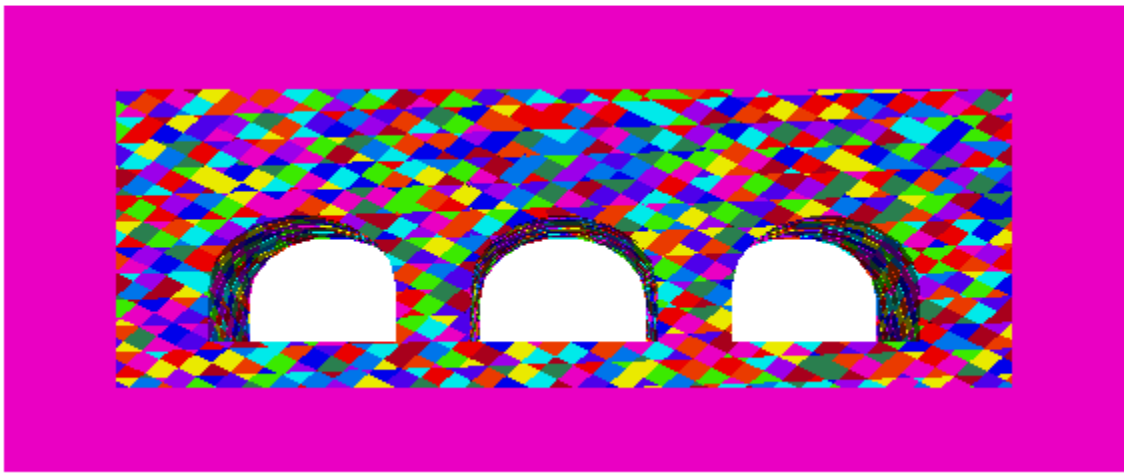

Figure 174. Model 20. Layout

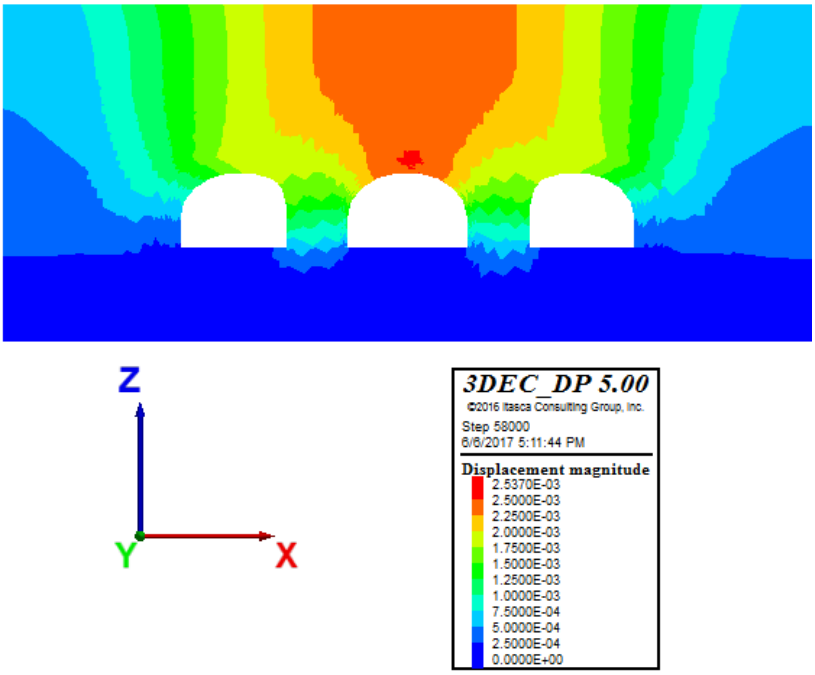

Figure 175. Model 20. Displacement magnitude (m)

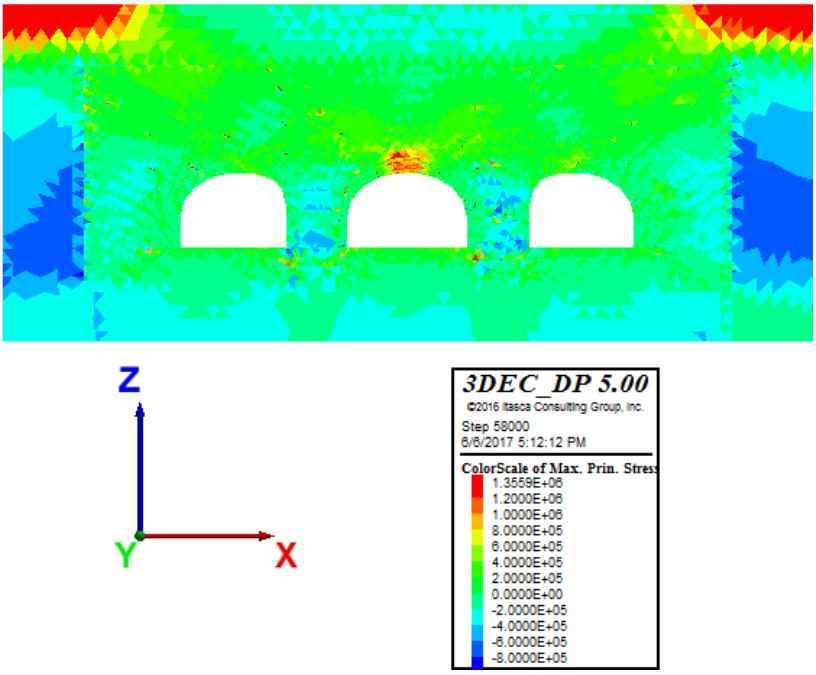

Figure 176. Model 20. Max. principal stresses (Pa)

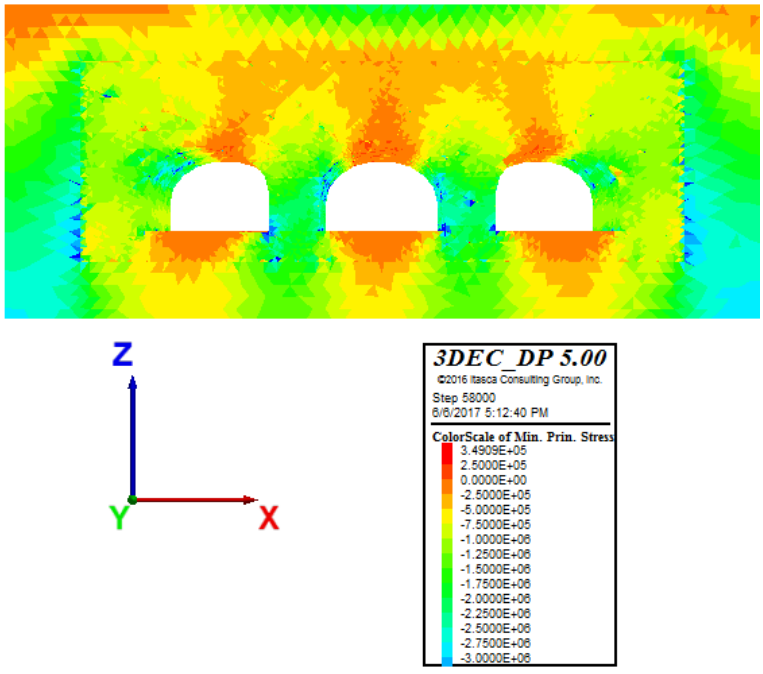

Figure 177. Model 20. Min. principal stresses (Pa)

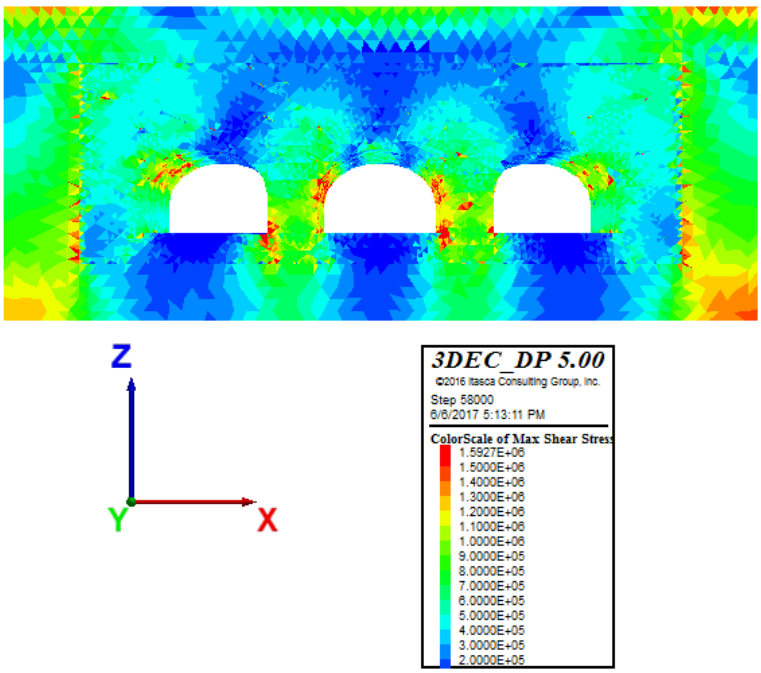

Figure 178. Model 20. Max shear stresses (Pa)

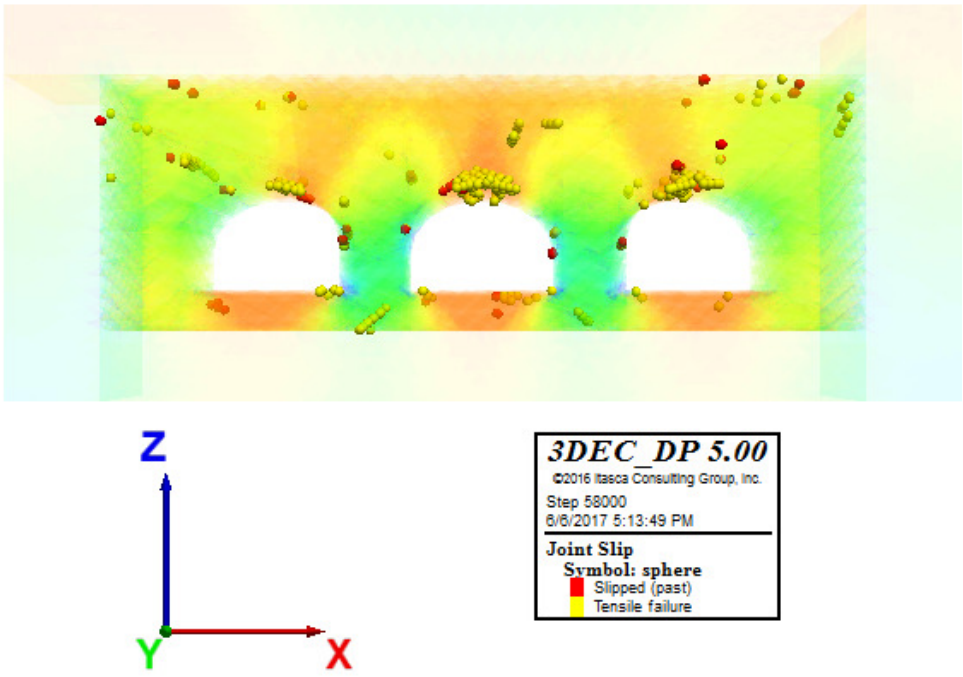

Figure 179. Model 20. Joint slip - Plasticity Limit indicator

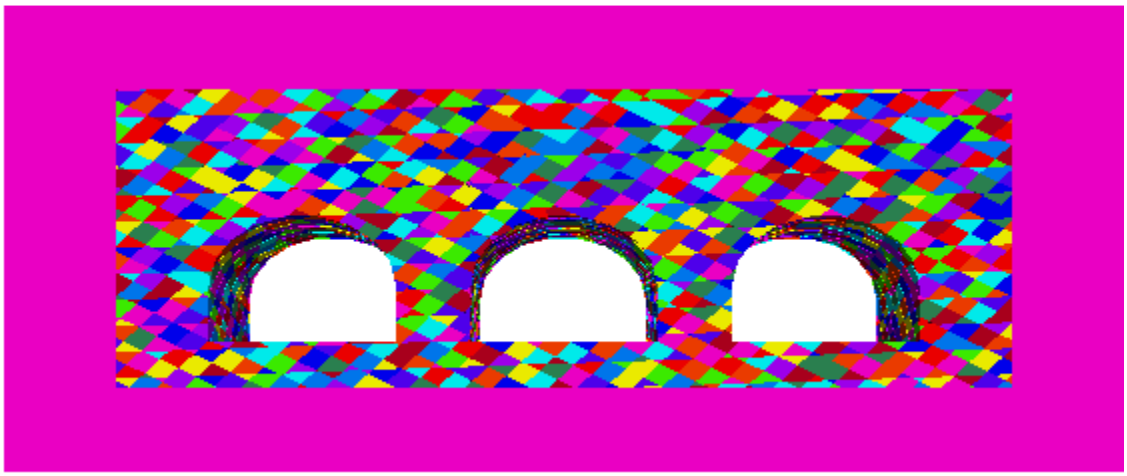

Figure 180. Model 21. Layout

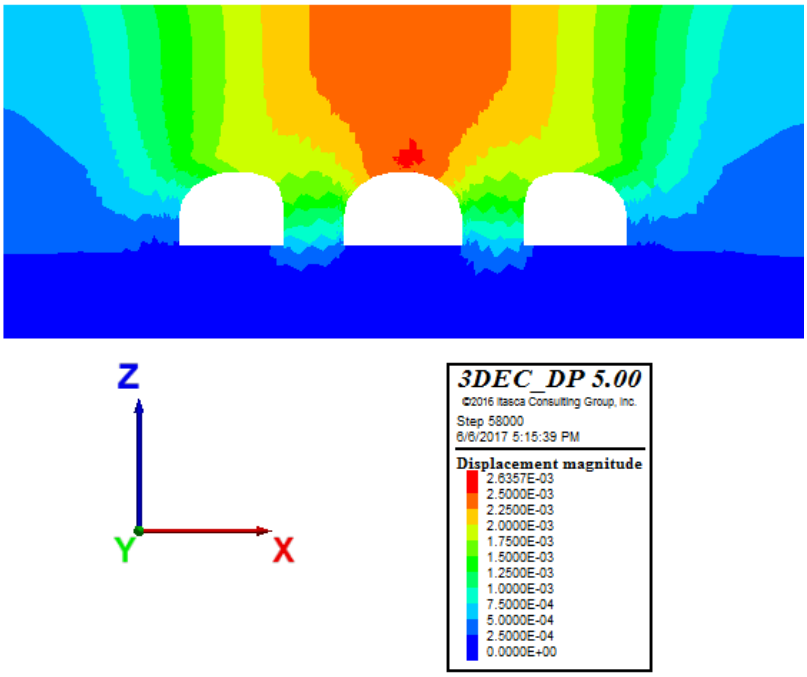

Figure 181. Model 21. Displacement magnitude (m)

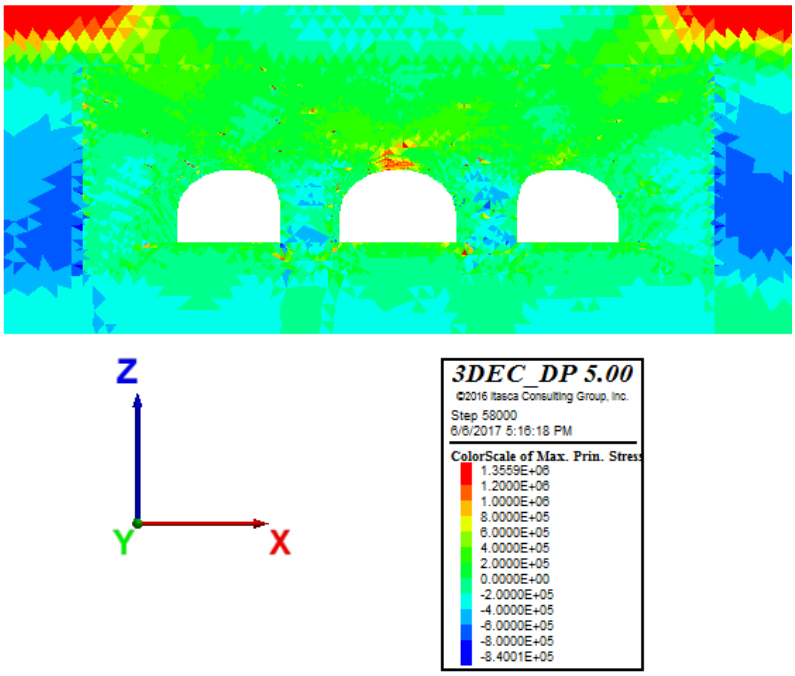

Figure 182. Model 21. Max. principal stresses (Pa)

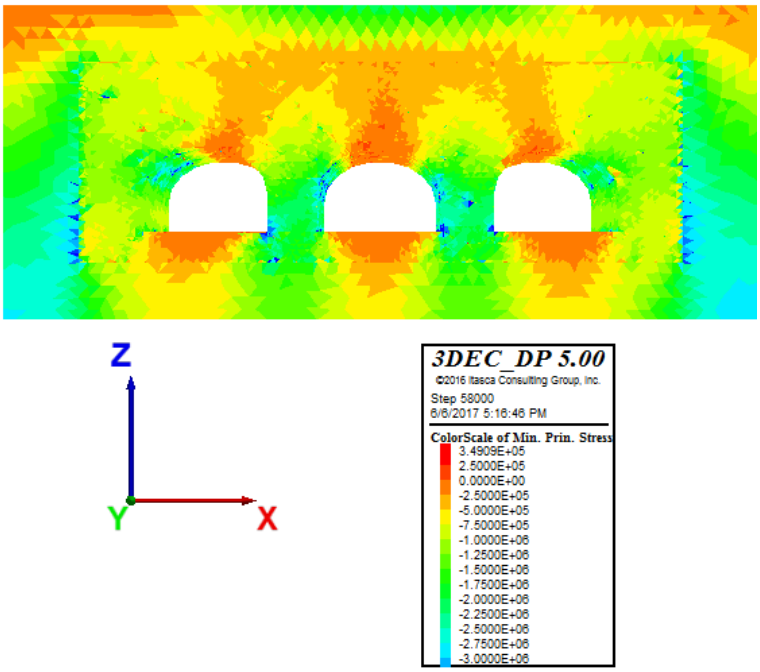

Figure 183. Model 21. Min. principal stresses (Pa)

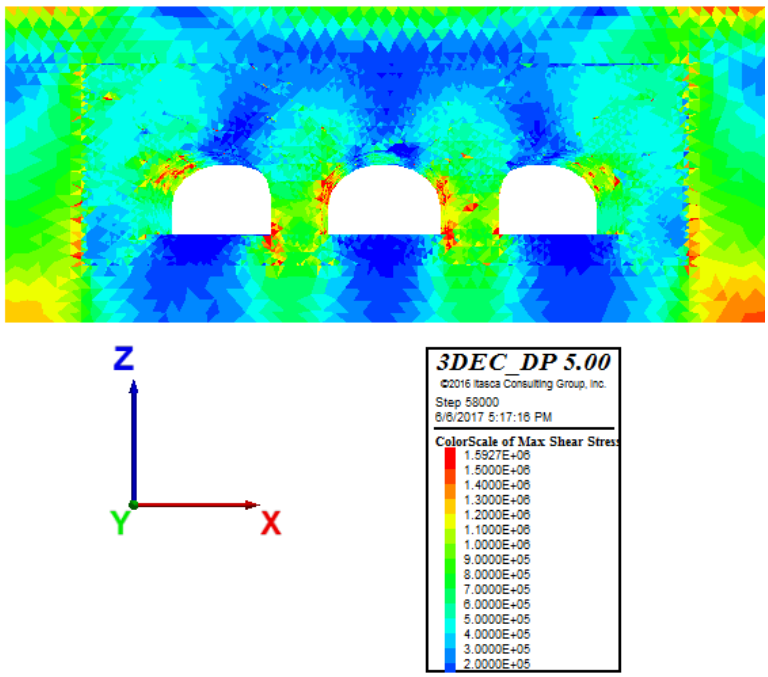

Figure 184. Model 21. Max shear stresses (Pa)

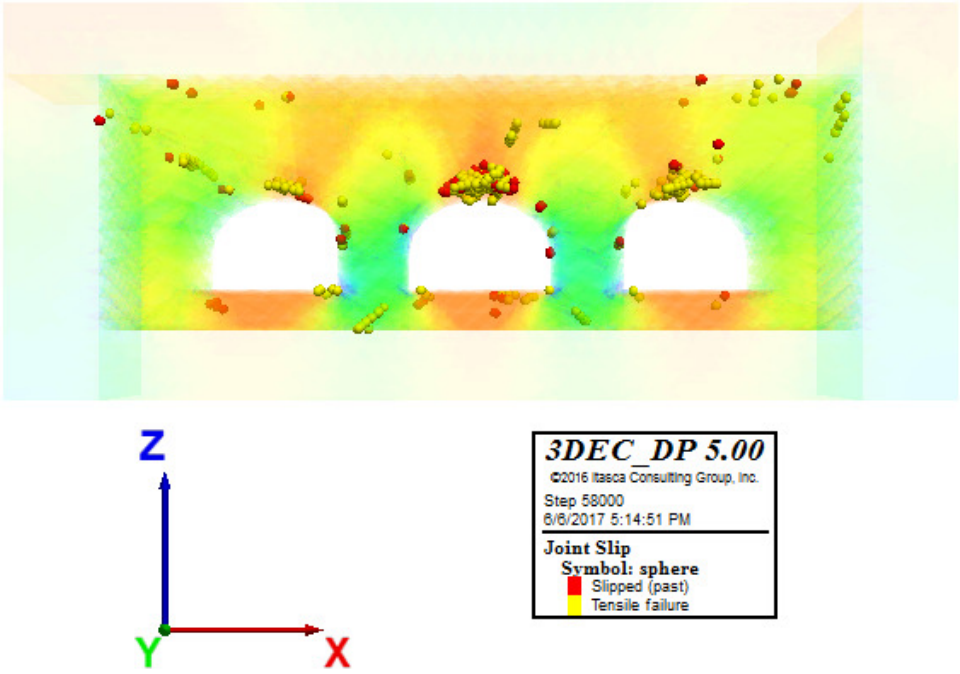

Figure 185. Model 21. Joint slip - Plasticity Limit indicator

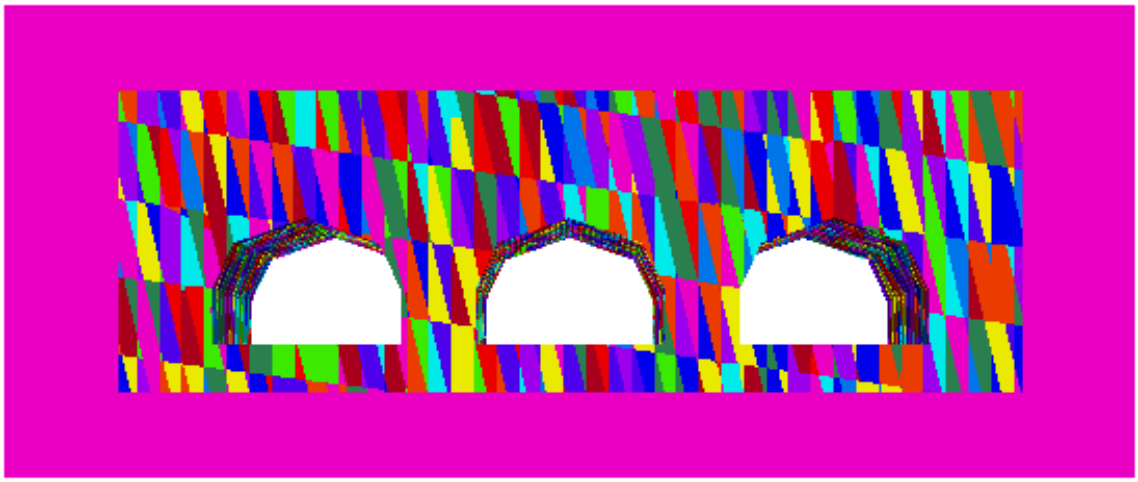

Figure 186. Model 22. Layout

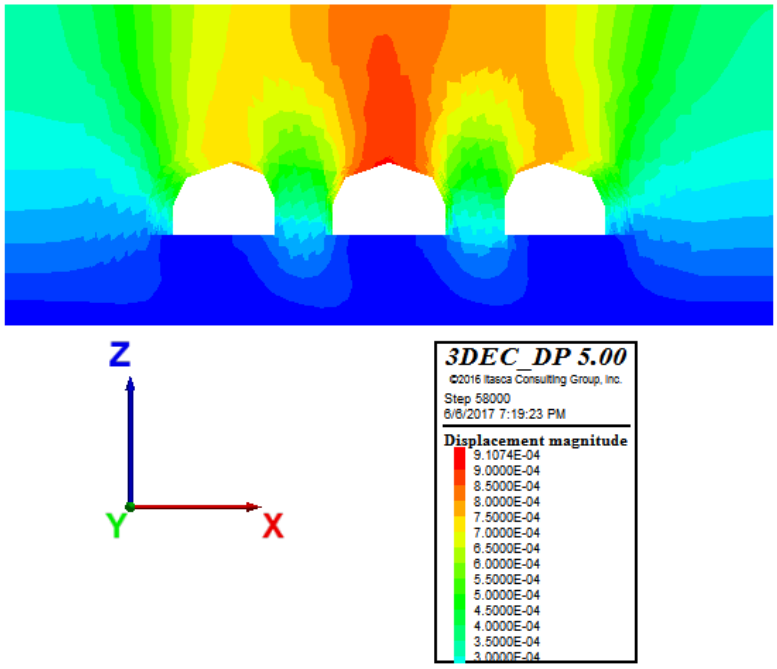

Figure 187. Model 22. Displacement magnitude (m)

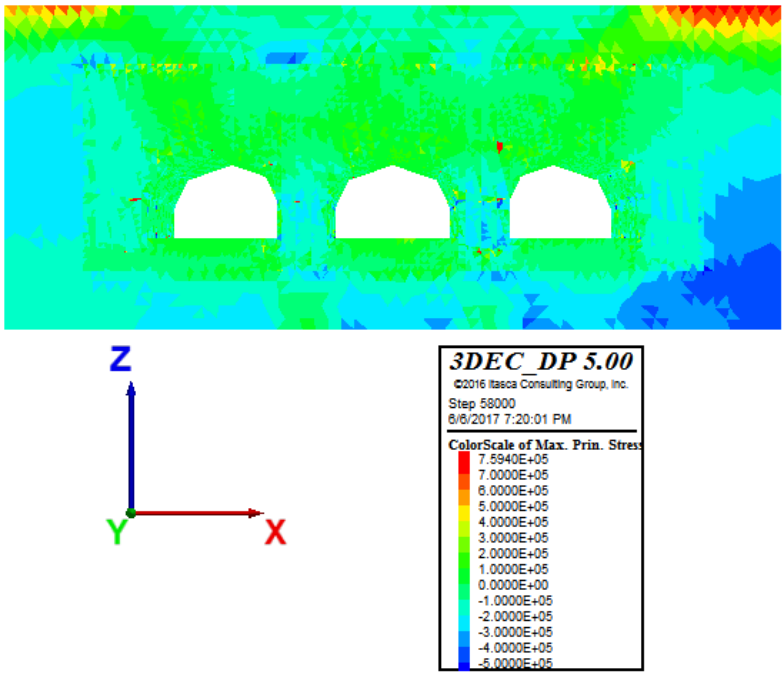

Figure 188. Model 22. Max. principal stresses (Pa)

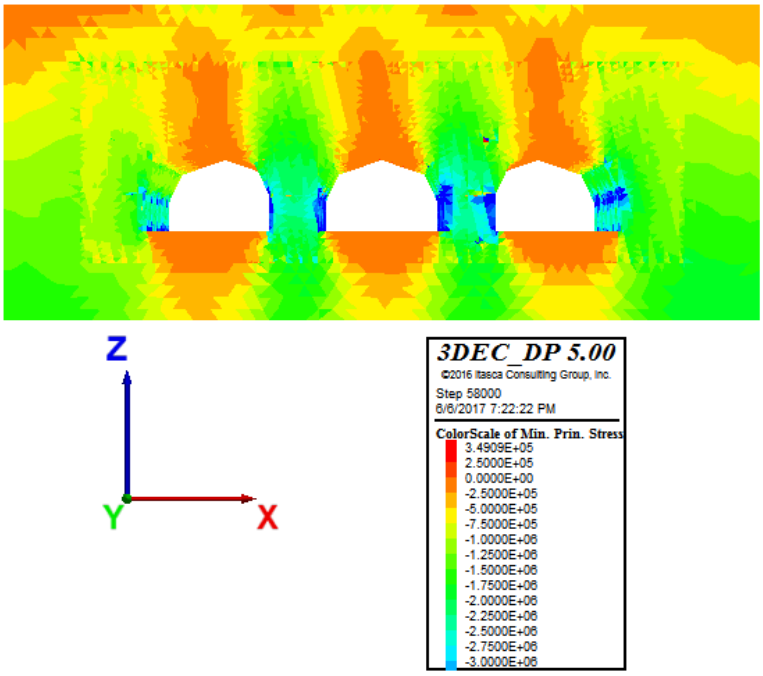

Figure 189. Model 22. Min. principal stresses (Pa)

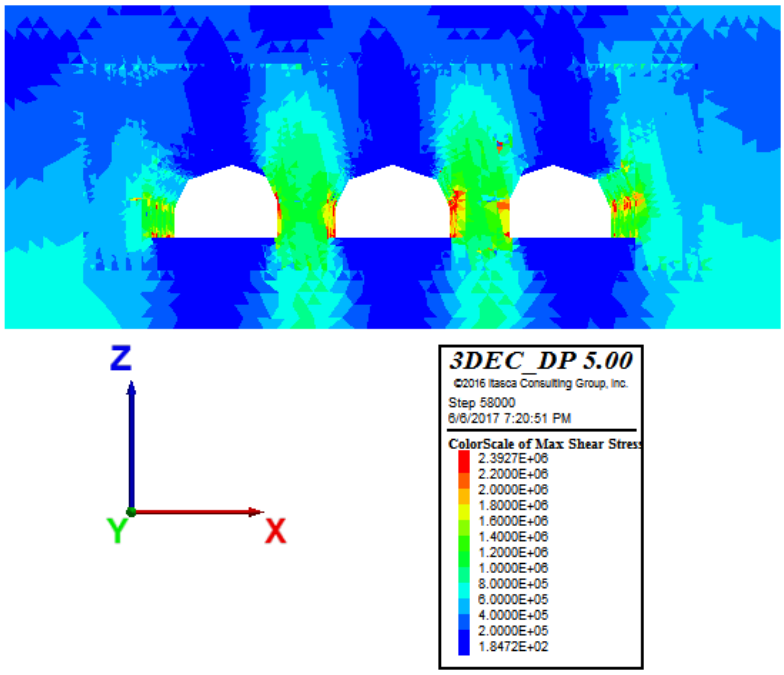

Figure 190. Model 22. Max shear stresses (Pa)

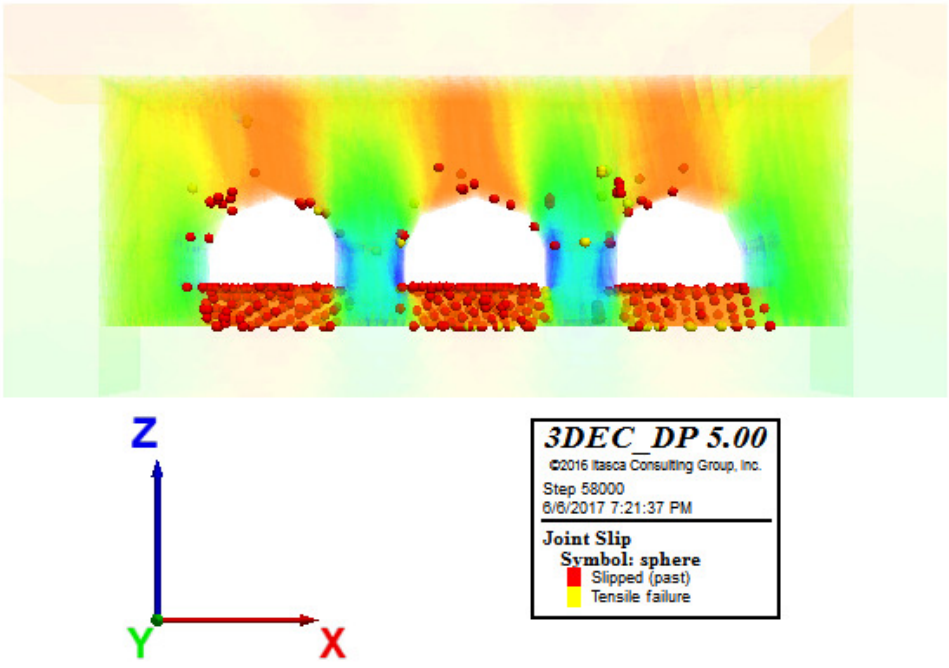

Figure 191. Model 22. Joint slip - Plasticity Limit indicator

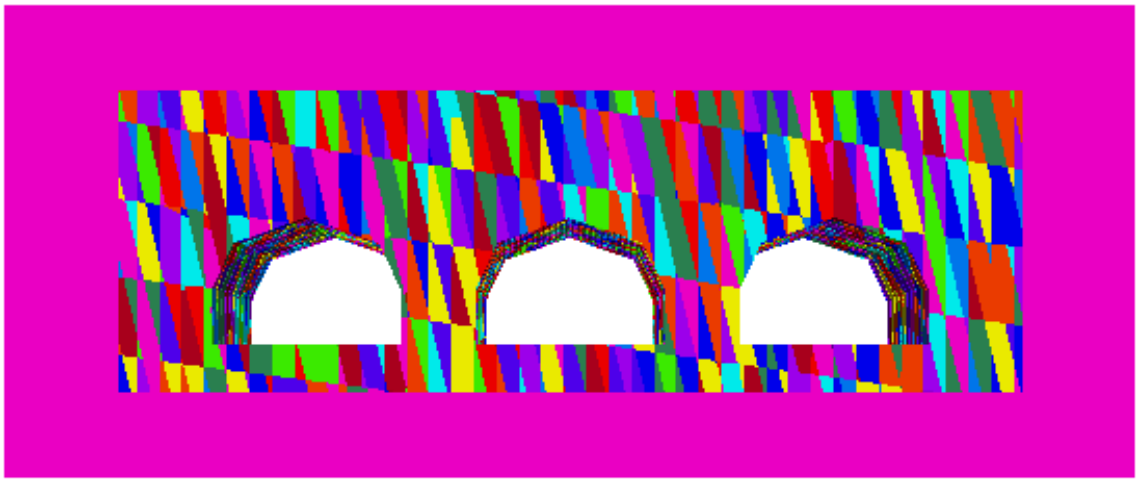

Figure 192. Model 23. Layout

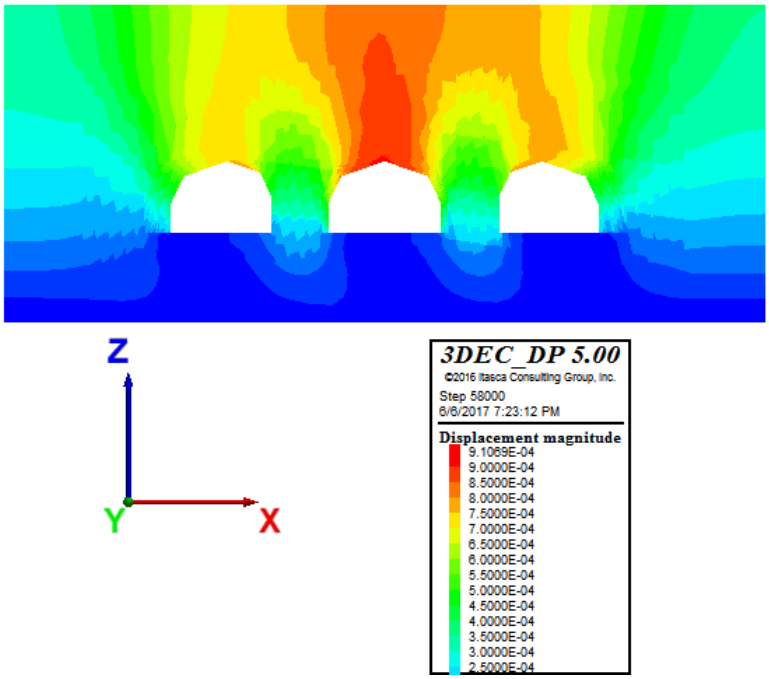

Figure 193. Model 23. Displacement magnitude (m)

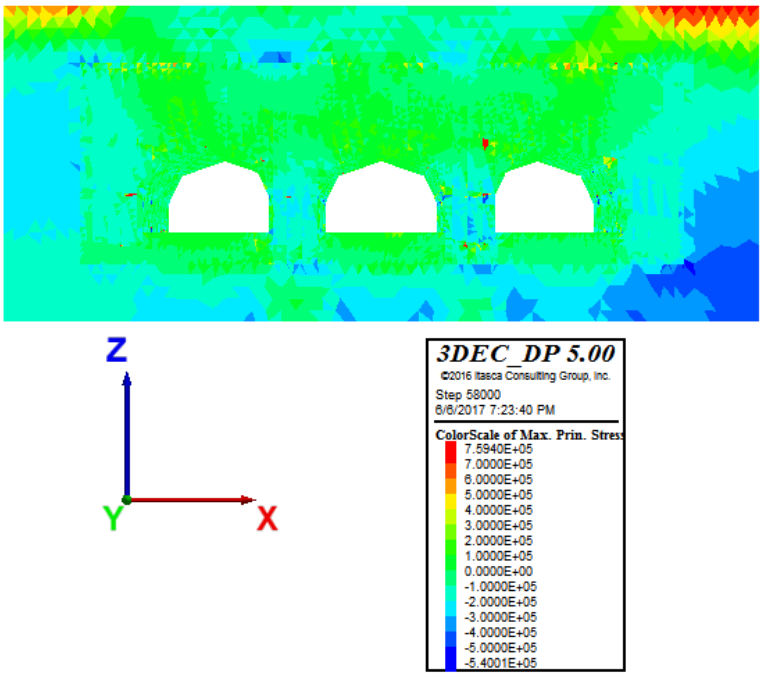

Figure 194. Model 23. Max. principal stresses (Pa)

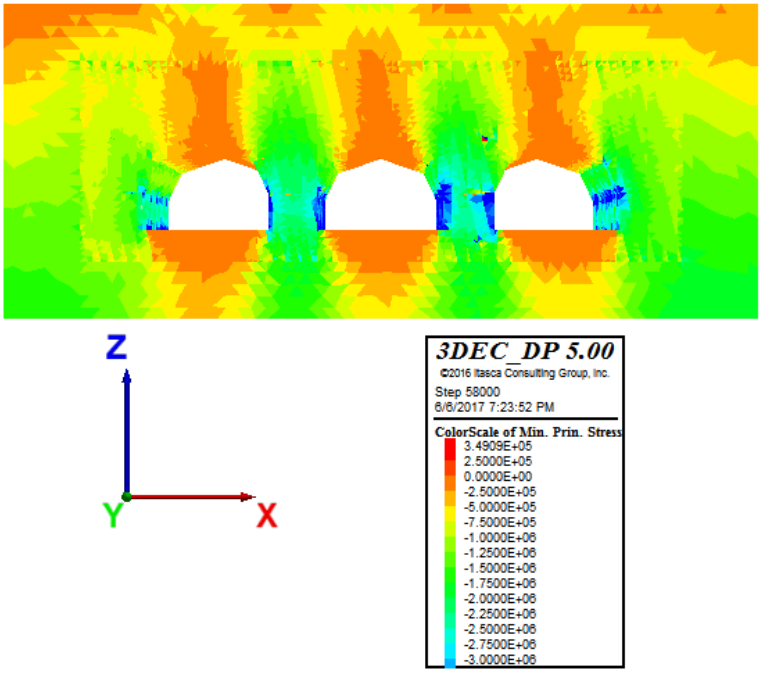

Figure 195. Model 23. Min. principal stresses (Pa)

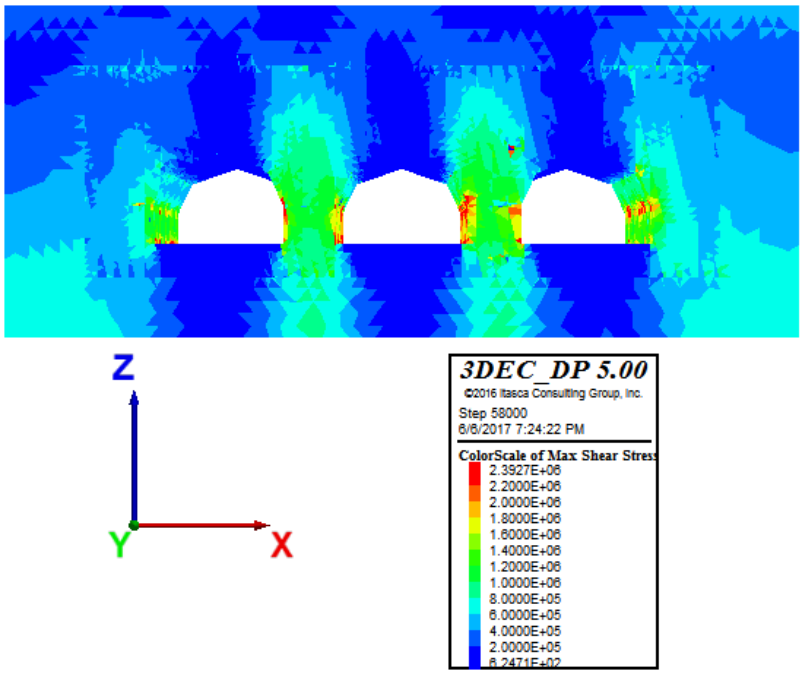

Figure 196. Model 23. Max shear stresses (Pa)

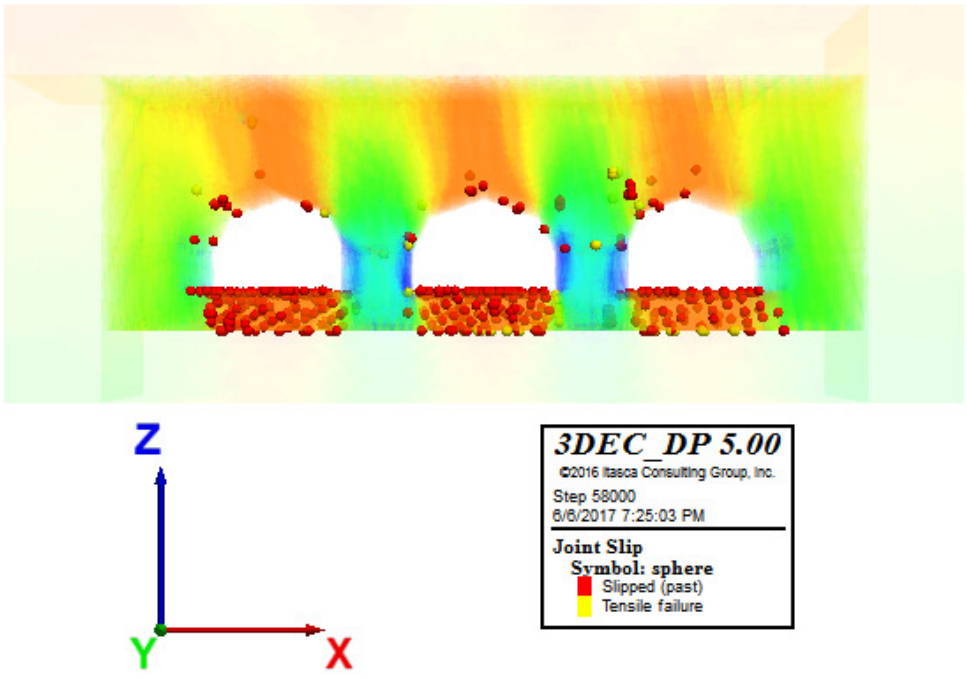

Figure 197. Model 23. Joint slip - Plasticity Limit indicator

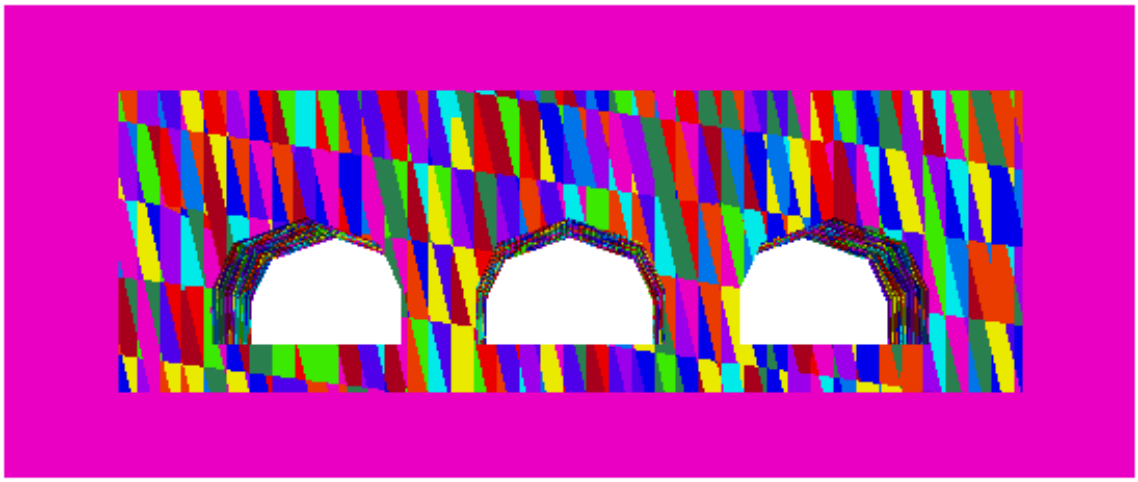

Figure 198. Model 24. Layout

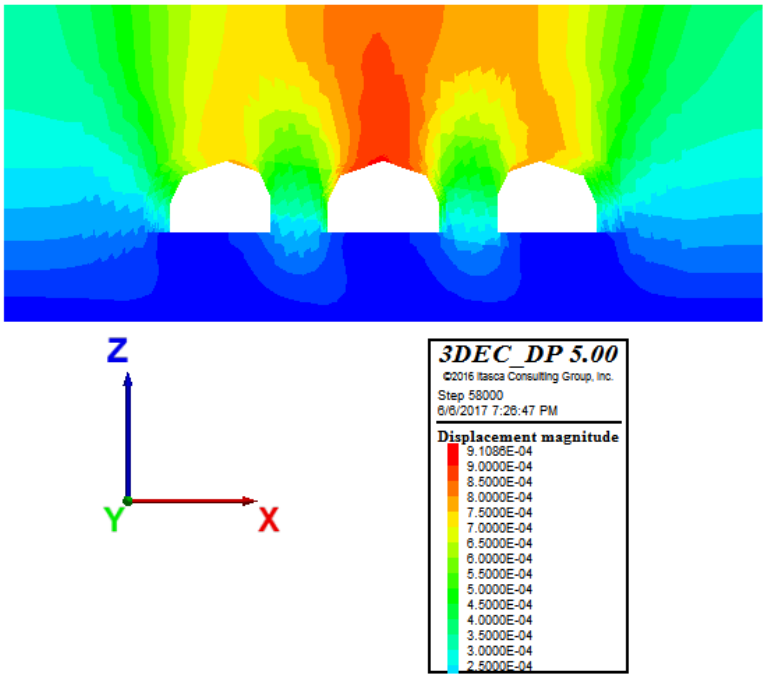

Figure 199. Model 24. Displacement magnitude (m)

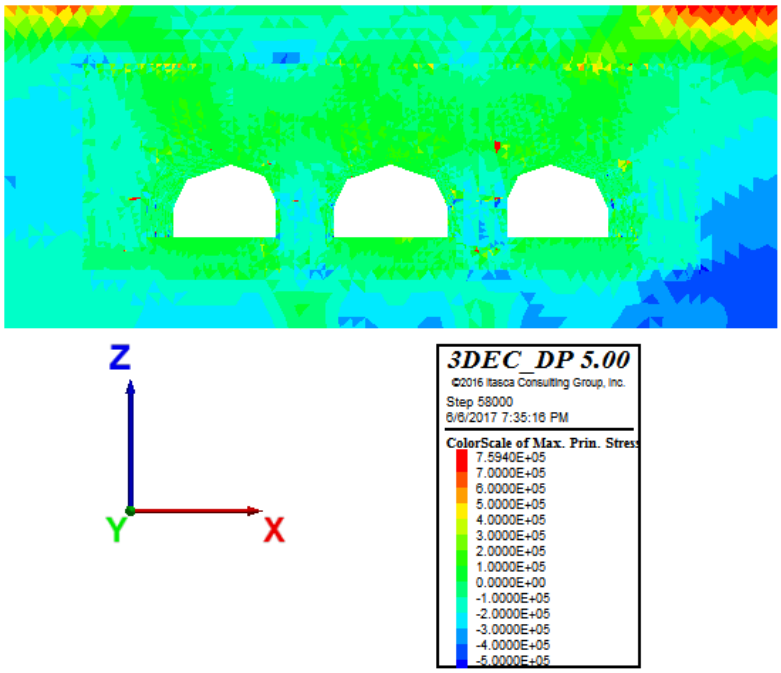

Figure 200. Model 24. Max. principal stresses (Pa)

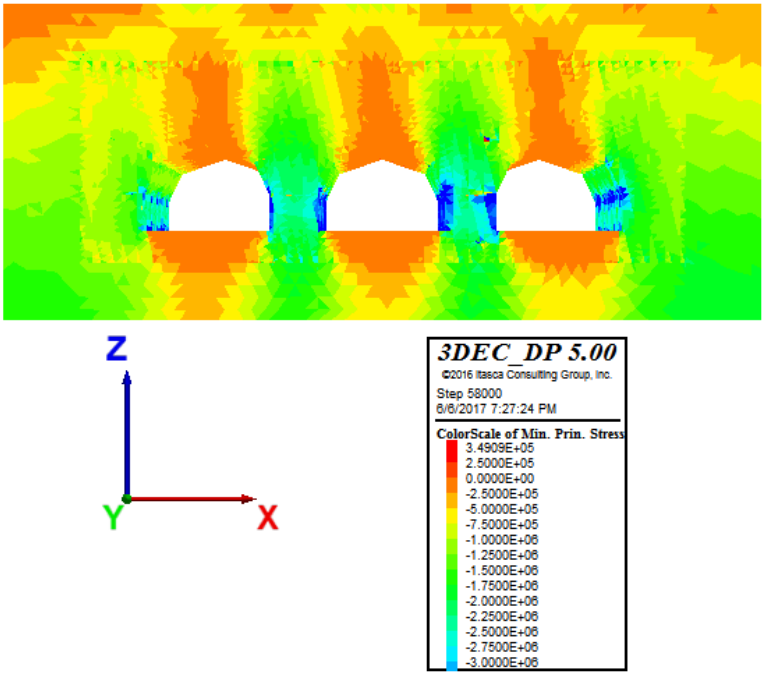

Figure 201. Model 24. Min. principal stresses (Pa)

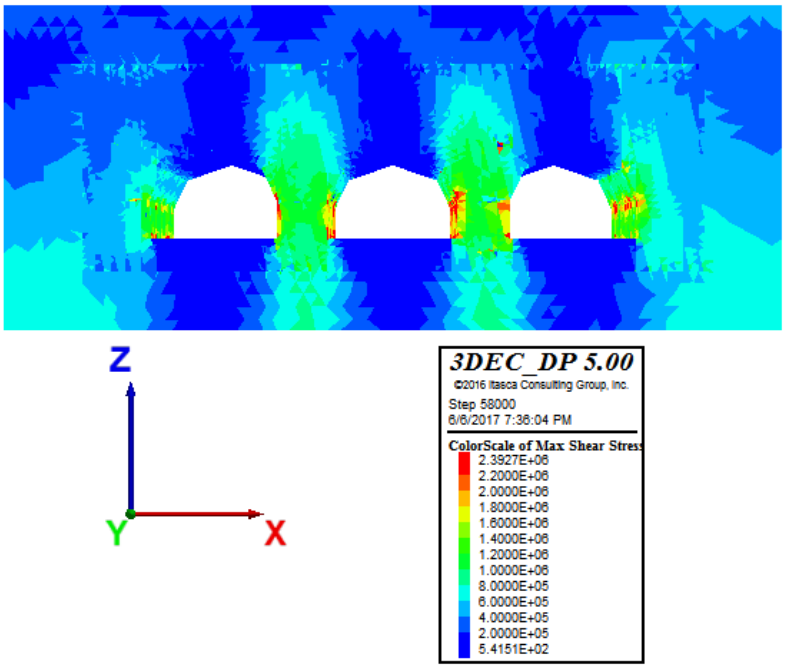

Figure 202. Model 24. Max shear stresses (Pa)

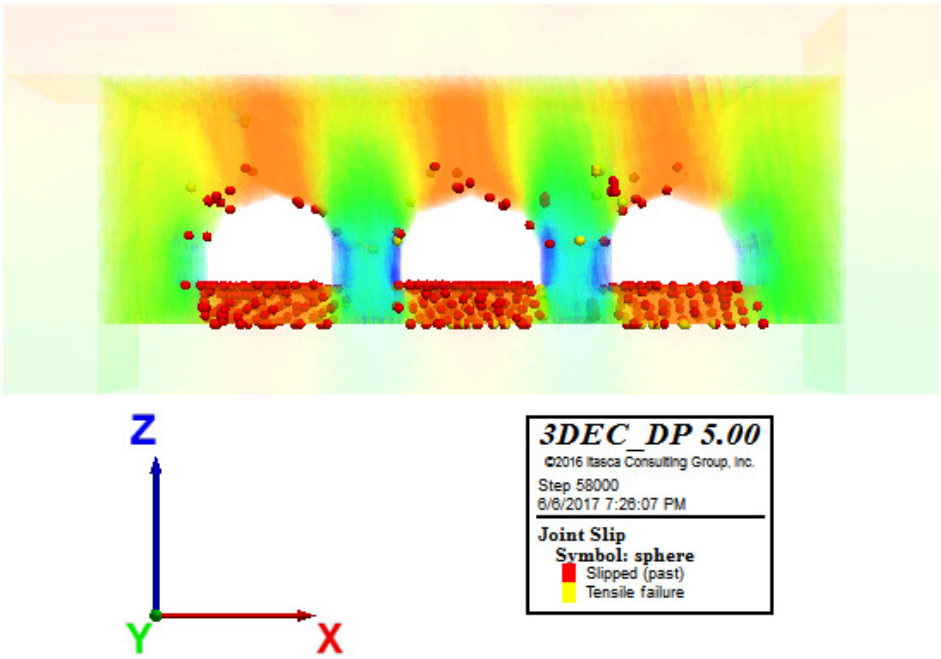

Figure 203. Model 24. Joint slip - Plasticity Limit indicator

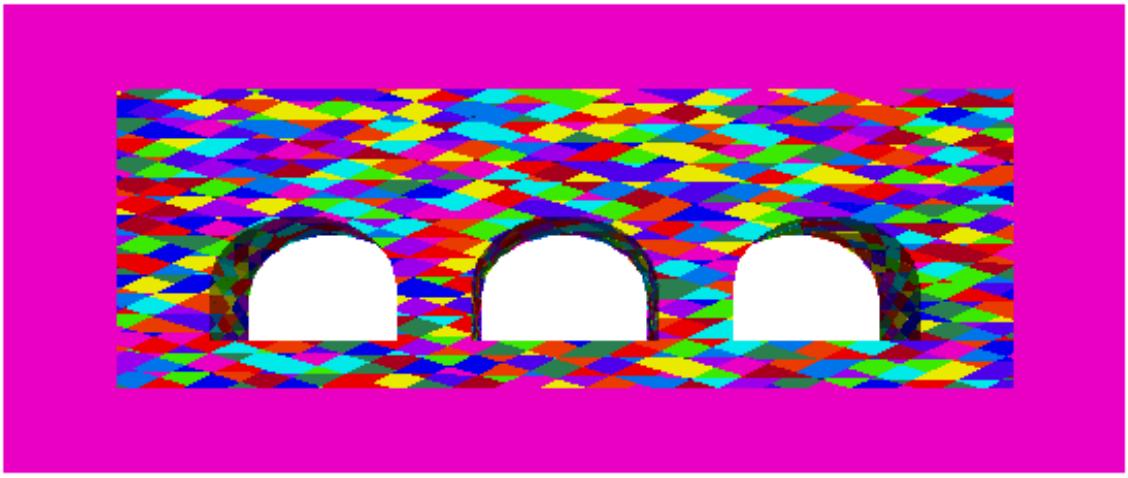

Figure 204. Model 25. Layout

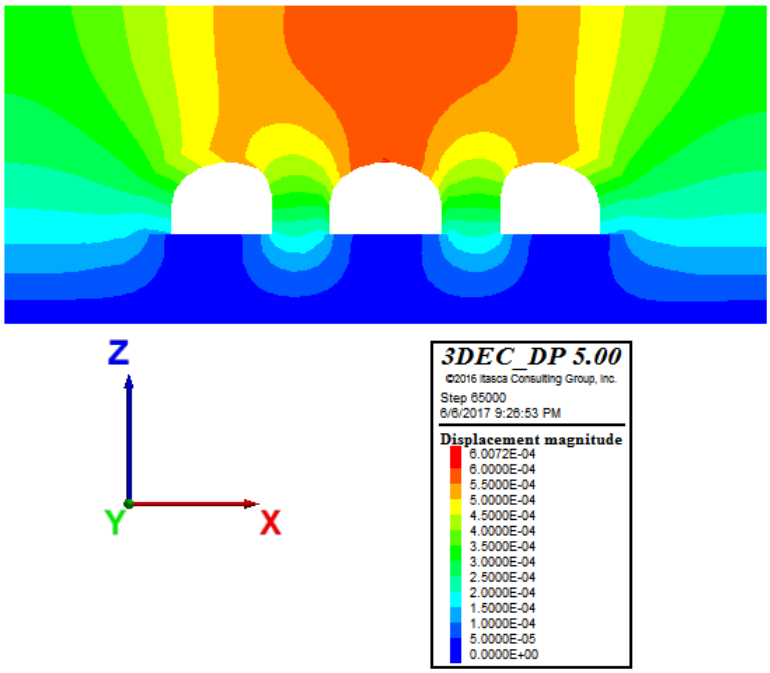

Figure 205. Model 25. Displacement magnitude (m)

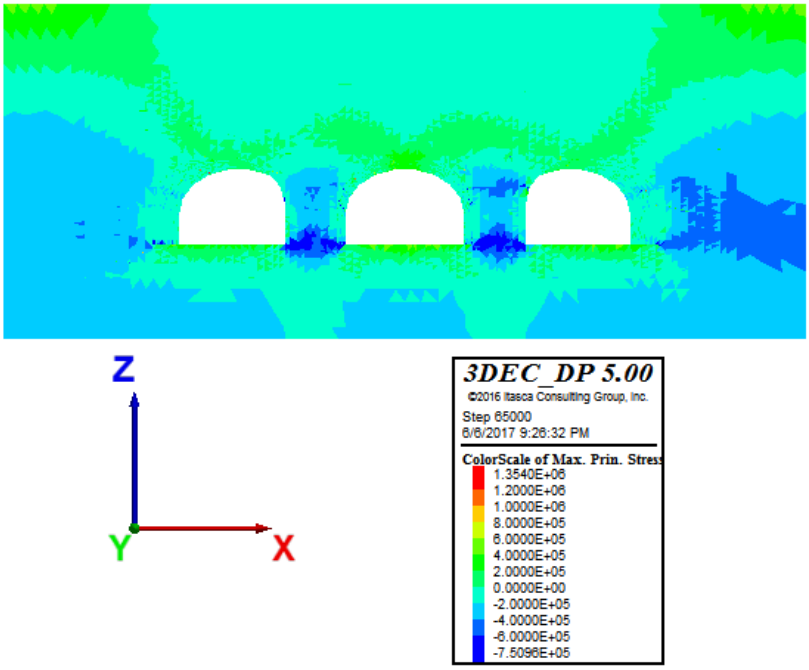

Figure 206. Model 25. Max. principal stresses (Pa)

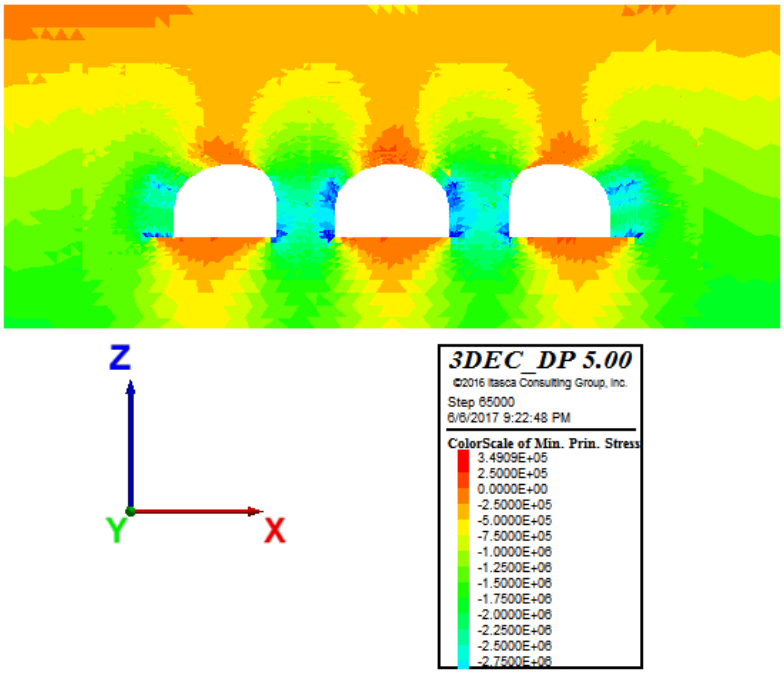

Figure 207. Model 25. Min. principal stresses (Pa)

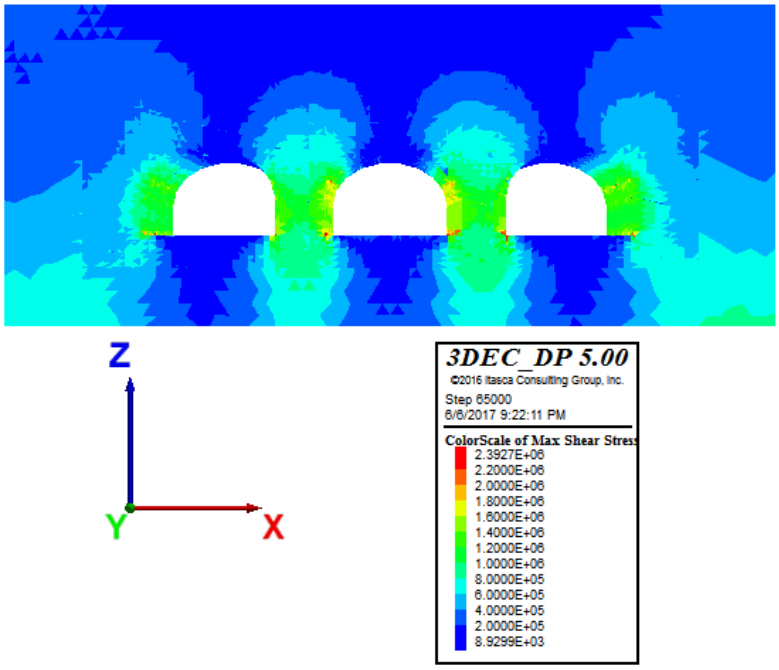

Figure 208. Model 25. Max shear stresses (Pa)

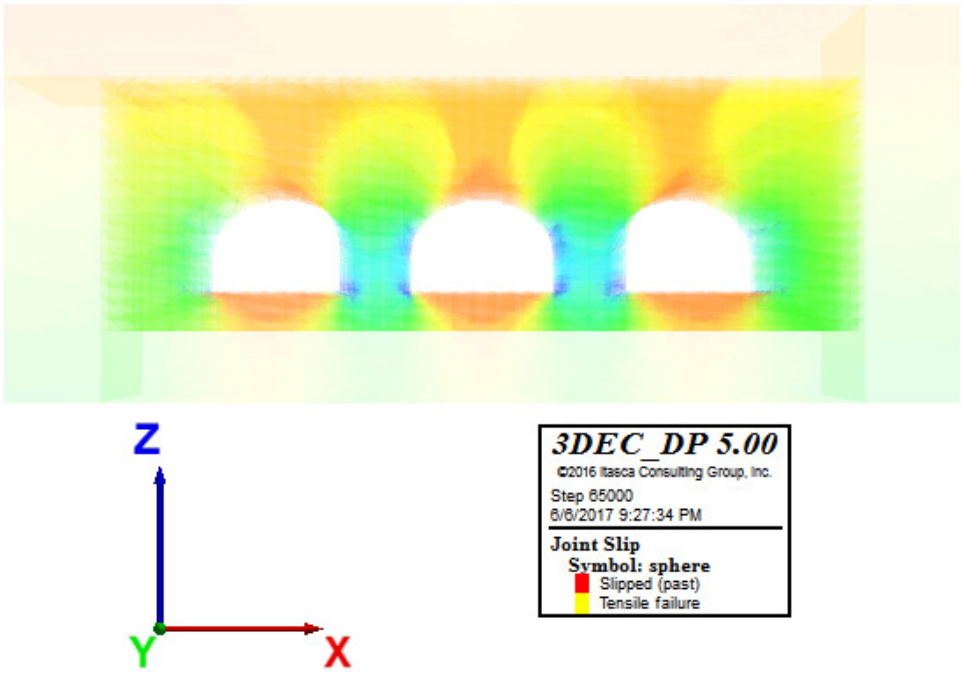

Figure 209. Model 25. Joint slip - Plasticity Limit indicator

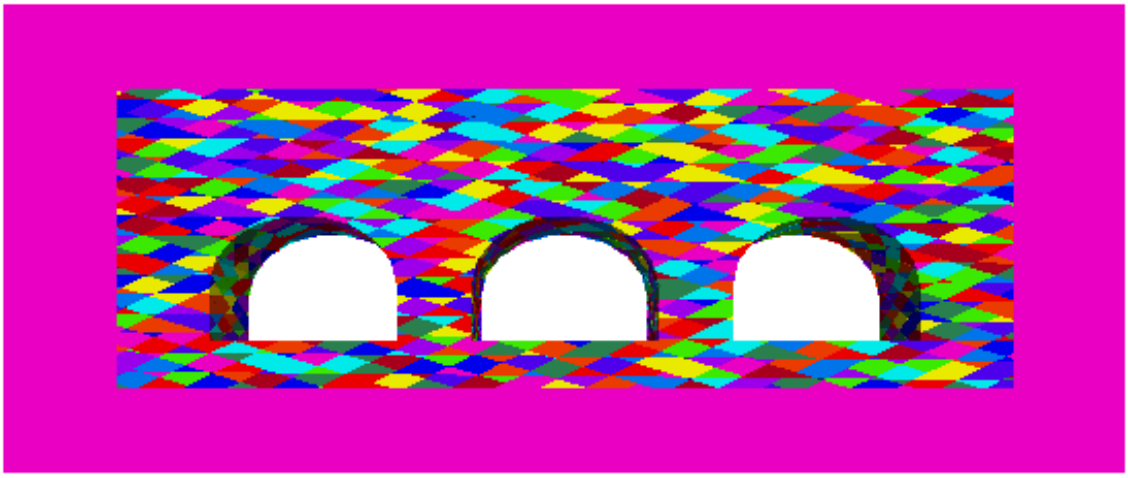

Figure 210. Model 26. Layout

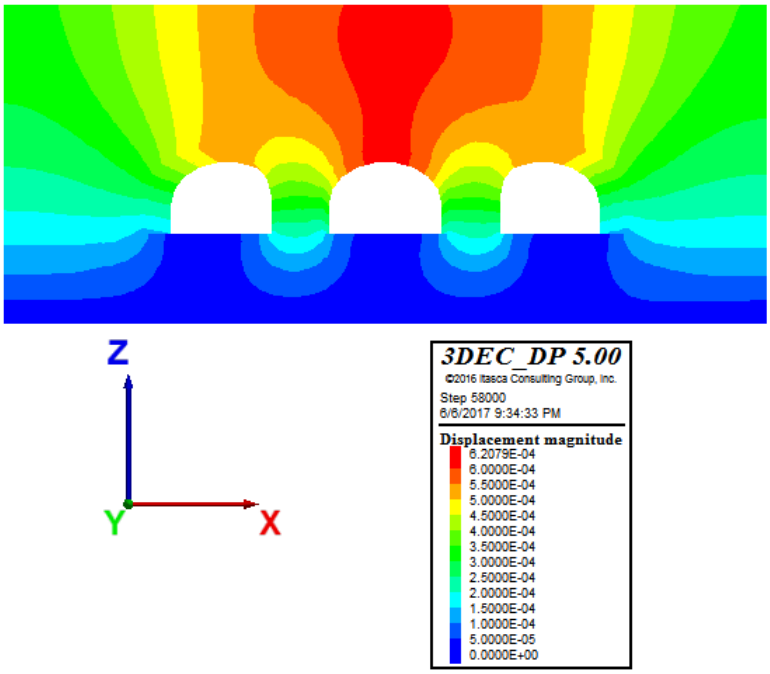

Figure 211. Model 26. Displacement magnitude (m)

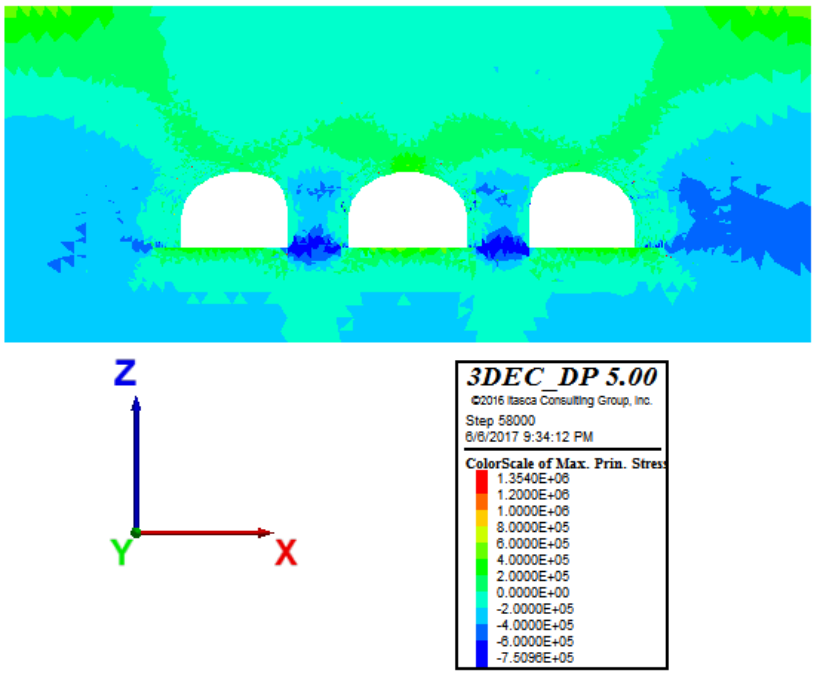

Figure 212. Model 26. Max. principal stresses (Pa)

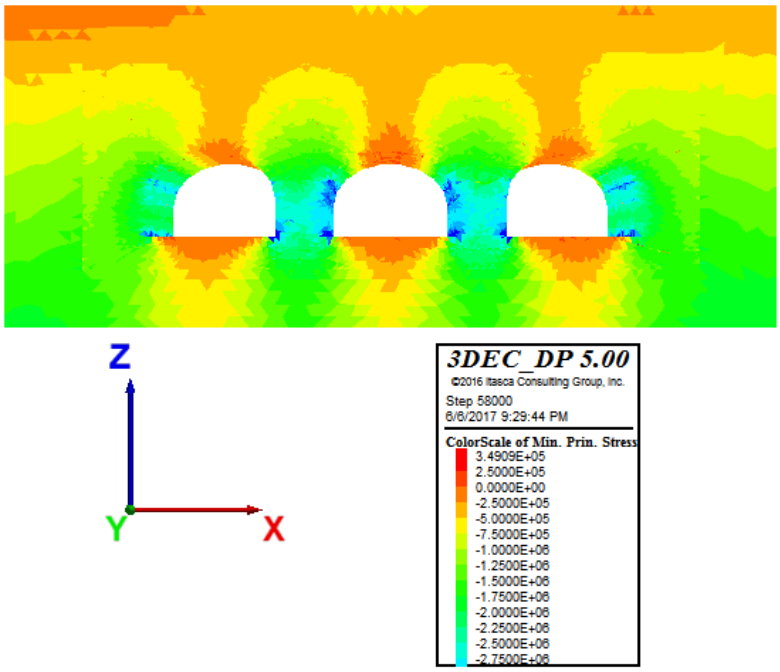

Figure 213. Model 26. Min. principal stresses (Pa)

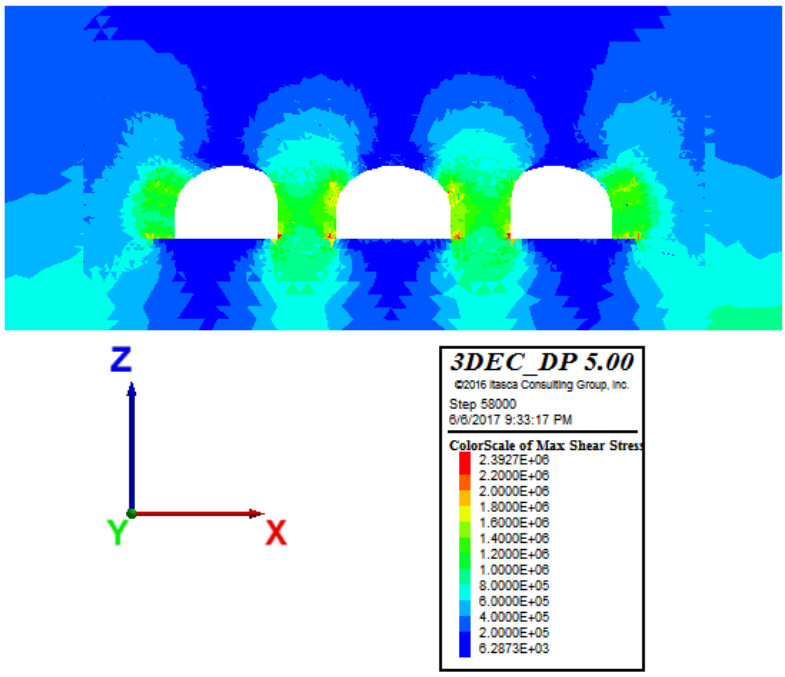

Figure 214. Model 26. Max shear stresses (Pa)

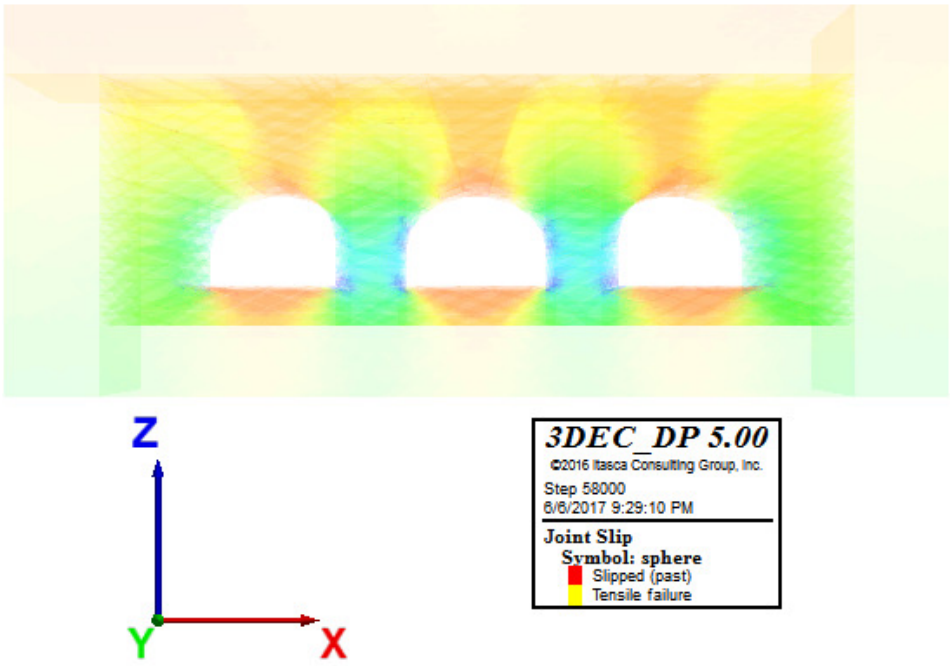

Figure 215. Model 26. Joint slip - Plasticity Limit indicator

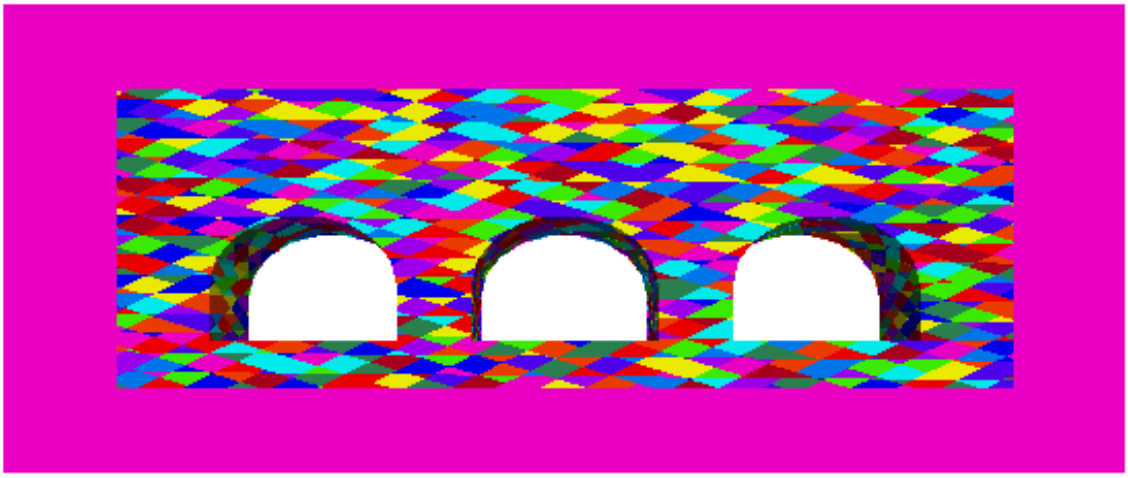

Figure 216. Model 27. Layout

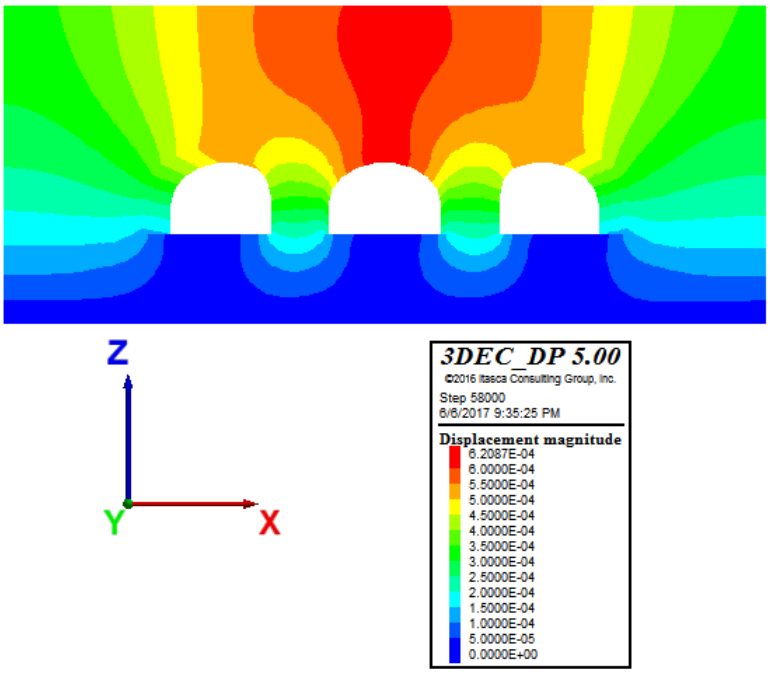

Figure 217. Model 27. Displacement magnitude (m)

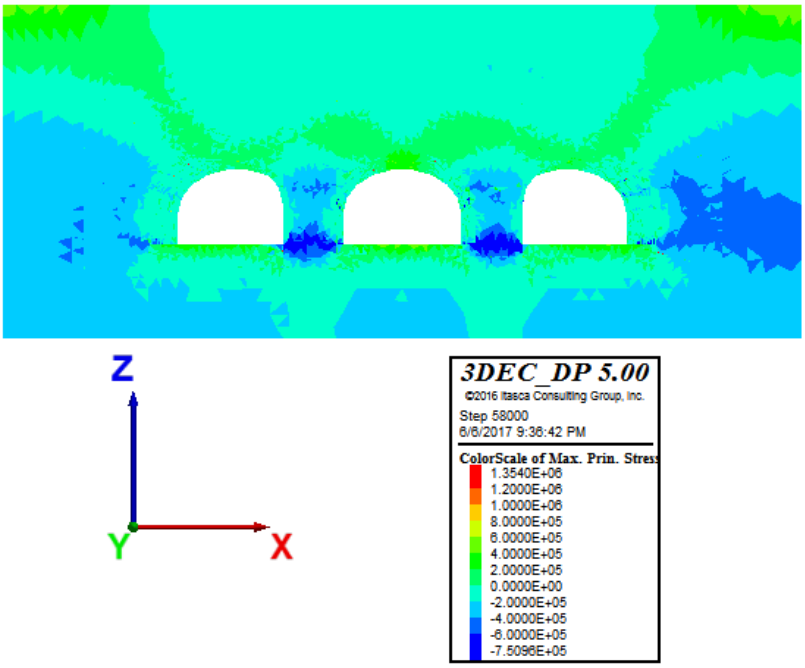

Figure 218. Model 27. Max. principal stresses (Pa)

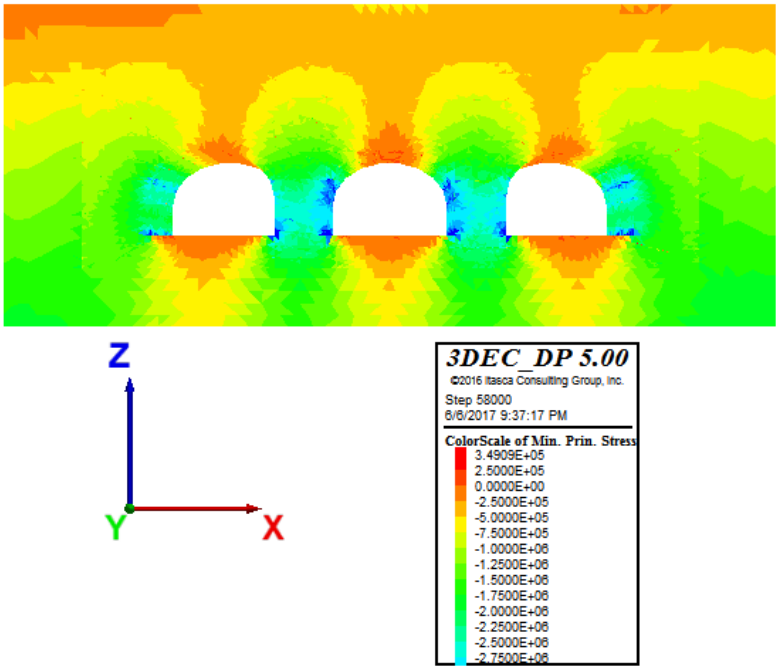

Figure 219. Model 27. Min. principal stresses (Pa)

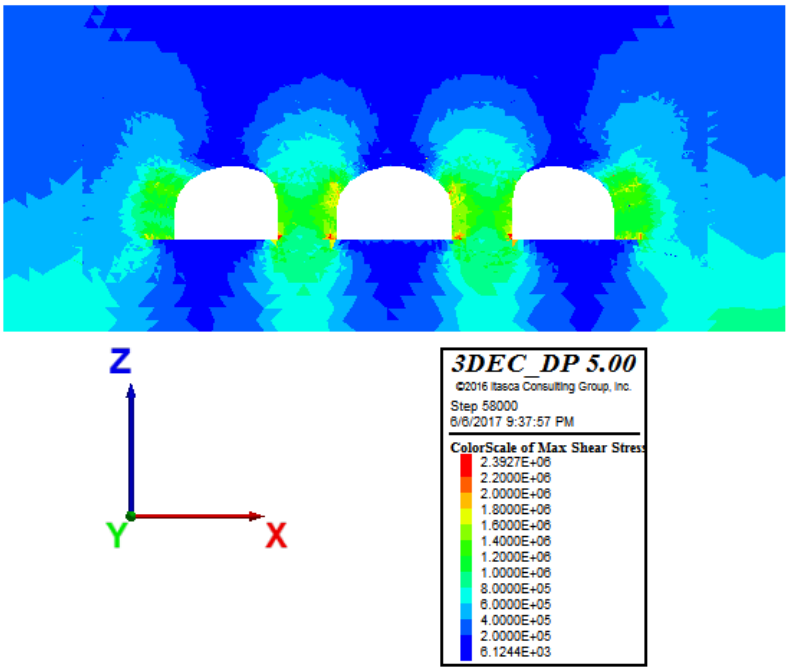

Figure 220. Model 27. Max shear stresses (Pa)

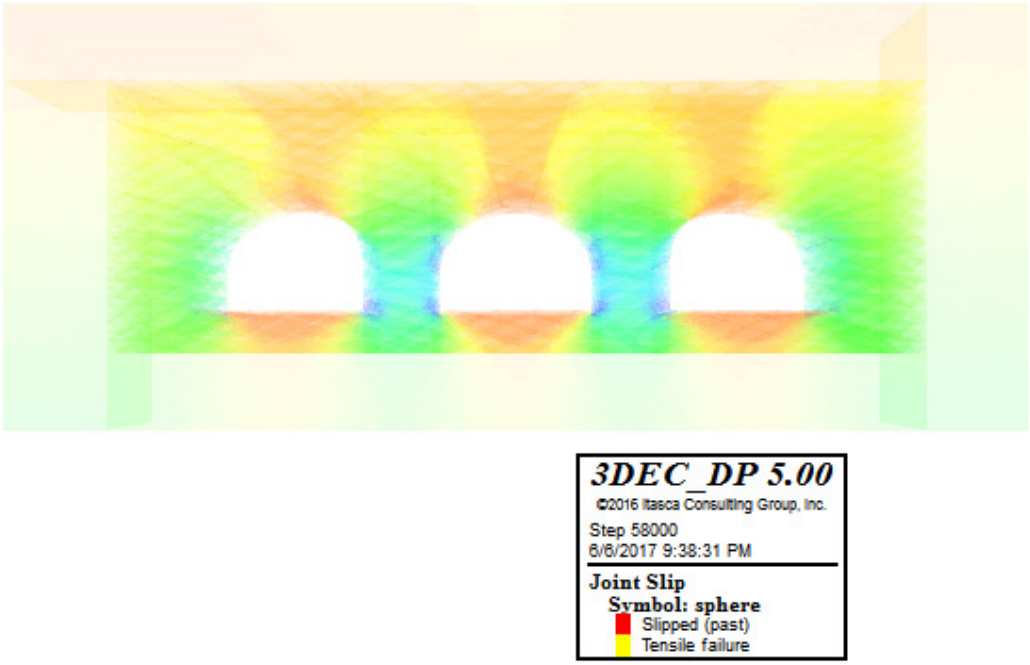

Figure 221. Model 27. Joint slip - Plasticity Limit indicator

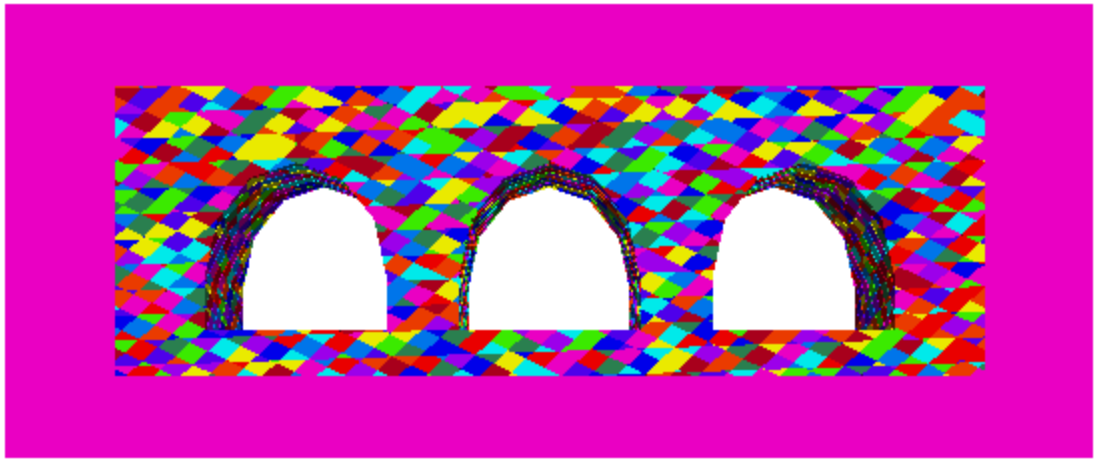

Figure 222. Model 28. Layout

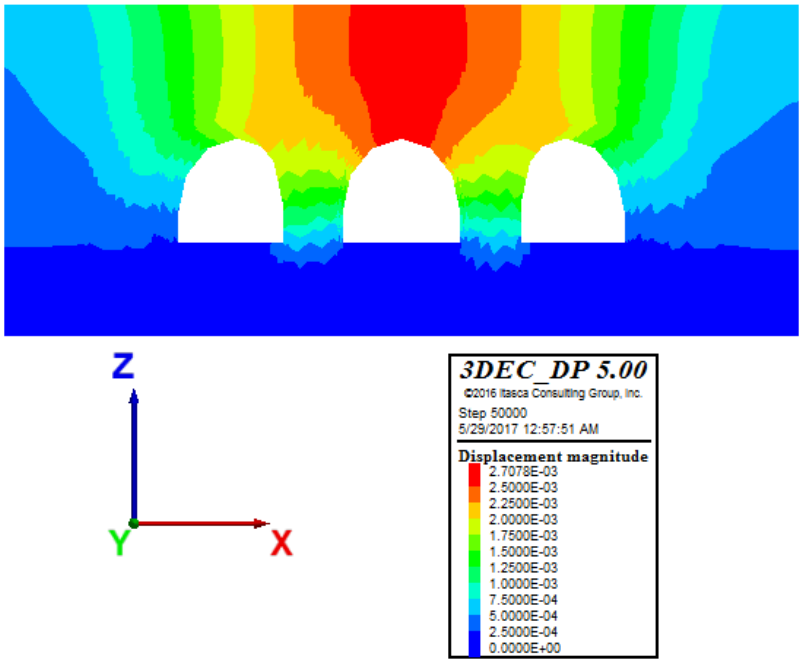

Figure 223. Model 28. Displacement magnitude (m)

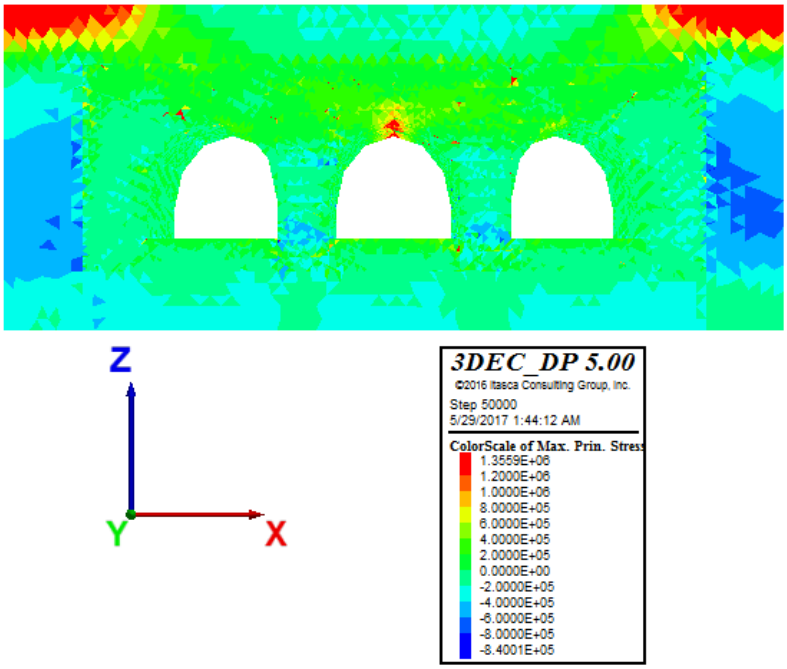

Figure 224. Model 28. Max. principal stresses (Pa)

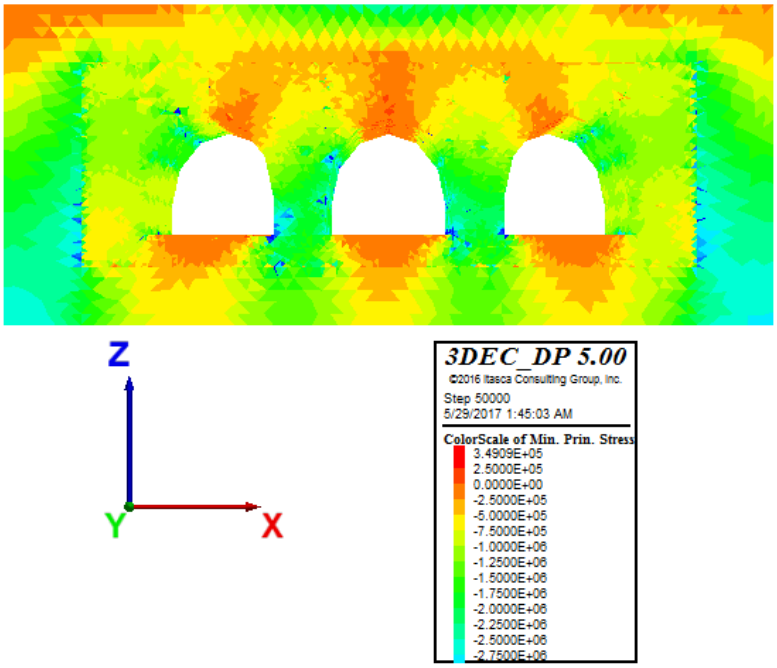

Figure 225. Model 28. Min. principal stresses (Pa)

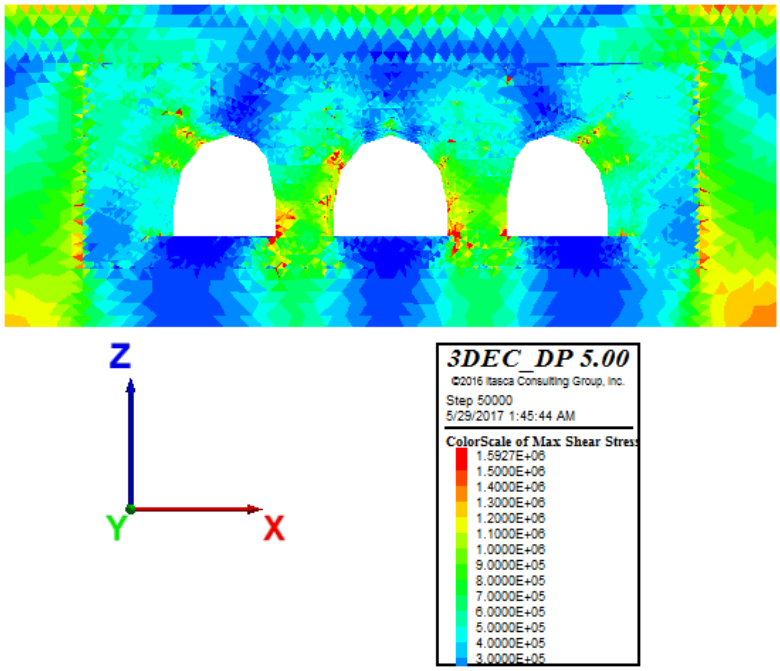

Figure 226. Model 28. Max shear stresses (Pa)

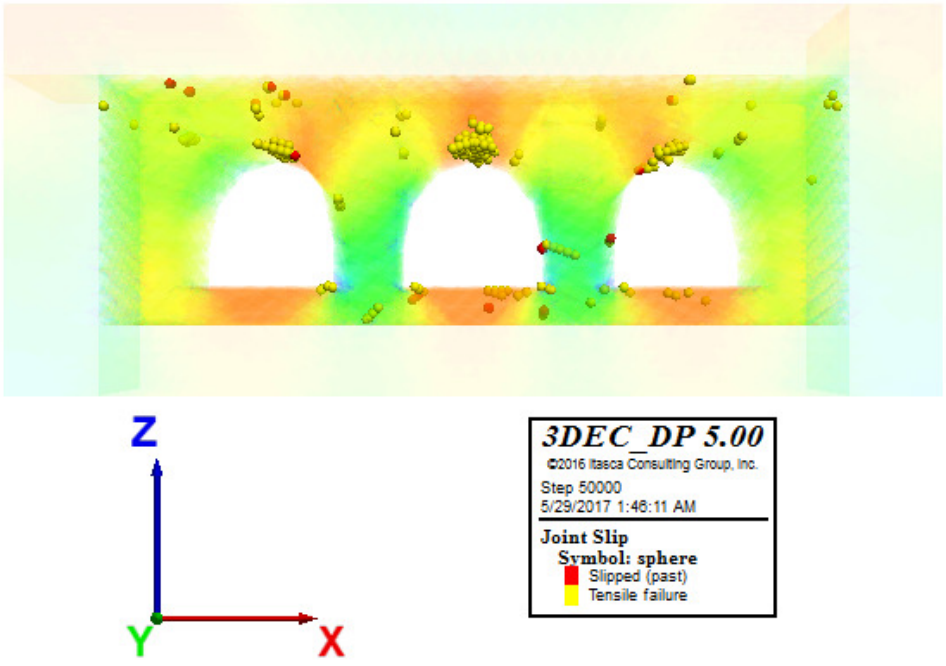

Figure 227. Model 28. Joint slip - Plasticity Limit indicator

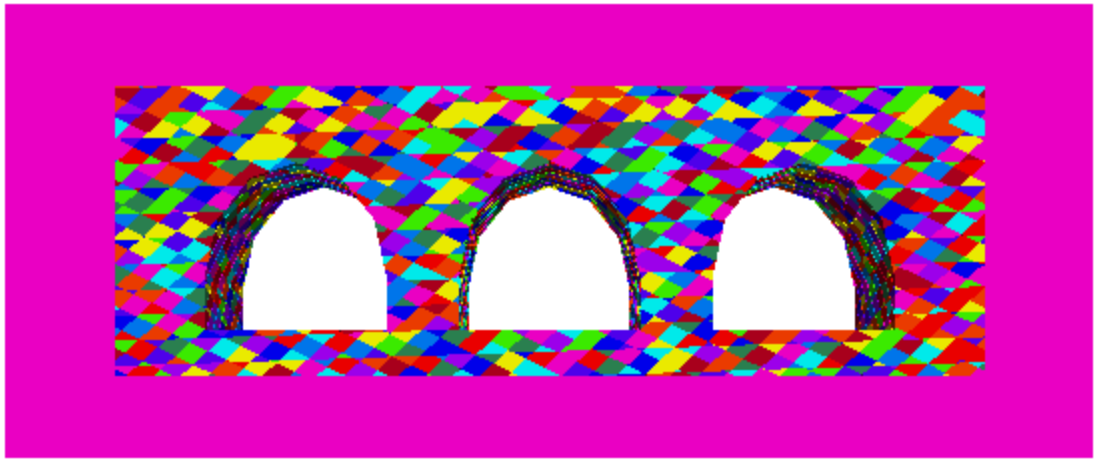

Figure 228. Model 29. Layout

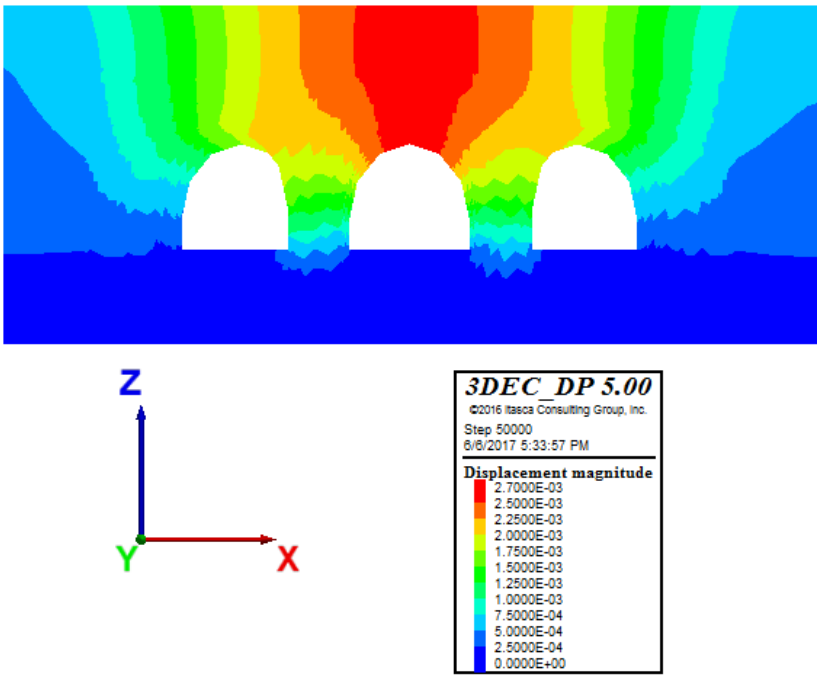

Figure 229. Model 29. Displacement magnitude (m)

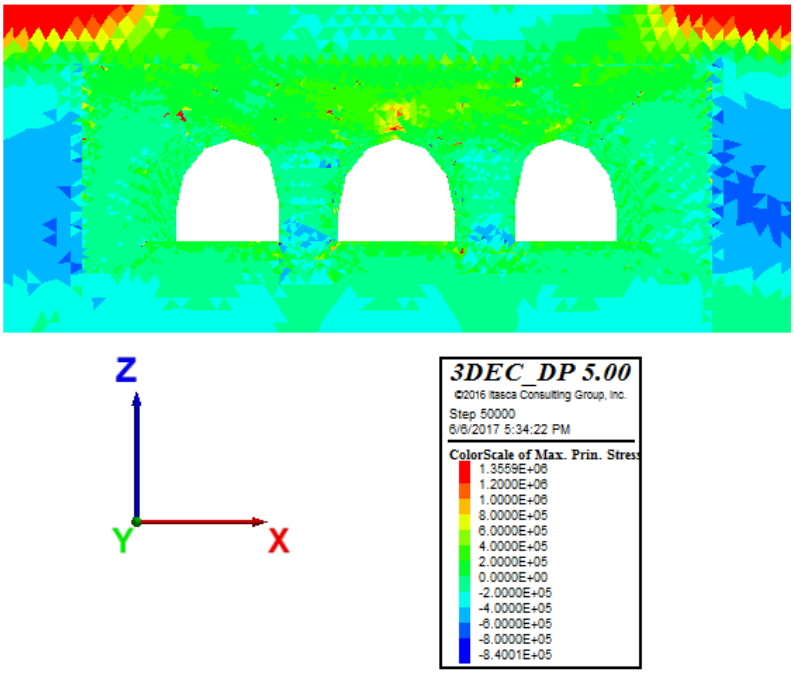

Figure 230. Model 29. Max. principal stresses (Pa)

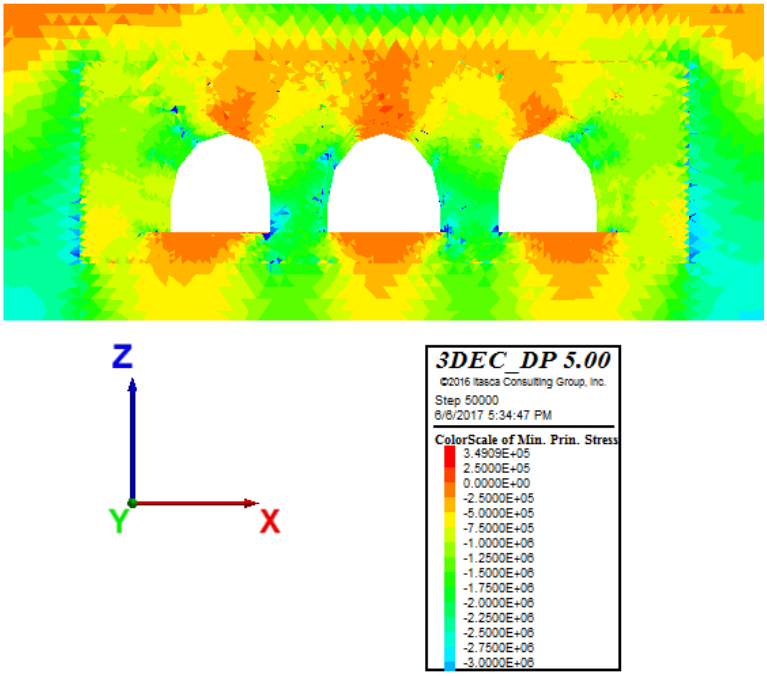

Figure 231. Model 29. Min. principal stresses (Pa)

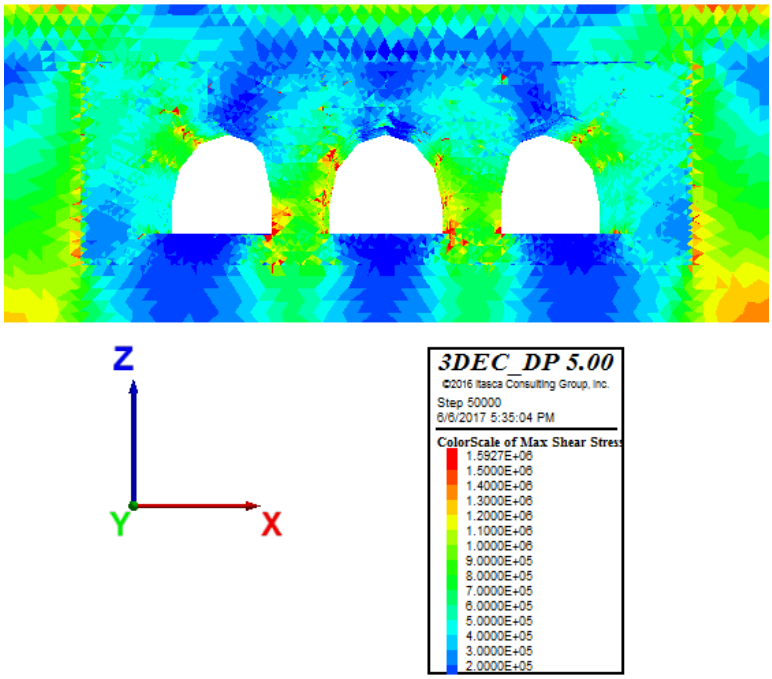

Figure 232. Model 29. Max shear stresses (Pa)

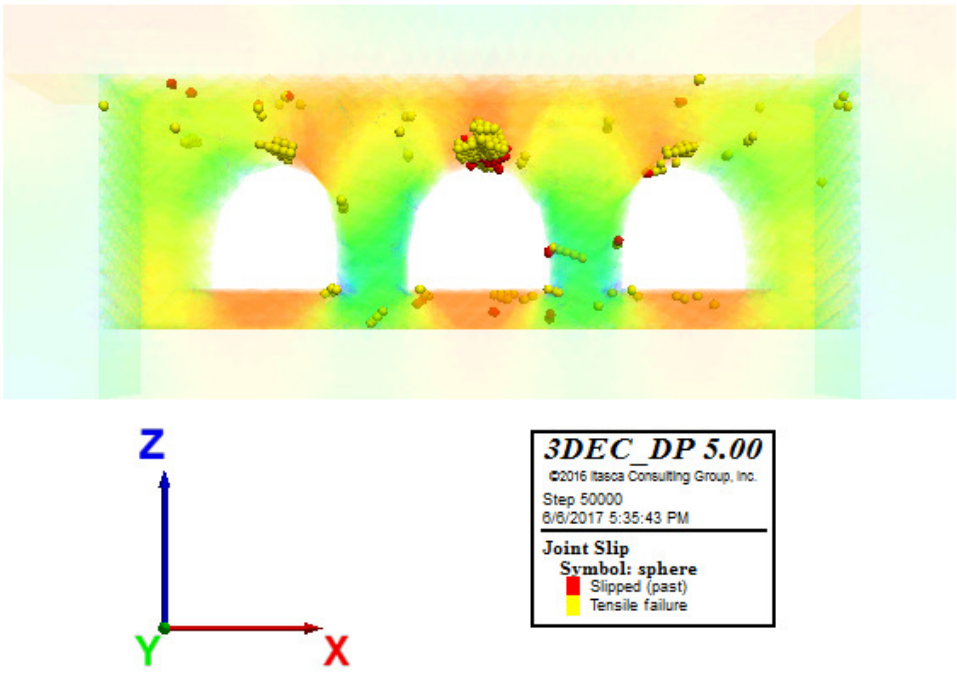

Figure 233. Model 29. Joint slip - Plasticity Limit indicator

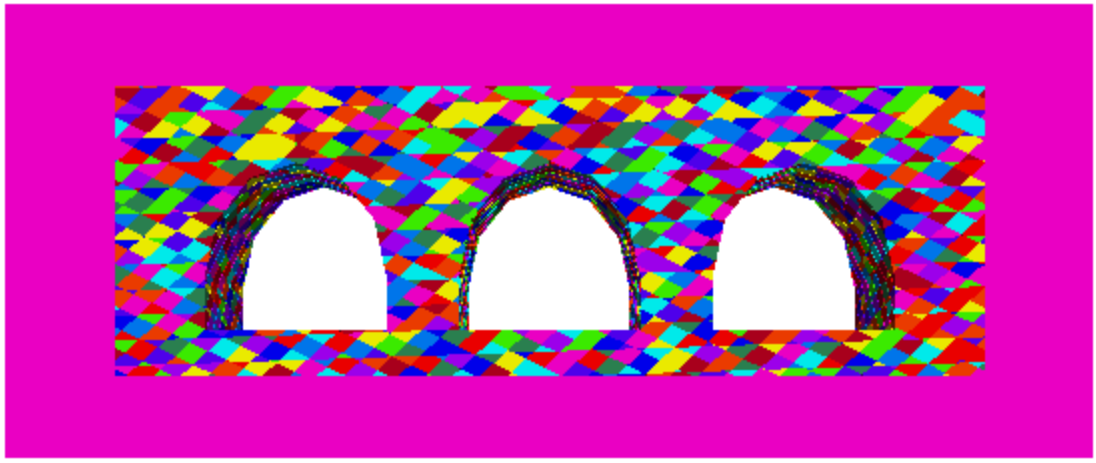

Figure 234. Model 30. Layout

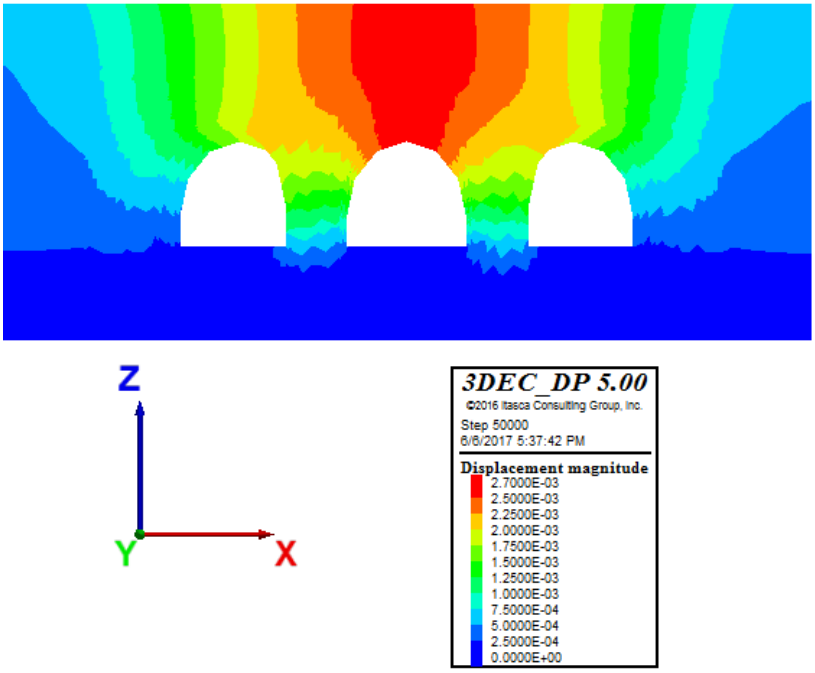

Figure 235. Model 30. Displacement magnitude (m)

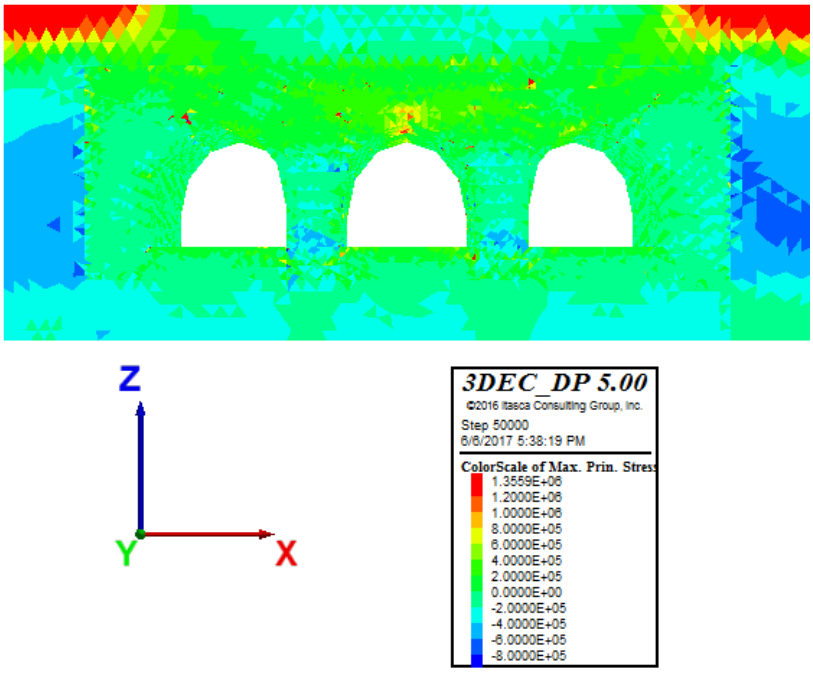

Figure 236. Model 30. Max. principal stresses (Pa)

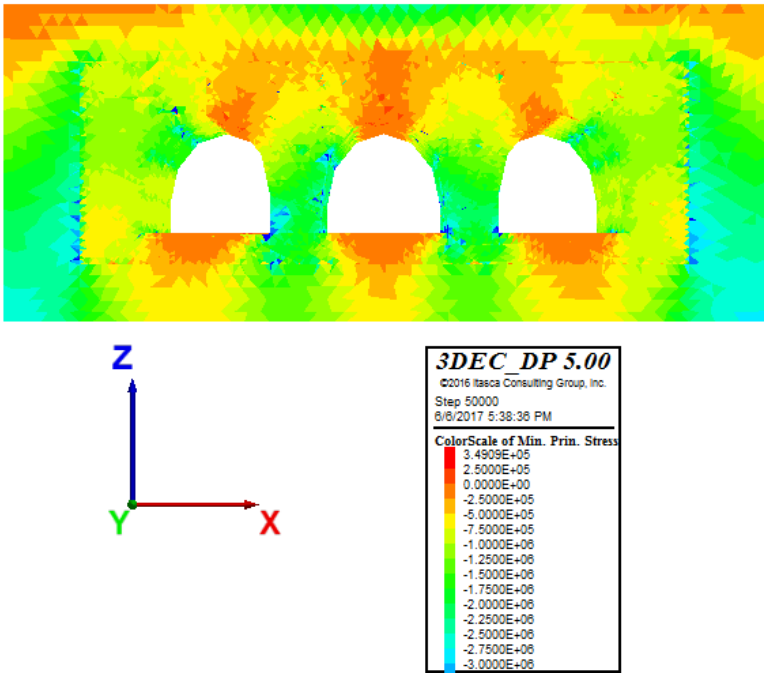

Figure 237. Model 30. Min. principal stresses (Pa)

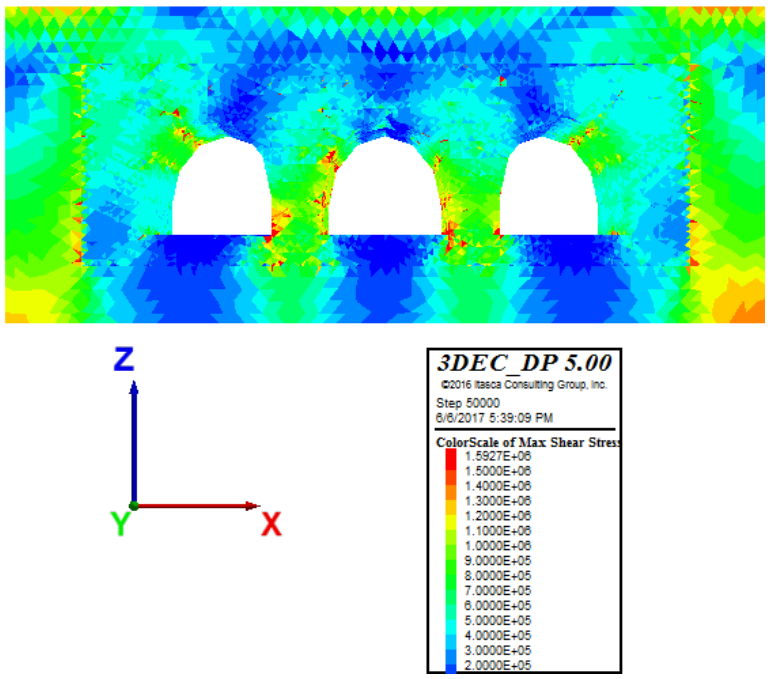

Figure 238. Model 30. Max shear stresses (Pa)

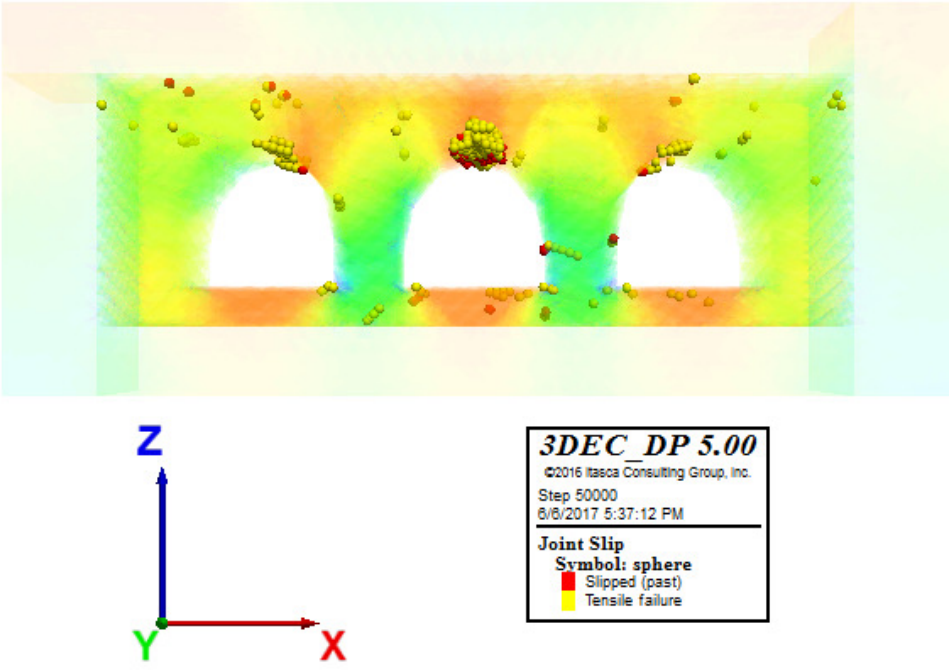

Figure 239. Model 30. Joint slip - Plasticity Limit indicator

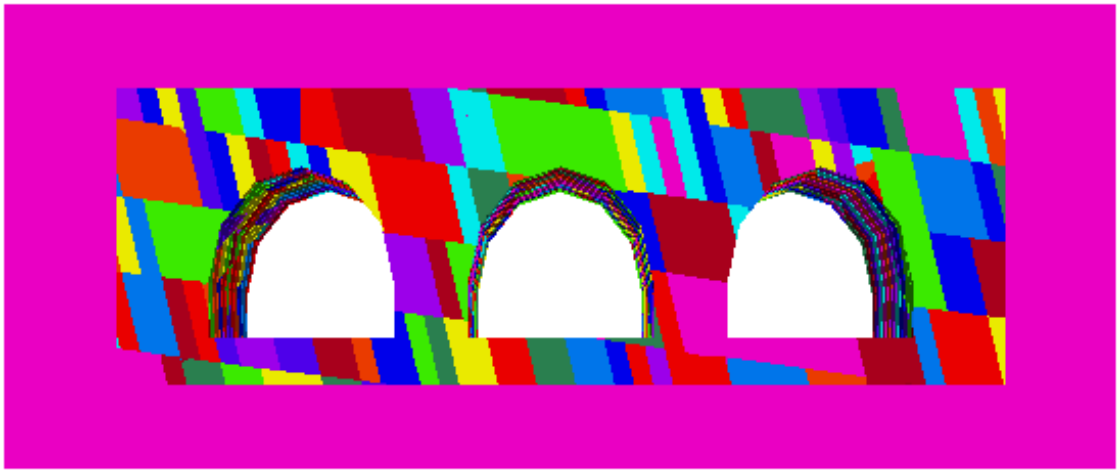

Figure 240. Model 31. Layout

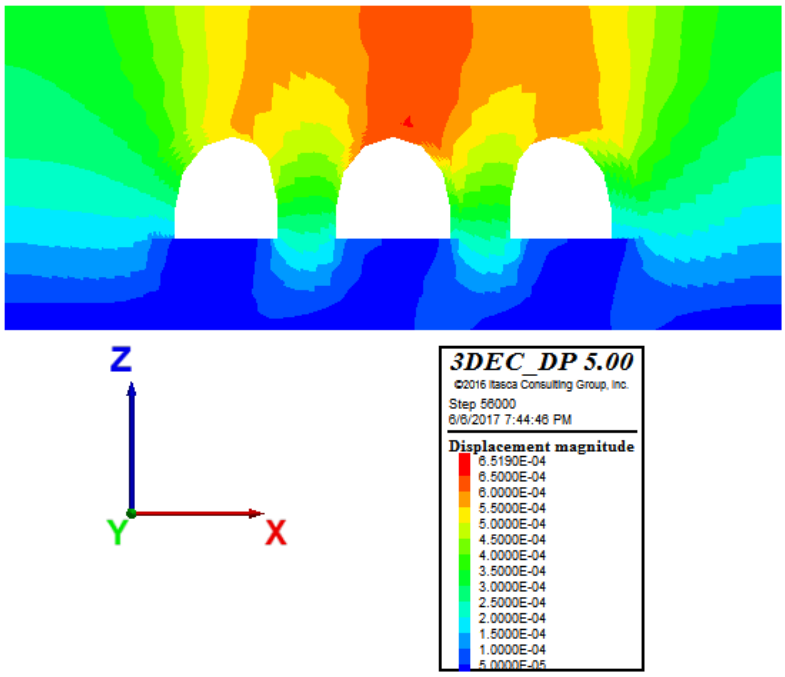

Figure 241. Model 31. Displacement magnitude (m)

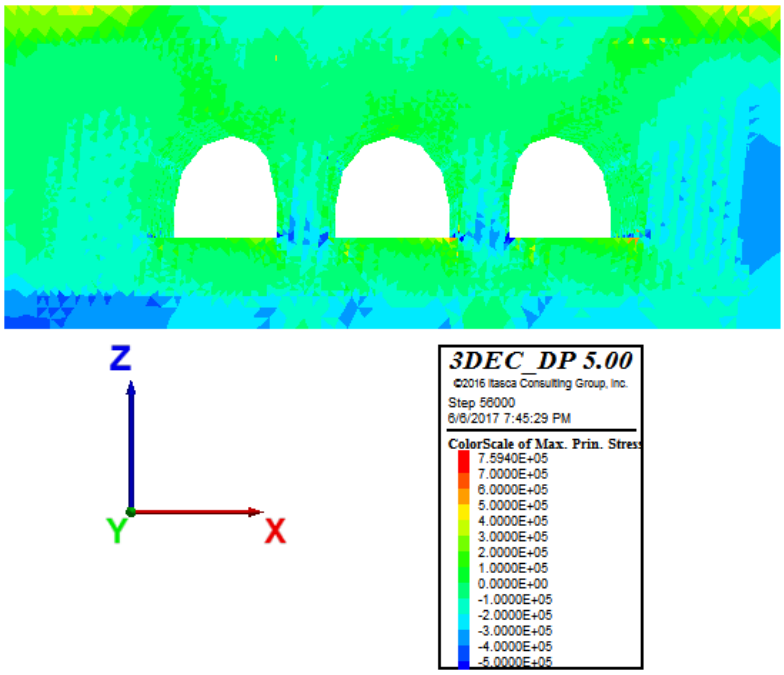

Figure 242. Model 31. Max. principal stresses (Pa)

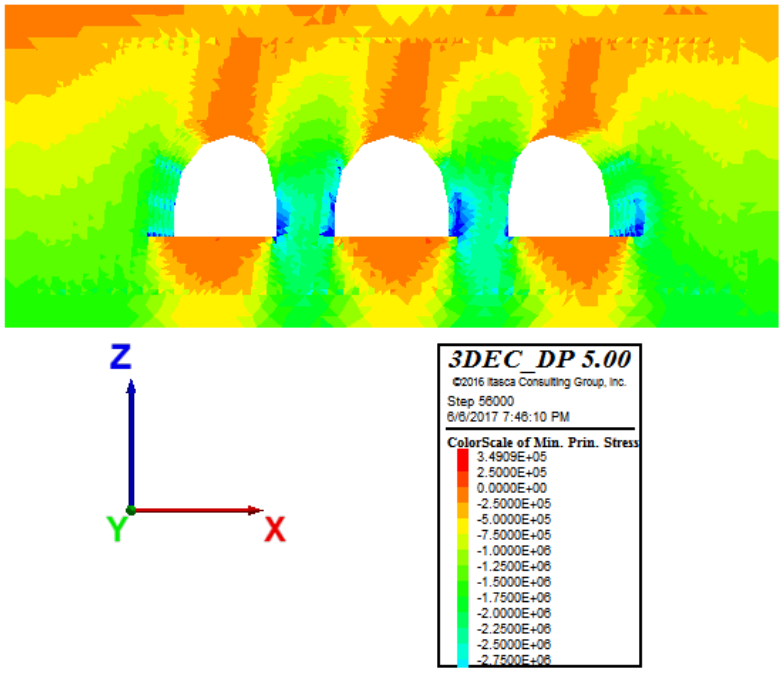

Figure 243. Model 31. Min. principal stresses (Pa)

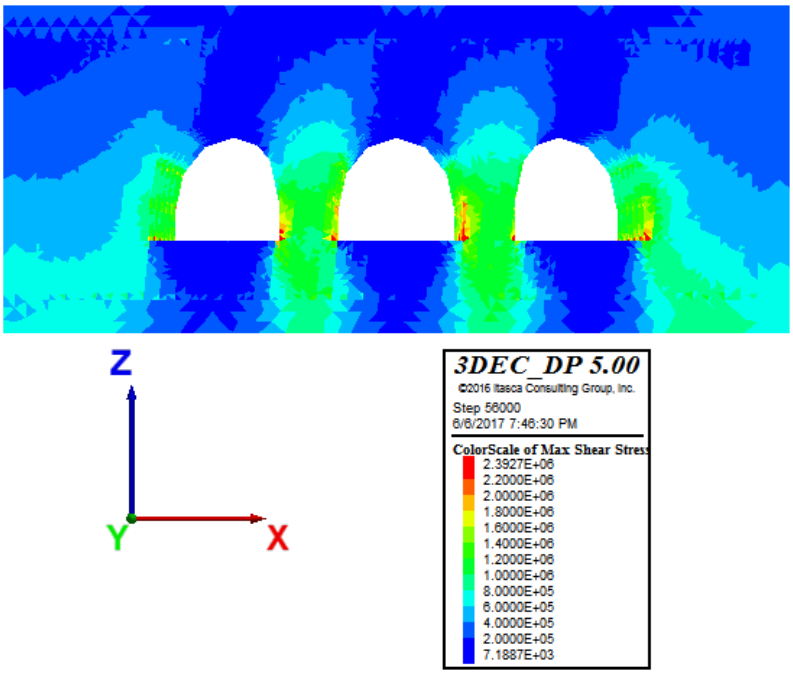

Figure 244. Model 31. Max shear stresses (Pa)

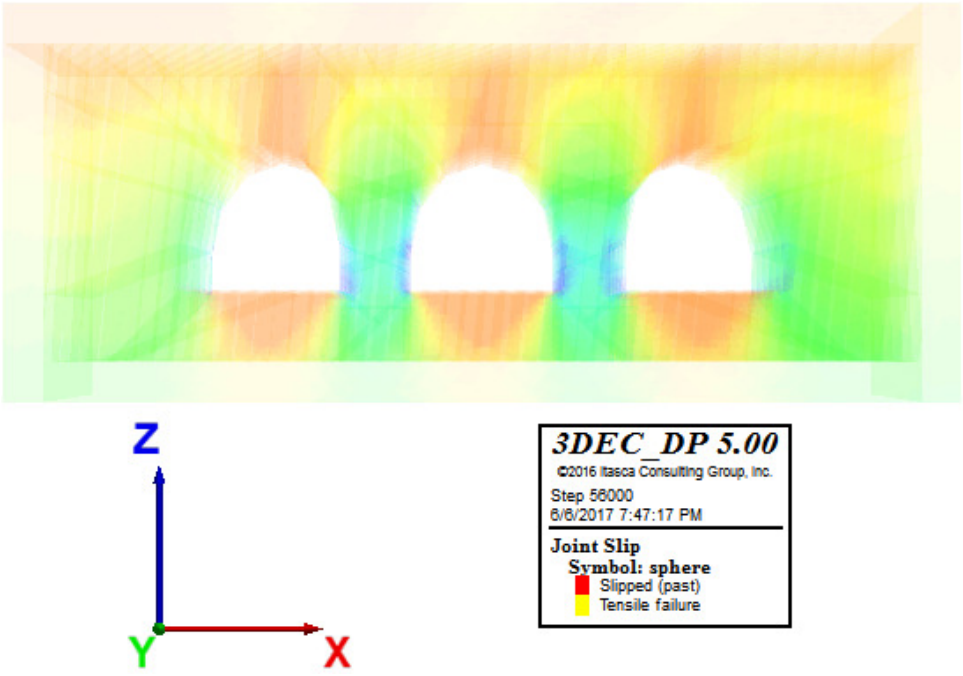

Figure 245. Model 31. Joint slip - Plasticity Limit indicator

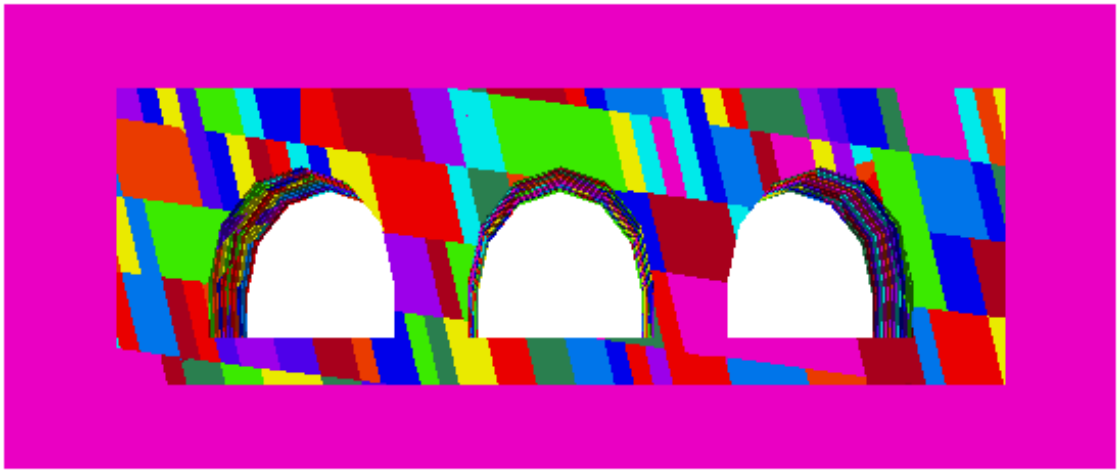

Figure 246. Model 32. Layout

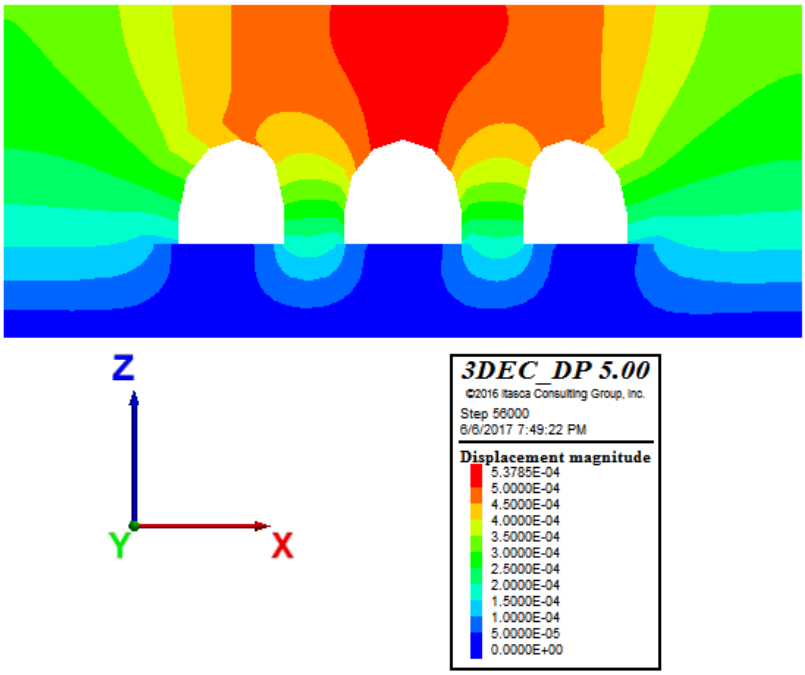

Figure 247. Model 32. Displacement magnitude (m)

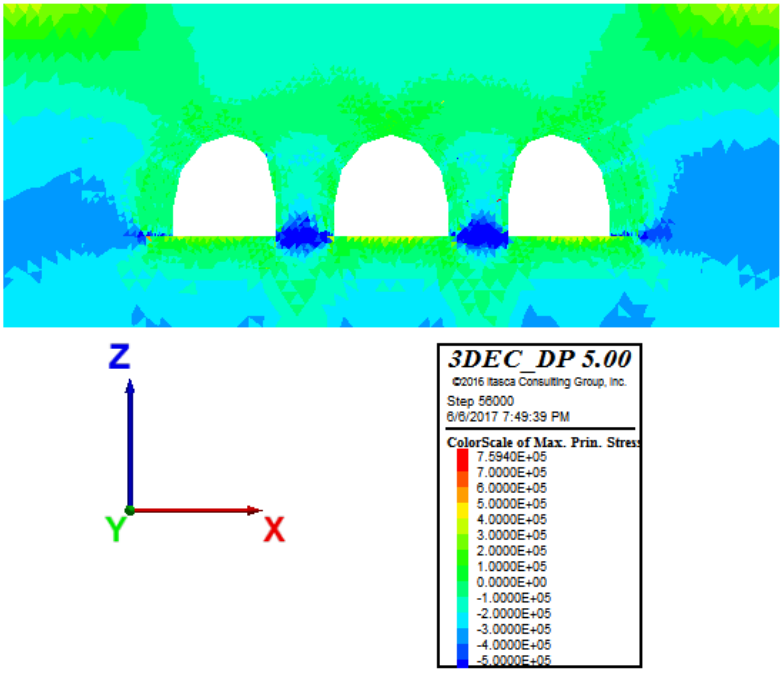

Figure 248. Model 32. Max. principal stresses (Pa)

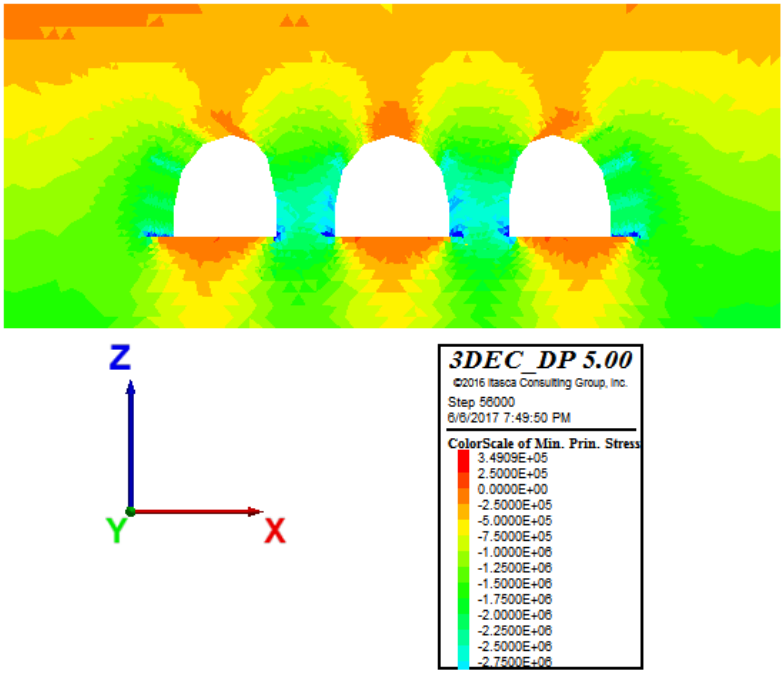

Figure 249. Model 32. Min. principal stresses (Pa)

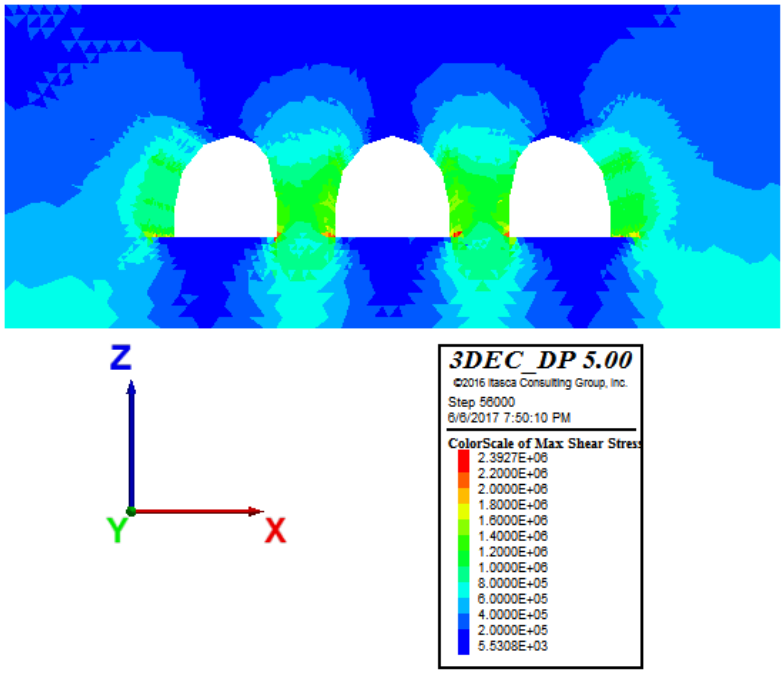

Figure 250. Model 32. Max shear stresses (Pa)

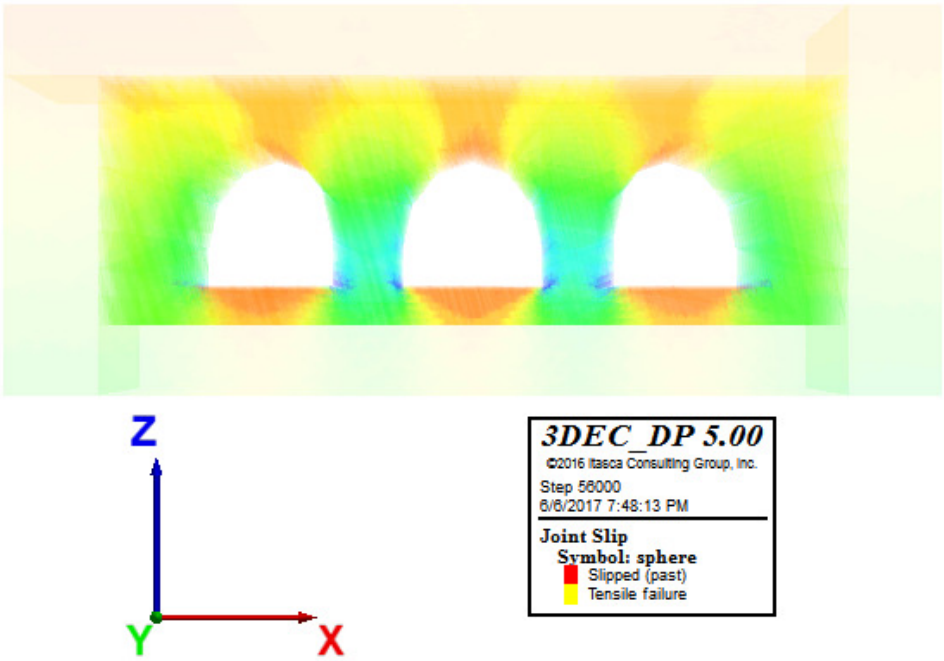

Figure 251. Model 32. Joint slip - Plasticity Limit indicator

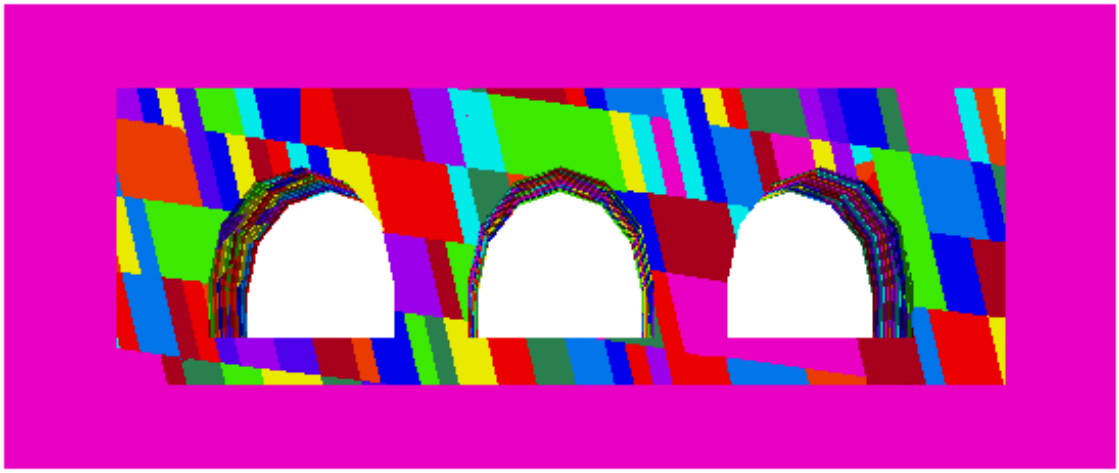

Figure 252. Model 33. Layout

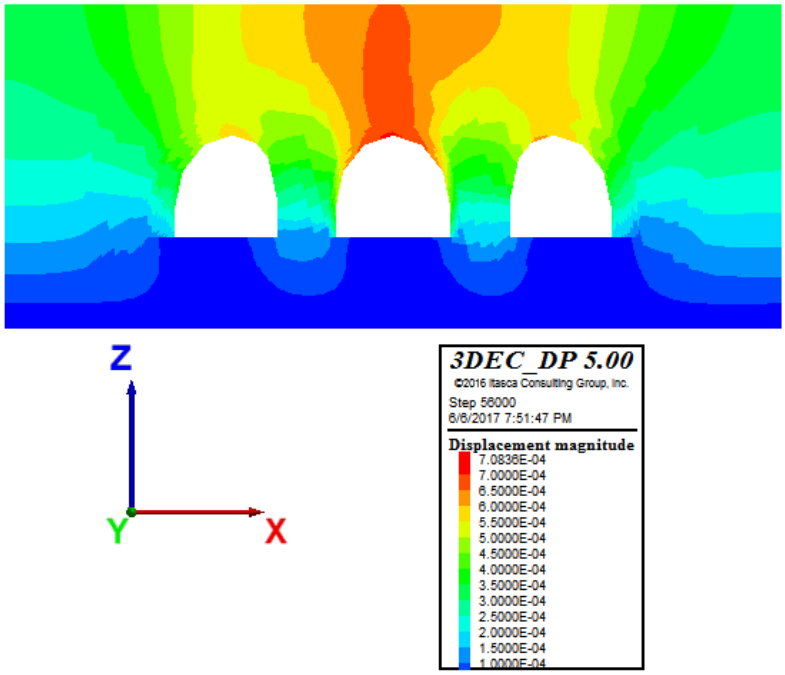

Figure 253. Model 33. Displacement magnitude (m)

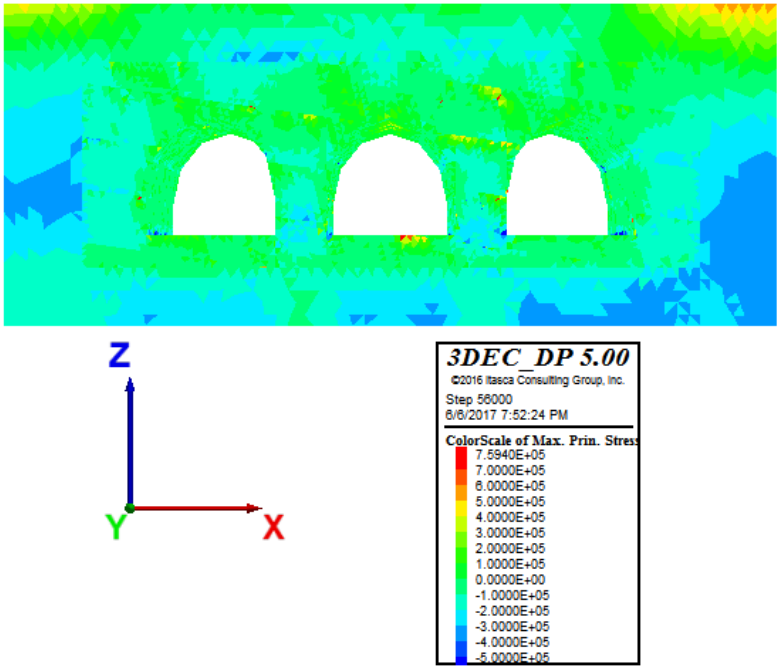

Figure 254. Model 33. Max. principal stresses (Pa)

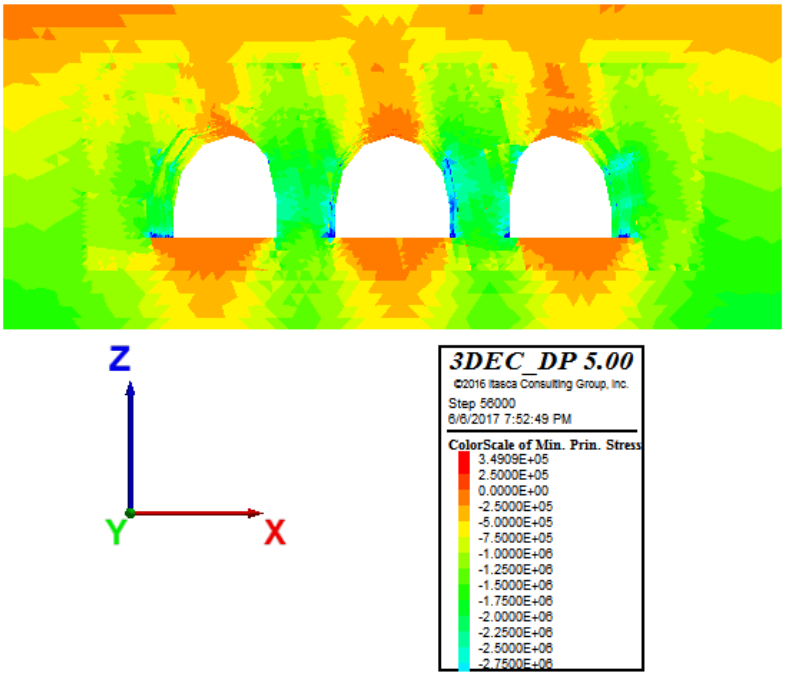

Figure 255. Model 33. Min. principal stresses (Pa)

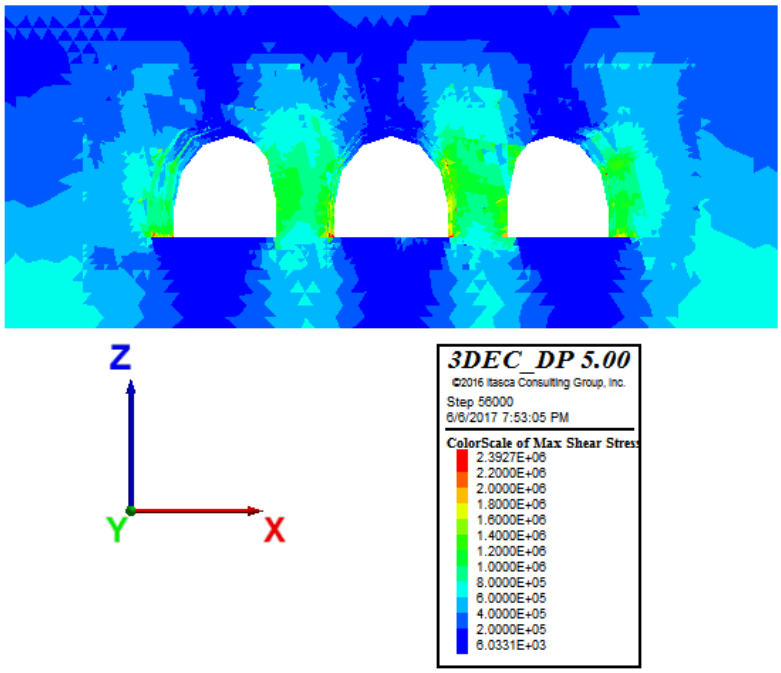

Figure 256. Model 3. Max shear stresses (Pa)

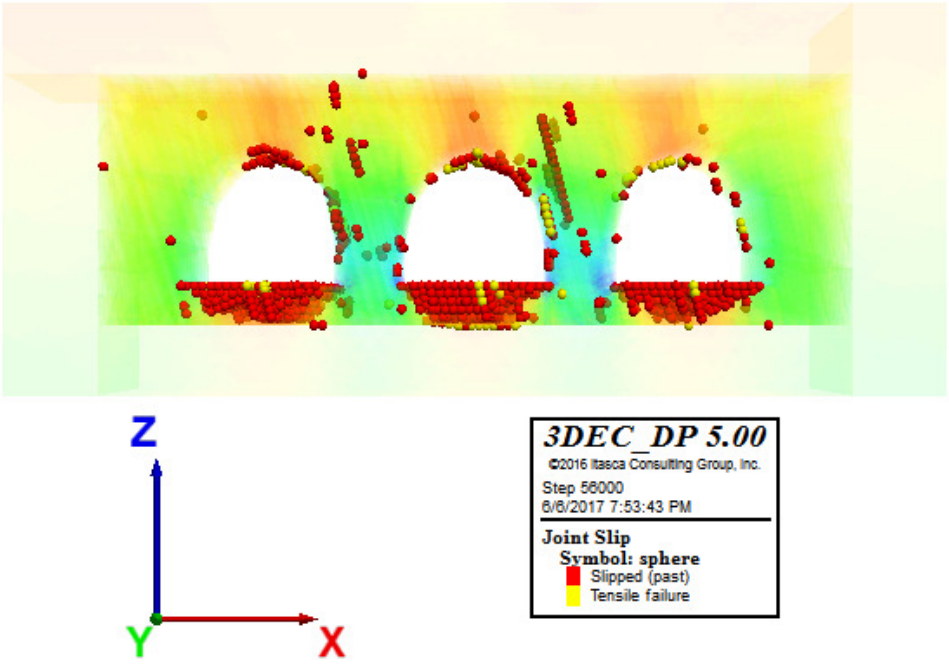

Figure 257. Model 33. Joint slip - Plasticity Limit indicator

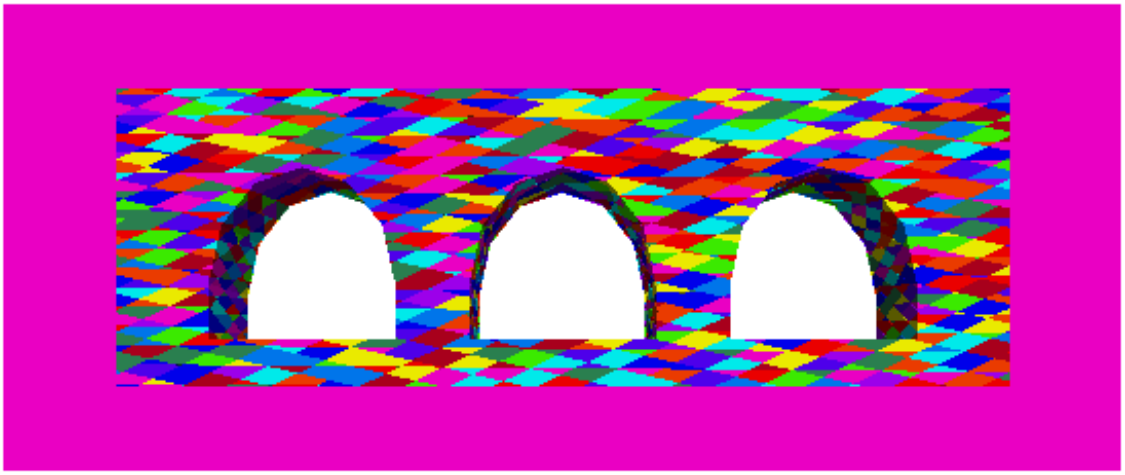

Figure 258. Model 34. Layout

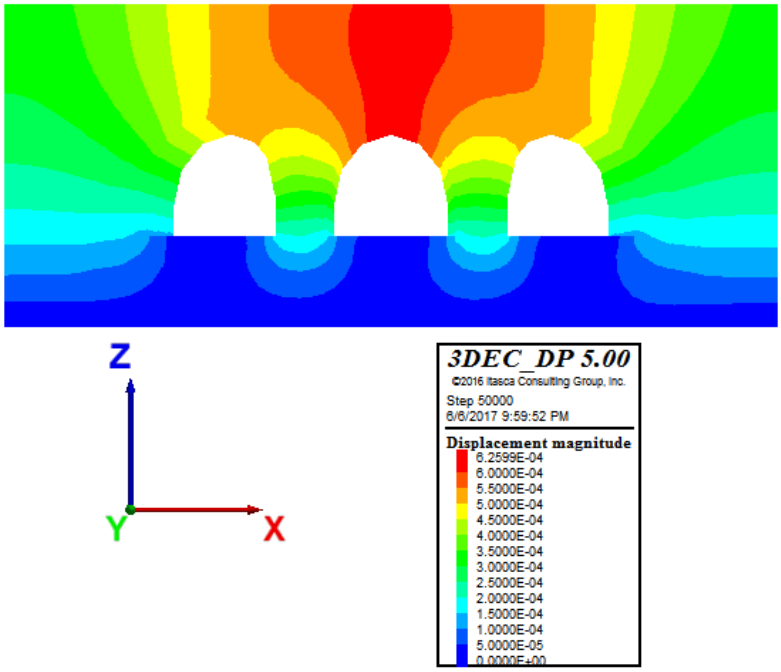

Figure 259. Model 34. Displacement magnitude (m)

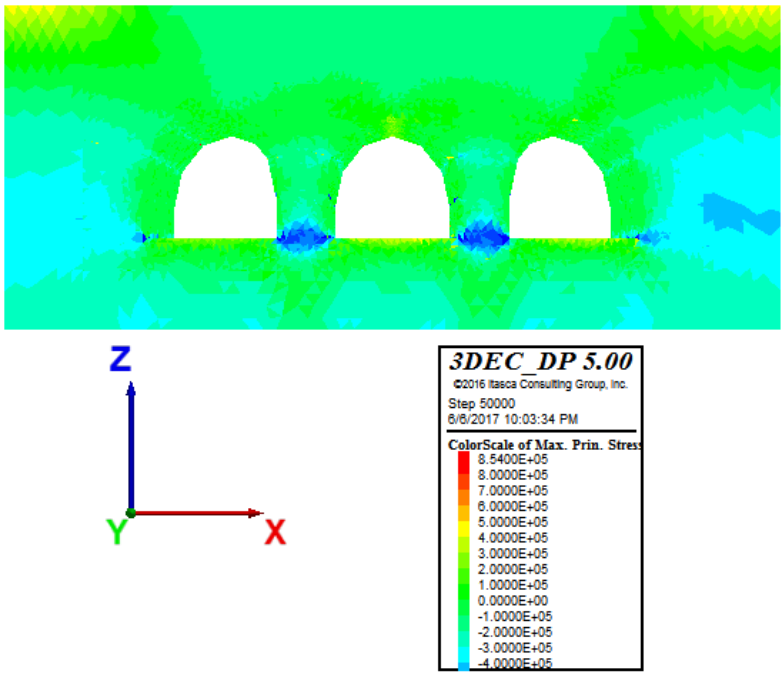

Figure 260. Model 34. Max. principal stresses (Pa)

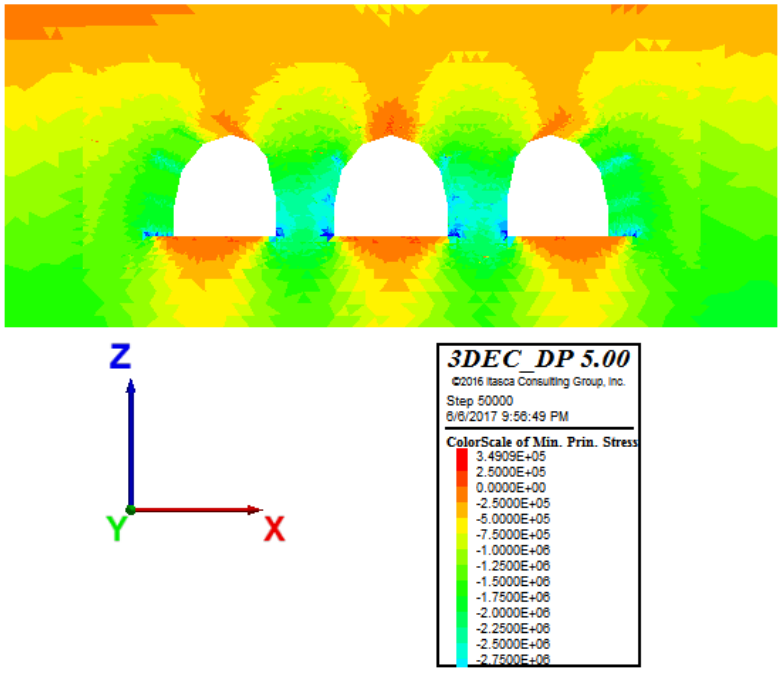

Figure 261. Model 34. Min. principal stresses (Pa)

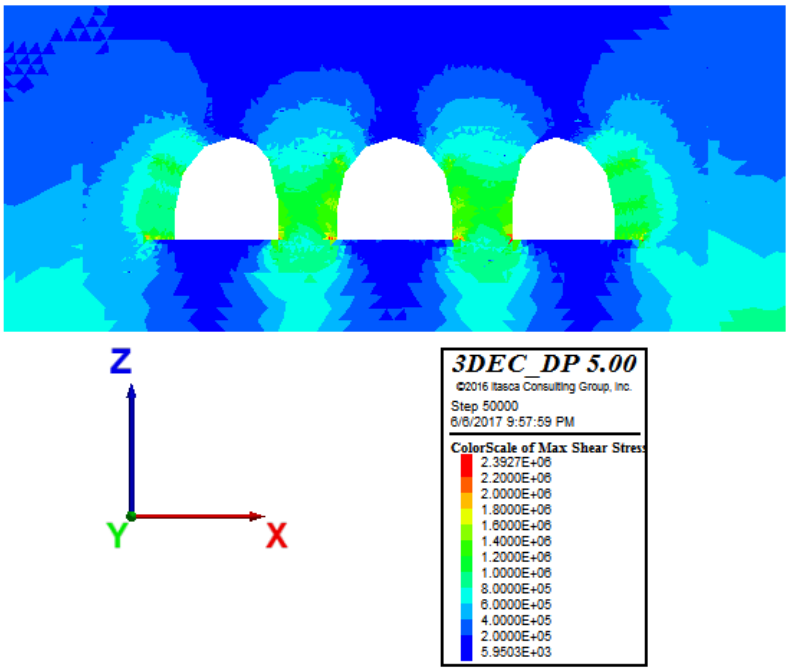

Figure 262. Model 34. Max shear stresses (Pa)

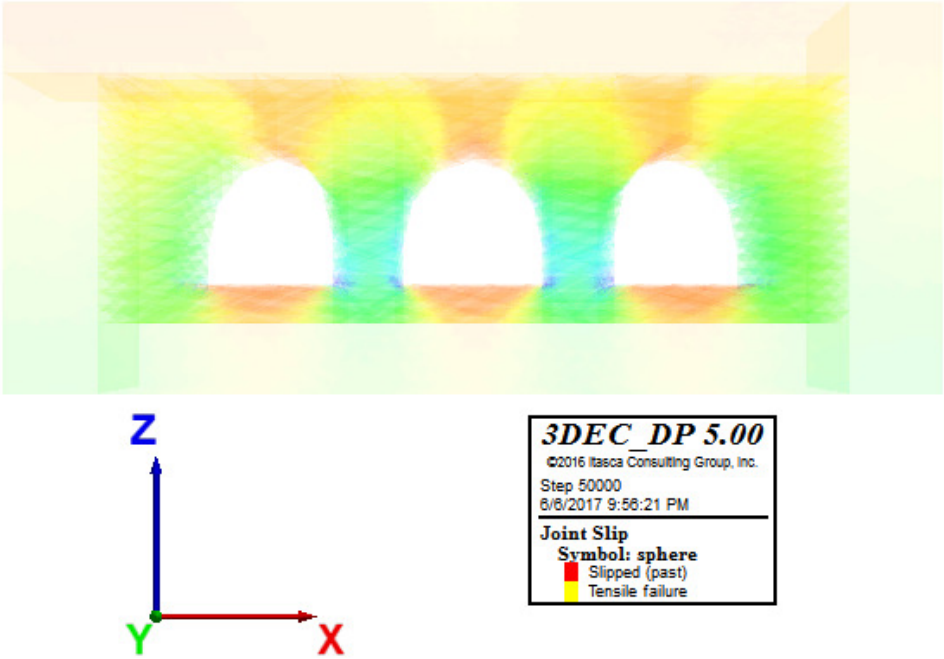

Figure 263. Model 34. Joint slip - Plasticity Limit indicator

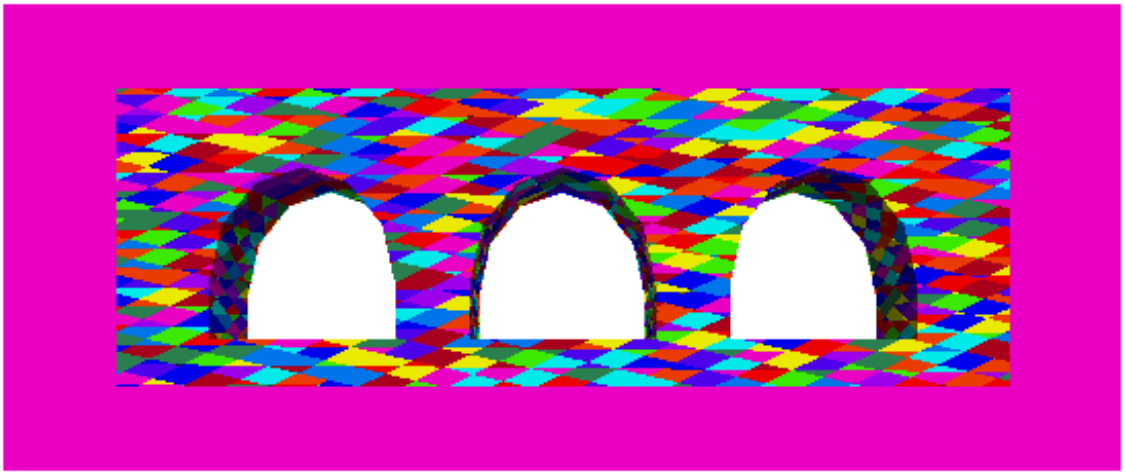

Figure 264. Model 35. Layout

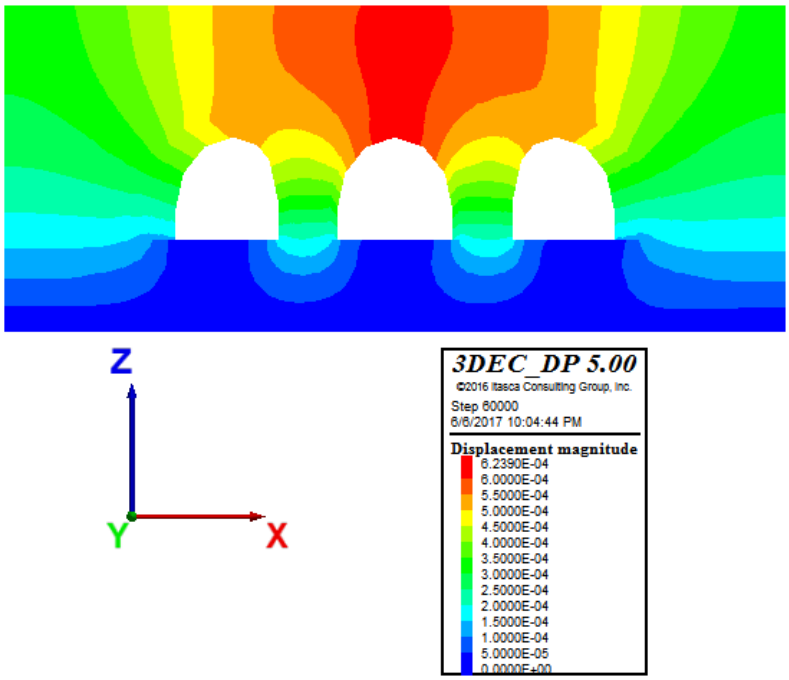

Figure 265. Model 35. Displacement magnitude (m)

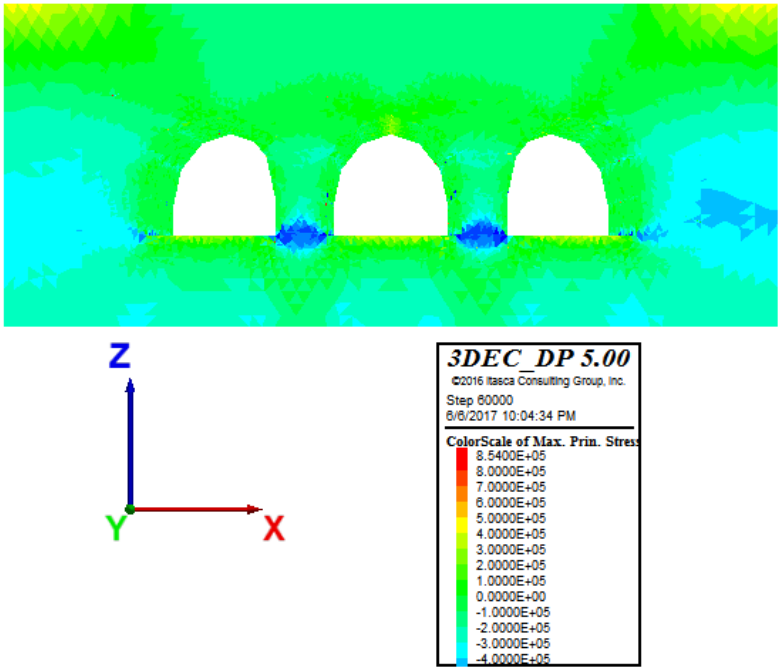

Figure 266. Model 35. Max. principal stresses (Pa)

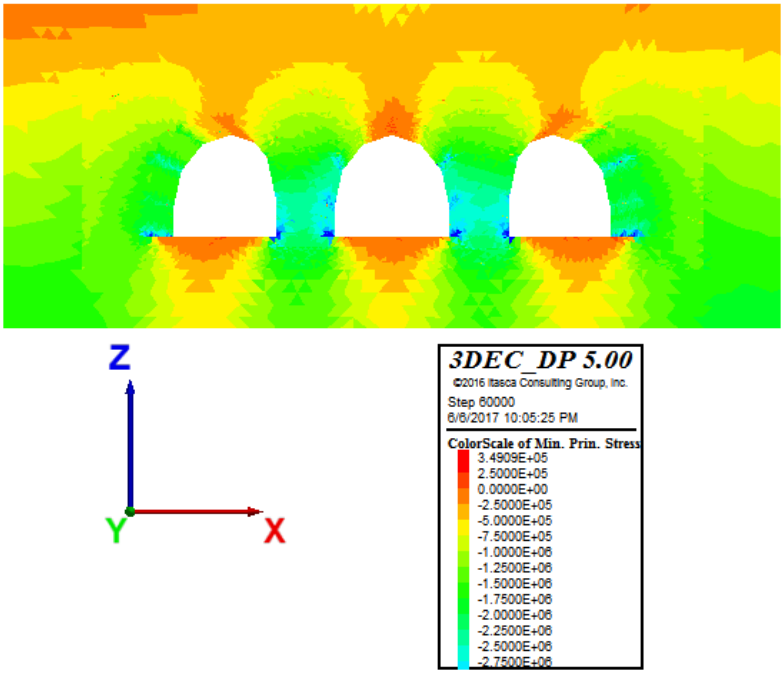

Figure 267. Model 35. Min. principal stresses (Pa)

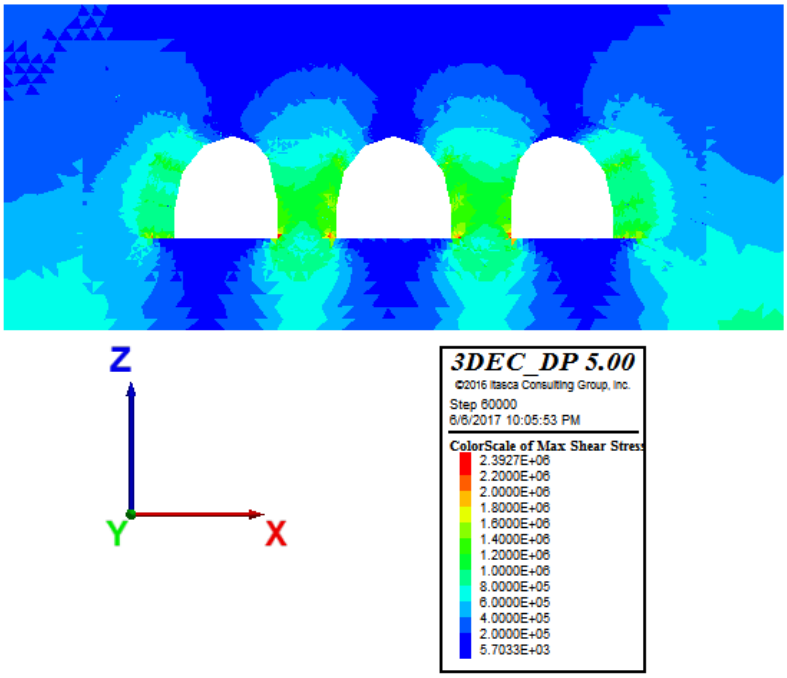

Figure 268. Model 35. Max shear stresses (Pa)

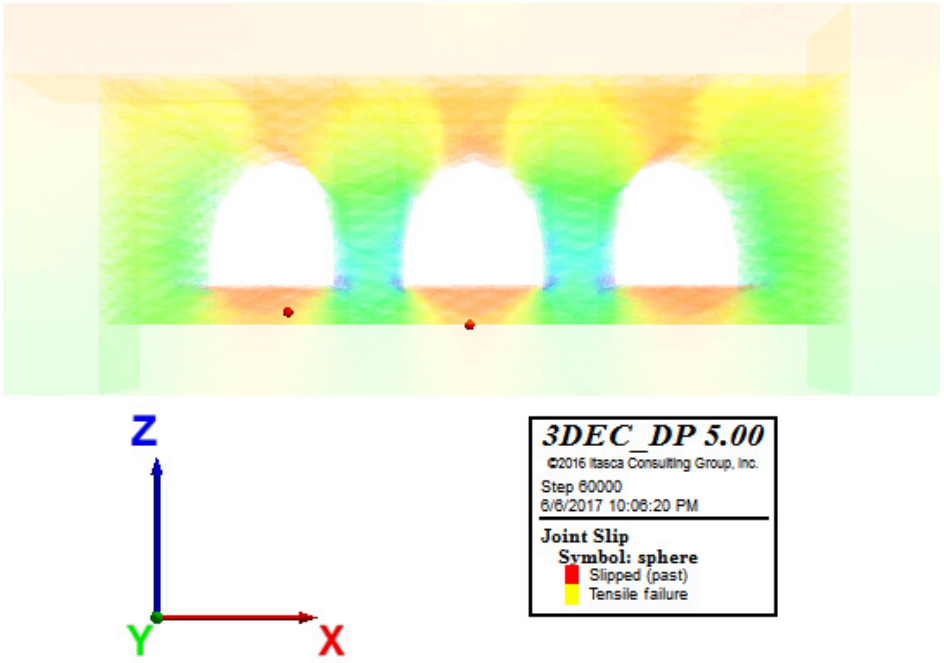

Figure 269. Model 35. Joint slip - Plasticity Limit indicator

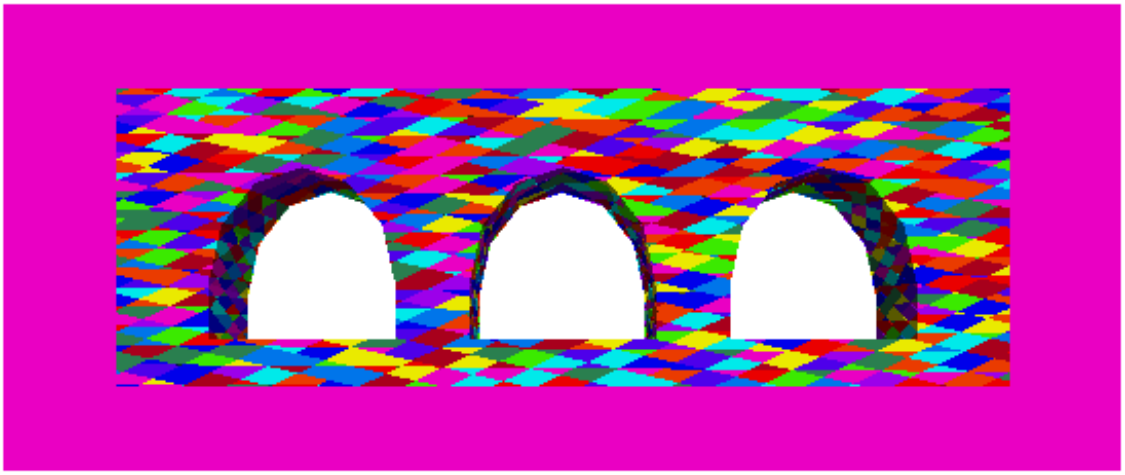

Figure 270. Model 36. Layout

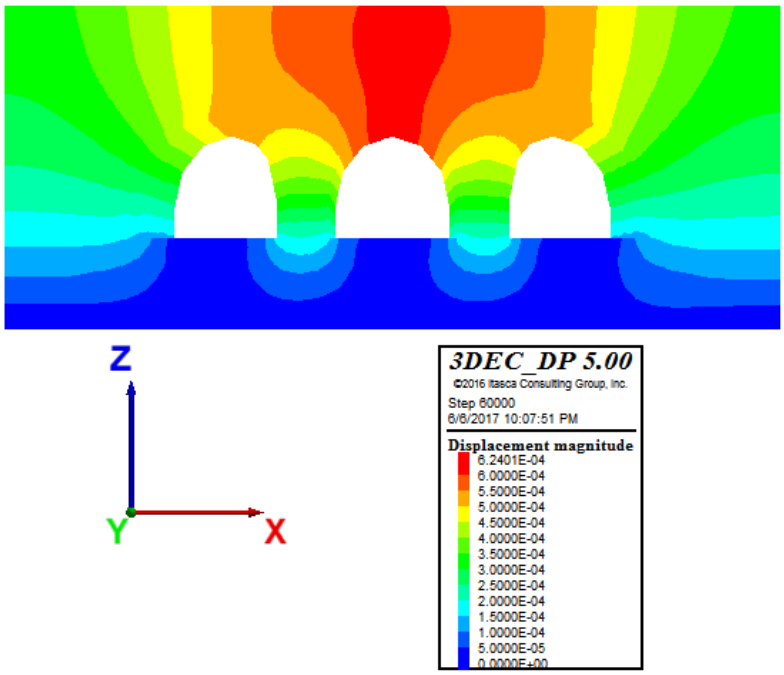

Figure 271. Model 36. Displacement magnitude (m)

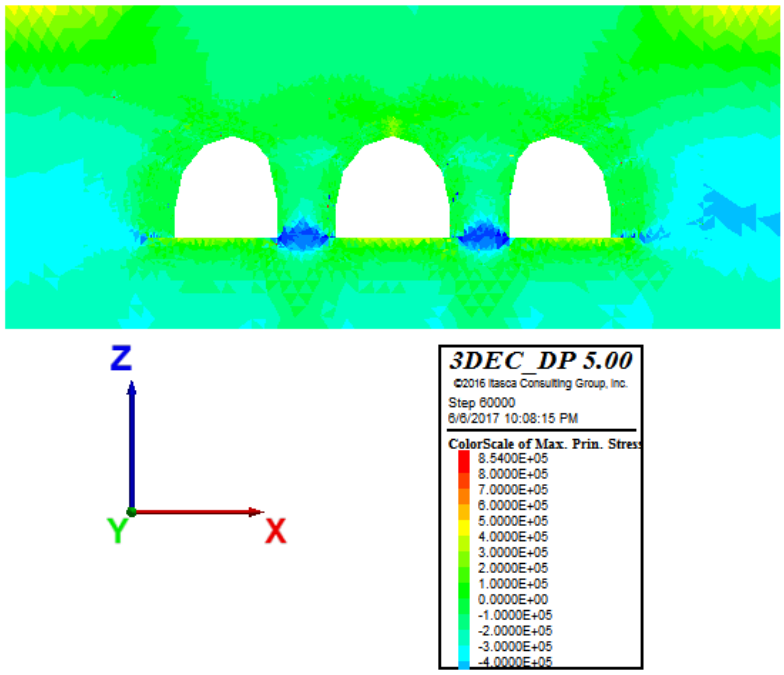

Figure 272. Model 36. Max. principal stresses (Pa)

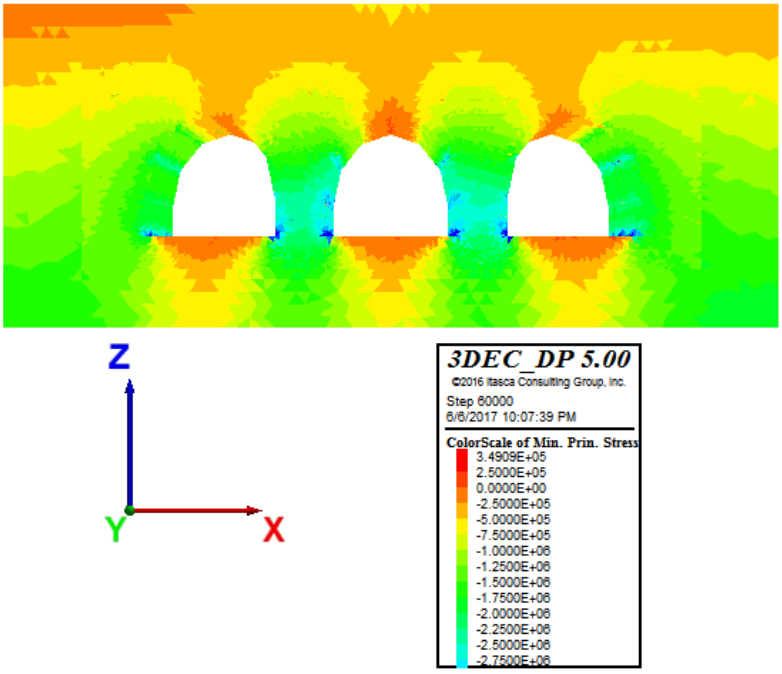

Figure 273. Model 36. Min. principal stresses (Pa)

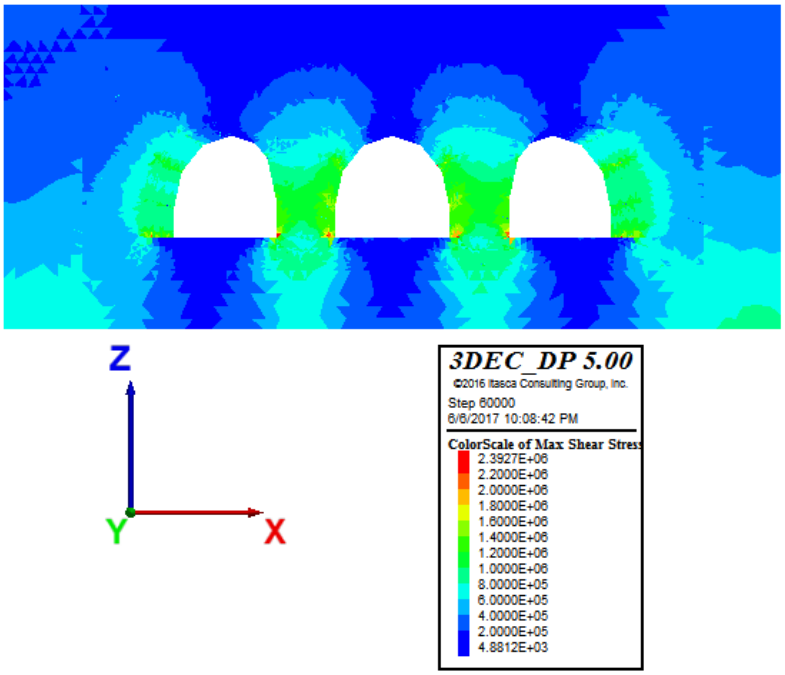

Figure 274. Model 36. Max shear stresses (Pa)

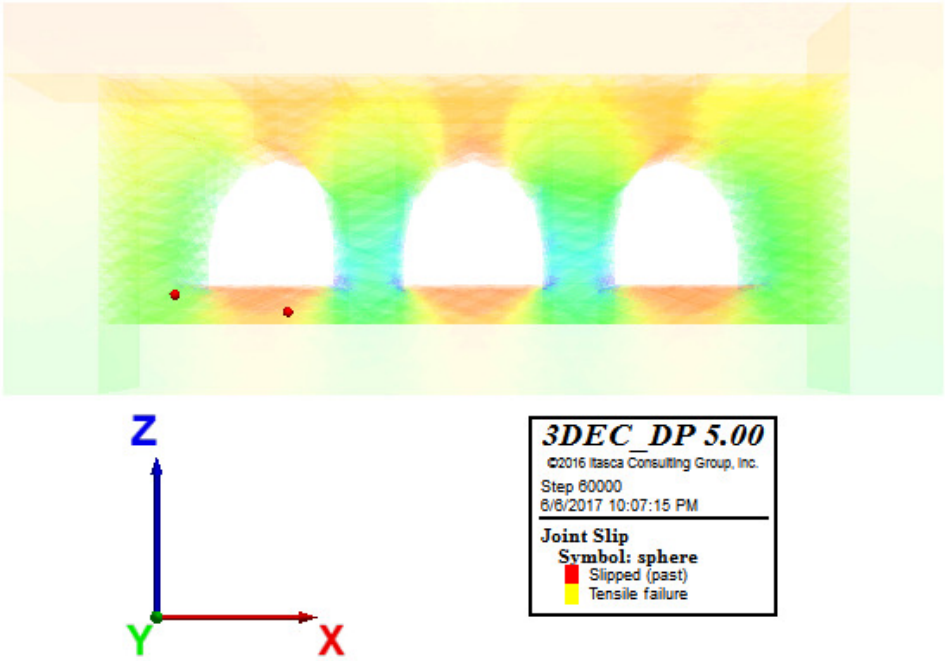

Figure 275. Model 36. Joint slip - Plasticity Limit indicator